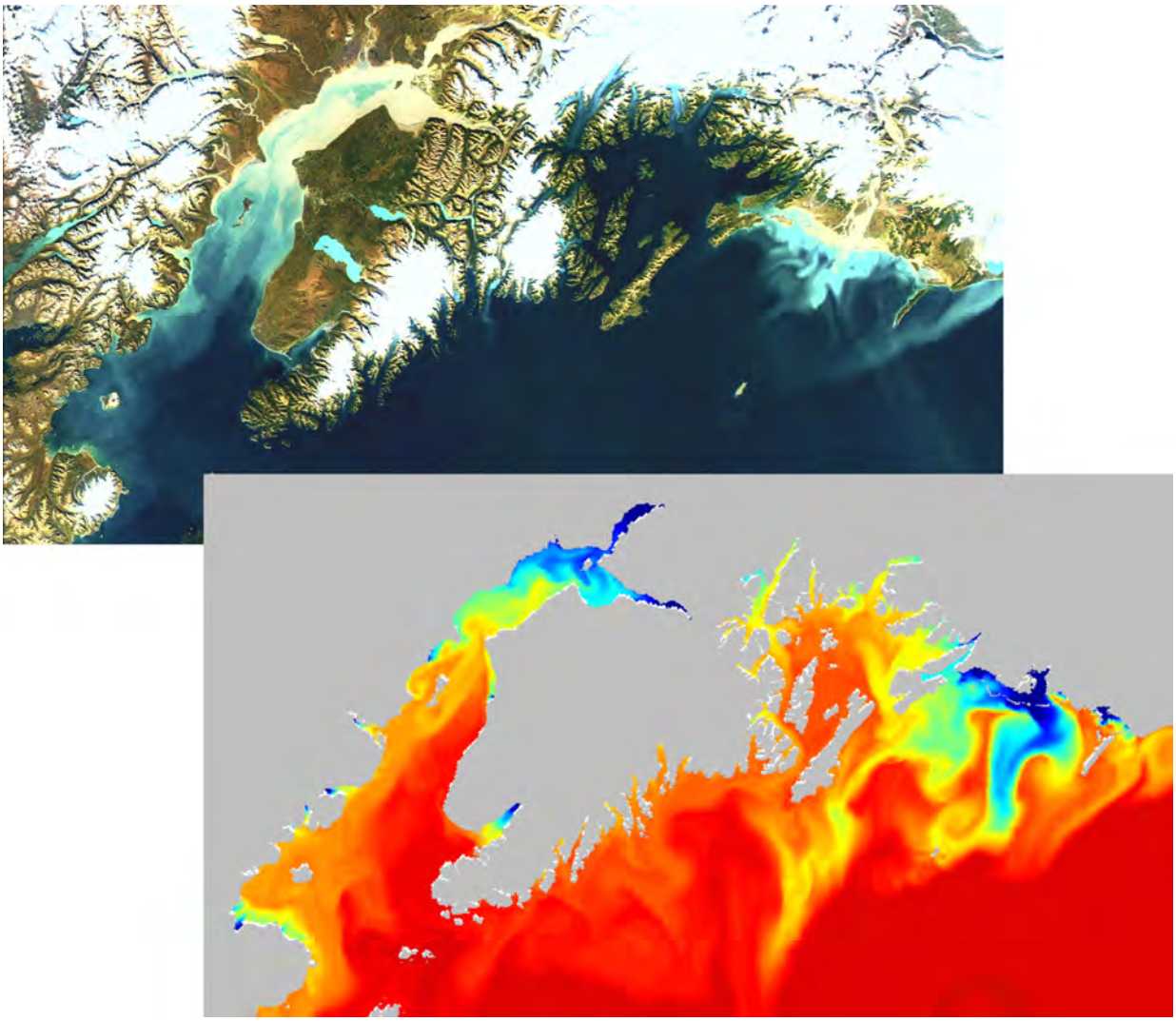

Cook Inlet Circulation Model Calculations

Final Report to the

U.S. Department of the Interior Bureau of Ocean Energy Management

Contract No. M14AC00014

Seth L. Danielson[1] sldanielson@alaska.edu
Katherine S. Hedstrom[1] kshedstrom@alaska.edu
Enrique Curchitser[2] enrique@marine.rutgers.edu

[1]Institute of Marine Science
School of Fisheries and Ocean Science
University of Alaska Fairbanks
905 N. Koyukuk Dr., Fairbanks AK, 99775
907 474-7834 (Office)
907 474 7204 (Fax)

[2]Institute of Marine and Coastal Sciences
Rutgers University
71 Dudley Rd., New Brunswick, NJ 08901
732-932-7889 (Office)
732- 932-8578 (Fax)

Cook Inlet Circulation Model Calculations

This collaboration between
the U.S. Department of the Interior Bureau of Ocean Energy Management,
the University of Alaska Fairbanks
and Rutgers University

was funded by the

the U.S. Department of the Interior
Bureau of Ocean Energy Management
Alaska Outer Continental Shelf Region
Anchorage AK 99503
under Contract No. M14AC00014

as part of the
Bureau of Ocean Energy Management
Alaska Environmental Studies Program

18 November 2016

Citation: Danielson, S. L., K. S. Hedstrom, E. Curchitser, 2016. Cook Inlet Model Calculations, Final Report to Bureau of Ocean Energy Management, M14AC00014, OCS Study BOEM 2015-050, University of Alaska Fairbanks, Fairbanks, AK, 149 pp.

Cover Image: NWGOA model sea surface salinity and Aqua Satellite 250 m pixel resolution false-color image of the northern Gulf of Alaska. Aqua image provided by NASA Rapid Response Land, Atmosphere Near real-time Capability for EOS (LANCE) system operated by the NASA/GSFC/Earth Science Data and Information System (ESDIS) with funding provided by NASA/HQ.

Table of Contents

List of Figures and Figure Captions

List of Tables and Table Captions

Abstract

This report describes the configuration, forcing, integration, and evaluation of a moderately high-resolution (~ 1.5 km horizontal resolution with 50 vertical layers) three-dimensional ocean circulation numerical model. The model domain encompasses the Northern and Northwestern Gulf of Alaska, including Cook Inlet, Shelikof Strait, Kodiak Island, Prince William Sound, and Kayak Island and it was integrated over the 10-year interval from January 1999 through December 2008. Model features include a modern high-resolution bathymetric digital elevation dataset, sea ice, a wetting-and-drying algorithm, moderately high-resolution reanalysis atmospheric forcing, tidal forcing with eight constituents, and a spatially explicit high-resolution coastal fresh water discharge time series. The coastal discharge has a daily time step so the coastal discharges include freshets associated with large precipitation or snow pack melt events.

We find that the model exhibits appreciable skill in reproducing observed tidal current directions, magnitudes and phases; tidal amplitude magnitudes and phases; and wind and buoyancy forced mean flow features on and near the northern Gulf of Alaska continental shelf. Observed tidal currents that are poorly reproduced by the model generally occur in constricted regions that are not well resolved by the model's grid spacing and bathymetry. We also find that the model hindcasts of the temperature and salinity fields reproduce those observed in Cook Inlet with a nearly 1:1 relation on average for 79 hydrographic CTD transects occupied during the model integration's time range, although there is a depth-dependent bias such that the model tends to be somewhat too saline and cool at depth and somewhat too fresh and warm at the surface. For all CTD data on these transects the average temperature offset is 0.65 °C (σ = 1.07), with the model slightly cooler than the observations; for salinity, the model hindcast is slightly more saline than the observations with a mean offset of 0.47 (σ = 1.05). Combined, 43% of the hindcast/observation pairs simultaneously agree to within 1 for both temperature and salinity and 86% agree to within 2 (°C and salinity units).

The model results provide new insights to the pathways of fresh coastal discharges and nutrient-rich basin waters and their variability.

1.0 Introduction

This section provides a brief review of the physical oceanography of the northwestern Gulf of Alaska, including thermohaline field characteristics, dominant flow field forcings, high frequency flow variations, and subtidal flows. We also summarize the project's relevance and underlying objectives in order to help place this report's findings within a broader context.

1.1 Background

The domain of the greater Gulf of Alaska (Figure 1) encompasses a tightly coupled set of basin, shelf, and estuary sub-domains whose characteristics each intimately depend upon physical forcings and processes occurring upon and within the adjacent sub-domains. Oceanic communication (waves, currents) between adjacent domains transmit volume fluxes, heat, fresh water and energy from one to another. For example, semidiurnal tides from the open ocean are resonant with the Cook Inlet embayment, and these dominate the local current, sea surface elevation, and mixing fields [*Muench et al.,* 1978; *Isaji and Spaulding,* 1987; *Foreman et al*., 2000; *Oey et al*., 2007]. Coastal fresh water discharges affect cross-shelf communications and the mean along-shelf background circulation field, including that of the nearshore (~ 30 km) Alaska Coastal Current (ACC) [*Muench et al.,* 1978; *Royer*, 1982; *Stabeno et al*., 2004; *Weingartner et al*., 2005; *Dobbins et al., 2009; Williams et al.,* 2010]. Long (~1000 km; e.g., low pressure systems) and short (< 100 km; e.g., gap winds) spatial structures in the wind field force local and region-wide flow responses [*Muench et al.,* 1978; *Wilson and Overland*, 1986; *Macklin et al.*, 1990; Ladd et al., 2016]. In addition, the basin, shelf and estuary bathymetry and topography exert defining control on the region's complex flow field. Below, we review the regional and local oceanographic conditions that contribute to these characteristics and the important processes and forcing mechanisms that maintain them. Their interactions help define the trajectory and fate of oil spilled in the ocean.

The eastward-flowing North Pacific Current (Figure 2) bifurcates as it approaches North America and the northward-flowing branch, the Alaska Current, forms the broad eastern leg of the Gulf of Alaska subarctic gyre, a system driven by the regional wind stress curl that is imposed by storm systems associated with the Aleutian Low atmospheric pressure distribution [*Wilson and Overland*, 1986; *Isoguchi et al,* 1997]. The southern branch of the North Pacific

Current bifurcation feeds the southward-flowing California Current. In the northern Gulf of Alaska, the Alaska Current accelerates westward as a western boundary current, labeled the Alaskan Stream in Figure 2. Large (> 100 km) eddies spawned in the northeastern and eastern gulf may be advected westward within the Alaskan Stream and these features influence physically, chemically, and biologically important shelf-basin exchanges [*Okkonen et al.,* 2003; *Ladd et al*. 2005; *Fiechter et al*., 2009; *Wu et al*., 2009; *Janout et al*., 2011].

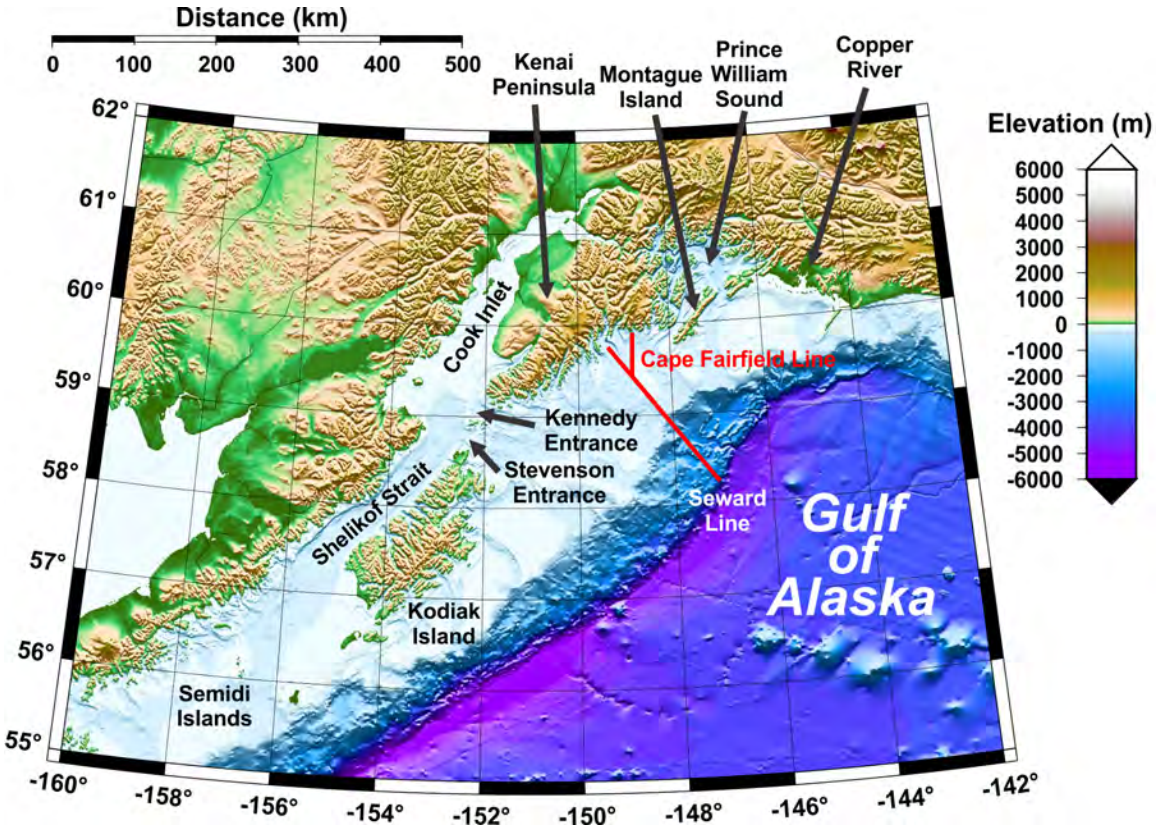

Figure 1. Map of Cook Inlet, Shelikof Strait and the adjoining Gulf of Alaska with place names and shaded relief based on the 1-km Alaska Region Digital Elevation Model (ARDEM). The Seward Line and Cape Fairfield Line hydrographic transects are shown with red lines.

The Gulf of Alaska is subject to the strongly seasonally varying cycles of winds, coastal discharge, and incident solar radiation [*Wilson and Overland*, 1986; *Reed and Schumacher*, 1989; *Stabeno et al*., 2004; *Weingartner*, 2005; *Hermann et al.,* 2009; *Janout et al.,* 2010]. With an increase in fall storm activity associated with the Aleutian Low, downwelling winds (negative upwelling) are prevalent between October and April and weakly downwelling or upwelling winds persist through summer months (Figure 3). These winds carry moist marine air over

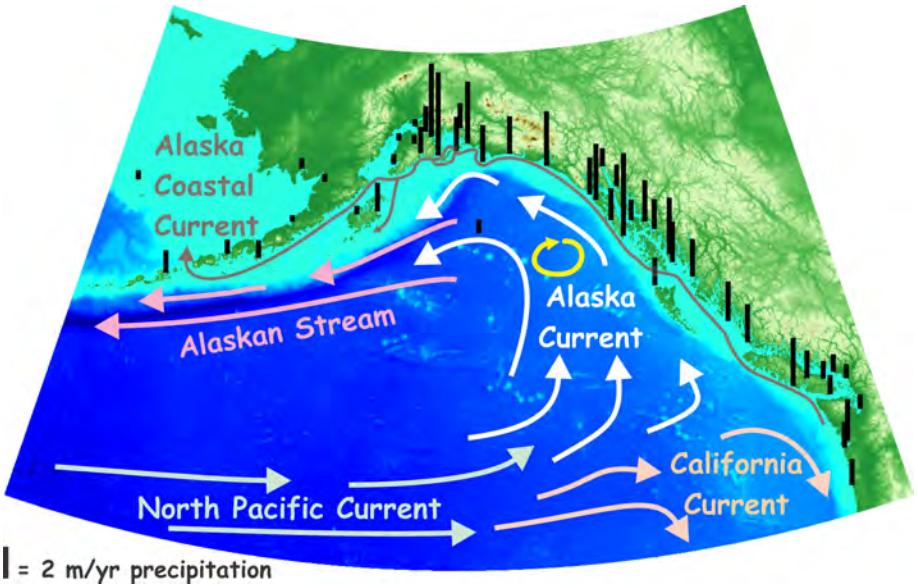

Figure 2. Map of the Gulf of Alaska surface mean circulation features and precipitation rates (vertical bars).

southcentral and southeast Alaska, where tall (> 2000 m) mountains extend from the Kenai Peninsula southeastward along the northeast Pacific coast.

Atmospheric convergence over the coastal mountains results in high precipitation rates (2-6 m yr^{-1}) in the coastal zone (Figure 2) [*Royer*, 1982; *Weingartner et al., 2*005] that eventually makes it way to the ocean. Precipitation is primarily stored as snow during winter. The high elevation snow pack melts during summer and storms increase in frequency in the fall so the annual discharge cycle of fresh water into the coastal zone (Figure 3) is maximum between September and November [*Royer*, 1979; *Royer*, 1982; *Weingartner et al.,* 2005; *Hill et al.,* 2015]. Surface heat fluxes along with the advection of heat from farther south drive the annual cycle of water column heat content and together with winds and salinity stratification [*Janout et al*., 2010] the vertical and horizontal density gradients in the coastal Gulf of Alaska define the ACC.

Over the inner shelf, the ACC represents a buoyancy and wind-driven coastal flow that is sensitive to the coastal discharge of fresh water [*Royer*, 1981; *Royer*, 1982; *Stabeno et al.,* 2004; *Weingartner et al.,* 2005]. The ACC undergoes a seasonal modulation in response to the cycles of fresh water and wind forcing (Figure 3). The balance maintains a “wedge” of low-salinity waters near the coast in fall that coincides with the annual maximum accumulation of fresh

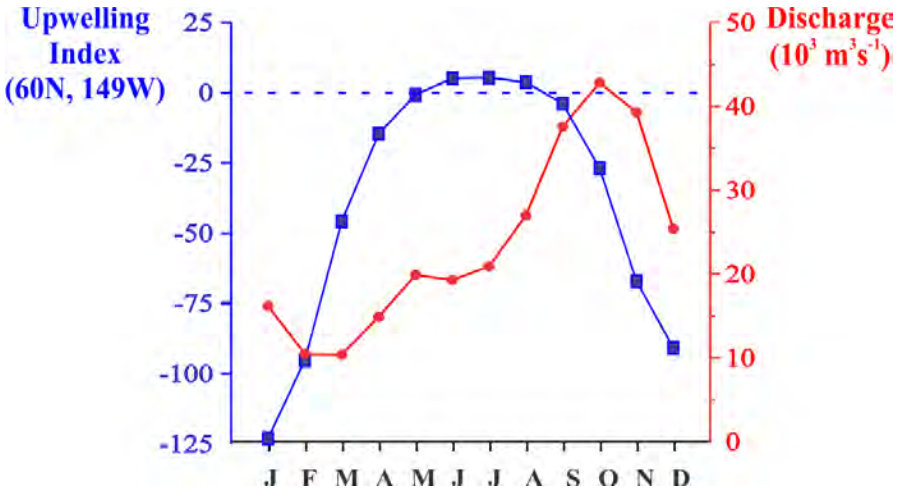

Figure 3. Annual cycles of two of the primary sub-tidal forcing mechanisms in the northern Gulf of Alaska: the (along-shore) upwelling wind index (blue) and the coastal runoff (red) following Royer [1982].

water discharge on the inner shelf (Figure 4, bottom panel). As fall and winter progress, these low-salinity waters are mixed downward and maintained close to shore under the influence of the typically downwelling winds, so that by early spring the fresh wedge transforms into a bottom-attached frontal system with nearly vertical isopycnals (Figure 4, top panel). In summer, weaker and occasionally upwelling winds in conjunction with increasing levels of solar radiation transforms the ACC into a surface-advected low-salinity plume in which the fresh waters can be readily advected offshore (Figure 4, middle panel). The ACC bottom-attached front during fall and winter is typically maintained within ~ 40 km of shore [*Weingertner et al.,* 2005], however it is susceptible to forming eddies and meanders as the coastal runoff increases and as it flows along the corrugated northern Gulf of Alaska coastline [*Johnson et al.,* 1988; *Ahlnas et al*., 1989]. Portions of the ACC may split and flow on either side of Montague Island, which separates Prince William Sound from the northern Gulf. Likewise, the ACC bifurcates near the southern tip of the Kenai Peninsula such that a portion flows into Cook Inlet and another portion attaches to the outer coast of Kodiak Island, bypassing Cook Inlet and Shelikof Strait [*Stabeno et al*., 1995]. The ACC is one of the important regional flow pathways (it carried Exxon Valdez oil from Prince William Sound to Shelikof Strait in 1989 [*Galt et al*., 1991]), so modeling and verifying an accurate representation of the ACC is of first order importance to the modeling study described here.

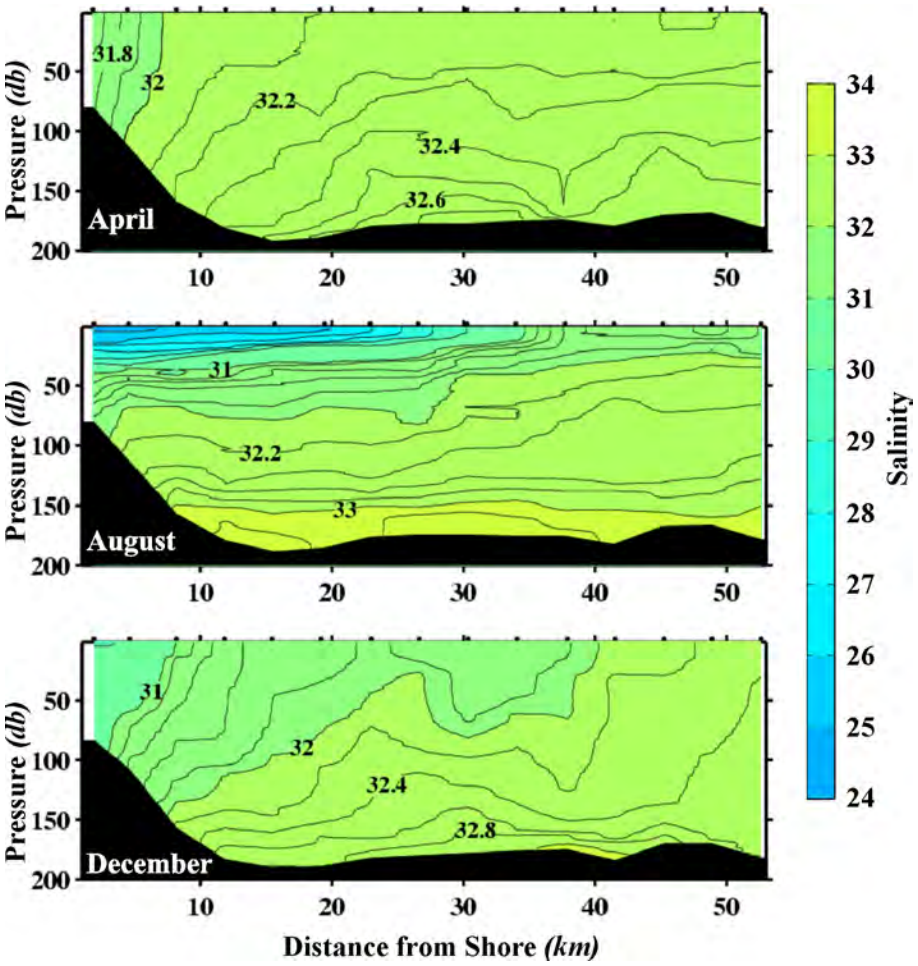

Figure 4. Horizontal cross-sections of vessel-measured salinity from the Cape Fairfield Line, which is just upstream of the focus study area (see Figure 1). The transects show the seasonal variability of the Gulf of Alaska's inner shelf haline structure. Black dots at the top of the sections locate the CTD profiles. Achieving an accurate depiction of the ACC upstream of Cook Inlet is critical to a realistic reproduction of the buoyancy forced currents within the study focus area.

The influence of wind forcing on the ACC was investigated with idealized numerical modeling by Williams [2003] and *Williams et al.* [2010], but the role of real-world winds in controlling the nearshore flow regime remains uncertain. In particular, temporal and spatial variations in the wind field and their effect on the ACC position and structure are poorly understood. Orographic influences on the wind field are likely important locally where the atmospheric pressure gradient is aligned parallel to the axis of topographically restricted channels, and such "gap wind" events with strong, spatially restricted winds are documented in the study region [*Lackmann and Overland*, 1989; *Maklin et al.,* 1990].

Tides are the dominant feature of the high frequency portion of the ocean current

spectrum in the Gulf of Alaska, and in Cook Inlet in particular [*Muench et al*., 1978; *Isaji and Spaulding*, 1987] and provide the bulk of the total kinetic energy. Cook Inlet's geometric proportions give rise to a strongly resonant semidiurnal tide (Figure 5 and Figure 6), with amplitudes of 3.5 m and 1.0 m for the M2 and S2 constituents, respectively, as measured at the port of Anchorage. The semi-enclosed Cook Inlet basin is ~250 km long and 30 - 50 m deep. Here, the wavelength of a freely propagating tide wave closely matches the resonance scale of 200-250 km [*Gill*, 1982; *Oey et al.* 2007; *Danielson et al.,* 2011]. The large tidal amplitude is further set over the greater Gulf of Alaska, where a large-scale amplification in the northeast Pacific may be due to the combination of the shelf width, L_S, with the tidal and inertial frequencies and the shelf bottom slope, α [*Clarke and Battisti*, 1981]. In the northern GOA, L_s is ~100-200 km, and while the bathymetry is highly irregular, α is primarily between 10^{-3} and 10^{-4} and the lower portion of this range satisfies the resonance criterion [*Danielson et al.,* 2011].

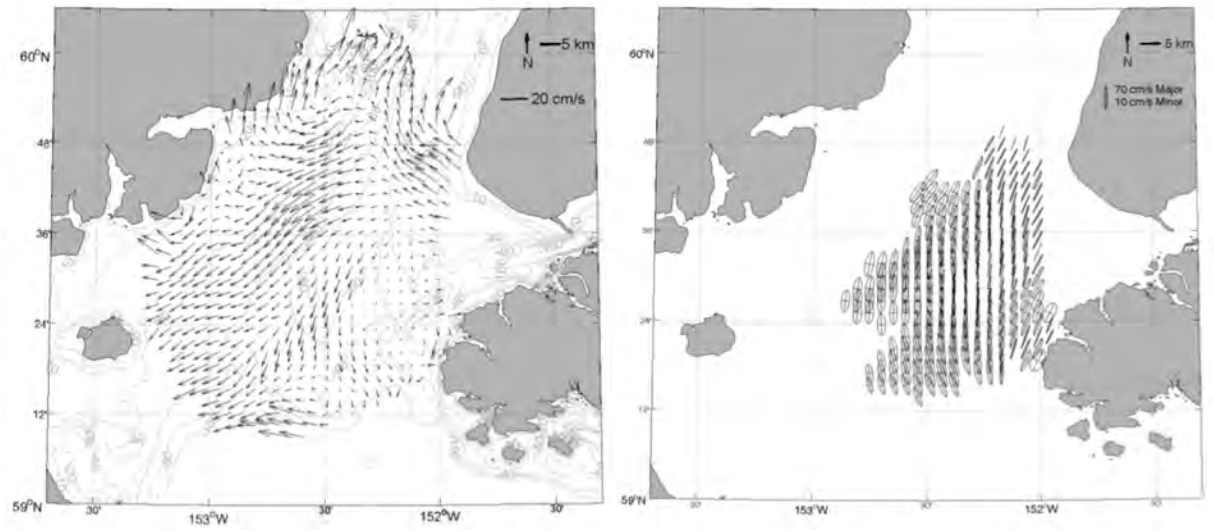

Figure 5. Stucture of the mean flow (left) and M2 tidal ellipses (right) in lower Cook Inlet as captured by high-frequency (HF) radar measurements. Reproduced from Weingartner et al. 2009.

Tidal currents in Cook Inlet are exceedingly strong, with instantaneous speeds that can exceed 4 m s^{-1}, and a tidal bore in upper Cook Inlet with peak heights of ~ 3 m [*Oey et al*., 2007]. M2 tidal currents alone are ~ 50-250 cm s^{-1} [*Muench et al*., 1978; *Muench and et al*, 1981a; *Isaji and Spaulding*, 1987; *Johnson*, 2008; *Potter and Weingartner*, 2009] and contribute to eddy kinetic energy levels exceeding 100 cm^2 s^{-2}, as measured by satellite-tracked drifters

[*Johnson,* 2008]. Previous observational and modeling studies reveal the importance of Cook Inlet and Shelikof Strait tidal and subtidal currents to the instantaneous ocean current field [*Johnson and Okkonen,* 2000; *Schumacher*, 2005; *Potter and Weingartner*, 2009], energy fluxes and dissipation [*Foreman et al*., 2000], tide-tsunami interactions [*Kowalik and Proshutinsky*, 2010], tide runup on exposed mudflats [*Oey et al.*, 2007], and physical controls on ecosystem dynamics [*Hermann et al.,* 1996; *Cheng et al.*, 2012; *Ezer et al.,* 2013]. As the dominant contributor to kinetic energy in the region, tides will have a strong influence on the dispersal of ocean-borne contaminants.

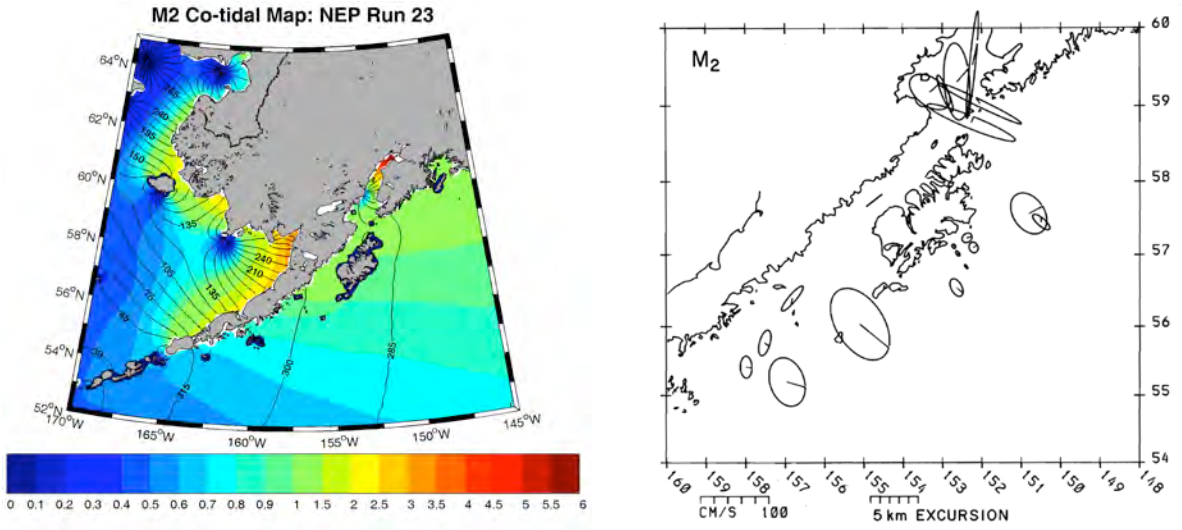

Figure 6. Left: Modeled co-tidal chart of the northwestern Gulf of Alaska and the eastern Bering Sea showing the M2 constituent tidal amplitude (color contours, given in meters) and phase (black contours, labeled in degrees). A quantitative analysis of the performance of the 3D model that generated the co-tidal map on the left is in *Danielson et al.* [2011]. Right: Moored current meter observed M2 tidal ellipses in the western Gulf of Alaska [*Muench and Schumacher*, 1980].

Although the majority of the total kinetic energy in the Cook Inlet and Shelikof Strait currents is tidal, buoyancy-driven subtidal currents are important for setting up the background flow features that contribute to the net circulation (Figure 5 and Figure 7). *Burbank* [1977] described the sub-tidal circulation of lower Cook Inlet based on Lagrangian current measurements and a survey of marine operators and this depiction today still qualitatively reflects our basic understanding of the flow field. *Muench et al.,* [1978] provided the first

modern oceanographic assessment of the region, documenting a southward flow along the western coast of Cook Inlet, a strong westward flow through Kennedy Entrance and a northward flow along Cook Inlet's eastern shore, and emphasizing the importance of strong vertical motions to mixing, biological processes and the fate of contaminants.

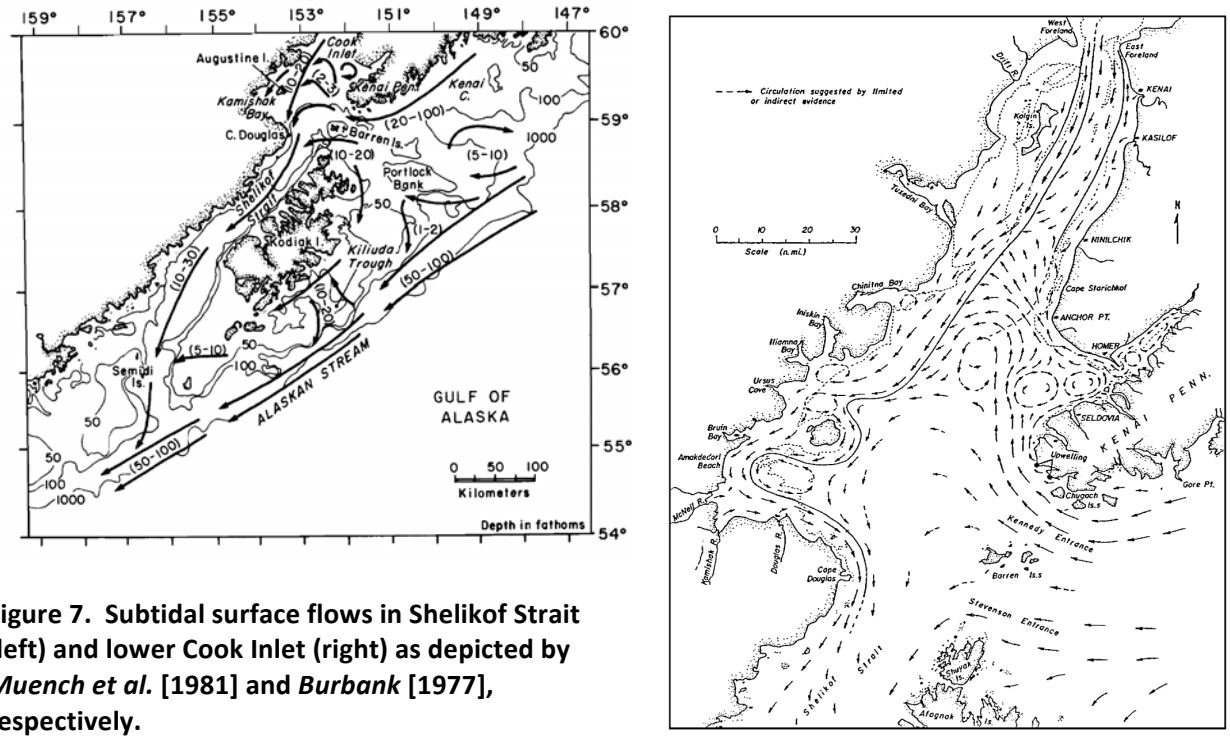

Figure 7. Subtidal surface flows in Shelikof Strait (left) and lower Cook Inlet (right) as depicted by *Muench et al.* [1981] and *Burbank* [1977], respectively.

While a portion of the ACC enters Cook Inlet through Kennedy and Stephenson entrances along the southern coast of the Kenai Peninsula and leaves Cook Inlet along its western shore, exiting Shelikof Strait to the southwest of Kodiak Island [*Muench et al*., 1978; *Schumacher and Reed*, 1980], the remainder of the ACC likely cuts across the Kennedy-Stephenson entrances and flows along the outside coast of Kodiak Island toward the southwest [*Stabeno et al*., 1995; *Stabeno et al., 2016*]. Flow is southward through Shelikof Strait on average, with strongest currents occurring in fall months that are associated with the annual maximum in buoyancy forcing due to coastal fresh water discharge [*Reed et al*., 1987; *Reed and Schumacher*, 1989], with a geostrophic transport on the order of 0.5-0.6 Sv (1 Sv = 10^6 m^3 s^{-1}) [*Reed and Schumacher,* 1989; *Reed and Bograd*, 1995]. Total transport could be ~ 0.65-0.85 Sv [*Schumacher et al.,* 1989; *Stabeno et al*., 1995] with daily peak transports of up to 2.5 Sv

[*Stabeno et al*., 1995]. The mean flow is prone to generating instabilities, and the seasonally varying mean background current likely influences their formation [*Mysak et al.,* 1981; *Schumacher et al*., 1990; *Schumacher et al.,* 1993]. Isothermal and isohalines are generally deeper on the right hand side (Alaska peninsula side) of the Strait as viewed from the northeast and these are associated with the swiftest baroclinic flows [*Reed et al.,* 1987].

The basic nature of the Cook Inlet-Shelikof Strait region is well described but we lack a comprehensive understanding about the combined role of wind, tide and buoyancy forcing on these waters, the associated short time and space scale spatial and temporal variabilities, and the impact of these variations on the regions' subtidal circulation. Studies that address these complex interactions are just now beginning to address and clarify their effects on the physical and biological systems that depend on them [e.g, *Cheng et al*., 2012; *Colas et al.* 2013; *Coyle et al.,* 2012; *Coyle et al*., 2013].

1.2 Relevance of this study

The results from this project will be used for BOEM Oil Spill Risk Analysis (OSRA) in the study region by providing the necessary model output fields to generate oil-spill trajectory estimates. The OSRA will inform the management decisions that BOEM will need to make as it oversees oil and gas leasing, exploration, and development and production on the Outer Continental Shelf. Thus, the results generated by this project could directly impact coastal sites and stakeholders in and beyond the Cook Inlet Planning Area. Stakeholders include petroleum development companies, the State of Alaska, the Cook Inlet Regional Citizen's Advisory Council (CIRCAC), local communities and their residents, marine vessel operators, and commercial and sport fishermen, in addition to the marine birds, fish, mammals and invertebrates that reside in or migrate through areas potentially subject to the effects of petroleum development or oil spills. Therefore, it is of highest importance that the numerical integrations that inform the OSRA are carried out with the best available modeling approach and tools.

Our approach to model validation is better described as model-data comparison and assessments. These are designed to highlight both the strengths and the weaknesses of the numerical model results. With this approach, we ensure that BOEM and the other stakeholders listed above can more easily interpret the model and OSRA results in the context of real-world

applications.

Additionally, the results of this study will be able to inform many scientific studies beyond the scope of this immediate project that will increase our understanding of the oceanography of the study area. A better understanding of ecosystem functioning and linkages in the Gulf of Alaska marine system is needed, and numerical model outputs such as that described herein provide an important tool for analysis and hypothesis generation. The region's currents are subject to the hourly, synoptic, seasonally, and inter-annually varying impact of winds, fresh water discharges, solar radiation, and astronomical tides, and they further interact with the region's bathymetry to set and adjust to the vertical and horizontal density gradients. Application of a multi-year high-resolution numerical model that incorporates sufficient domain extent and small enough horizontal scales (e.g., below the internal Rossby radius of deformation) offers promise for significant advances in our understanding of the Cook Inlet and Shelikof Strait physical and biological oceanography.

1.3 Objectives and deliverables

The objective of this project was to apply state-of-the-art numerical modeling methods to generate and validate a 10-year ocean circulation hindcast for the waters of the Northwest Gulf of Alaska (NWGOA), with particular focus on Cook Inlet and Shelikof Strait. We accomplished this by nesting a moderately high-resolution (~1.5 km) numerical model within a well-tested and extensively applied medium-resolution (10 km) regional model that spans the greater Northeast Pacific (NEP) [*Curchitser et al*., 2005; *Curchitser et al*., 2010; *Danielson et al.,* 2011] and modifying the NWGOA model (with accompanying sensitivity tests) to meet the project objectives. The model results were compared with a broad suite of observational data from the study region. These analyses are carried out in order to assess the model's ability to reproduce the study region's oceanographic characteristics.

A detailed ROMS operators manual (update of *Hedstrom* [2009]) accompany the model results so that BOEM employees and others will be able to properly interpret and apply the model results or even run their own ROMS model integrations. Model outputs were delivered to BOEM in the form of hourly gridded 3-D velocity and surface wind fields that required in total 22 TB of hard drive disk space.

2.0 Technical Approach: Coupled ocean-sea ice models

The main research tool for this study is a coupled ocean/sea ice numerical model based on the Regional Ocean Modeling System (ROMS). ROMS is a free-surface, hydrostatic primitive equation ocean circulation model whose core was developed at Rutgers University and UCLA with significant contributions from a large community of users.

ROMS is a terrain-following, finite volume (Arakawa C-grid) model with the following advanced features: extensive restructuring for sustained performance on multi-processor computing platforms (using MPI); high-order, weakly dissipative algorithms for tracer advection; a unified treatment of surface and bottom boundary layers [e.g., K-Profile Parameterization; *Large et al*., 1994], atmosphere-ocean flux computations based on the ocean model prognostic variables using bulk-formulae [*Fairall et al.,* 2003; *Large and Yeager*, 2009] and an integrated set of procedures for data assimilation (e.g., optimal interpolation and adjoint-based methods [*Moore et al*., 2004]. ROMS also has an integrated float tracking capability. The vertical discretization is based on a terrain-following coordinate system with the ability to increase the resolution near the surface and bottom boundary layers. ROMS has been coupled to a sea-ice model [*Budgell*, 2005] consisting of the elastic-viscous-plastic (EVP) rheology [*Hunke and Dukowicz*, 1997] and the *Mellor and Kantha* [1989] thermodynamics. The ice module is fully explicit and implemented on the ROMS Arakawa C-grid and is therefore fully parallel using MPI, just as ROMS is. The model also includes frazil ice growth in the ocean being passed to the ice [*Steele et al*., 1989]. It currently follows a single ice category, which exhibits accurate results in a marginal ice zone such as Cook Inlet.

2.1 Configuration and forcing

To date, we have carried out multi-decadal integrations of ROMS-based coupled ocean/sea ice models in the North Pacific, the Bering Sea, the North Atlantic, and the Arctic and Southern Oceans [e.g., *Curchitser et al.,* 2005; *Hermann et al*., 2009*; Kang and Curchitser*, 2013, *Meccia et al., 2013*]. The present application is with the moderate-resolution Northeast Pacific (NEP) model (Figure 7) and the high-resolution Northwest Gulf of Alaska (NWGOA) model (Figure 8). The NWGOA model is nested within the NEP model to achieve a higher fidelity downscaling to better resolve the study region's local flow dynamics.

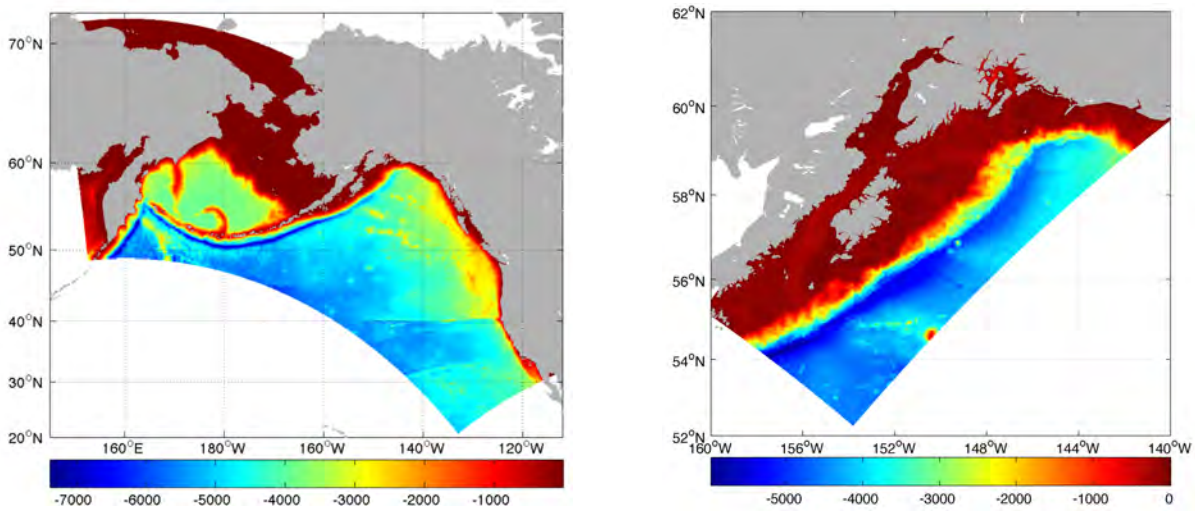

Figure 8: Bathymetric depths (m) and domain extent (colored regions) of the 10 km NEP model (left), and the NWGOA model (right).

The NEP model domain (Figure 8) extends from approximately 20°N to 71°N and extends 2250 km offshore from the North American coast at a nominal horizontal resolution of 10 km and with 50 vertical levels stretched towards the surface boundary. The grid (a rectangle in a Lambert Conical projection) is rotated relative to lines of constant latitude and longitude so as to minimize computations over land. The terrain-following coordinate system has distinct advantages for modeling shelf regions. The full vertical coordinate system is compressed over the shelf resulting in high vertical resolution in the region of interest and as a consequence no computations are wasted in the bathymetry. The NEP model bathymetry is based on the high-resolution ~ 1 km soundings-based Alaska Region Digital Elevation Model (ARDEM) assembled by PI Danielson [*Danielson et al*., 2011; *Danielson et al., 2015*]. This digital elevation model avoids the errors associated with bathymetric grids that are based off of digitized chart contours [*Marks and Smith,* 2006] and gravimetric anomalies inherent within satellite-based depth products over shelf regions.

The NEP model (and the NWGOA model, in turn) is forced via one-way nesting of global ocean reanalysis using a hybrid of nudging and radiation approaches [*Marchesiello et al*., 2001] for the open boundary condition. This global-to-regional-to-local downscaling via open boundary conditions has several distinct advantages for the implementation of regional models. Some of these include the following. For multi-decadal integrations, climate signals project onto

the high-resolution inner domains through boundary forcing. Tidal forcing [*Egbert and Erofeeva*, 2002] is naturally implemented on the domain open boundaries.

Surface forcing comes from NASA's 1979-2012 Modern Era Retrospective Analysis for Research and Applications (MERRA) high-resolution global reanalysis model to force the NWGOA model. MERRA provides wind, air temperature, sea level pressure and specific humidity, and shortwave and downwelling longwave radiation, with 1-hour time steps (subsampled to 3-hourly) on a 1/2° latitude by 2/3° longitude grid. While this grid resolution is not sufficient to resolve the smallest atmospheric spatial scales, it is sufficient to represent some of the finer details of the pressure systems and orographic effects that are not well captured by the 2.5° reanalysis products typically used for multi-year hindcasts. For example, the MERRA resolution is very close to the 1/2° latitude by 1/2° longitude winds derived from the National Center For Environmental Prediction's (NCEP's) operational Global Data assimilation System that forces the Wavewatch III model used for operational wave forecasting in the Gulf of Alaska [*Chao*, 2003]. This wind product exhibits appreciable skill in resolving small-scale wind structures in the Gulf of Alaska (see http://polar.ncep.noaa.gov/waves/).

The air-sea fluxes are computed using bulk formulae [*Large and Yeager*, 2009], which are appropriate for high-latitude situations. Oceanic mixing is computed using a generic length-scale mixing scheme [Umlauf and Burchard, 2003; Warner et al. 2005]. Riverine inputs are derived from the monthly and interannually varying dataset of *Dai et al.,* [2009]. Boundary and initial conditions for the NEP domain are derived from the global 1/12° data-assimilating and reanalysis/real time HYbrid Coordinate Ocean Model (HYCOM) project [e.g., *Chassignet et al*., 2009], a facet of the U. S. Global Ocean Data Assimilation Experiment (GODAE) after 2008 and the Simple Ocean Data Assimilation (SODA) reanalysis prior to 2008 [Carton et al., 2000; Carton et al., 2000b]. Tidal forcing comes from the Oregon State University tidal inversion based on satellite altimeter sea surface height measurements [*Egbert and Erofeeva,* 2002], and over the Gulf of Alaska shelf the NEP model typically achieves constituent M2 amplitude relative error (compared to amplitude derived from analyses of coastal tide station records and shelf mooring data) of less than 5%.

The above description of the NEP model forcing and implementation also applies to the

NWGOA domain (Figures 7 and 8). However, the latter grid incorporates a number of additional improvements that take advantage of the nested grid methodology. The NWGOA grid resolution is ~ 1.5 km, the domain size is 1100 x 550 km, and the model domain contains 733 x 367 grid points. Hence, the NWGOA model horizontal resolution provides it the ability to better resolve the fronts, eddies, and constricted flows within Cook Inlet, Shelikof Strait, and Prince William Sound. The NWGOA model extends from west of the Shumagin Islands to east of the Copper River and Kayak Island (~ 1100 km in length) and offshore beyond the continental shelf break (~ 550 km wide). With this large domain, we ensure that the important upstream conditions that set the character of the ACC (e.g., fresh water discharge from the Copper River and in Prince William Sound) and its buoyancy-forced jet can evolve and adjust prior to entering Cook Inlet and Shelikof Strait. The model extends far enough west so that drift trajectories emanating from within Shelikof Strait will remain within the integration domain for on average at least 30 days (15 cm s^{-1} average flow rate would carry a drifter 388 km; the domain extends ~450 km west of Shelikof Strait proper). Oil from the Exxon Valdez Oil Spill moved at ~ 10-13 km day^{-1} while in the ACC outside of Prince William Sound [*Galt et al*., 1991] We note that previous 3D modeling in Shelikof Strait with a 9-layer sigma-coordinate numerical model having 4 km horizontal resolution was able to reproduce observed mean current patterns and satellite-tracked drifter trajectories over a limited comparison [*Hermann and Stabeno*, 1996; *Hermann et al*., 1996; *Stabeno et al.*, 1996].

The large tidal range that exposes the extensive mud flats of upper Cook Inlet suggests that a numerical modeling approach that incorporates a wetting and drying (WAD) algorithm would improve tidal predictions. Indeed, *Oey et al*. [2007] find that a WAD approach appreciably influences the tide's amplitude and propagation of phase in upper Cook Inlet. The ROMS model includes a WAD algorithm and the ARDEM bathymetric grid used for the NEP and the NWGOA models includes both land topography and ocean bathymetry elevations, enabling us to implement the WAD algorithm. While the bathymetry used for the NWGOA model began as only the ARDEM version 2.0 grid, in the course of our model evaluations we determined that the ARDEM grid underestimated water depths in Cook Inlet, leading to inaccurate tidal amplitudes and phases. A modified ARDEM bathymetric DEM provided the best fit to observed

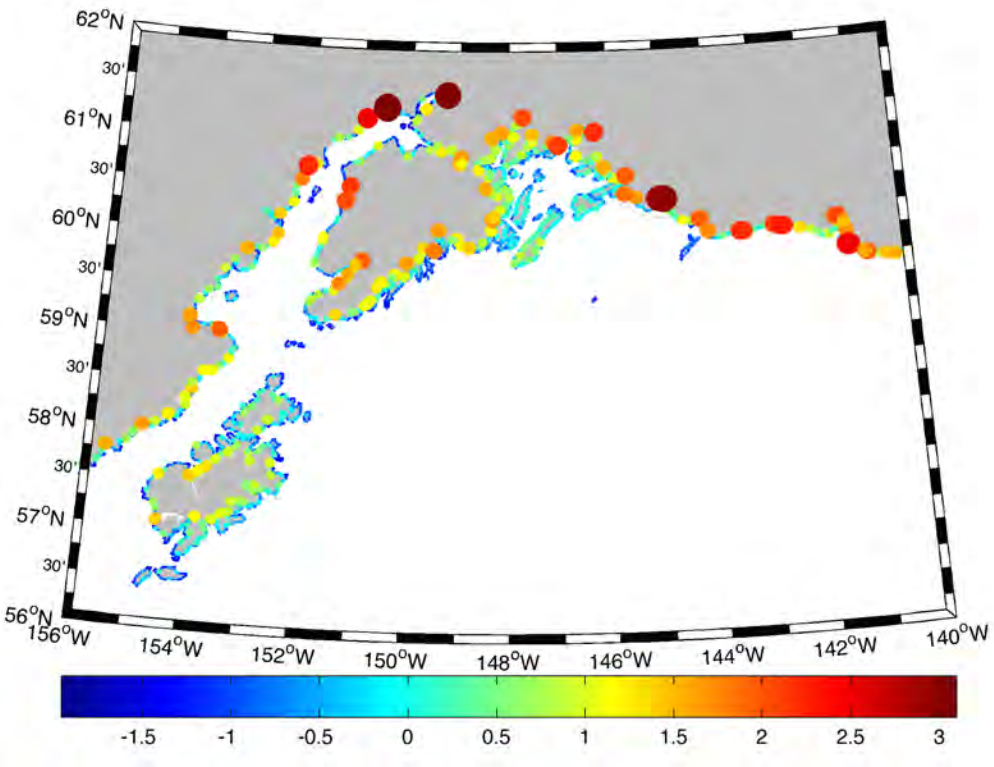

Figure 9. Ten-year (1999-2008) mean discharge along the Gulf of Alaska coast from the *Beamer et al.* [2016] terrestrial discharge model into the NWGOA model. Colors and circle sizes are scaled to show the log (base 10) of the mean annual discharge at individual NWGOA grid points. Color shading depicts units of $m^3 s^{-1}$.

tidal amplitudes and phases (see Section 3.1 below for details of the model evaluation and implemented adjustments).

Given the importance of the seasonally varying fresh water discharge to this region's coastal dynamics [*Royer,* 1982; *Wang et al*., 2004; *Dobbins et al., 2009; Hill et al.,* 2015], the explicit inclusion of both large and small discharges across the domain is critical to achieving more realistic current simulations on the inner shelf and determining the fate of advected material across the entire shelf. We note that even recent high-resolution numerical models of the northern Gulf of Alaska have difficulty in reproducing the strength of the ACC stratification and achieving bias-free haline fields [*Coyle et al.,* 2012; *Farrara, et al.,* 2013; *Li et al*., 2013]. Therefore, we implemented multiple point-source river inputs to force these inflows. The terrestrial "pour point" discharges are calibrated against USGS gauged discharge measurements as described in *Beamer et al.* [2016], using a land-based hydrological model that routes runoff, snow pack melt, glacial melt and groundwater discharges using a temporally and spatially

explicit reanalysis weather and precipitation field and static land topography. An example of one of the major Cook Inlet discharge time series, at the Kenai River, is shown in Figure 10.

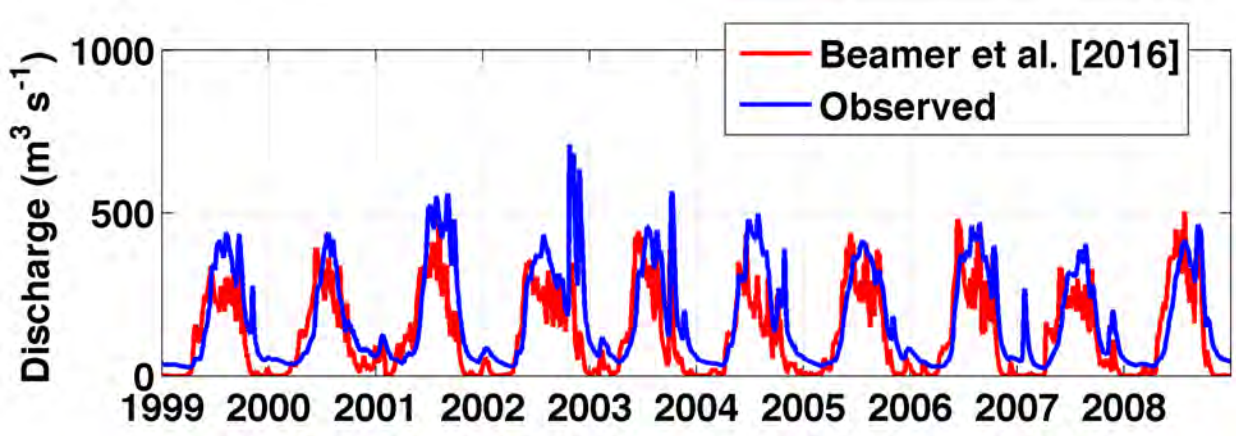

Figure 10. Daily discharge time series from the USGS streamflow measurements on the Kenai River (blue) and from *Beamer et al*. [2016] over the full hindcast integration period.

The *Beamer et al*. [2016] time series is a high-resolution (~ 1 km) 1979-2009 gridded coastal discharge time series for the Gulf of Alaska that accounts for the Gulf of Alaska discharge "line source" attributable to the many ungauged discharges in the region [*Royer*, 1982]. In some cases, individual rivers enter the model domain through more than one grid cell wall. For example, the Kenai River has three primary pour points, the Susitna River has five, and the Copper River has six. As the most temporally limiting forcing field available to the model runs described here (ending in 2009), we carried out our integrations to overlap with the most recent ten years of the *Beamer et al*. [2016] data product.

There exist some aspects of the *Beamer et al.* [2016] reconstructed discharge times series that do not perfectly reproduce the observational record. For example, the observed discharge at Kenai (Figure 10) maintains a somewhat higher minimum streamflow through winter months and exhibits higher peaks during most summers. We note that the version of the *Beamer et al*. [2016] time series provided to our effort was an early release of this data and that some discharge model improvements have been implemented since. Nonetheless, the discharge time series does provide a spatially and temporally explicit discharge record with daily variations that capture the magnitude (usually to better than a factor of two) and phasing of the coastal runoff. For the purposes of forcing a model that is developed to reproduce the statistics of the actual ocean, the runoff model provides a significant step in the direction of this

goal. Although not well shown in Figure 10, comparison of the two discharge records shows that the hydrology model does (at times) reasonably capture the magnitude and phase of individual precipitation and discharge events on the order of days in length. Hence, this forcing field provides a more advanced fresh water forcing signal than is available from any other source and allows us to better capture the seasonally adjusting response of the shelf waters to the coastal runoff.

2.2 Model Integrations

The existing NEP model regional-scale integration results provided oceanic boundary conditions for the high-resolution NWGOA domain (Figure 8) multi-year hindcast. A previous BOEM study helped fund the development of the NEP model, including the implementation and validation of tides and sea ice [*Curchitser et al.,* 2010; *Danielson et al*., 2011]. Under support from the National Science Foundation, the NEP model was recently updated and run through calendar year 2012.

The NWGOA model simulations incorporated the following setup, features, and integration parameters:

- Ten-year (1999-2008) hindcast (timed to take advantage of the best and most complete observational data for comparisons and the highest resolution forcing fields)
- 50 vertical levels
- 1.5 km horizontal grid spacing
- 900 km x 550 km domain size
- Domain includes the Copper River delta and Prince William Sound, where important Gulf of Alaska fresh water discharges enter the system.
- Bathymetry based on the updated 1-km ARDEM bathymetric/topographic grid
- Distributed hybrid line source/point source coastal fresh water discharge forcing based on an early version of Beamer et al. [2016]
- Atmospheric forcing from the NASA MERRA reanalysis
- Oceanic boundary conditions from the NEP regional model
- Sea ice algorithm
- Tidal forcing
- Wetting and drying algorithm for run-up computations over Cook Inlet and Copper River area tidal flats

Hourly model output history files that included the full 3-D advective and tracer fields were archived. To facilitate analysis and evaluation, we also deployed passive floats at select sites within and upstream of Cook Inlet and Shelikof Strait in order to better understand

transport pathways, flow trapping locations, residence times, and the effect of wind on the ACC. Floats were initiated at 50 sites and two depth levels (5 m and 50 m) once every 30 days and then tracked for a year or when they left the NWGOA domain, whichever came first. We also archived hourly 3-d fields in a time series mode at approximately 200 select locations that are co-located with many historical tide and current meter mooring stations as well as repeat transect stations. The floats and the time series stations data, while not part of the BOEM data deliverables, are nonetheless available on request from the science team.

3.0 Model Results and Model-Data Comparisons

An integral part of this study is a quantitative analysis of the model performance. We rely on a combination of historical and recent observational datasets for model validation, with particular focus on current meter mooring velocity and shipboard hydrographic data collections from the study region within the time period of the model hindcast. Our incorporation of the model assessments into the design process ensures an efficient path to model improvements in each iteration of the design-integrate-evaluate-redesign model development spiral. The analyses provide users of the model output a better understanding of the strengths and limitations of integration results.

3.1 Tide Amplitude and Phase

Because the semidiurnal and diurnal portion of the velocity spectrum account for a dominant fraction of the total kinetic energy budget in Cook Inlet, we devoted particular effort early in the model development phase to evaluating and improving the model's ability to accurately reproduce Cook Inlet tides.

Conservation of volume and momentum dictates that the tidal amplitude, phase, and currents are all intimately linked through a numerical model's basin lateral geometry and depths [*Gill,* 1982]. Initial integrations showed (a) that too much tidal wave damping occurred in Cook Inlet when the ARDEM bathymetry was used (see integration #9 results in Table 1) and (b) that reducing the bottom friction did not sufficiently address the problem. From this we deduced that the ARDEM Cook Inlet bottom depths were on average somewhat too shallow. We obtained a second modern bathymetric grid for the Cook Inlet region only (a bathymetric grid used in some unrelated NOAA high-resolution modeling). The NOAA bathymetry was found to be a bit deeper on average than the ARDEM bathymetry. In replacing the ARDEM depths in Cook Inlet with these new depths, the integration showed too little damping for the M_2 constituent, although the diurnal amplitudes were fairly close to those observed (see integration #11 in Table 1). An average of these two bathymetric grids depths produced tidal amplitudes that were closest to those observed along the length of Cook Inlet and for reasonable values of bottom friction (see integration #12 in Table 1).

Table A1. Observed and modeled tide harmonics parameters (M_2, S_2, K_1, and O_1) for sea level gauges at Anchorage, Nikiski, Seldovia, and Kodiak in model integrations #9, #11 and #12. The integration #12 (in bold) bathymetry configuration was used for all other results described below.

Station	Constituent	Integration	Amplitude (m)		Phase (°)	
			Model	Observed	Model	Observed
Anchorage	M2	#9	1.9	3.57	131	103
		#11	5.12		119	
		#12	**3.51**		**132**	
	S2	#9	0.43	0.80	158	147
		#11	1.23		149	
		#12	**0.76**		**160**	
	K1	#9	0.29	0.89	333	345
		#11	0.87		319	
		#12	**0.62**		**331**	
	O1	#9	0.06	0.39	217	334
		#11	0.34		314	
		#12	**0.16**		**315**	
Kodiak	M2	#9	0.92	0.97	315	308
		#11	0.93		313	
		#12	**0.92**		**314**	
	S2	#9	0.25	0.27	340	343
		#11	0.27		338	
		#12	**0.25**		**339**	
	K1	#9	0.44	0.53	302	290
		#11	0.44		303	
		#12	**0.44**		**303**	
	O1	#9	0.22	0.25	299	267
		#11	0.22		300	
		#12	**0.22**		**299**	
Seldovia	M2	#9	1.98	2.23	337	325
		#11	1.66		340	
		#12	**1.81**		**338**	
	S2	#9	0.58	0.67	359	1
		#11	0.49		1	
		#12	**0.53**		**0**	
	K1	#9	0.64	0.76	285	282
		#11	0.64		285	
		#12	**0.64**		**285**	
	O1	#9	0.29	0.36	279	262
		#11	0.29		280	
		#12	**0.29**		**279**	
Nikiski	M2	#9	3.29	2.50	56	33
		#11	2.90		66	
		#12	**3.04**		**61**	
	S2	#9	0.93	0.69	79	67
		#11	0.79		89	
		#12	**0.83**		**85**	
	K1	#9	0.9	0.85	303	311
		#11	0.9		299	
		#12	**0.91**		**302**	
	O1	#9	0.43	0.39	298	296
		#11	0.43		296	
		#12	**0.43**		**298**	

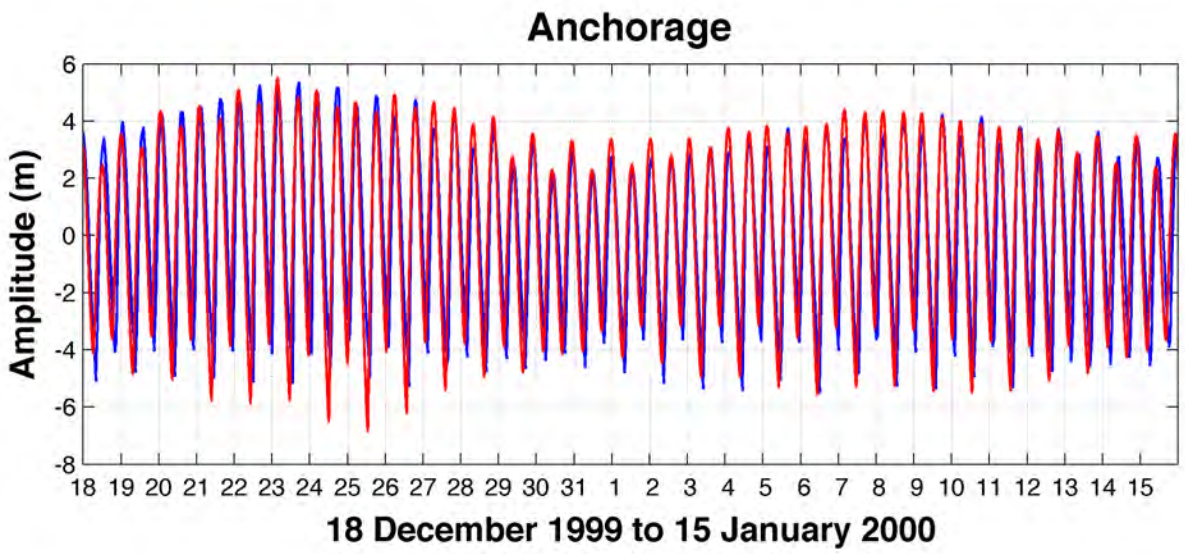

Figure 11. Modeled (blue) and observed (red) sea surface elevation at the Anchorage tidal station for 18 December 1999 to 15 January 2000 in NWGOA model integration #12.

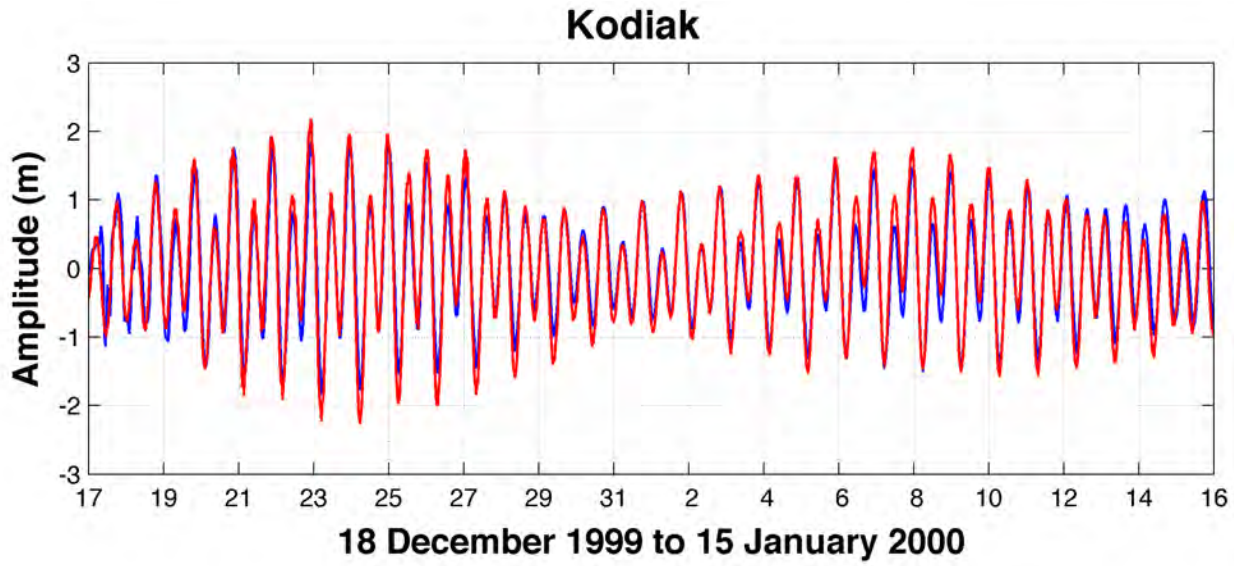

Figure 12. Modeled (blue) and observed (red) sea surface elevation at the Kodiak tidal station for 18 December 1999 to 15 January 2000 in NWGOA model integration #12.

The modeled and observed records from the Anchorage tidal station are shown in Figure 11 for integration #12. The root-mean-square difference (RMSD) between these two time series is 1.38 m with a Pearson's cross-correlation of r = 0.83. A maximum correlation of 0.96 occurs at a lag of 1 hour, for which the RMSD is 0.61 m. This lag corresponds nearly exactly to the 29° M_2 phase offset between the model and observations for integration #12 (Table 1). In aggregate, with a one-hour offset (model lagging observations), the model reproduces 92%

of the observed variance at Anchorage with a typical error that is ~ 15% of the instantaneous amplitude. For the tide gauge station at Kodiak, at the opposite side of Cook Inlet (Figure 12), the maximum correlation for the same time interval occurs at zero phase lag with a Pearson's correlation of r=0.96 and RMSD of 0.21 m.

Although integration #11 showed diurnal constituent amplitudes that were generally closer to those observed than integrations #9 and #12, the predicted parameters in integration #12 were appreciably closer to those observed for the more energetic semi-diurnal constituents (Table 1). On balance, we decided that the integration #12 provided the optimal configuration and all results reported below in this study employ the hybrid Cook Inlet bathymetry used in this integration.

In order to assess model performance at both semi-diurnal and diurnal frequencies, we select the dominant semi-diurnal tide (constituent M_2) and the dominant diurnal tide (constituent K_1) to support the majority of our analyses. Cotidal charts generated from the NWGOA model integrations for these two constituents are shown in Figures 13-14 for M_2 and Figures 15-16 for K_1. These charts compare reasonably well to amplitude and phase patterns depicted in prior Cook Inlet and Gulf of Alaska tide model and observation studies (e.g., *Muench and Schumacher* [1980]; *Foreman et al*. [2000]).

We note that a weak but discernable enhancement of the K_1 constituent appears along the outer shelf region. A similar trapping of the diurnal constituent was observed in the modeling by *Foreman et al*. [2000], whose high-resolution barotropic finite element model was well configured to resolve the shelf break topography although we note that the *Foreman et al*. [2000] model was a hybrid of the 5-minute ETOPO-5 elevation model and an early version of the *Smith and Sandwell* [1997] satellite gravimetrics bathymetry. Neither of these bathymetric datasets are today considered state-of-the art. The *Foreman et al*. [2000] model was 2-dimensional, and the authors point out that the structure of the amplitudes and phases are presumably somewhat less accurate with such a setup. Nonetheless, our results depict a K1 amplitude greatest near the Kodiak Island shelf break and weaker farther along the slope to the east. We find also that K_1 currents are also enhanced to the south and east of Kodiak Island (shown below in Section 3.2).

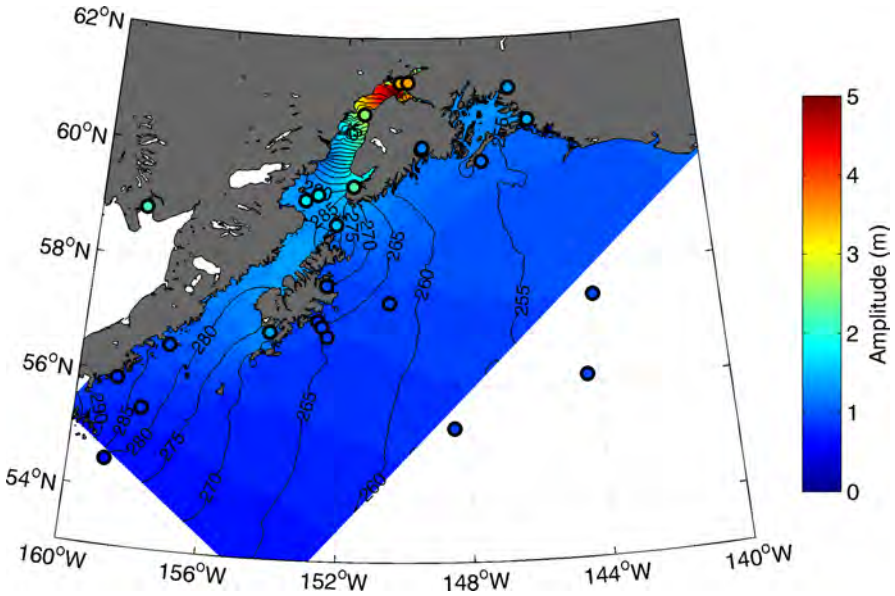

Figure 13. Amplitude (color shading) and phase (black contour lines) cotidal chart for the M_2 constituent over the NWGOA model domain. Observed amplitudes are plotted inside thick black circles using the same color scale as for the model amplitudes.

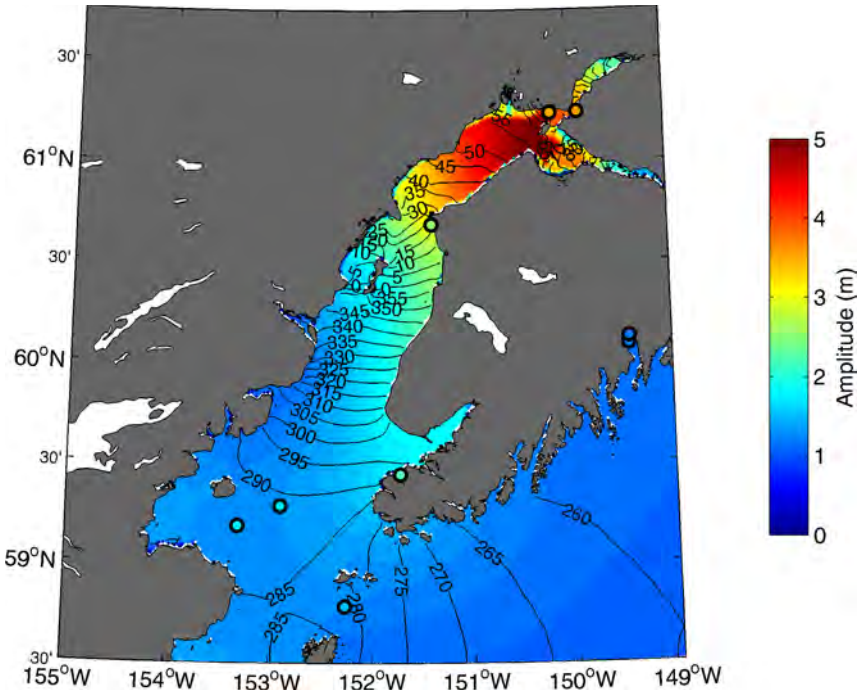

Figure 14. Amplitude (colors) and phase (black contour lines) cotidal chart for the M_2 constituent in Cook Inlet. Observed amplitudes are plotted inside thick black circles using the same color scale as for the model amplitudes.

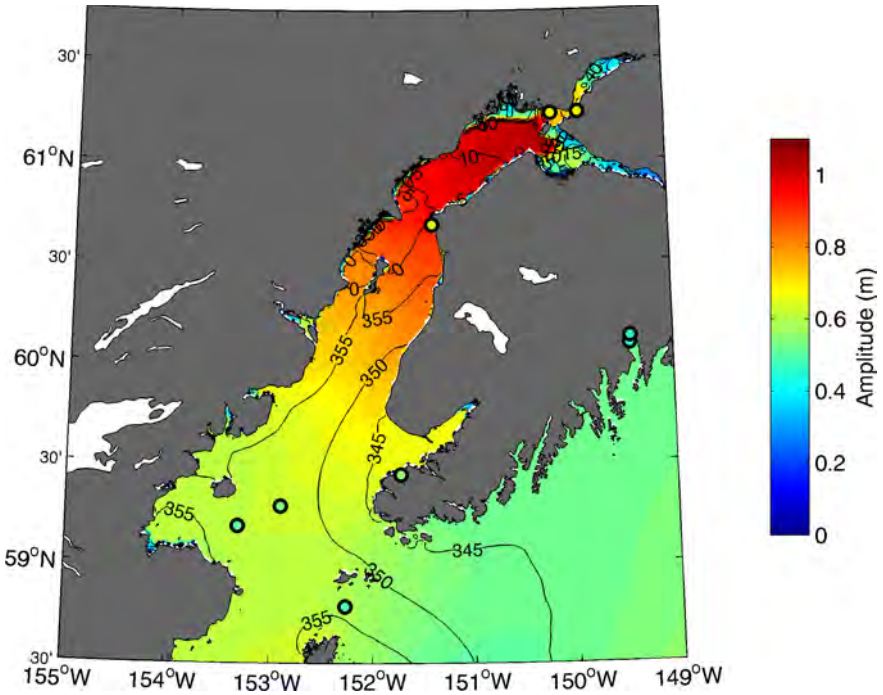

Figure 15. Amplitude (colors) and phase (black contour lines) cotidal chart for the K_1 constituent over the NWGOA model domain. Observed amplitudes are plotted inside thick black circles using the same color scale as for the model amplitudes.

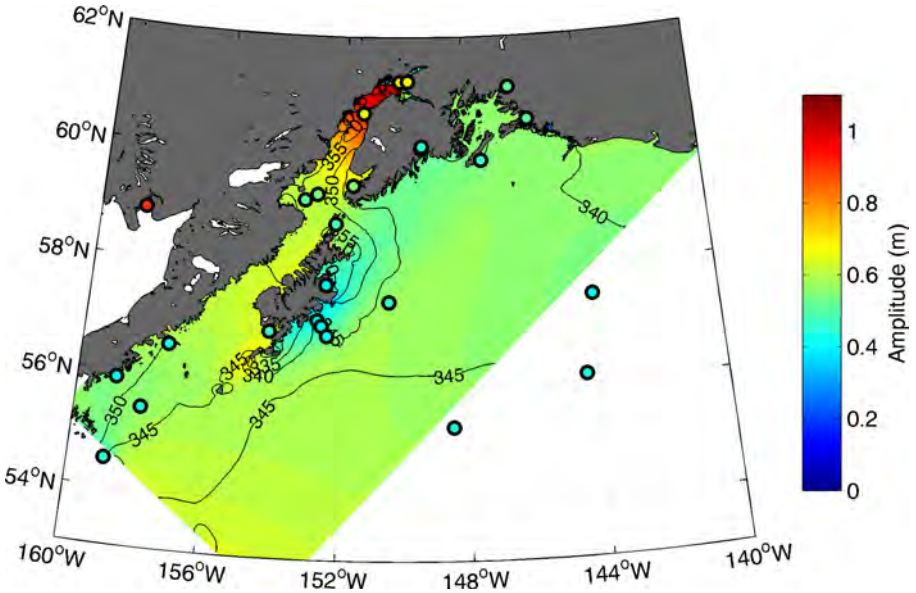

Figure 16. Amplitude (colors) and phase (black contour lines) cotidal chart for the K_1 constituent in Cook Inlet. Observed amplitudes are plotted inside thick black circles using the same color scale as for the model amplitudes.

3.2 Tidal Currents

Modeled tidal current ellipses for the M_2 and K_1 constituents are shown in Figures 16-22 along with tidal ellipses from moored current meter stations shown in red and black. Recent data were collected using acoustic Doppler current profilers (ADCP), while data from the 1970s and 1980s were collected using rotary current meters (RCM). The modeled ellipses are subsampled for clarity in these figures, and the ellipses from only every 5th grid point are depicted. The observed current harmonic parameters are taken from existing compilations (e.g., *Danielson et al*., 2011) and from tidal parameters computed directly from raw data obtained at the NOAA Currents Measurements Interface for the Study of Tides (CMIST), which can be found online at: *https://cmist.noaa.gov/cmist/*. The CMIST Internet portal is an archive of data developed by the Center for Operational Oceanographic Products and Services (CO-OPS), a branch of NOAA's National Ocean Service (NOS).

The CMIST datasets are collected with typically 1-2 month deployment durations and six-minute averaging ensembles using Teledyne RDI 300 KHz Workhorse acoustic Doppler current profilers (ADCPs). A minimum of one month's worth of data collected with hourly intervals is required for computation of 29 tidal frequencies, so the deployment parameters are sufficient to capture the majority of the tidal energy. However, these datasets can not be used to resolve constituent K1 from P1 nor will the analyses capture many of the higher order shallow water tides

For station COI0419, a 2004 current meter mooring deployment in southern Cook Inlet, the deployment and operations parameters are described with the following metadata, which is representative of the CMIST datasets:

```
Station ID                     : COI0419
Station Name                   : Anchor Point West
Project Name                   : Cook Inlet 2004 Current Survey
Project Type                   : Tidal Current Survey
Requested Data Start           : 2004/08/06 00:00
Requested Data End             : 2004/09/15 12:00
Deployment Depth (m)           : 51.5
Deployment Latitude (deg)      : 59.83933
Deployment Longitude (deg)     : -152.36833
GMT Offset (hrs)               : 9
Sensor Type                    : Workhorse ADCP
Sensor Orientation             : up
Sensor Frequency (khz)         : 300
Number of Beams                : 4
Number of Bins Sampled         : 40
Bin Size (m)                   : 2.0
Blanking Distance (m)          : 1.76
Center to Bin 1 Distance (m)   : 4.22
Platform Height From Bottom (m) : 8.53
```

Tidal ellipses are elongated with high eccentricity in regions that the effects of shallow depths and bottom or sidewall friction are strongly felt. We note that the model accurately produces ellipse magnitudes in some of the constricted regions such as in the passages connecting Prince William Sound to the greater Gulf (Figures 17 and 21 and Table A1). On the other hand, the model has difficulty in reproducing observed tidal ellipses at many sites close to Kodiak Island (Figures 18 and 22 and Table 1A), where many of the current meter deployments took place in constricted flow fields between islands within inlets. Many of these passages, while important to mariners, are often not well resolved by even the NWGOA model's relatively high horizontal resolution.

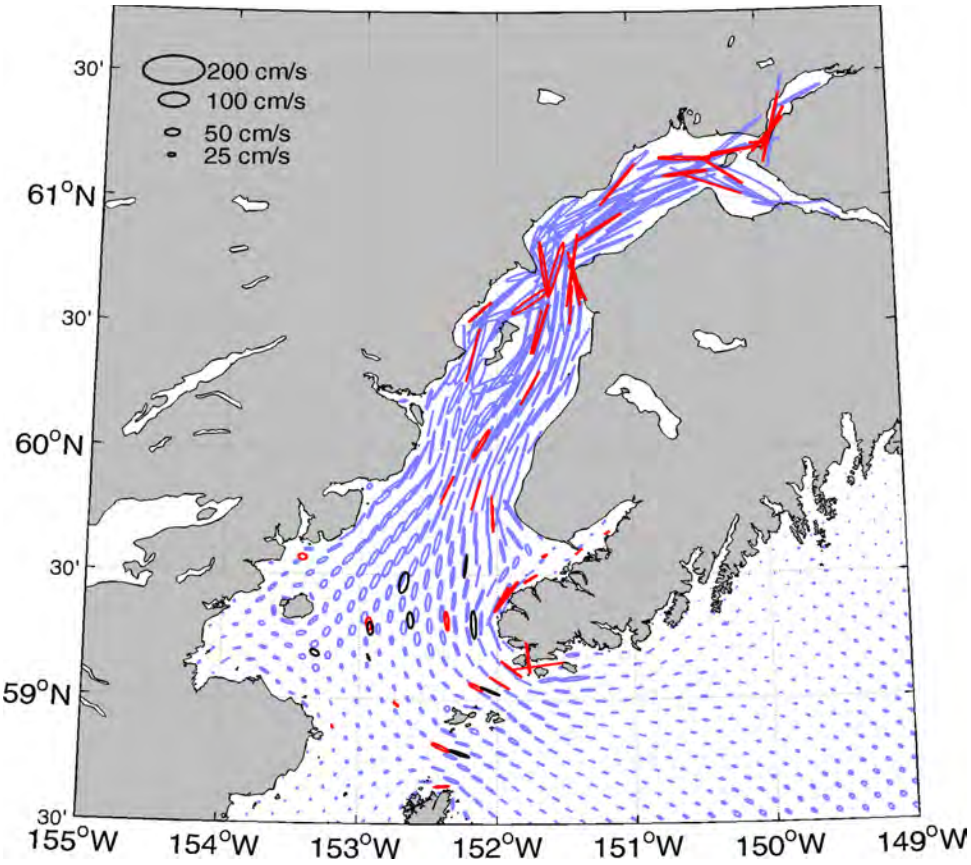

Figure 17. Constituent M_2 tidal current ellipses in Cook Inlet from the model (blue), and observed (red=ADCP; black=RCM). Ellipses from every 5th model grid point are plotted. Scale ellipses have an eccentricity of 1:2.

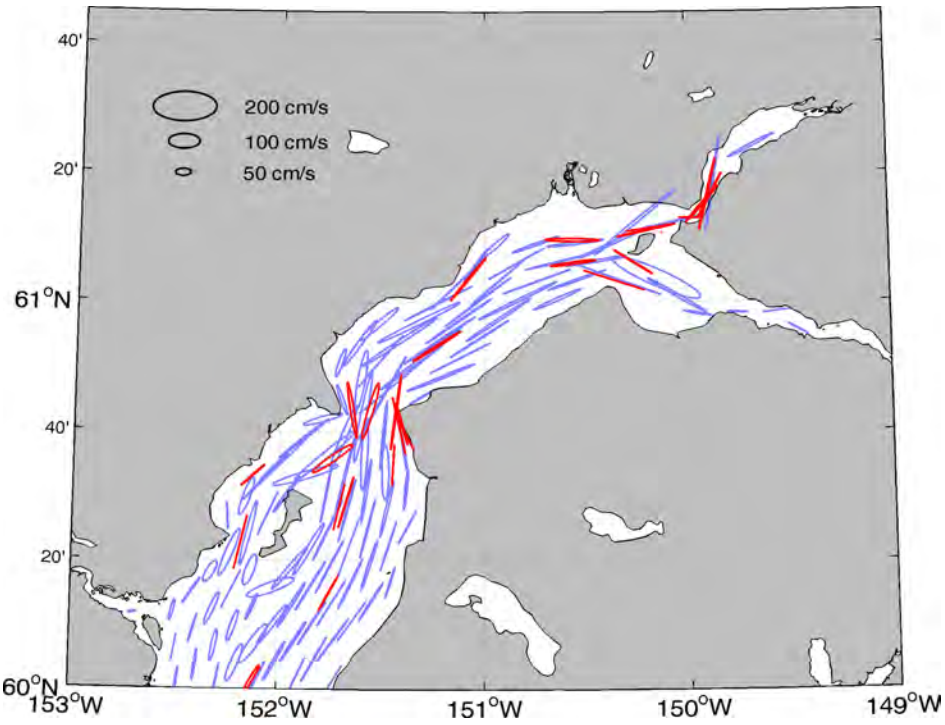

Figure 18. Constituent M_2 tidal current ellipses in Upper Cook Inlet from the model (blue), and observed (red=ADCP; black=RCM). Ellipses from every 5th model grid point are plotted. Scale ellipses have an eccentricity of 1:2.

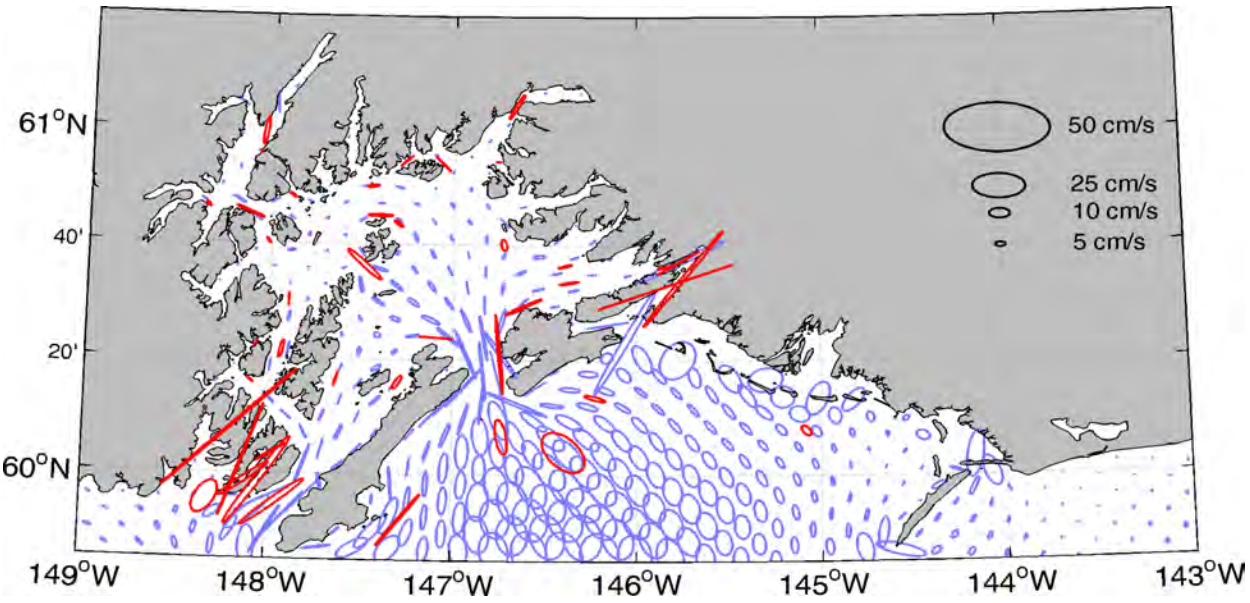

Figure 19. Constituent M_2 tidal current ellipses in Prince William Sound and the Copper River delta from the model (blue), and observed (red=ADCP; black=RCM). Ellipses from every 5th model grid point are plotted. Scale ellipses have an eccentricity of 1:2.

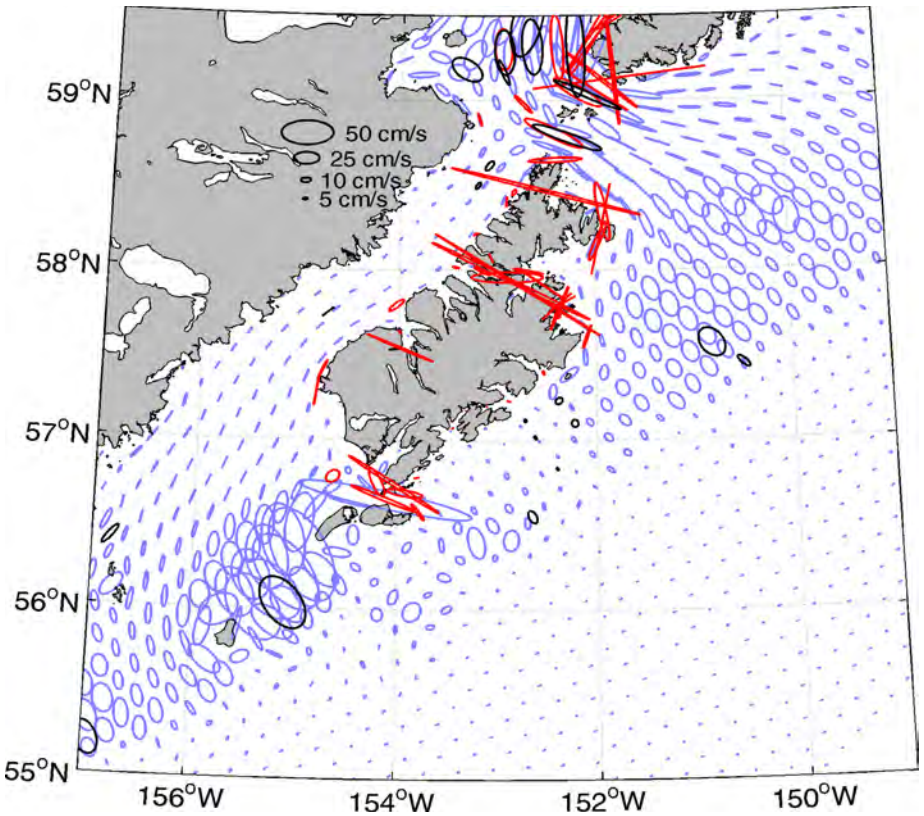

Figure 20. Constituent M_2 tidal current ellipses near Kodiak Island from the model from the model (blue), and observed (red=ADCP; black=RCM). Ellipses from every 5th model grid point are plotted. Scale ellipses have an eccentricity of 1:2.

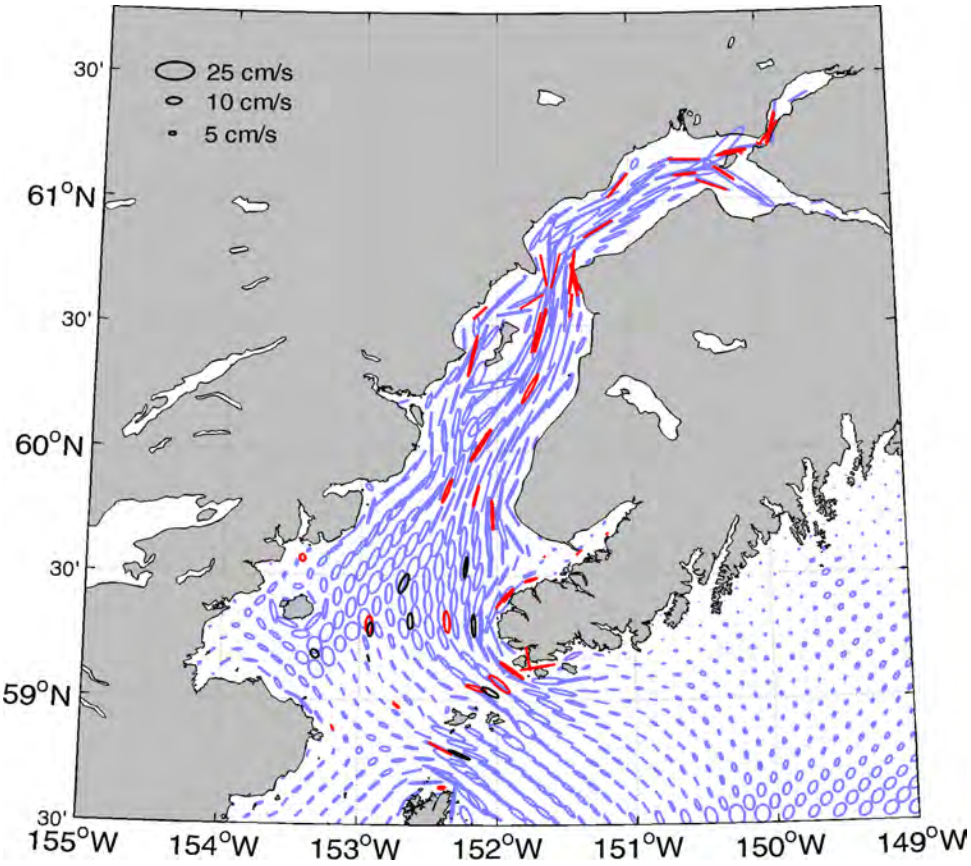

Figure 21. Constituent K_1 tidal current ellipses in Cook Inlet from the model (blue), and observed (red=ADCP; black=RCM). Ellipses from every 5th model grid point are plotted. Scale ellipses have an eccentricity of 1:2.

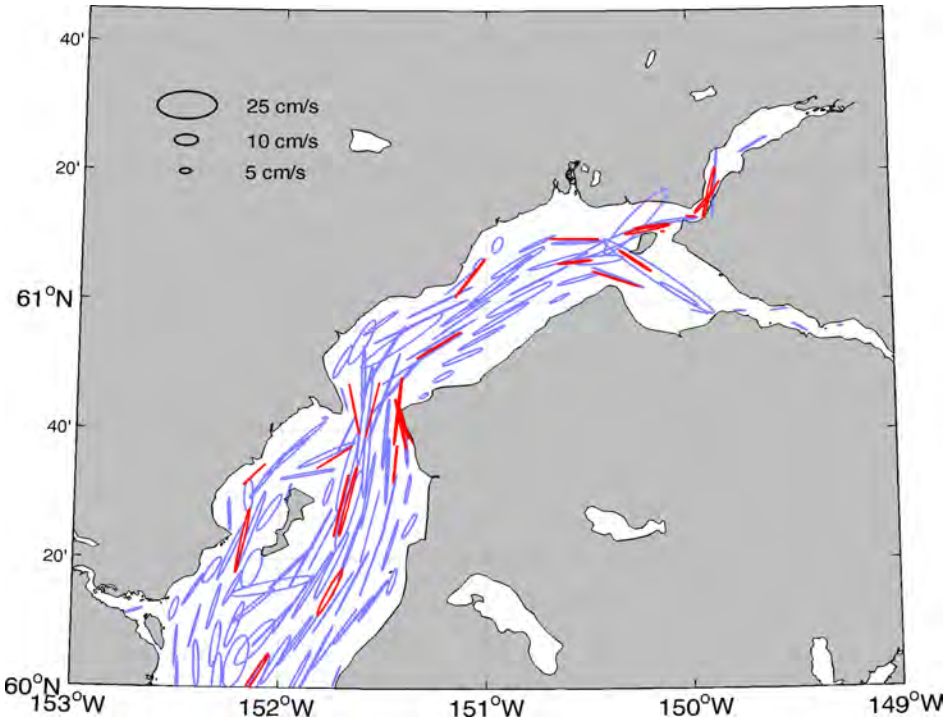

Figure 22. Constituent K_1 tidal current ellipses in upper Cook Inlet from the model from the model (blue), and observed (red=ADCP; black=RCM). Ellipses from every 5th model grid point are plotted. Scale ellipses have an eccentricity of 1:2.

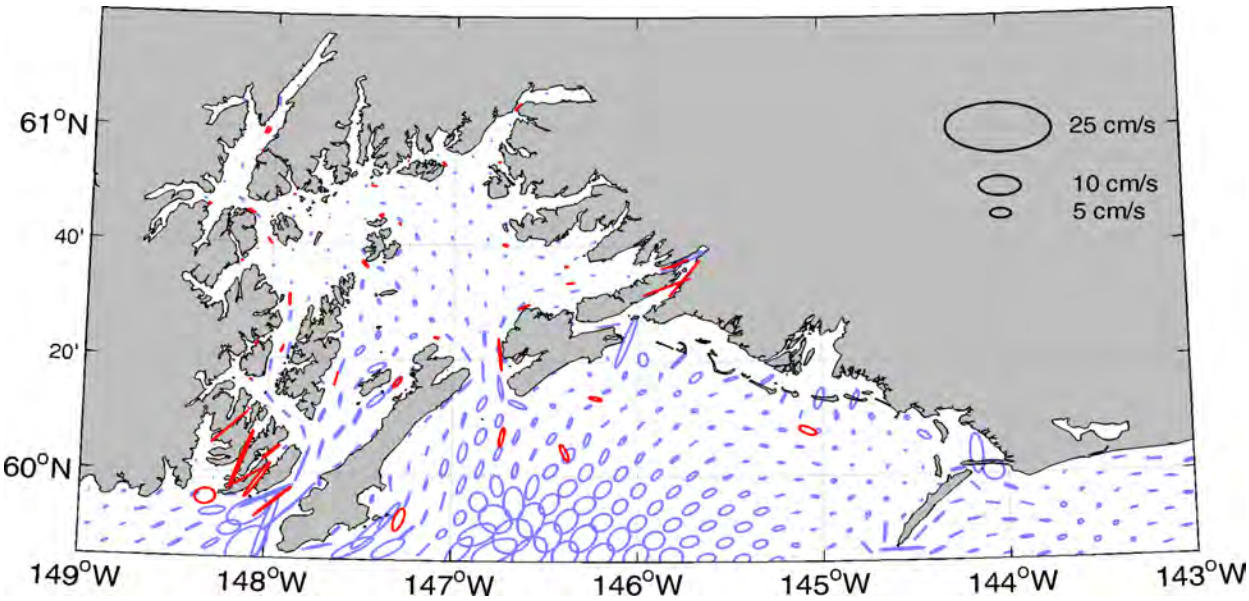

Figure 23. Constituent K_1 tidal current ellipses in Prince William Sound and near the Copper River delta from the model (blue), and observed (red=ADCP; black=RCM). Ellipses from every 5th model grid point are plotted. Scale ellipses have an eccentricity of 1:2.

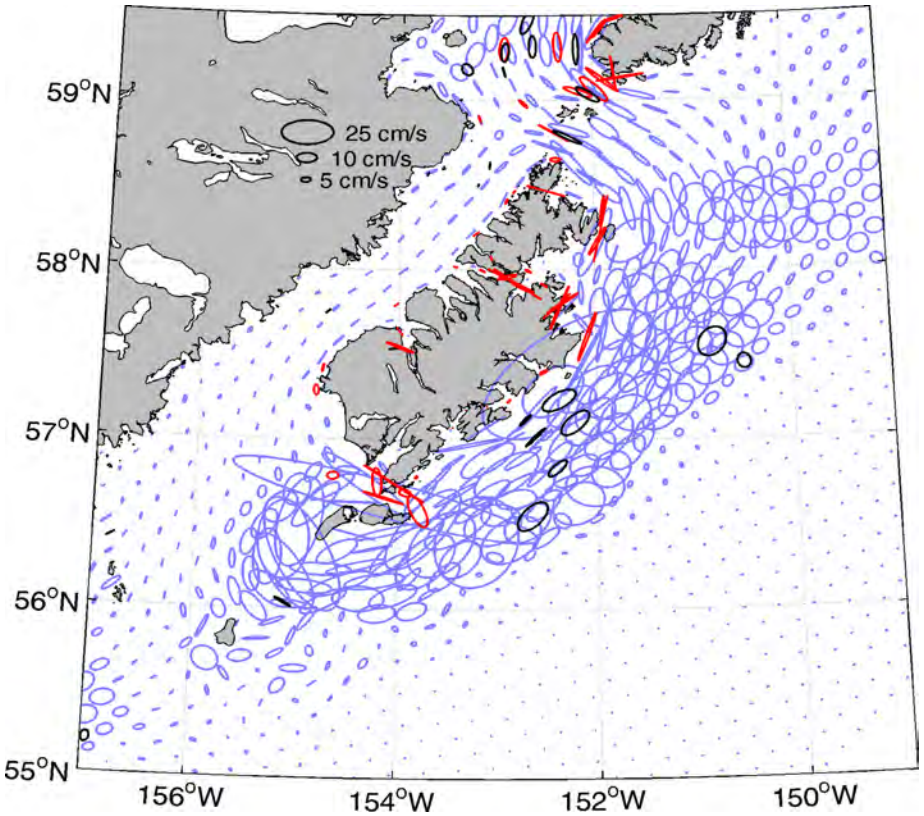

Figure 24. Constituent K_1 tidal current ellipses near Kodiak Island from the model from the model (blue), and observed (red=ADCP; black=RCM). Ellipses from every 5th model grid point are plotted. Scale ellipses have an eccentricity of 1:2.

3.3 Subtidal Flow Field

Figures 25 and 26 depict the 10-year mean near-surface and near-bottom subtidal velocity fields. We can discern the broad, swift Alaskan Stream that flows along the shelf break and the narrow and swift Alaska Coastal Current that flows close to shore. While the surface flow appears to conform to a generally smooth mean field having long length scales and predominantly along-isobath currents, the near-bottom flow field exhibits shorter length scales and many of the most prominent flows are directed across the shelf.

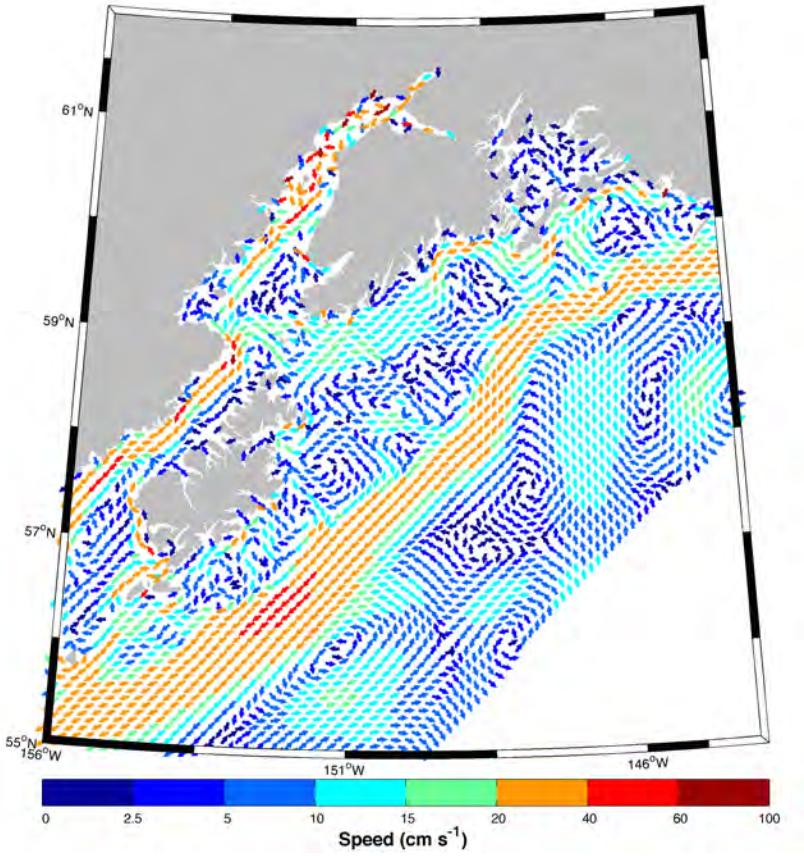

Figure 25: Surface velocity field averaged over the 10-year hindcast for the NW Gulf of Alaska. Every 7th grid point velocity vector is shown. Arrows denote flow direction and colors denote flow speed in cm s^{-1}.

Cross-shelf near-bottom flows are steered by the seafloor topography; subsurface satellite-tracked drifters have shown the tendency for currents in the Gulf of Alaska to flow up the eastern side of the canyons then turn and flow down the western side [*Ladd et al., 2005*]. These pathways represent conduits for nutrient-rich waters and plankton to leave the basin and advect to the mid-shelf and inner-shelf domains. Of course, there exists significant short-term variability imposed upon (and that average into) the mean velocity fields, including the tides, inertial motions and wind-driven flows. While the instantaneous flow field may never resemble

the mean field at any given moment, the location and strength of the enhanced flow pathways shown in Figure 25 likely do represent the locations that the primary near surface transport likely occurs.

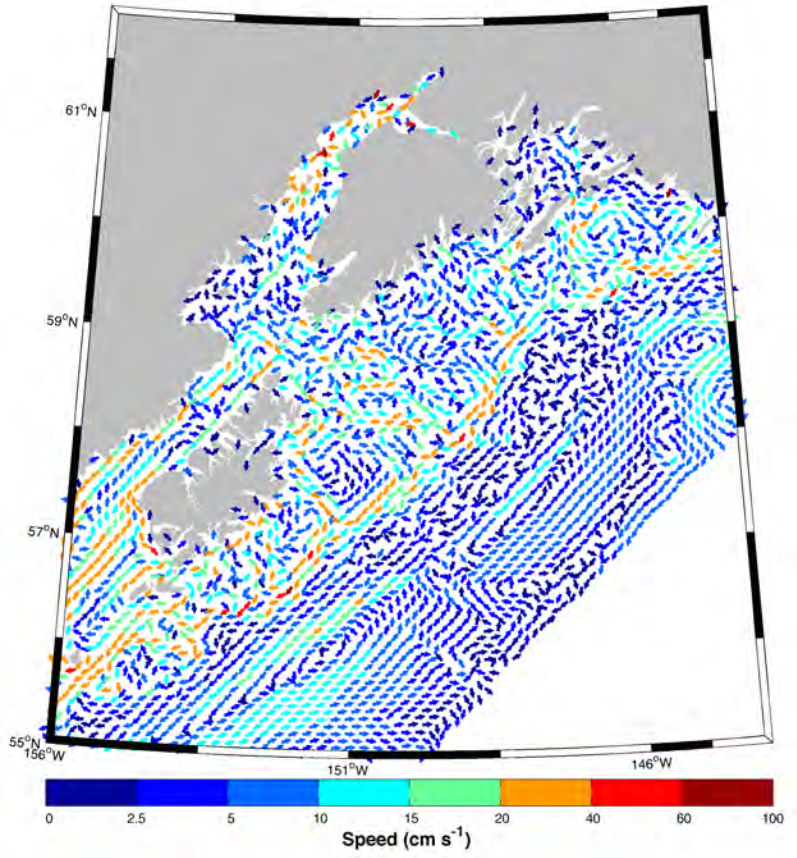

Figure 26: Near-bottom velocity field averaged over the 10-year hindcast for the NW Gulf of Alaska. Every 7th grid point velocity vector is shown. Arrows denote flow direction and colors denote flow speed in cm s^{-1}.

Dozens of near-surface satellite tracked oceanographic drifters (drogued at 1-20 m depths) have deployed in Cook Inlet between 2003 and 2015 [*Johnson et al.,* 2008; *Doroff et al.,* 2016; *Johnson*, 2016]. Compilations of these data and the modeled near-surface subtidal flow field are shown in Figures 27 and 28. Drifter data represent geographically binned means of velocity data that were previously detided with a 36-hour lowpass filter. The drifter data in total represent many thousands of drifter-hours worth of data, but these are spread out in time though all seasons, are unevenly distributed in space and they represent observations that may be dependent upon the deployment locations. Along all shorelines and south of Augustine Island most data vectors shown represent the mean of fewer than 30 drifter-hour records; elsewhere each vector represents as many as 300 drifter-hour samples. Hence, the

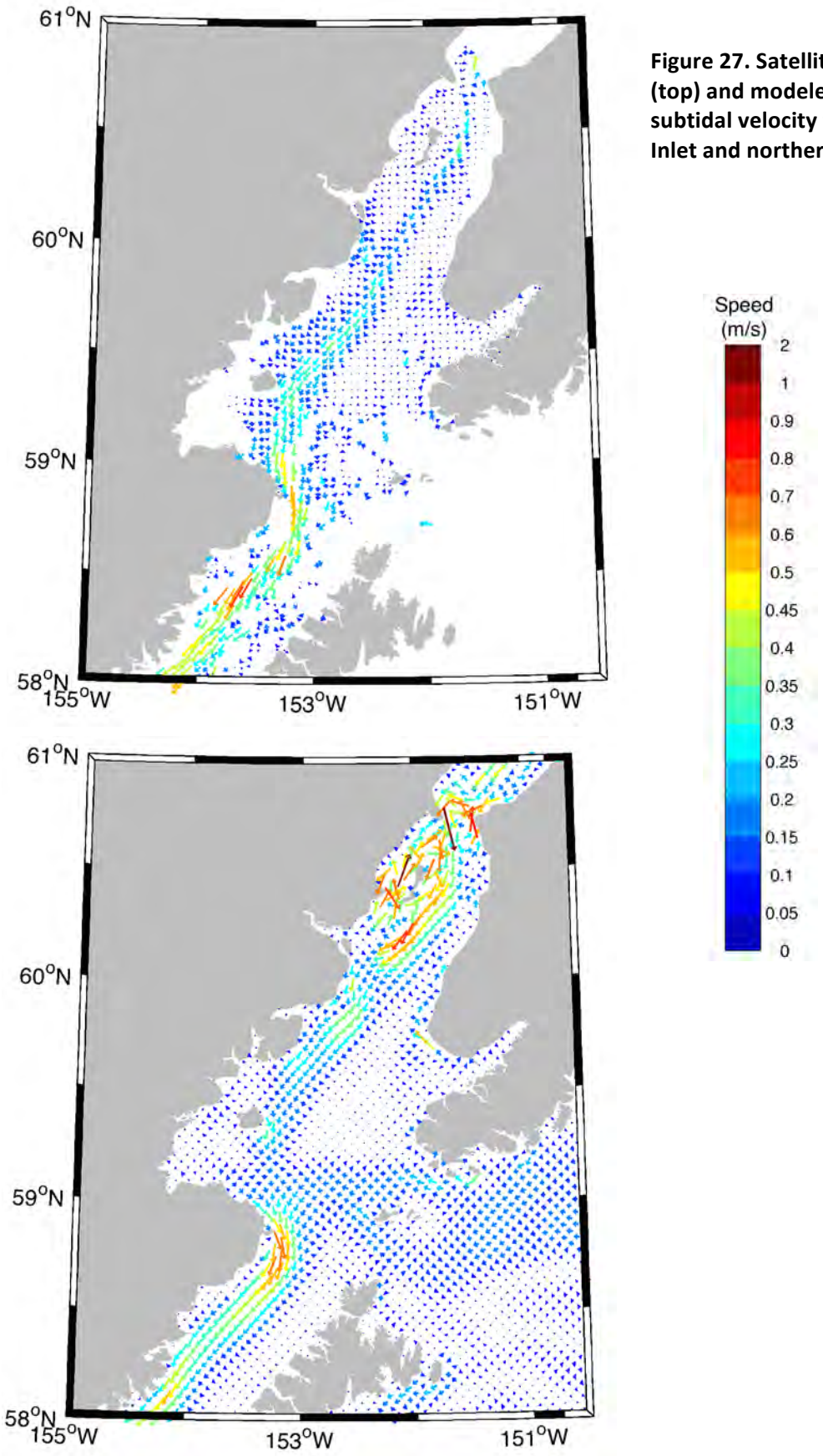

Figure 27. Satellite-tracked drifter (top) and modeled (bottom) mean subtidal velocity fields for lower Cook Inlet and northern Shelikof Strait.

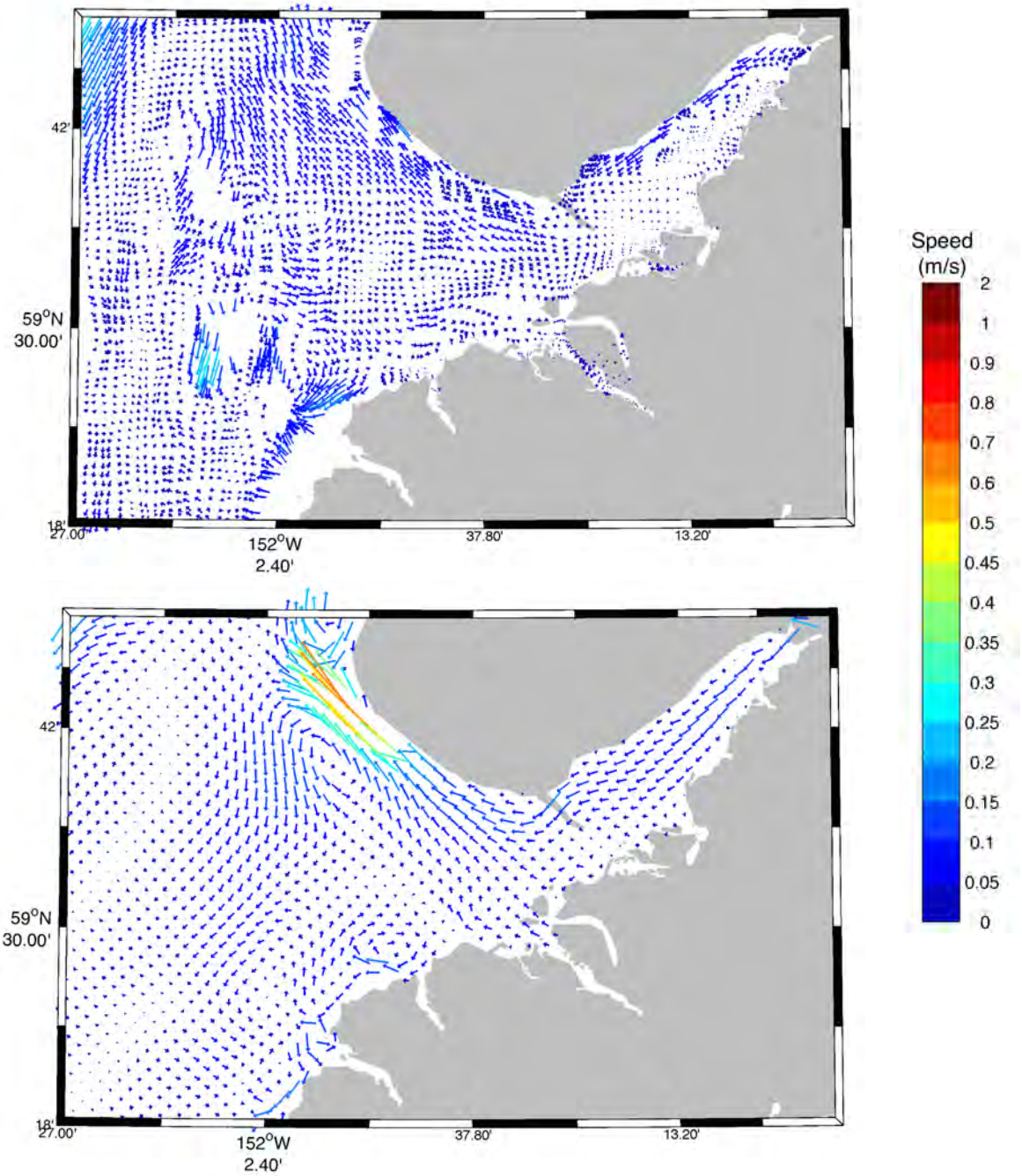

Figure 28. Satellite-tracked drifter (top) and modeled (bottom) mean subtidal velocity fields for the Kachemak Bay region.

mean drifter velocity fields likely exhibit some bias with respect to the true long-term mean at any given location and at many locations the bias may be considerable.

The modeled and observed depictions of the mean flow field in Figures 27 and 28 share a number of similar features and also exhibit some notable differences. Similarities include the tendency for waters to flow into and up Cook Inlet along the eastern shoreline near Anchor Point and for outflow along the western portion. In both depictions the flow field accelerates as it rounds Cape Douglas and enters Shelikof Strait. Within Shelikof Strait, both flow fields show weaker currents near the coasts and a strong jet along the middle that is somewhat displaced toward the peninsula side of the strait. A primary difference between the two flow fields is the strength of the currents near Kalgin Island: the model shows much stronger currents here. We note that this region is a well-documented site of tidal rips and suggest that the summer season bias of the drifter dataset may play a role in setting the magnitude of the observations here. Lending credence to this idea, inspection of the model output for only summer months shows that the velocities near Kalgin Island are appreciably weaker during summer.

HFR data collected in lower Cook Inlet from late 2006 to late 2007 and the model hindcasts (Figure 29) provide an alternate set of subtidal flow field depictions. We note that the modeled 1-year mean flow field over this time interval is very similar to the 10-year mean. Both the model and HFR data show southwestward flow just outside Port Graham, with weaker flow farther offshore. This stands in contrast to the drifters, which showed strong offshore (northwestward) flow here and other "mean flow" diagrams that often depict a current moving into Cook Inlet that flows along the Kenai Peninsula shoreline (e.g., Burbank [1977]). The model shows along-coast northward flow near Anchor Point, some of which deflects southwestward down the central portion of the Inlet with weaker flow to either side. The HFR data also show southwestward flow in the westward part of the region with good HFR data coverage, but it is not clear if these currents are part of the stronger flow field found in western Cook Inlet or if these are part of a retroflection of the flow as it moves past Anchor Point. We note that both the model and the HFR data depict a "banded" structure of stronger-weaker-stronger-weaker-stronger flows progressing across lower Cook Inlet. The model does not capture the exact location of the observed bands.

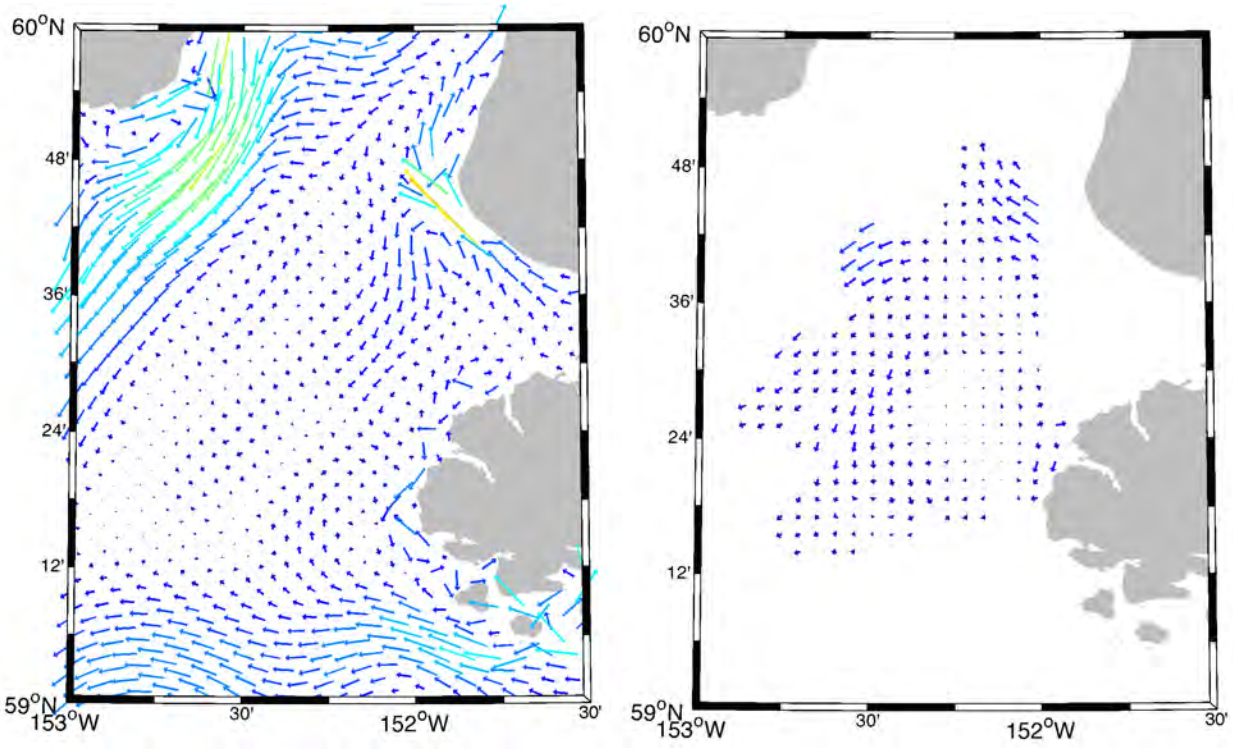

Figure 29. Lower Cook Inlet mean velocity for November 2006 – November 2007 from the model (left) and from HFR measurements (right). Note that only HFR cells with at least 50% data coverage during this time are shown. Color scheme same as for Figures 28.

In addition to the various mean velocity fields depicted in Figures 25-29, we provide plots of the near-surface and near-bottom (2nd sigma level) monthly climatologies in Appendix 2 for the entire Gulf of Alaska within the NWGOA domain and Appendix 5 for the Cook Inlet region only. A number of features in the mean and climatology velocity plots that conform to our general understanding of the Gulf of Alaska flow field as described above in Section 1.1. These include:

- An energetic and seasonally varying Alaskan Stream shelf-break jet flowing from east to west [*Reed a et al., 1984*].
- An energetic and seasonally varying Alaska Coastal Current flowing from east to west along the inner shelf [*Johnson et al., 1988; Weingartner et al., 2005*].
- An Alaskan Coastal Current that crosses the mouth of lower Cook Inlet from east to west [*Muench and Schumacher, 1980; Okkonen et al., 2009*].
- On-shelf flow just to the east of Middleton Island that varies in strength seasonally [*Stabeno et al., 2016*].

- Surface flow into Prince William Sound through Hinchinbrook Entrance and out of the Sound through Montague Strait, along with bi-directional subsurface flows in both straits [*Neibauer et al., 1994; Halvorson et al., 2012*].
- A surface flow field that is not strongly coupled to the near-bottom flow field except in relatively shallow waters.

We note that the NWGOA model develops a weak but persistent anti-cyclonic flow around and in close proximity to Kodiak Island (Figure 30). This flow field is consistent with the cross-strait shear shown in *Stabeno et al.* [1995] and *Stabeno et al*. [2016] and the southward-flowing branch of the ACC that heads toward the southwest along the southeastern shore of Kodiak. However, we are not aware of presence in the literature of a northward-flowing current on the Kodiak side of Shelikof Strait that extends the length of the island. Such a flow would be consistent with a coastal buoyancy-driven flow forced by island runoff; a second possibility of a driving force is that of a tidally rectified flow. Many coarser numerical models do exhibit a cross-strait shear in the mean flow field but with all mean flows to the southwest. Our model may be able to generate this flow field, if it exists, because of the NWGOA high horizontal resolution configuration and/or because of the NWGOA's approach to incorporating fresh water discharge.

Shelikof Strait is known to regularly spawn mesoscale eddies that are important aggregations centers for fish and crab and larvae. Even the 10-year vertically average flow mean (Figure 30) shows eddies within Shelikof Strait, suggesting that these features may persist in particular regions of the strait longer than in other regions. We note that it is also possible that temporal averaging of a feature that varies in both space and time could alias such features into the mean. However, because such features can aggregate water-borne contaminants in addition to plankton and upper trophic level organisms that may seek out the plankton aggregations for feeding, the location of these features may be important in the event of an oil spill even if they are relatively ephemeral events.

The NWGOA model results also suggest that between Kamishak Bay and Kachemak Bay there exists a seasonally varying gyre [*Muench and Schumacher,* 1980*; Okkonen et al.* 2009]. Summer months tend be dominated by a cyclonic gyre, while fall, winter and spring months are dominated by an anti-cyclonic gyre (Figures in Appendix A5), although in some of the monthly

climatologies gyres of both orientations may be discerned (e.g., Figure A5.9). It is unclear if the seasonal transitions in the size and rotation of this gyre occur in Cook Inlet in addition to in the model.

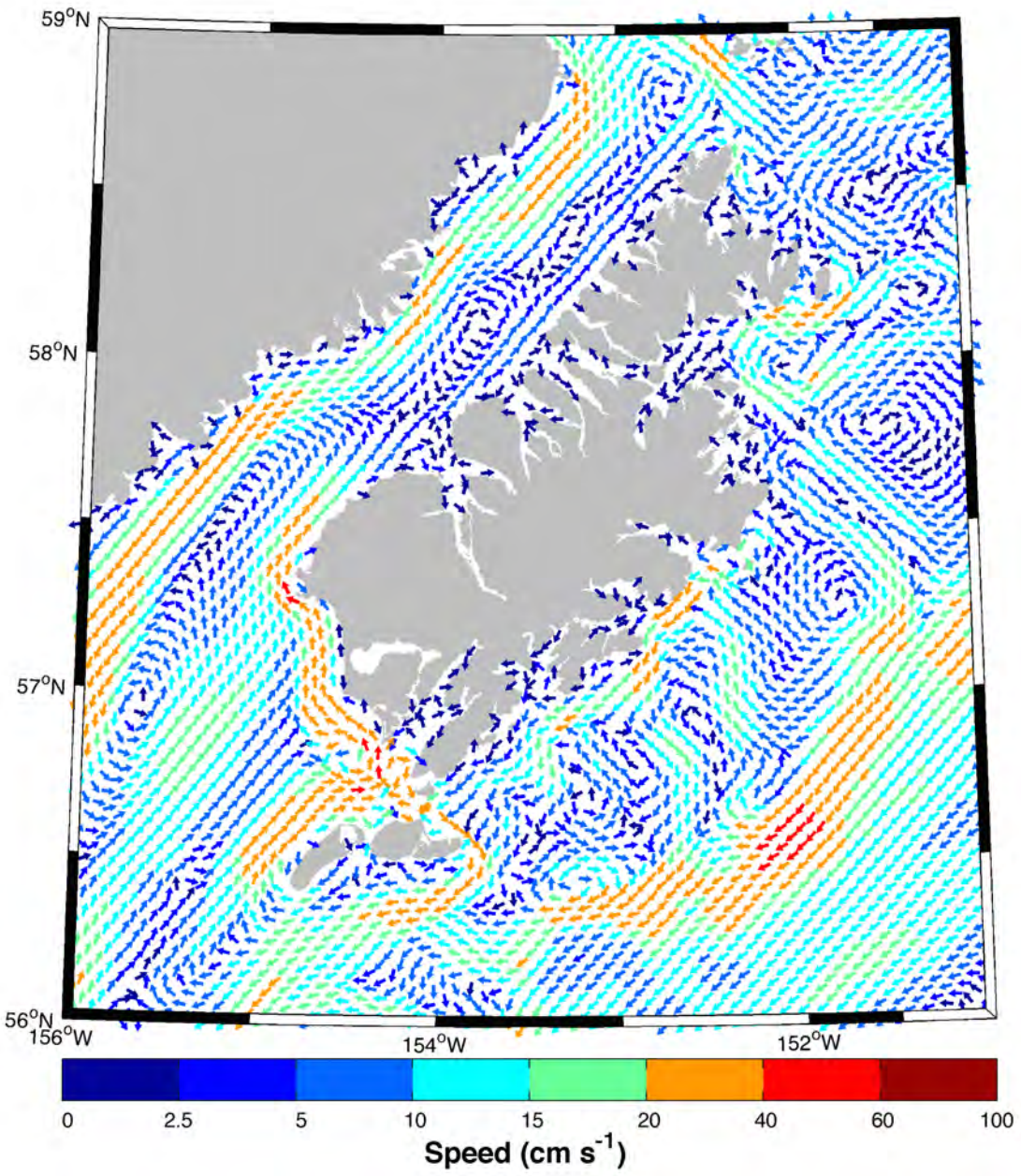

Figure 30. Modeled structure of the vertically averaged flow field near Kodiak Island. The model suggests the presence of a clockwise current that flows around and near to the island. In Shelikof Strait it flows to the northeast, in opposition to the primary Strait flow that is directed to the southwest. A similar nearshore anticyclonic flow field is observed encircling Sitkinak and Tugidak islands. Velocity vectors are plotted at every third gridpoint.

3.4 Thermohaline Properties

In this section we examine the model's ability to reproduce the temperature and salinity values along with their vertical and horizontal gradients because the density field – set by both of the thermohaline properties but primarily controlled by salinity in the North Pacific – exerts fundamental control over the circulation field.

Monthly mean climatological sea surface temperature (SST) and sea surface salinity (SSS) fields are shown in Appendix 2 and Appendix 3, respectively, for the greater NWGOA domain and Appendix 5 and Appendix 6, respectively, for Cook Inlet only. These depictions are useful because they provide insight to the seasonally varying advective pathways and the fate of the fresh water discharges upstream of Cook Inlet (e.g., Prince William Sound) and they provide insight to the surface density fronts that play a role in determining the speed of the Alaska Coastal Current and the Alaskan Stream.

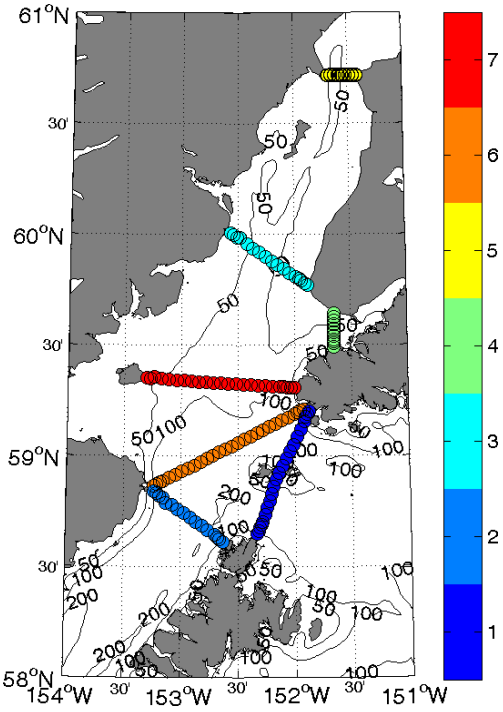

Figure 31. Locations of seven repeat CTD transects [*Okkonen et al.*, 2009] in lower Cook Inlet, Kennedy-Stevenson Entrances and upper Shelikof Strait used for model-data comparisons. The CTDs of each transect are plotted with circles that are color-coded based on transect number.

As part of the research supported by BOEM's Coastal Marine Institute (CMI), a set of conductivity-temperature-depth (CTD) observations were conducted in Cook Inlet between 2004 and 2006 [*Okkonen, 2004; Okkonen and Howell, 2003; Okkonen et al., 2009*]. The transect locations and their number designators are shown in Figure 31. These data, which are all used in our Cook Inlet hydrography comparisons, are comprised of a total of 79 individual transects,

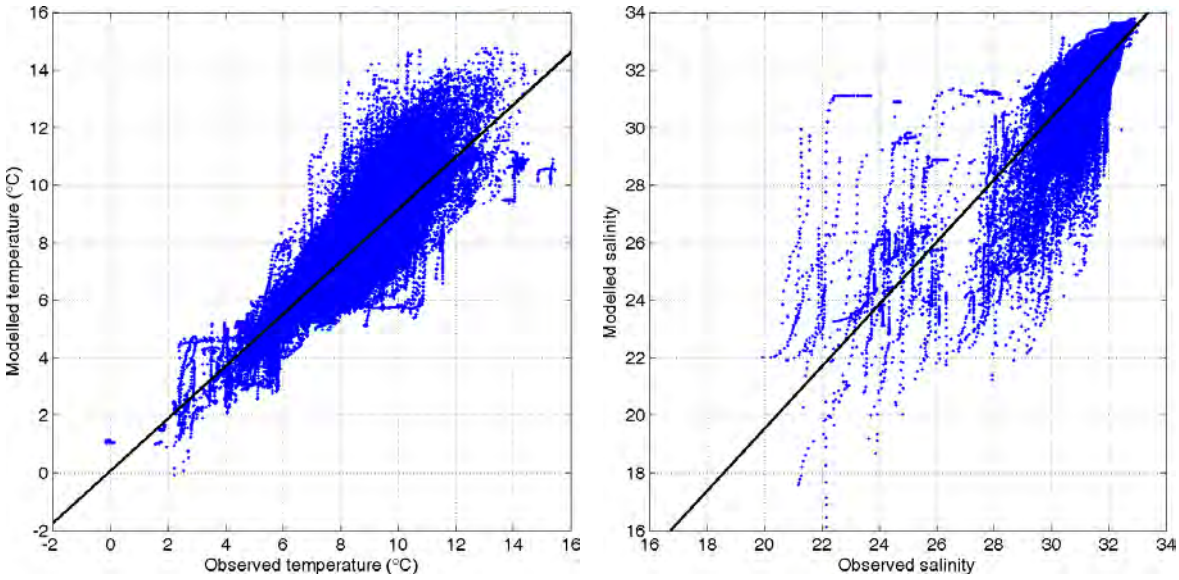

Figure 32. All CTD temperature (left) and salinity (right) data from the 81 transects listed in Table A3 regressed against the model temperature and salinity for the closest year, month, day and hour in the computation to the CTD observation time. Solid black lines show the best fit least squares regression between the model and observed datapoints.

1,225 individual CTD profiles and 99,517 discrete 1-m depth bin observations.

Scatter plots (Figure 32) of the modeled and observed temperature in the region shown in Figure 8 shows that in each case the model-to-data relation is very nearly 1:1 on average, with maximum scatter of up to 4 degrees in temperature and up to 10 salinity units. Volumetric T-S diagrams of each (Figure 33) show how the biases tend to manifest in temperature-salinity space. The plots suggest that the model stratification is too strong on average (too warm and

Table 2. Bulk statistics of the temperature and salinity for the seven transects shown in Figure 31. Parameters include the number of transect occupations (N), the temperature (T) and salinity (S) mean, standard deviation (STD), and the Pearson's correlation between the two datasets. Correlations that are significant for N-2 degrees of freedom at the 95% level for a 1-tailed test are shown in bold type.

Transect	N	T Mean		S Mean		T STD		S STD		Temperature Correlation	Salinity Correlation
		M	O	M	O	M	O	M	O		
1	18	7.49	7.02	31.75	32.30	1.78	2.04	0.49	0.95	**0.85**	**0.74**
2	14	7.09	6.61	31.71	32.35	2.02	2.14	0.63	1.36	**0.93**	**0.85**
3	16	8.79	7.80	30.35	30.18	2.94	2.79	1.05	2.12	**0.95**	**0.81**
4	17	7.99	7.44	31.19	31.47	2.47	2.73	0.48	0.91	**0.95**	**0.77**
5	8	9.75	7.72	25.24	26.46	3.86	2.39	1.84	2.74	**0.97**	0.38
6	4	8.55	7.72	31.60	32.18	1.33	1.84	0.58	1.28	0.80	0.80
7	4	10.12	9.41	30.86	30.74	0.72	1.58	0.67	1.50	0.50	0.66

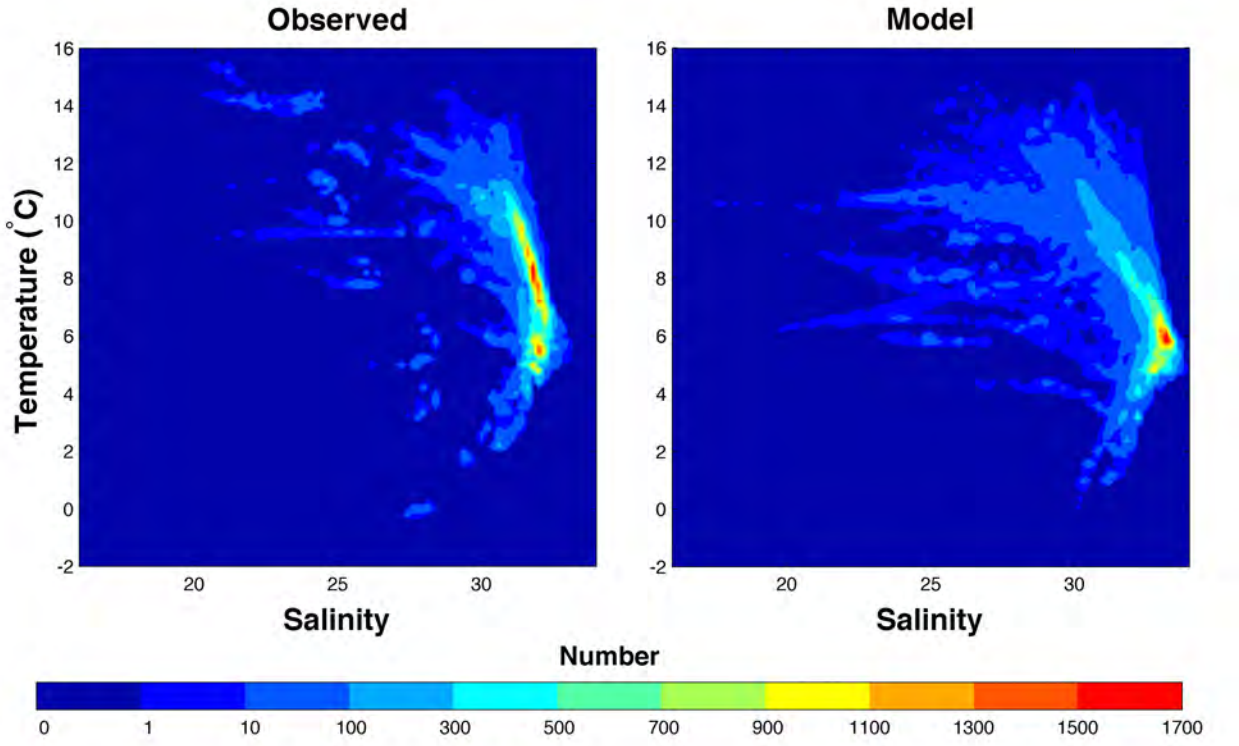

Figure 33. Volumetric T-S diagrams for the observed CTD data (left) and the modeled CTD data (right). The integration interval at each T-S water type pair is 0.2 °C and 0.2 salinity units.

fresh at the surface and too cool and salty at depth). Nonetheless, aggregate statistics of the model-data comparisons summarize as follows. The model-observed Pearson's cross-correlation is $r = 0.89$ with $p < 0.001$ for temperature and $r = 0.58$ with $p < 0.001$ for salinity. On a transect-by-transect basis, Table 2 shows that the transects with the fewest number of observations (Transects 5, 6 and 7) also have the weakest correlations. In all comparisons that result in significant correlations the correlation of the temperature fields is stronger than the correlation of the salinity fields.

Graphical comparisons of all 79 hydrographic cross-sections are provided in Appendix 8. While some of these comparisons show large offsets between the observed and modeled parameters, many others show relatively modest offsets. The average temperature offset, with the observations slightly warmer than the model, is 0.65 °C ($\sigma = 1.07$) and 58% of the observations were associated with a hindcast value that was within 1 °C of the observations; 90% are within 2 °C. For salinity, the observations are slightly less saline than the model on

average with a mean offset of 0.47 (σ = 1.05) and 66% of all observations were associated with a hindcast salinity that was within 1 salinity unit of that observed, while 95% are within 2 salinity units. Combined, 43% of the hindcast-observation pairs for the 79 transects simultaneously agree to within 1 (°C and salinity units) for both temperature and salinity. For a threshold of 2 (°C and salinity units), 86% of the hindcast values fall within the range.

3.5 Sea Ice

In addition to the thermohaline and water velocities, the numerical model dynamically freezes, thaws and advects sea ice based on the atmosphere-ocean, atmosphere-ice and ocean-ice heat balances. This section provides a climatological overview and analysis of the model's sea ice fields.

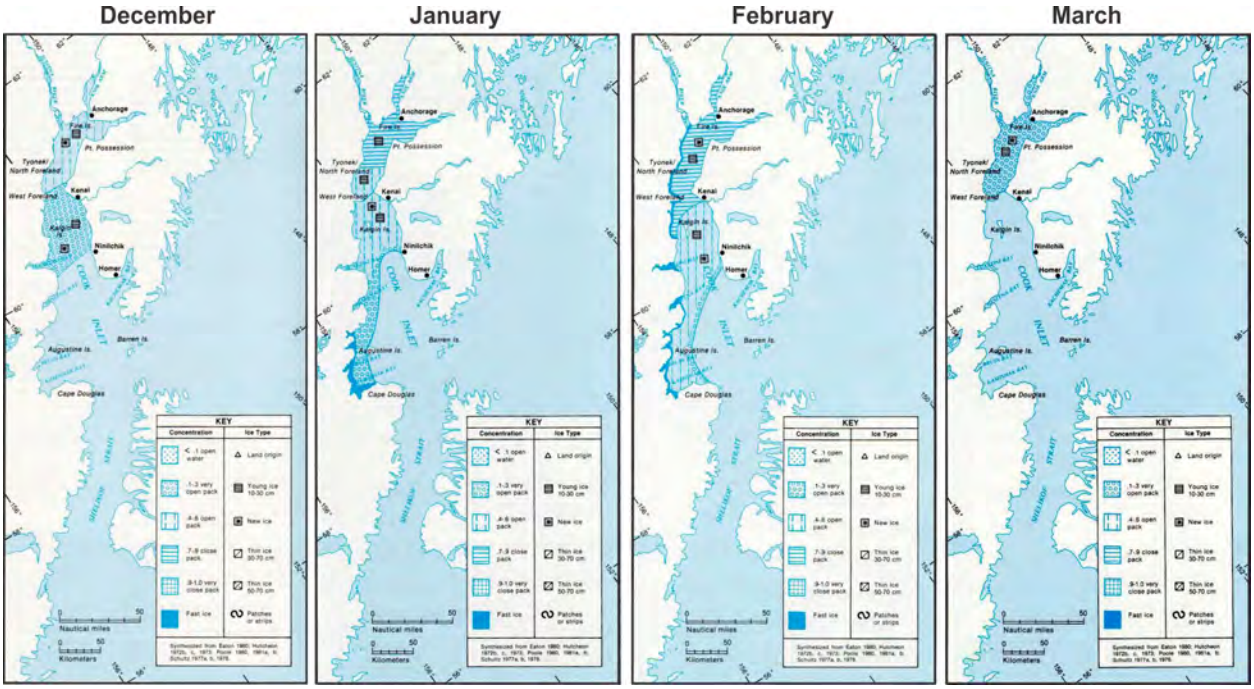

Figure 34. Cook Inlet December (left) through March (right) sea ice climatology. Reproduced from *Brower et al*. (1988).

We qualitatively compare the modeled sea ice extent, concentration and thickness climatology as provided in Figures 34 and 35 by *Brower et al.* [1988] and *Mulherin et al*., [2001], respectively. Observed sea ice concentration (Figure 33) data come from the 12.5 km Artist Sea Ice (ASI) data product developed at the University of Bremen [*Kaleschke et al.,* 2001; *Ezraty et al.,* 2007]. Ice concentrations of greater than 80% are uncommon over broad areas; regions

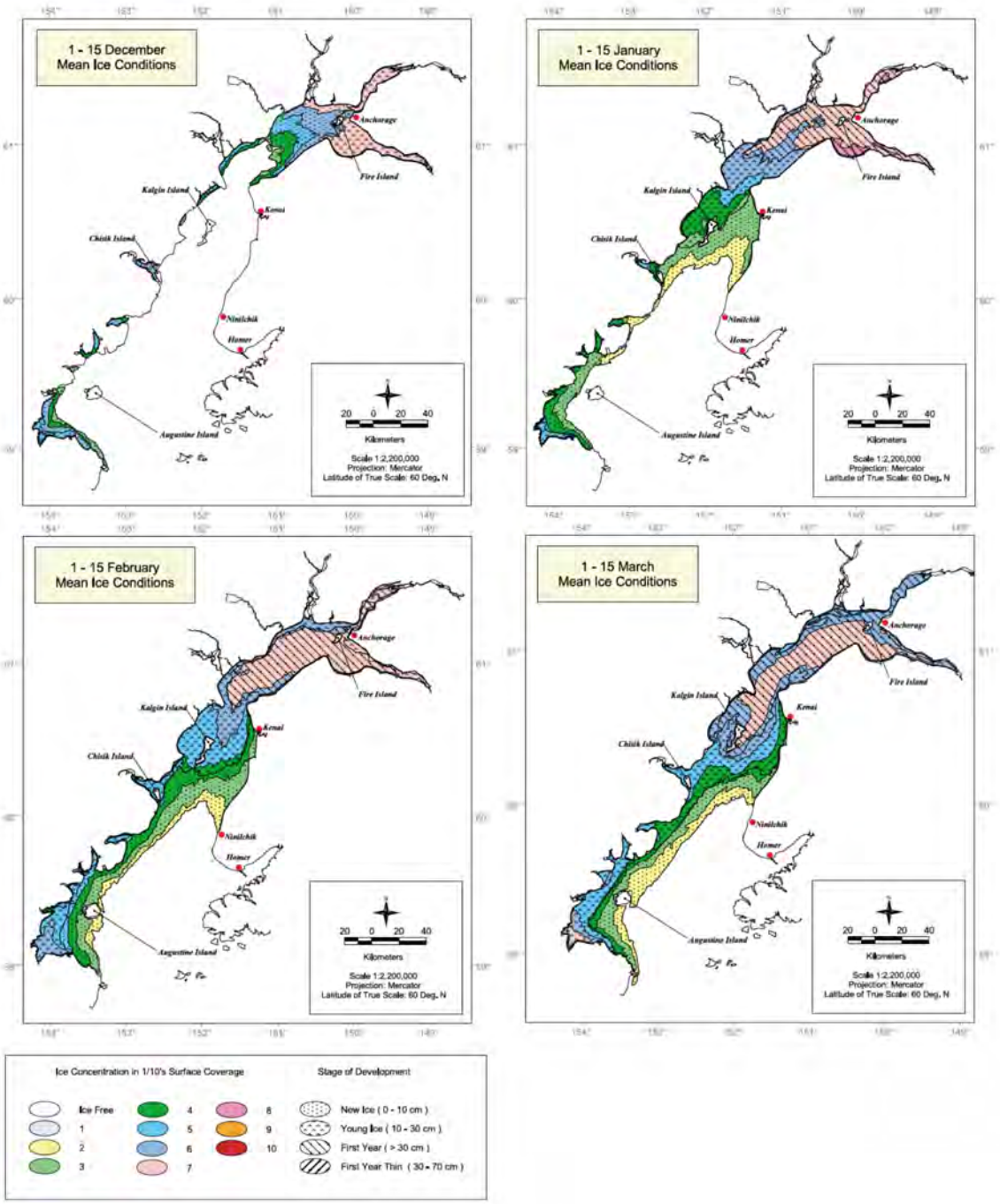

Figure 35. Cook Inlet Sea ice extent, concentration and thickness climatology for the first 15 days of December (upper left), January, February and March (lower right). Reproduced from *Mulherin et al*. (2001).

with ice concentrations of more than 30% are common in Upper Cook Inlet and along the western coast of Lower Cook Inlet. The ice is nearly all in free drift: it is readily advected by the underlying flow field. A notable exception is in southwestern Cook Inlet (Kamishak Bay; see Figure 7), where the ice can become grounded and anchored to the coast.

Remotely observed sea ice concentrations (Figure 36) are necessarily accompanied by important caveats because the passive microwave satellites that provide measures of the sea ice concentration around the globe are not well suited to resolving the Cook Inlet sea ice. In particular, the confined, narrow, geometry of Cook Inlet means that the relatively coarse Special Sensor Microwave Imager (SSM/I) ice concentration data products (6.25 to 25 km depending on version) have many cells that are contaminated by the land. For the 12.5 km ASI product that we show here, the users manual warns that land contamination is possible in the three pixels closest to shore (Ezraty et al., 2007), or over a 37.5 km distance from each coast. In addition, Cook Inlet has very high sediment loads that also can contaminate the passive microwave data. For example, inspection of the satellite ice data from Cook Inlet during July and August often will reveal the presence of sea ice at a time of year that is well known to be ice free. Because of these issues, we limit our examination of the sea ice data to that of the mean monthly ice climatology shown in Figure 36.

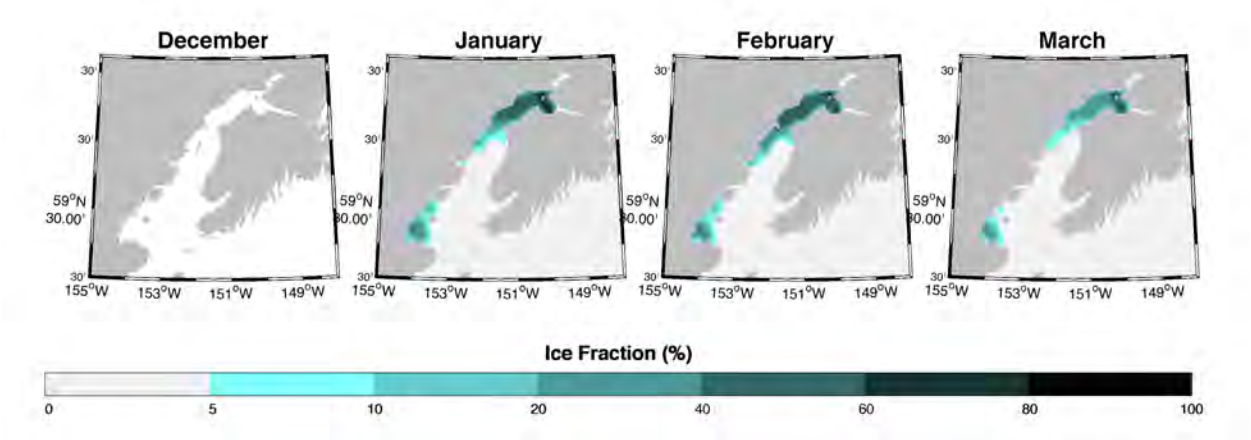

Figure 36: Sea ice concentrations in December through March from the ASI passive microwave satellite data algorithm. See text for notes describing important data caveats describing possible contamination.

Modeled sea ice thickness and ice concentration fields are shown in Figure 37. The ice extent bears considerable similarity to the sea ice extent shown by the SSM/I data and the *Brower et al.* [1988] and *Mulherin et al.* [2001] climatologies in Figures 34-35. Sea ice accumulates primarily north of the Forelands (~60.5 ^{o}N) and within Kamishak Bay in southwestern Cook Inlet. Thickest ice (0.2-0.6 m) in the model accumulates in Kamishak Bay, a location that is noted as a site of lastfast ice formation by *Brower et al*. [1988]. Especially in this region the ice has potential to influence the local circulation field by reducing coupling between the winds and the subtidal flow field.

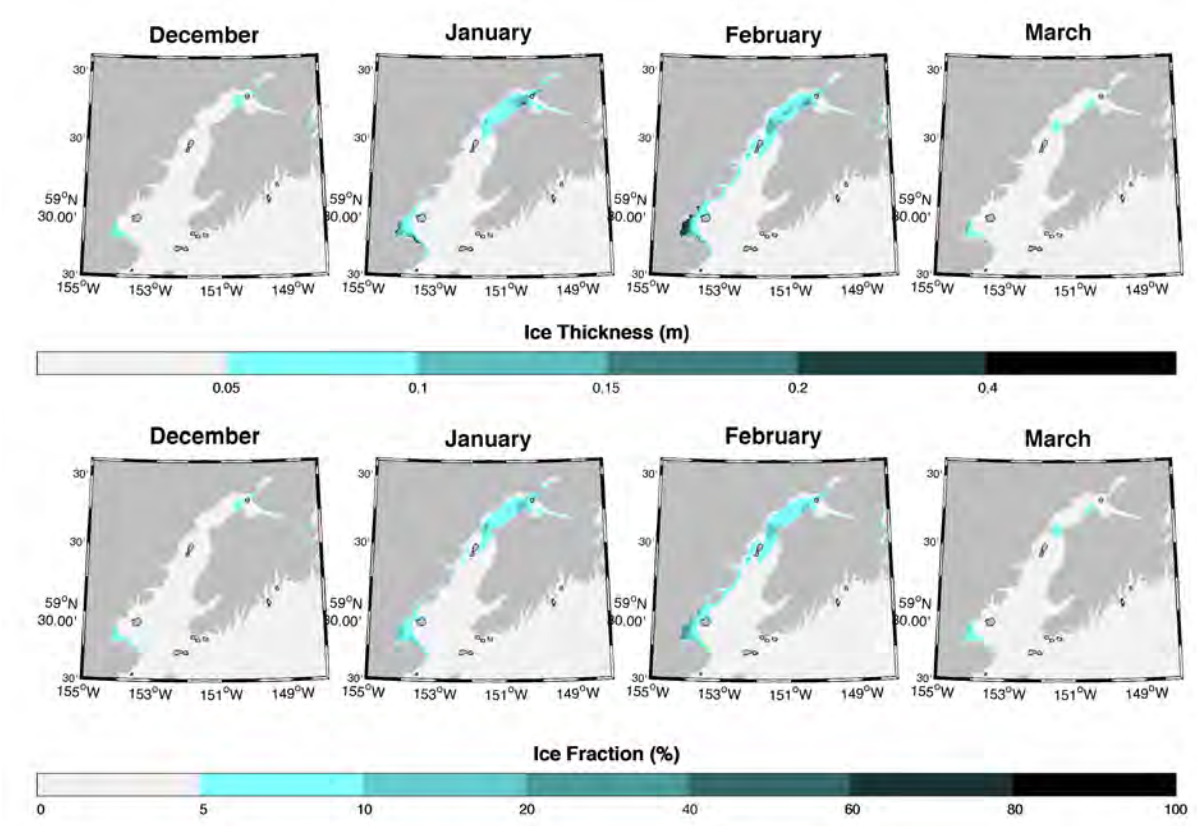

Figure 37. Modeled sea ice thickness (top) and concentration (bottom) for December (left) through March (right).

4.0 Concluding remarks

This report describes the NWGOA three-dimensional ocean circulation numerical model and conducts an assessment of the model's behavior with respect to the tides, subtidal circulation, sea ice and thermohaline properties. We find that the model exhibits appreciable skill in all aspects of the quantitative comparisons but there is also room for improvement in a number of specific areas. Qualitative comparisons lend further support to our understanding of the model's ability to reproduce many of the known features and their characteristics inherent within this continental shelf system.

Deviations of the model results away from the observed data and expected behavior provide insights to the physical processes that may be missing in the model formulation. If addressed, such additions could further improve the model results. We note that the hydrographic comparisons showed too much stratification in many of the Cook Inlet CTD profiles. We also find that the fresh plume from the Copper River delta has a propensity to advect very fresh water far offshore. There are few reliable salinity measurements between Middleton Island and the Copper River delta, so it is impossible to say if the modeled fresh water plume behavior here is unrealistic, but we have little evidence to show that the plume does extend so far offshore with salinities of less than 30. Additional near-surface mixing could potentially improve both of these behaviors (stratification and surface vs. subsurface salinity offsets) by providing a de-stratifying influence on the upper water column. Wind wave mixing has been applied in other modeling studies using parameterizations of the wind or wave environment. In the latter case, these are often forced by the output from an explicit wave model such as the Simulating Waves Nearshore (SWAN) model. In ROMS, such parameterizations are a focal area of active development and we look forward to implementing them when they are sufficiently developed to warrant inclusion.

In addition to the model improvements that we recommend, this report reveals that dedicated field efforts will be needed to further improve our understanding of Cook Inlet and Shelikof Strait circulation. For example, verification of a possible persistent clockwise circulation that encircles all of Kodiak Island is needed. The most reliable observational approach would include multiple current meter mooring deployments at select sites around the

island. Our analysis also highlights some differences between the long-cited mean circulation scheme of *Burbank* [1977] and the model results, such as the direction of the flow in southeastern of Cook Inlet. Again, extended current meter mooring deployments would be appropriate tools, possibly in conjunction with HF radar and satellite-tracked drifter deployments.

The NWGOA model output provides a first-ever opportunity to examine the fate and pathways of a spatially explicit and temporally varying high-resolution terrestrial discharge forcing field in the coastal Gulf of Alaska. While the analyses that will examine these aspects of the flow field are just begun, this report provides an important start to the objective evaluations required to build confidence in the model's performance across the important underlying components, including the temperature and salinity fields, tidal currents and tidal elevations, and the subtidal flow field.

Acknowledgements

This research was funded by the Bureau of Ocean Energy Management (BOEM), US Department of Interior under a Collaborative Agreement between BOEM, the University of Alaska Fairbanks (UAF) and Rutgers University. Additional support for the project came from Rutgers University and the University of Alaska Fairbanks in the form of computational resources, provided in part by the UAF's Arctic Region Supercomputing Center (ARSC). We acknowledge the use of Rapid Response imagery from the Land, Atmosphere Near real-time Capability for EOS (LANCE) system operated by the NASA/GSFC/Earth Science Data and Information System (ESDIS) with funding provided by NASA/HQ. MERRA data used in this study have been have been provided by the Global Modeling and Assimilation Office (GMAO) at NASA Goddard Space Flight Center through the NASA GES DISC online archive. Funding for the development of HYCOM has been provided by the National Ocean Partnership Program and the Office of Naval Research. Data assimilative products using HYCOM are funded by the U.S. Navy. Computer time for HYCOM was made available by the DoD High Performance Computing Modernization Program. Tidal forcing is provided by the OSU TOPEX/Poseidon global inverse solution TPXO from: http://volkov.oce.orst.edu/tides/global.html. The HYCOM output is publicly available at http://hycom.org. We thank Steve Okkonen (UAF) for providing the hydrographic data, Chris Paternostro (NOAA) and NOAA's Currents Measurements Interface for the Study of Tides (CMIST) for providing access to current meter mooring data, David Hill and Jordan Beamer (both OSU) for providing the coastal discharge model time series, and Jonathan Whitefield (UAF) for assistance with the analyses of model results and assembly of CMIST data. We are extremely grateful to Heather Crowley and Walter Johnson (BOEM), whose assistance and guidance throughout this program helped us complete such an ambitious modeling project, which is replete with new model development activities, application of previously unavailable forcing fields, and a robust set of data for model evaluations.

References

Ahlnas, K., T.C. Royer, and T.H George, 1987. Multipole dipole eddies in the Alaska Coastal Current detected with Landsat thematic mapper data. *J. Geophys. Res*. 92, 13041–13047.

Barrick, D.E., 1978. HF Surface-current mapping radar 1977 Alaskan operations – lower Cook Inlet. In: Environmental Assessment of the Alaskan Continental Shelf. Annual Reports. 39pp.

Beamer, J. P., D. F. Hill, A. Arendt, and G. E. Liston, 2016. High-resolution modeling of coastal freshwater discharge and glacier mass balance in the Gulf of Alaska watershed, Water Resour. Res., 52, 3888–3909, doi:10.1002/2015WR018457.

Brower, W.A., Jr., R.G. Baldwin, C.N. Williams, Jr., J.L. Wise, and L.D. Leslie (1988) Climatic Atlas of the Outer Continental Shelf Waters and Coastal Regions of Alaska; Vol. I. Gulf of Alaska, Final report to U.S. Minerals Management Service, Alaska Outer Continental Shelf Region., OCS Study MMS 87–0011, 551pp

Budgell, W.P., 2005. Numerical simulation of ice-ocean variability in the Barents Sea region: Towards dynamical downscaling, *Ocean Dyn.*, 55, 370-387.

Burbank, D.C. 1977. Circulation studies in Kachemak Bay and Lower Cook Inlet. In Environmental Studies of Kachemak Bay and Lower Cook Inlet. L.L.Trasky, L.B. Flagg. and D.C. Burbank eds. vol III. 207 pp.

Carton, J. A., G. Chepurin, X. Cao and B. S. Giese, 2000. A simple ocean data assimilation analysis of the global upper ocean 1950--1995, part 1: methodology, *J. Phys. Ocn.,* 30, 294-309

Carton, J. A., G. Chepurin and X. Cao, 2000b. A simple ocean data assimilation analysis of the global upper ocean 1950--1995, part 2: results, *J. Phys. Ocn.,* 30, 311-326

Chao, Y.Y., L.D. Burroughs, and H. L. Tolman, 2003. Wave forecasting for Alaskan waters. NWS/NCEP Technical Procedures Bulletin 496

Cheng, W., A. Hermann, K. Coyle, E. Dobbins, N. Kachel, and P. Stabeno, 2012. Macro- and micro-nutrient flux to a highly productive submarine bank in the Gulf of Alaska: a model-based analysis of daily and interannual variability. *Prog. Oceanogr*. 101, 63–77.

Clarke, A. J., and D. S. Battisti, 1981. The effect of continental shelves on tides, *Deep-Sea Res. A,* 28(7), 665–682.

Chassignet, E.P., H.E. Hurlburt, E.J. Metzger, O.M. Smedstad, J. Cummings, G.R. Halliwell, R. Bleck, R. Baraille, A.J. Wallcraft, C. Lozano, H.L. Tolman, A. Srinivasan, S. Hankin, P. Cornillon, R. Weisberg, A. Barth, R. He, F. Werner, and J. Wilkin, 2009. U.S. GODAE: Global Ocean Prediction with the HYbrid Coordinate Ocean Model (HYCOM). *Oceanography*, 22(2), 64-75.

Colas, F., X. Wang, X. Capet, Y. Chao, J. C. McWilliams, 2013. Untangling the roles of wind, run-off and tides in Prince William Sound*, Cont. Shelf Res*., 63, pp S79-S89, ISSN 0278-4343, http://dx.doi.org/10.1016/j.csr.2012.05.002.

Coyle, K.O., Cheng, W., Hinckley, S., Lessard, E.J., Whitledge, T., Hermann, A.J., Hedstrom, K., 2012. Model and field observations of effects of circulation on the timing and magnitude of nitrate utilization and production on the northern Gulf of Alaska shelf. *Prog. Oceanogr*. 103, 16–41.

Coyle, K.O., G.A. Gibson, K. Hedstrom, A.J. Hermann, and R.R. Hopcroft, 2013. Zooplankton biomass, advection and production on the northern Gulf of Alaska shelf from simulations

and field observations, *J. Mar. Syst.* http://dx.doi.org/10.1016/j.jmarsys.2013.04.018

Curchitser, E.N., D. B. Haidvogel, A. J. Hermann, E. L. Dobbins, T. M. Powell and A. Kaplan, 2005. Multi-scale modeling of the North Pacific Ocean: Assesment and analysis of simulated basin-scale variability (1996-2003), *J. Geophys. Res.*, 110, C11021, doi:101029/2005JC002902.

Curchitser, E.N., K. Hedstrom, S. Danielson and T. J. Weingartner, 2010. Modeling of Circulation in the North Aleutian Basin. Department of Interior, OCS Study BOEMRE 2010-028.

Curchitser, E.N., K. Hedstrom, S. Danielson and T. J. Weingartner, in prep., Adaptation of and Arctic Circulation Model, Program No. M10PC00116

Dai, A., T. Qian, K. E. Trenberth, and J. D Milliman (2009), Changes in continental freshwater discharge from 1948–2004. J. Climate, 22, 2773–2791

Danielson, S. L., E. N. Curchitser, K. S. Hedstrom, T. J. Weingartner, and P. J. Stabeno, 2011. On ocean and sea ice modes of variability in the Bering Sea, *J. Geophys. Res.*, doi:10.1029/2011JC007389

Danielson, S. L., E. L. Dobbins, M. Jackobsson, M. J. Johnson, T. J. Weingartner, W. J. Williams, and Y. Zarayskaya, 2015. Sounding the Northern Seas: A New Western Arctic and North Pacific Digital Elevation Model, Eos, 96, doi:10.1029/2015EO040975.

Dobbins, E. L., A. J. Hermann, P. J. Stabeno, N. A. Bond and R. C. Steed, 2009. Modeled transport of freshwater from a line-source in the coastal Gulf of Alaska. *Deep Sea Res. II*, doi:10.1016/j.dsr2.2009.02.004

Doroff, A., M Johnson, G. Gibson, 2016. Ocean circulation mapping to aid monitoring programs for harmful algal blooms and marine invasive transport in South-Central Alaska. Final Performance Report to the Alaska Department of Fish and Game, Grant T-34-1, Project P-01.

Egbert, G.D., S.Y. Erofeeva, 2002. Efficient Inverse Modeling of Barotropic Ocean Tides. *J. Atmos. Oceanic Technol.*, 19, 183–204. doi: http://dx.doi.org/10.1175/1520-0426(2002)019<0183:EIMOBO>2.0.CO;2

Ezer, T., J. R. Ashford, C. M. Jones, B. A. Mahoney and R. C. Hobbs, 2013. Physical-biological interactions in a subarctic estuary: How do environmental and physical factors impact the movement and survival of beluga whales in Cook Inlet, Alaska?, J. Mar. Sys., Vol. 111-112, 120-129, doi:10.1016/j.jmarsys.2012.10.007

Ezraty, R. F. Girard-Ardhuin, J-F. Piolle, L. Kaleschke and G. Heygster, 2007, Arctic & Antarctic sea ice concentration and arctic sea ice drift estimated from special sensor microwave data, User's Manual V. 2.1, Laboratoire d'Oceanographie Spatiale, IFREMER, Brest, France, 22 pp.

Fairall, C.W., E.F. Bradley, J.E. Hare, A.A. Grachev and J.B. Edson, 2003. Bulk parameterization of air-sea fluxes: Updates and modification for the COARE algorithm, J. Climate, 16, 571-591.

Farrara, J.D., Y. Chao, Z. Li, X. Wang, X. Jin, H. Zhang, P. Olsson, G.C. Schoch, M. Halverson, M.A. Moline, 2013. A data-assimilative ocean forecasting system for the Prince William Sound and an evaluation of its performance during Sound Predictions 2009. *Cont. Shelf Res*., in pres

Fiechter, J., A.M. Moore, C.A. Edwards, K.W. Bruland, E. Di Lorenzo, C.V.W. Lewis, T.M. Powell, E.N. Curchitser, K. Hedstrom, 2009. Modeling iron limitation of primary production in the coastal Gulf of Alaska. Deep Sea Research II 56, 2503–2519

Foreman, M. G. G., W. R. Crawford, J. Y. Cherniawsky, R. F. Henry, and M. R. Tarbotton, 2000. A high-resolution assimilating tidal model for the northeast Pacific Ocean, *J. Geophys. Res*., 105, 28,629-28,651.

Galt, J. A. W. J. Lehr and D. L. Payton, 1991. Fate and transport of the Exxon Valdez oil spill. Environmental Science and Technology, 25:202-209

Gill, A. E., 1982. *Atmosphere–Ocean Dynamics*, Academic Press, San Diego, CA.

Greisman, P., 1985. Western Gulf of Alaska tides and circulation, 112 pp., Natl. Oceanic and Atmos. Admin., Anchorage, Alaska

Halverson, J.J, C. Bélanger, S.M. Gay III, 2012. Seasonal transport variations in the straits connecting Prince William Sound to the Gulf of Alaska. Continental Shelf Res., http://dx.doi.org/10.1016/j.csr.2012.06.017

Hedstrom, K., 2009. Technical Manual for a Coupled Sea-Ice/Ocean Circulation Model (Version 3), Minerals Management Service Report OCS Study MMS 2009-062, 155pp.

Hermann, A.J., W.C. Rugen, P.J. Stabeno, and N.A. Bond, 1996. Physical transport of young pollock larvae (*Theragra chalcogramma*) near Shelikof Strait as inferred from a hydrodynamic model. *Fish. Oceanogr.*, 5(Suppl. 1):58-70.

Hermann, A.J., and P.J. Stabeno, 1996. An eddy-resolving circulation model for the western Gulf of Alaska Shelf: I. Model development and sensitivity. *J. Geophys. Res.*,

Hermann, A. J., S. Hinckley, E. L. Dobbins, D. B. Haidvogel, N. A. Bond, C. Mordy, N. Kachel, and P. J. Stabeno, 2009. Quantifying cross-shelf and vertical nutrient flux in the Gulf of Alaska with a spatially nested, coupled biophysical model, *Deep-Sea Res. II,* 56, 2472-2486, doi:10.1016/j.dsr2.2009.02.008.

Hermann, A.J., E.N. Curchitser, D.B. Haidvogel, E.L. Dobbins, 2009. A comparison of remote vs. local influence of El Niño on the coastal circulation of the northeast Pacific, *Deep Sea Res. II*, 56, 24, pp. 2427-2443, ISSN 0967-0645, http://dx.doi.org/10.1016/j.dsr2.2009.02.005.

Hill, D. F., N. Bruhis, S. E. Calos, A. Arendt, and J. Beamer, 2015. Spatial and temporal variability of freshwater discharge into the Gulf of Alaska, J. Geophys. Res. Oceans, 120, 634–646, doi:10.1002/2014JC010395.

Hunke, E. C., and J. K. Dukowicz, 1997. An elastic-viscous-plastic model for sea ice dynamics, *J. Phys. Oceanogr.,* 27, 1849-1868.

Isaji, T. and M. L. Spaulding, 1987. A numerical-model of the M2 and K1 tide in the northwestern Gulf of Alaska. *J. Phys. Oceanogr*. 17, 698–704.

Isoguchi, O., H. Kawamura and T. Kono, 1997. A study on wind-driven circulation in the subarctic North Pacific using TOPEX/POSEIDON alti-meter data. J. of Geophys. Res. Oceans 102 (C6), 12457–12468.

Janout, M. A., T. J. Weingartner, T. C. Royer, and S. L. Danielson, 2010. On the nature of winter cooling and the recent temperature shift on the northern Gulf of Alaska shelf, *J. Geophys. Res*., 115, C05023, doi:10.1029/2009JC005774.

Janout, M.A., T.J. Weingartner, S.R. Okkonen, T.E. Whitledge, and D.L. Musgrave, 2011. Some characteristics of Yakutat Eddies propagating along the continental slope of the Northern Gulf of Alaska Deep-Sea Res. (2010) http://dx.doi.org/10.1016/j.dsr2.2009.02.006

Johnson, W.R., T. C. Royer, and J. L. Luick, 1988. On the seasonal variability of the Alaska Coastal Current. *J. Geophys. Res.,* 93, 12423–12437.

Johnson, M.A., and S.R. Okkonen [eds.]. 2000. Proceedings Cook Inlet Oceanography Workshop.November 1999, Kenai, AK. Final Report. OCS Study MMS 2000-043. UA Coastal Marine Institute, UAF and USDOI, MMS, Alaska OCS Region. 118 p.

Johnson, M., 2008. Water and Ice Dynaics in Cook Inlet. University of Alaska Coastal Marine Institute, University of Alaska, Final Rport OCS Study MMS2008-061. 105 pp.

Johnson, M. 2016. Circulation studies of Kachemak Bay, Alaska using satellite-tracked drifters. Final Report to the Community Coastal Impact Assistance Program. FWS Grant F12AF7021.

Kaleschke, L., C. Lüpkes, T. Vihma, J. Haarpaintner, A. Bochert, J. Hartmann and G. Heygster, 2001. SSM/I Sea ice remote sensing for mesoscale ocean-atmosphere interaction analysis, Canadian Journal of Remote Sensing, Vol. 27, n° 5, pp. 526-537

Kang, D. and E.N. Curchitser, 2013. Gulf Stream eddy characteristics in a high-resolution ocean model, J. Geophys. Res., doi:10.1002/jgrc.20318

Kowalik, Z. and A. Proshutinsky, 2010. Tsunami-tide interactions: A Cook Inlet case study, Cont. Shelf Res. 30(6), 633–642.

Lackmann, G.M., and J. E. Overland, 1989. Atmospheric structure and momentum balance during a gap-wind event in Shelikof Strait, Alaska. *Mon. Wea. Rev*. 116:1817-1833.

Ladd, C., Cheng, W., Salo, S., 2016. Gap winds and their effects on regional oceanography Part II: Kodiak Island, Alaska. Deep-Sea Res. II 132, 54–67. http://dx.doi.org/10.1016/j.dsr2.2015.08.005.

Ladd, C., Kachel, N.B., Mordy, C.W., Stabeno, P.J., 2005. Observations from a Yakutat eddy in the northern Gulf of Alaska. J. Geophys. Res.: Oceans 110, C03003. http: //dx.doi.org/10.1029/2004JC002710.

Large, W.G., J. C. McWilliams and S. C. Doney, 1994. Oceanic vertical mixing: a review and a model with a nonlocal boundary layer parameterization, *Rev. Geophys*., 32, 363-403

Large, W.G., and S. G. Yeager, 2009. The global climatology of an interannually varying air-sea flux data set, *Clim. Dyn*., 33, 341-364

Li, Z., Y. Chao, J. Farrara, X. Wang, H. Zhang, X. Jin, P. Olsson, 2013. Quantifying impacts of distinct observations in data assimilation and forecast during the 2009 Prince William Sound Field Experiment. *Cont. Shelf. Res.,* 63, http://dx.doi.org/10.1016/j.csr.2012.06.018

Luick, J.L., Royer, T.C., Johnson, W.R., 1987. Coastal atmospheric forcing in the Northern Gulf of Alaska*. J. Geophys. Res*. 92, 3841–3848.

Marchesiello, P., J. C. McWilliams and A. Shchepetkin, 2001. Open boundary conditions for long-term integration of regional oceanic models, *OM*, 3,1-20

Marks K.M. and W.H.F. Smith, 2006. An evaluation of publicly available global bathymetry grids. Mar Geophys Res 27:19–34. doi:10.1007/s11001-005-2095-4

Macklin, S., N. A. Bond, and J. P. Walker, 1990. Structure of a low-level jet over lower Cook Inlet, Alaska. *Mon. Wea. Rev.,* 118, 2568– 2578

Macklin, S. A., N. A. Bond, and J. P. Walker, 1990. Structure of a Low-Level Jet over Lower Cook Inlet, Alaska. *Mon. Wea. Rev.*, 118, 2568–2578. doi: http://dx.doi.org/10.1175/1520-0493(1990)118<2568:SOALLJ>2.0.CO;2

Meccia, V., I. Wainer, M. Tonelli, and E. Curchitser, 2013. A numerical study of the Southern Ocean including a thermodynamic active ice shelf – Part1: Weddell Sea, *Geosci. Model Dev. Discuss*., 5, 4037–4069, doi:10.5194/gmdd-5-4037-2012

Mellor, G. L. and L. Kantha, 1989. An ice-ocean coupled model, *J. Geophys. Res.,* 94, 10,937-

10,954
Moore, A.M., Arango, H.G., DiLorenzo, E., Cornuelle, B.D., Miller, A.J., Neilsen, D.J., 2004. A comprehensive ocean prediction and analysis system based on the tangent linear and adjoint of a regional ocean model. *Ocean Model.* 7, 227–258
Muench, R.D., H.O. Mofjeld, and R.L. Charnell. 1978. Oceanographic conditions in Lower Cook Inlet: Spring and Summer 1973, *J. Geophys. Res*., 83:5090-5098.
Muench, R. D., and J. D. Schumacher, 1980. Physical oceanographic and meteorological conditions in the northwest Gulf of Alaska, Tech. Memo. ERL PMEL-22, 147 pp., Natl. Oceanic and Atmos. Admin., Silver Spring, MD
Muench, R.D., J.D. Schumacher, and C.A. Pearson. 1981a. Circulation in the lower Cook Inlet, Alaska. NOAA Technical Memorandum ERL PMEL-28. Seattle. 26 pp.
Mulherin, N.D., Tucker, W.B., III, Smith, O.P., and Lee, W.J. 2001. Marine ice atlas for Cook Inlet, Alaska. ERDC- CRREL Technical Report 01-10. Hanover, New Hampshire: U.S. Army Corps of Engineers, Engineer Research and Development Center, Cold Regions Research and Engineering Laboratory. 147 p.
Mysak, L., R. D. Muench, and J. D. Schumacher, 1981. Baroclinic instability in a downstream varying channel: Shelikof Strait, Alaska, *J. Phys. Oceanogr*., 11, 950-969
Niebauer, H.J., T.C. Royer, T.J. Weingartner, 1994. Circulation of Prince William Sound, Alaska, J. Geophys. Res., 14113–14126
Oey, L.Y., T. Ezer, C. Hu, and F.E. Muller-Karger, 2007. Baroclinic tidal flows and inundation processes in Cook Inlet, Alaska: numerical modeling and satellite observations, *Ocean Dyn.*, 57: 205-211.
Okkonen, S., T. J. Weingartner, S. L. Danielson, D. L. Musgrave, and M. Schmidt, 2003. Satellite and hydrographic observations of eddy-induced shelf-slope exchange in the northwestern Gulf of Alaska. *J. Geophys. Ress.,*108 (C2), 3033.
Okkonen, S.R. 2004. Observations of hydrography and currents in central Cook Inlet, Alaska during diurnal and semidiurnal tidal cycles. OCS Study MMS 2004-058, University of Alaska Coastal Marine Institute, UAF and USDOI, MMS, Alaska OCS Region, 27 p.
Okkonen, S.R. and S.S. Howell. 2003. Measurements of temperature, salinity, and circulation in Cook Inlet, Alaska. Final Report. OCS Study MMS 2003-036, University of Alaska Coastal Marine Institute, UAF and USDOI, MMS, Alaska OCS Region, 28 pp.
Okkonen, S.R., S. Pegau, and S. Saupe. 2009. Seasonality of Boundary Conditions for Cook Inlet, Alaska. MMS OCS Study 2009-041. Final Report. 64 pp.
Potter, R. A. and T.W. Weingartner, 2009. Surface Circulation Ratar Mapping in Alaskan Coastal Waters: Beaufort Sea and Cook Inlet, Final Report MMS Contract 1435-01-04-CT-35579, M04PC00002, M08PC20006, University of Alaska Fairbanks, 143 pp.
Reed, R.K., 1984. Flow of the Alaskan Stream and its variations. *Deep Sea Res.,* 31:369- 386.
Reed, R.K., J. D. Schumacher, and L.S. Incze, 1987. Circulation in Shelikof Strait, Alaska. *J. Phys. Oceanogr*. 17:154&1554.
Reed, R. K., and J. D. Schumacher, 1989. Transport and physical properties in central Shelikof Strait, Alaska, *Cont. Shelf. Res*., 261-268
Reed, R. K., and S. Bograd, 1995. Transport in Shelikof Strait, Alaska: An update, *Cont. Shelf Res.,*
Royer T. C., On the effect of precipitation and runoff on coastal circulation in the Gulf of Alaska, *J. Phys. Oceanogr*., 9, 555-63, 1979.

Royer, T. C., Baroclinic transport in the Gulf of Alaska, II, Fresh water driven coastal current, *J. Mar. Res.,* 39, 251-266, 1981

Royer, T.C., 1982. Coastal freshwater discharge in the Northeast Pacific. *J. Geophys. Res.* 87, 2017–2021.

Royer, T.C. 2005. Hydrographic responses at a coastal site in the northern Gulf of Alaska to seasonal and interannual forcing. *Deep-Sea Res. II,* 52:267-288.

Schumacher, J. D., and R. K. Reed, Coastal flow in the northwest Gulf of Alaska: The Kenai Current, *J. Geophys. Res*., 85,6680-6688, 1980.

Schumacher, J. D., P. J. Stabeno, and A. T. Roach, 1989. Volume transport in the Alaska Coastal Current, *Cont. Shelf Res*., 9, 1071-1089

Schumacher, J.D., Stabeno, P.J., Roach, A.T., 1990. Volume transport in the Alaska Coastal Current. *Cont. Shelf Res.* 9, 1071–1083.

Schumacher, J.D., Stabeno, P.J., and Bograd, S.J., 1993. Characteristics of an eddy over a continental shelf: Shelikof Strait, Alaska. *J. Geophys. Res.* 98:8395-8404.

Schumacher, J.D. [ed.]. 2005. Cook Inlet Physical Oceanography Workshop Proceedings, http://doc.aoos.org/other_meetings/2005/cook_inlet_physical_oceanography_workshop_proceedings-combined%20sections-final-2006.pdf

Smith, W.H.F. and Sandwell, D.T., 1994, Bathymetric prediction from dense satellite altimetry and sparse shipboard bathymetry, J. Geophys. Res. 99, 21803–21824.

Stabeno, P.J., R. K. Reed, and J.D. Schumacher, 1995. The Alaska Coastal Current: continuity of transport and forcing. *J. Geophys. Res.,* 100, 2477–2485.

Stabeno, P.J., and A.J. Hermann, 1996. An eddy-resolving circulation model for the western Gulf of Alaska Shelf: 2. Comparison of results to oceanographic observations. *J. Geophys. Res.*, 101(C1):1151-1161.

Stabeno, P.J., N.J. Bond, A. J. Hermann, N. Kachel, C.W. Mordy, and J.E. Overland, 2004. Meteorology and Oceanography of the northern Gulf of Alaska. *Cont. Shelf Res.*, 24, 859–897.

Stabeno, P.J., S. Bell, W. Cheng, S. Danielson, N.B. Kachel, C.W. Mordy, 2016. Long-term observations of Alaska Coastal Current in the northern Gulf of Alaska Deep-Sea Res. II, 132 (2016-a), pp. 24–40, http://dx.doi.org/10.1016/j.dsr2.2015.12.016

Steele, M., G. L. Mellor, and M. G. McPhee, 1989. Role of the molecular sublayer in the melting or freezing of sea ice, *J. Phys. Oceanogr.*, 19, 139-147.

Taylor, K. E. (2001), Summarizing multiple aspects of model performance in a single diagram, *J. Geophys. Res*., 106, 7183–7192, doi:10.1029/ 2000JD900719.

Umlauf, L. and H. Burchard, 2003. A generic length-scale equation for geophysical turbulence models*, J. Mar. Res*., 61, 235-265

Warner, J. C., C. R. Sherwood, H. G. Arango and R. P. Signell, 2005. Performance of four turbulence closure models implemented using a generic length scale method, *Ocean Modelling*, 8, 81-113

Wang, J., M. Jin, D.L. Musgrave, M. Ikeda, 2004. A hydrological digital elevation model for freshwater discharge into the Gulf of Alaska. *J. Geophys. Res.,* 109, 55, http://dx.doi.org/10.1029/2002JC001430

Weingartner, T. J., S. L. Danielson, and T. C. Royer, 2005. Freshwater variability and predictability in the Alaska Coastal Current, Deep Sea Res., Part II, 52, 169–191,

doi:10.1016/j.dsr2.2004.09.030
Williams, W.J., 2003. Idealized modeling of seasonal variation in the Alaska Coastal Current. Ph.D. thesis, University of Alaska, Fairbanks, 100pp.
Williams, W. J., T. J. Weingartner, and A. J. Hermann, 2010. Idealized Two-Dimensional Modeling of a Coastal Buoyancy Front, or River Plume, under Downwelling-Favorable Wind Forcing with Application to the Alaska Coastal Current. *J. Phys. Oceanogr.*, 40, 279–294. doi: http://dx.doi.org/10.1175/2009JPO4206.1
Wilson, J.G., Overland, J.E., 1986. Meteorology. In: Hood, D.W., Zimmerman, S.T. (Eds.), The Gulf of Alaska, Physical Environment and Biological Resources. Alaska Office, Ocean Assessments Division, National Oceanic and Atmospheric Administration, US Department of Commerce, pp. 31–53.
Wu, J., Aguila-Islas, A., Rember, R., Weingartner, T., Danielson, S., Whitledge, T., 2009. Size fractionated iron distribution on the northern Gulf of Alaska. *Geophys. Res. Lett*. 36, L11606. http://dx.doi.org/10.1029/2009GL038304

Appendices

Appendix 1: Modeled and Observed Tidal Current Ellipse Harmonic Parameters
Appendix 2: Monthly climatology: NWGOA velocity, near-surface and near-bottom.
Appendix 3: Monthly climatology: NWGOA sea surface temperature.
Appendix 4: Monthly climatology: NWGOA sea surface salinity.
Appendix 5: Monthly climatology: Cook Inlet velocity, near-surface and near-bottom.
Appendix 6: Monthly climatology: Cook Inlet sea surface temperature.
Appendix 7: Monthly climatology: Cook Inlet sea surface salinity.
Appendix 8: Modeled and Observed Hydrographic Transects

Appendix 1: Modeled and Observed Tidal Current Ellipse Harmonic Parameters

Table A1.1. Current meter mooring site names and locations along with associated modeled and observed tidal current harmonics parameters from the CMIST mooring locations computed using T_Tide. Parameters include the semi-major and semi-minor ellipse axes (cm s^{-1}) and the sign of the semi-minor axis denotes clockwise rotation for negative values. Column labels denote modeled (M) and observed (O) parameters.

Site	Latitude (°N)	Longitude (°E)	Semi-Major Axis		Semi-Major Axis Error		Semi-Minor Axis		Semi-Minor Axis Error	
			M	O	M	O	M	O	M	O
COI0206	61.188	209.941	64.4	63.4	4.1	3.0	-9.7	-0.8	3.3	0.6
COI0207	61.168	209.863	49.4	1.8	1.7	16.9	12.7	-0.3	2.2	2.4
COI0213	61.176	209.763	260.9	157.0	7.6	2.3	-6.9	0.5	6.7	1.3
COI0301	61.209	210.058	28.7	248.0	1.2	3.5	1.2	-4.3	0.2	0.9
COI0302	61.209	210.058	28.7	168.8	1.2	2.4	1.2	-3.5	0.2	1.6
COI0303	61.208	210.019	79.5	158.8	3.6	2.2	0.9	7.9	0.3	2.1
COI0306	61.094	209.374	198.2	167.9	2.0	2.1	1.0	-9.5	1.7	0.5
COI0307	61.028	209.398	164.6	144.7	5.9	3.2	15.8	-7.3	3.5	1.1
COI0418	58.992	207.972	48.5	77.6	1.5	2.1	-4.8	-0.1	1.4	2.1
COI0419	59.773	207.565	101.9	106.4	2.4	3.3	-3.0	1.6	1.5	2.2
COI0420	59.751	207.776	114.9	108.1	2.2	3.2	-2.1	2.9	0.5	1.4
COI0421	59.506	208.275	31.1	16.7	0.7	0.9	0.6	6.6	0.7	0.8
COI0422	59.594	208.757	3.2	19.1	0.1	0.4	0.0	-0.1	0.0	0.3
COI0501	60.653	208.314	228.8	195.1	4.8	2.2	-17.6	11.3	2.3	1.8
COI0502	60.646	208.412	272.4	194.4	3.9	4.3	16.8	18.6	1.7	1.7
COI0503	60.649	208.528	196.8	256.4	12.1	3.9	8.2	4.3	2.4	0.8
COI0504	60.610	208.532	175.9	193.7	9.0	2.9	23.9	3.1	1.3	0.9
COI0505	60.526	208.191	79.2	155.9	3.2	2.6	-10.5	-19.1	3.4	2.4
COI0506	60.514	208.502	195.1	137.1	3.6	2.8	14.5	0.7	2.9	0.4
COI0507	60.478	207.808	99.7	101.0	6.2	1.3	24.6	-2.9	4.2	1.4
COI0508	60.414	208.280	212.2	179.4	3.4	2.3	-4.9	-1.0	1.9	1.1
COI0509	60.305	207.789	164.5	187.0	4.8	3.1	-21.9	2.4	5.6	0.9
COI0510	60.173	208.208	173.0	135.1	2.1	2.2	-0.6	2.4	1.8	1.6
COI0511	59.952	207.811	122.8	114.2	2.9	2.3	6.1	-9.4	1.7	1.7
COI0512	59.498	206.524	26.1	25.6	0.6	1.3	-8.1	-19.2	0.8	1.6
COI0513	59.456	208.186	26.3	49.8	0.9	1.6	0.2	-2.8	0.1	1.3
COI0514	59.229	207.012	28.6	41.9	1.2	1.1	-9.2	-16.0	1.0	1.1
COI0515	59.247	207.571	47.6	65.7	1.3	1.5	-12.4	-10.9	1.2	1.0
COI0516	59.327	207.993	112.5	97.2	2.4	1.3	4.5	-7.5	2.3	1.0
COI0517	58.818	206.771	12.6	13.9	0.7	0.7	-1.6	-0.7	0.5	0.5
COI0518	58.910	207.203	15.4	23.9	0.5	1.2	-6.5	-2.8	0.6	1.2
COI0519	58.740	207.538	35.2	62.1	0.9	1.4	-3.6	-10.0	1.0	1.1
COI0520	58.977	207.807	44.6	52.9	1.5	1.7	2.2	12.0	1.2	1.6
COI0521	59.051	208.040	48.1	88.6	1.3	1.3	-2.1	3.1	1.2	1.5
COI0522	59.142	208.236	32.0	8.9	1.2	0.9	11.1	-0.2	1.0	0.8
COI0523	59.093	208.185	66.9	109.3	2.4	3.0	3.0	-2.3	1.7	0.6
COI0524	59.066	208.243	59.0	165.4	2.1	4.6	1.0	-0.2	0.9	1.2
COI0801	60.620	208.551	167.1	144.9	10.4	4.3	17.3	-1.9	1.9	1.6

COI0802	60.601	208.552	161.6	137.9	9.4	3.4	22.1	2.1	1.1	2.2
COI1201	59.532	208.536	4.1	31.6	0.1	0.6	-0.1	0.0	0.0	0.5
COI1202	59.356	208.008	99.6	110.3	2.6	2.2	4.3	-4.1	2.0	1.9
COI1203	59.678	207.898	117.9	127.7	3.0	2.9	-2.1	-1.3	0.9	0.3
COI1204	60.990	208.870	276.7	183.4	2.0	2.4	1.2	5.8	1.6	2.3
COI1205	60.403	208.223	224.4	159.6	4.4	2.6	-3.7	0.2	2.9	0.8
COI1207	61.040	209.574	64.4	198.7	4.3	3.5	-6.8	2.2	2.7	1.5
COI1208	61.032	209.673	147.3	148.1	2.7	2.3	7.3	-1.9	2.8	2.0
COI1209	61.157	209.725	214.2	183.4	7.0	3.1	-23.1	-3.5	5.7	1.3
COI1210	60.815	208.728	285.3	182.6	6.1	2.4	-12.9	-5.5	6.0	2.1
KOD0901	57.661	207.607	0.7	5.5	0.0	0.6	0.1	-4.1	0.0	0.6
KOD0902	57.707	207.548	0.2	5.0	0.0	0.3	0.1	-0.1	0.0	0.4
KOD0903	57.717	207.565	1.4	39.6	0.1	0.7	-0.1	-0.1	0.1	0.7
KOD0904	57.737	207.598	1.7	29.4	0.1	0.5	-0.4	0.2	0.1	0.4
KOD0905	57.708	207.584	1.9	47.6	0.0	0.9	-0.2	-1.9	0.1	0.5
KOD0906	57.535	207.870	14.8	25.5	0.5	1.2	-2.8	-1.4	0.4	1.2
KOD0907	57.329	207.395	5.6	4.5	1.7	1.0	1.4	-1.1	1.0	0.9
KOD0910	57.157	207.151	3.6	3.6	1.3	0.3	0.3	0.1	1.0	0.4
KOD0911	57.165	206.832	0.2	1.1	0.0	0.2	0.0	0.1	0.0	0.1
KOD0912	57.108	206.610	0.8	0.8	0.0	0.1	0.0	0.0	0.0	0.2
KOD0913	56.998	206.502	2.2	2.2	0.1	0.2	0.1	0.0	0.1	0.2
KOD0914	56.705	206.142	12.5	5.4	1.5	0.3	0.0	0.0	1.3	0.3
KOD0915	56.614	206.033	78.2	34.3	5.1	1.3	-5.9	-6.3	4.4	1.5
KOD0916	56.504	206.154	24.3	21.8	4.0	1.0	-11.4	2.8	3.9	1.2
KOD0917	56.613	205.807	16.9	67.1	1.6	1.7	0.4	3.9	0.1	1.2
KOD0918	56.677	205.745	55.5	31.0	3.1	1.3	-0.8	-8.5	2.8	1.2
KOD0919	56.666	205.921	150.5	103.8	5.4	2.0	-8.2	3.8	3.1	1.6
KOD0920	56.712	205.285	21.9	14.2	0.6	0.5	-7.1	-10.1	0.7	0.5
KOD0921	57.213	205.145	8.3	31.1	0.7	1.3	2.7	-0.5	0.5	1.1
KOD0922	57.349	205.192	7.8	19.1	0.8	1.0	0.1	1.5	0.1	0.9
KOD0923	57.563	206.047	1.1	5.2	0.0	2.8	0.0	0.0	0.0	2.8
KOD0924	57.535	206.069	0.5	70.0	0.0	0.8	0.1	1.8	0.0	0.7
KOD0925	57.719	205.897	6.7	17.9	0.3	0.6	0.6	-4.2	0.2	0.6
KOD0926	58.148	206.754	4.4	5.3	0.1	0.6	0.5	1.2	0.1	0.5
KOD0927	57.975	206.507	4.4	7.4	0.2	0.3	0.0	-0.8	0.0	0.4
KOD0928	57.978	206.813	2.7	16.9	0.0	0.7	-0.1	-2.2	0.0	0.6
KOD0929	57.949	207.070	3.5	68.0	0.1	2.0	0.0	10.8	0.0	1.2
KOD0930	57.866	207.170	4.7	170.4	0.1	3.8	-0.3	3.9	0.1	3.0
KOD0931	57.846	207.137	6.1	188.6	0.1	3.9	-0.1	2.3	0.1	3.0
KOD0932	57.837	207.156	6.5	64.1	0.1	2.5	-0.1	0.8	0.1	2.3
KOD0933	57.914	207.452	0.4	55.6	0.0	1.5	0.1	0.9	0.0	1.2
KOD0934	57.927	207.271	2.7	28.7	0.0	1.4	0.1	-2.1	0.0	1.0
KOD0935	57.999	206.882	5.0	10.5	0.1	0.3	0.1	0.1	0.1	0.2
KOD0936	58.331	207.057	3.2	10.7	0.1	0.7	0.2	0.4	0.0	0.5
KOD0937	58.391	207.122	5.3	6.8	0.1	0.8	0.3	3.4	0.1	0.9
KOD0938	58.454	207.297	1.1	6.8	0.0	0.7	0.3	-0.6	0.0	0.4
KOD0939	58.395	207.541	0.7	186.0	0.0	3.7	0.1	-2.4	0.0	1.5
KOD0940	58.385	207.524	0.3	4.1	0.0	0.5	0.1	2.5	0.0	0.6
KOD0941	58.277	208.064	55.3	59.9	2.9	0.9	-6.2	-7.7	0.7	0.8
KOD0942	58.171	208.020	36.6	95.1	3.1	2.1	-3.2	0.3	2.2	0.6
KOD0943	58.102	207.973	10.5	42.7	1.6	1.6	-5.8	-4.7	1.4	2.2

KOD0944	58.616	207.571	0.2	51.5	0.0	1.9	0.0	4.7	0.0	1.3
PWS0701	60.922	211.896	1.6	14.3	0.0	0.8	0.0	-1.7	0.0	0.5
PWS0702	60.865	211.857	2.0	1.1	0.0	0.5	0.1	-0.7	0.0	0.5
PWS0703	60.703	211.642	0.9	3.4	0.0	0.7	0.0	-0.7	0.0	0.6
PWS0704	60.684	211.914	1.8	14.4	0.0	1.0	0.0	-0.8	0.0	0.7
PWS0705	60.750	212.051	3.0	4.0	0.1	0.4	0.0	-0.6	0.0	0.4
PWS0706	60.598	211.933	2.2	3.6	0.0	0.3	0.1	-0.3	0.0	0.3
PWS0707	60.541	211.777	0.3	0.6	0.0	0.2	0.0	0.0	0.0	0.1
PWS0708	60.435	212.067	3.3	7.3	0.1	0.6	0.0	0.3	0.0	0.3
PWS0709	60.302	211.988	3.4	3.4	0.1	0.3	0.0	0.2	0.0	0.3
PWS0710	60.293	212.007	8.1	9.3	0.1	0.6	-0.2	1.7	0.1	0.6
PWS0711	60.207	211.834	0.1	3.9	0.0	0.5	0.0	0.4	0.0	0.4
PWS0712	60.111	211.948	0.6	2.8	0.0	0.4	0.0	0.5	0.0	0.2
PWS0713	60.074	211.757	0.1	86.7	0.0	1.4	0.0	-1.0	0.0	1.4
PWS0714	59.988	211.814	0.5	61.2	0.0	1.7	0.0	-0.5	0.0	0.9
PWS0715	59.987	211.966	54.1	16.7	0.6	1.3	0.0	1.1	0.6	1.1
PWS0716	59.911	211.813	19.5	28.6	0.4	1.3	-2.3	2.7	0.3	1.2
PWS0717	59.911	211.889	25.6	54.3	0.5	1.1	-4.0	-3.3	0.3	1.2
PWS0718	59.854	211.623	6.2	18.0	0.3	1.2	-2.0	-9.1	0.3	1.6
PWS0719	59.844	211.984	25.7	37.5	2.0	0.8	-0.8	-2.9	1.7	0.9
PWS0720	59.682	211.926	30.7	82.5	1.8	3.5	-15.1	-28.0	1.8	3.4
PWS0721	59.793	212.647	16.0	33.3	0.4	1.6	-7.8	-0.8	0.4	1.7
PWS0722	60.046	213.209	14.5	17.8	0.3	4.7	-6.3	-4.8	0.5	1.9
PWS0723	60.206	212.294	4.2	7.7	0.0	0.2	0.2	-0.3	0.0	0.2
PWS0724	60.194	212.659	6.7	7.9	0.2	1.2	0.1	-1.9	0.2	0.9
PWS0725	60.345	212.895	0.2	15.4	0.0	0.6	0.0	0.1	0.0	0.3
PWS0726	60.284	213.200	30.6	41.0	0.3	1.4	0.9	1.2	0.5	0.6
PWS0727	60.436	213.323	5.6	18.9	0.2	1.8	0.0	-0.9	0.0	1.1
PWS0728	59.993	213.569	21.1	24.6	0.7	0.9	-11.9	-14.3	0.7	0.9
PWS0729	60.154	213.712	13.1	10.2	0.4	0.8	-4.8	-1.6	0.4	0.6
PWS0730	60.064	214.873	5.2	5.9	0.1	0.7	-2.1	-3.1	0.1	0.6
PWS0731	60.489	213.597	4.4	9.4	0.1	0.9	-0.2	0.8	0.1	0.5
PWS0732	60.538	214.143	2.4	7.7	0.3	0.9	1.9	-0.6	0.3	0.4
PWS0733	60.546	214.202	8.3	23.4	0.5	1.5	0.0	-0.1	0.5	1.3
PWS0734	60.546	214.202	8.3	60.9	0.5	1.1	0.0	-1.6	0.5	1.1
PWS0735	60.519	214.103	10.2	67.2	0.4	1.8	-0.6	0.0	0.4	1.0
PWS0736	60.538	213.542	5.3	6.7	0.1	0.3	-0.4	-0.6	0.1	0.4
PWS0737	60.599	213.234	4.7	5.4	0.1	0.5	1.2	-2.5	0.1	0.3
PWS0738	60.866	213.169	2.4	2.2	0.2	0.3	-0.1	0.3	0.2	0.1
PWS0739	60.539	212.475	8.3	22.0	0.1	1.0	-0.8	-2.4	0.0	0.9
PWS0740	60.671	212.634	0.2	5.2	0.0	0.2	0.0	1.4	0.0	0.3
PWS0741	60.700	212.538	0.2	11.8	0.0	0.9	0.0	-0.7	0.0	0.3
PWS0742	60.767	212.481	2.7	5.3	0.0	0.5	-0.4	-0.9	0.0	0.2
PWS0743	60.842	212.678	4.1	7.9	0.1	0.6	-0.4	0.6	0.1	0.7
PWS0744	60.831	212.893	1.3	10.3	0.1	0.6	0.4	-0.3	0.1	0.6
PWS0745	60.999	213.293	0.7	14.4	0.0	0.5	0.0	-1.3	0.0	0.5
PWS0746	61.090	213.573	0.5	0.2	0.0	0.2	0.0	0.0	0.0	0.0

Table A1.2. Current meter mooring site names and locations along with associated modeled and observed tidal current harmonics parameters from the CMIST mooring locations computed using T_Tide. Parameters include the ellipse inclination (degrees) and Greenwich Phase (degrees). Column labels denote modeled (M) and observed (O) parameters.

Site	Latitude (N)	Longitude (E)	Inclination		Inclination Error		Greenwich Phase		Greenwich Phase Error	
			M	O	M	O	M	O	M	O
COI0206	61.188	209.941	23	180	3	1	7	206	4	3
COI0207	61.168	209.863	104	160	3	10	111	347	2	241
COI0213	61.176	209.763	43	9	1	0	15	23	2	1
COI0301	61.209	210.058	179	79	0	0	207	36	2	1
COI0302	61.209	210.058	179	65	0	1	207	19	2	1
COI0303	61.208	210.019	178	52	0	1	209	22	2	1
COI0306	61.094	209.374	17	179	0	0	355	210	1	1
COI0307	61.028	209.398	25	8	1	0	324	12	2	1
COI0418	58.992	207.972	146	146	1	1	243	272	2	2
COI0419	59.773	207.565	68	66	1	1	302	315	2	2
COI0420	59.751	207.776	81	74	0	1	303	306	1	2
COI0421	59.506	208.275	33	28	1	3	240	235	1	3
COI0422	59.594	208.757	173	40	0	1	27	237	1	1
COI0501	60.653	208.314	69	98	1	1	315	350	1	1
COI0502	60.646	208.412	84	75	0	1	343	351	1	1
COI0503	60.649	208.528	89	82	1	0	310	345	3	1
COI0504	60.610	208.532	93	101	1	0	316	345	3	1
COI0505	60.526	208.191	65	37	2	1	281	345	2	1
COI0506	60.514	208.502	83	87	1	0	329	342	1	1
COI0507	60.478	207.808	73	43	3	1	274	337	4	1
COI0508	60.414	208.280	68	74	1	0	331	1	1	1
COI0509	60.305	207.789	65	77	2	0	321	339	2	1
COI0510	60.173	208.208	58	62	1	1	317	336	1	1
COI0511	59.952	207.811	70	60	1	1	303	333	1	1
COI0512	59.498	206.524	27	165	2	9	338	217	1	9
COI0513	59.456	208.186	4	34	0	2	227	261	2	2
COI0514	59.229	207.012	90	93	2	2	290	299	3	2
COI0515	59.247	207.571	100	95	2	1	269	277	2	1
COI0516	59.327	207.993	57	62	1	1	237	263	1	1
COI0517	58.818	206.771	64	108	2	2	326	286	3	3
COI0518	58.910	207.203	124	133	3	3	262	272	3	3
COI0519	58.740	207.538	162	153	2	1	228	270	2	2
COI0520	58.977	207.807	160	148	1	2	224	273	2	2
COI0521	59.051	208.040	143	140	2	1	248	254	2	1
COI0522	59.142	208.236	165	48	2	5	219	222	3	5
COI0523	59.093	208.185	152	96	1	0	254	233	2	2
COI0524	59.066	208.243	163	8	1	0	249	51	2	2
COI0801	60.620	208.551	93	105	1	1	306	336	4	2
COI0802	60.601	208.552	92	115	1	1	309	339	4	1
COI1201	59.532	208.536	11	43	0	1	174	238	1	1
COI1202	59.356	208.008	63	55	1	1	251	249	2	1
COI1203	59.678	207.898	91	92	0	0	297	300	2	1
COI1204	60.990	208.870	33	53	0	1	348	11	0	1

COI1205	60.403	208.223	64	77	1	0	326	355	1	1
COI1207	61.040	209.574	25	161	3	1	301	195	3	1
COI1208	61.032	209.673	146	147	1	1	152	201	1	1
COI1209	61.157	209.725	49	14	2	0	9	24	2	1
COI1210	60.815	208.728	32	34	1	1	318	2	1	1
KOD0901	57.661	207.607	29	122	2	15	7	235	2	16
KOD0902	57.707	207.548	161	87	13	4	174	232	6	3
KOD0903	57.717	207.565	146	45	3	1	186	228	2	1
KOD0904	57.737	207.598	135	33	2	1	187	244	2	1
KOD0905	57.708	207.584	162	69	2	1	188	237	2	1
KOD0906	57.535	207.870	72	72	2	3	242	253	2	3
KOD0907	57.329	207.395	83	111	11	13	223	224	20	14
KOD0910	57.157	207.151	74	163	17	6	131	220	22	5
KOD0911	57.165	206.832	49	17	2	6	356	37	2	9
KOD0912	57.108	206.610	91	47	1	11	167	196	3	12
KOD0913	56.998	206.502	101	85	2	4	170	209	3	5
KOD0914	56.705	206.142	16	11	6	3	312	359	7	3
KOD0915	56.614	206.033	159	169	4	2	187	185	3	2
KOD0916	56.504	206.154	54	126	14	3	176	229	13	3
KOD0917	56.613	205.807	3	156	0	1	288	195	6	1
KOD0918	56.677	205.745	137	113	3	3	176	205	3	3
KOD0919	56.666	205.921	160	145	1	1	160	196	2	1
KOD0920	56.712	205.285	47	39	2	6	241	275	2	6
KOD0921	57.213	205.145	82	81	4	2	207	248	6	3
KOD0922	57.349	205.192	92	63	0	2	226	238	7	3
KOD0923	57.563	206.047	60	127	2	30	17	180	3	35
KOD0924	57.535	206.069	114	156	2	1	29	233	2	1
KOD0925	57.719	205.897	5	39	2	2	214	250	2	2
KOD0926	58.148	206.754	131	26	2	5	21	265	2	8
KOD0927	57.975	206.507	3	164	0	3	215	132	3	2
KOD0928	57.978	206.813	180	152	0	2	4	172	1	3
KOD0929	57.949	207.070	180	180	0	1	6	183	2	2
KOD0930	57.866	207.170	52	152	1	1	1	193	1	1
KOD0931	57.846	207.137	49	146	1	1	1	193	1	1
KOD0932	57.837	207.156	49	146	1	2	2	199	1	3
KOD0933	57.914	207.452	17	144	1	1	321	158	2	1
KOD0934	57.927	207.271	50	168	1	2	360	215	1	3
KOD0935	57.999	206.882	146	112	1	1	5	66	1	2
KOD0936	58.331	207.057	93	88	0	3	306	20	2	4
KOD0937	58.391	207.122	122	61	1	11	329	11	1	12
KOD0938	58.454	207.297	6	22	1	3	286	355	3	5
KOD0939	58.395	207.541	52	165	3	0	27	182	3	1
KOD0940	58.385	207.524	56	140	2	15	26	163	3	15
KOD0941	58.277	208.064	86	101	1	1	213	234	3	1
KOD0942	58.171	208.020	67	79	4	0	236	257	5	1
KOD0943	58.102	207.973	76	68	14	3	234	259	15	2
KOD0944	58.616	207.571	48	3	4	1	22	33	4	3
PWS0701	60.922	211.896	59	80	1	2	169	184	1	3
PWS0702	60.865	211.857	58	169	1	66	164	136	1	67
PWS0703	60.703	211.642	59	128	2	12	343	179	1	11
PWS0704	60.684	211.914	91	153	0	3	157	185	1	4

PWS0705	60.750	212.051	180	139	0	6	154	182	1	6
PWS0706	60.598	211.933	137	125	1	4	155	216	1	5
PWS0707	60.541	211.777	89	45	2	16	311	352	3	15
PWS0708	60.435	212.067	89	88	0	2	141	194	1	4
PWS0709	60.302	211.988	89	44	0	5	154	127	1	5
PWS0710	60.293	212.007	75	76	0	4	161	187	1	5
PWS0711	60.207	211.834	135	141	2	7	345	217	2	7
PWS0712	60.111	211.948	60	73	2	5	347	132	2	9
PWS0713	60.074	211.757	135	42	2	1	343	154	2	1
PWS0714	59.988	211.814	169	69	2	1	343	187	5	1
PWS0715	59.987	211.966	45	31	1	5	141	167	1	5
PWS0716	59.911	211.813	25	35	1	2	179	189	1	3
PWS0717	59.911	211.889	29	54	1	1	167	176	1	1
PWS0718	59.854	211.623	69	57	3	8	183	204	3	6
PWS0719	59.844	211.984	55	37	4	1	180	204	4	1
PWS0720	59.682	211.926	118	111	5	3	159	168	5	3
PWS0721	59.793	212.647	50	51	2	3	208	207	2	3
PWS0722	60.046	213.209	94	100	2	7	168	188	2	15
PWS0723	60.206	212.294	59	73	0	1	177	225	1	1
PWS0724	60.194	212.659	52	56	1	7	185	236	1	9
PWS0725	60.345	212.895	44	175	6	1	357	184	6	2
PWS0726	60.284	213.200	93	95	1	1	166	203	1	2
PWS0727	60.436	213.323	87	24	0	3	148	206	2	5
PWS0728	59.993	213.569	122	134	3	3	155	194	3	3
PWS0729	60.154	213.712	146	165	2	4	151	197	2	5
PWS0730	60.064	214.873	120	133	2	8	137	148	2	9
PWS0731	60.489	213.597	31	9	1	4	160	206	1	5
PWS0732	60.538	214.143	159	10	24	3	294	224	24	7
PWS0733	60.546	214.202	43	31	4	3	40	189	3	4
PWS0734	60.546	214.202	43	52	4	1	40	41	3	1
PWS0735	60.519	214.103	39	20	2	1	191	49	2	1
PWS0736	60.538	213.542	11	15	1	4	167	207	1	3
PWS0737	60.599	213.234	81	101	1	5	170	140	1	6
PWS0738	60.866	213.169	52	175	5	4	140	18	5	7
PWS0739	60.539	212.475	87	135	0	2	148	189	1	2
PWS0740	60.671	212.634	44	139	3	3	344	208	3	3
PWS0741	60.700	212.538	45	179	7	1	178	222	6	4
PWS0742	60.767	212.481	16	5	1	3	15	70	1	6
PWS0743	60.842	212.678	164	41	1	5	186	21	2	5
PWS0744	60.831	212.893	129	131	3	3	170	216	3	3
PWS0745	60.999	213.293	85	59	0	2	156	194	3	2
PWS0746	61.090	213.573	172	180	0	11	344	349	2	48

Appendix 2: Monthly climatology, NWGOA modeled velocity near the surface and the bottom.

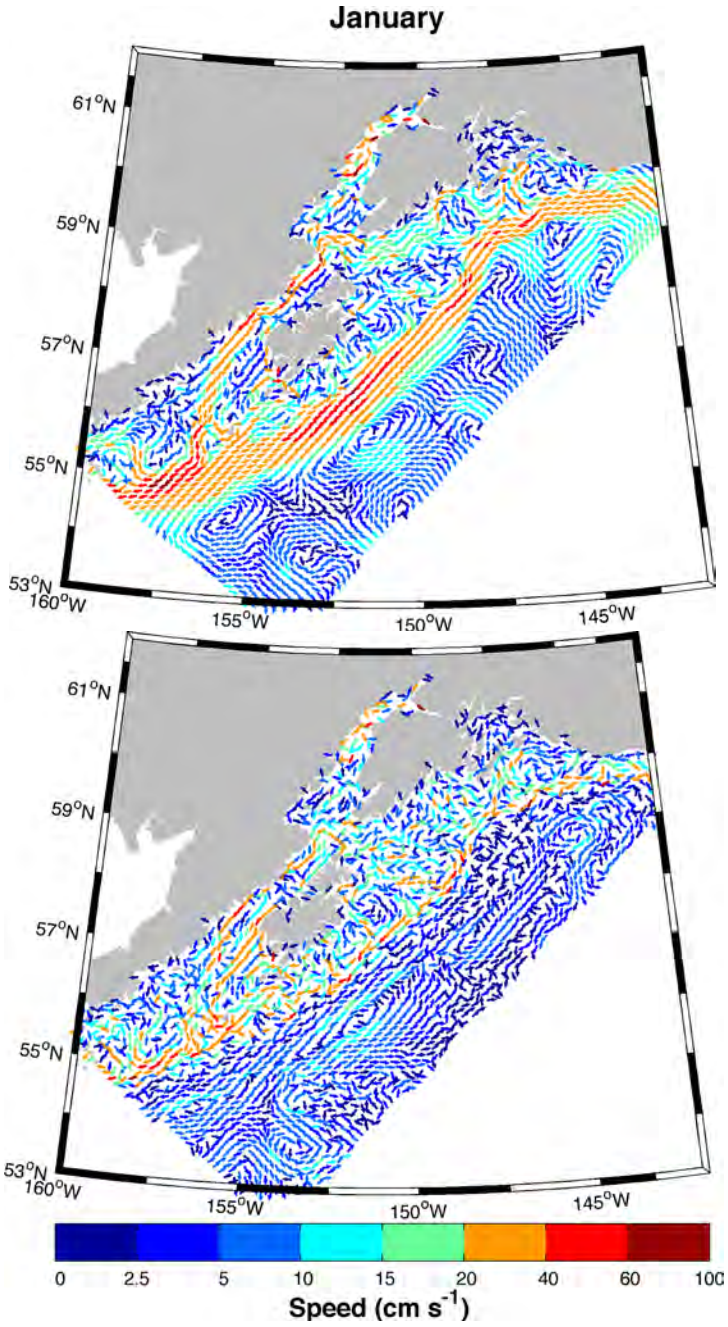

Figure A2.1: Surface (upper) and near-bottom (lower) mean velocity fields over the 10-year hindcast for January. Every 9th grid point velocity vector is shown. Arrows denote flow direction and colors denote flow speed in cm s^{-1}.

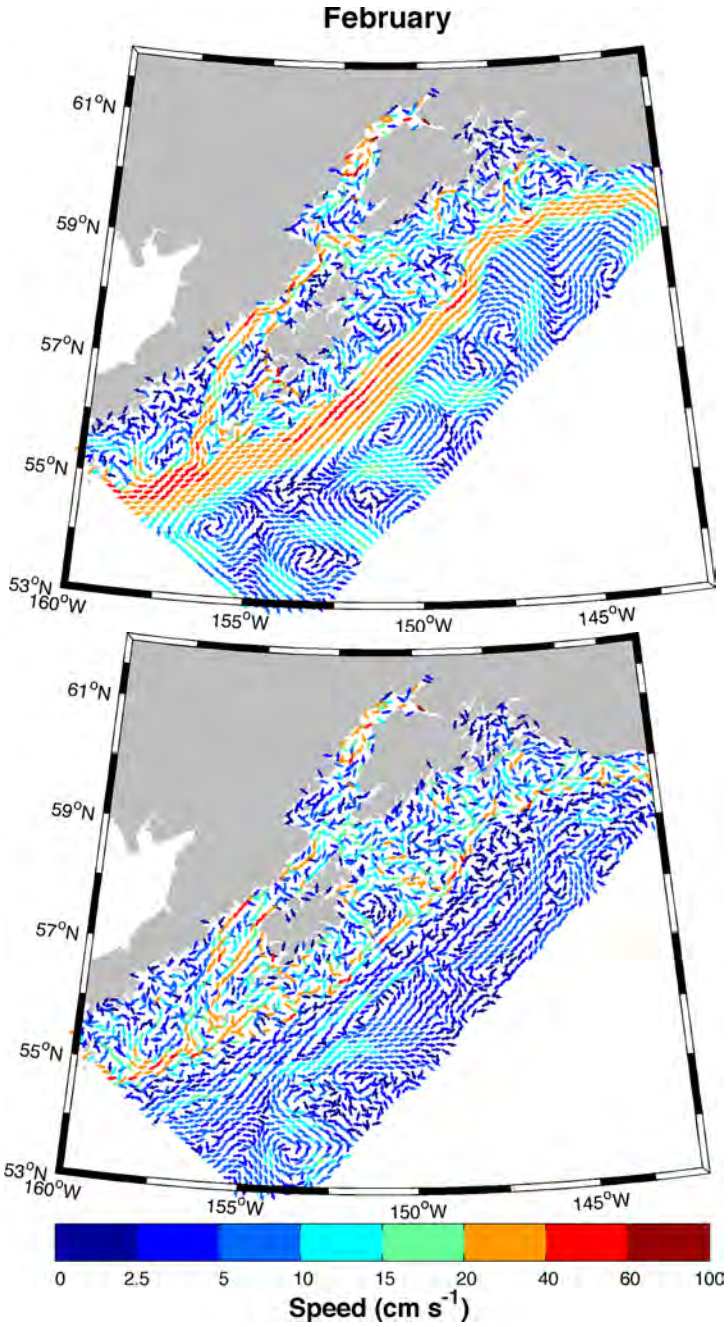

Figure A2.2: Surface (upper) and near-bottom (lower) mean velocity fields over the 10-year hindcast for February. Every 9th grid point velocity vector is shown. Arrows denote flow direction and colors denote flow speed in cm s^{-1}.

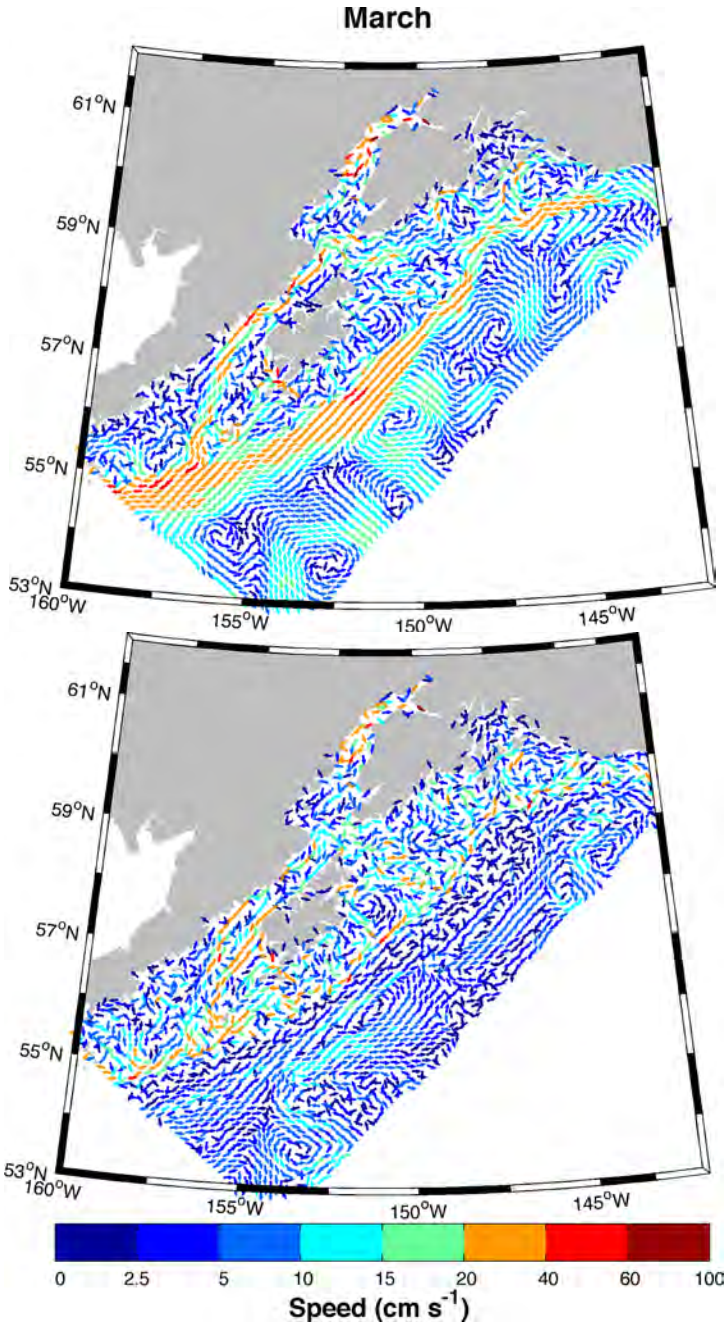

Figure A2.3: Surface (upper) and near-bottom (lower) mean velocity fields over the 10-year hindcast for March. Every 9th grid point velocity vector is shown. Arrows denote flow direction and colors denote flow speed in cm s^{-1}.

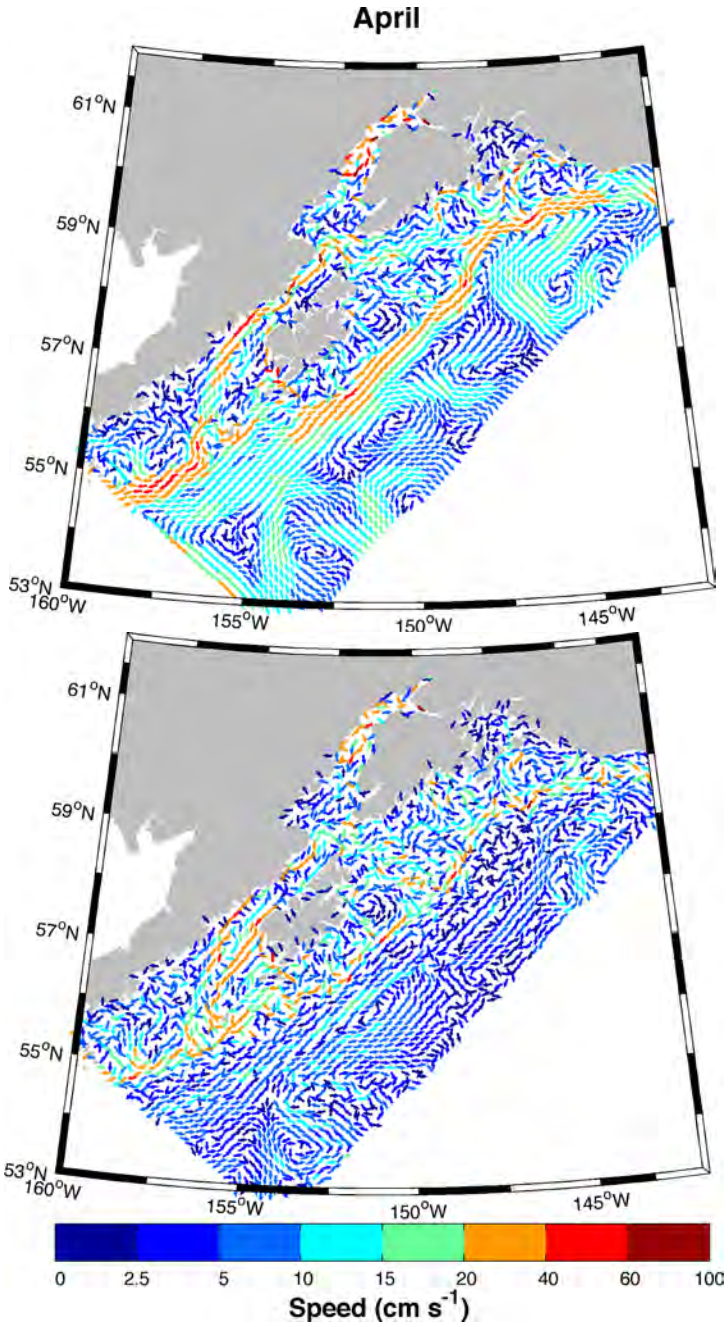

Figure A2.4: Surface (upper) and near-bottom (lower) mean velocity fields over the 10-year hindcast for April. Every 9th grid point velocity vector is shown. Arrows denote flow direction and colors denote flow speed in cm s^{-1}.

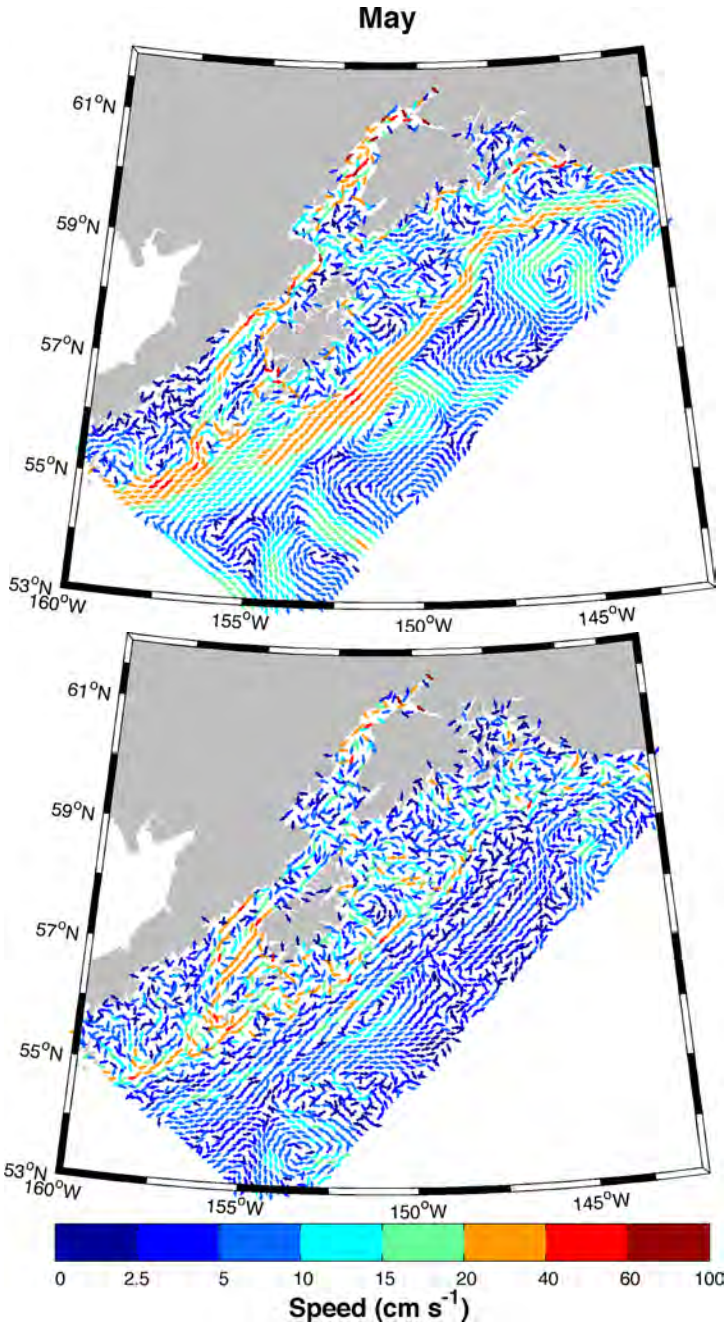

Figure A2.5: Surface (upper) and near-bottom (lower) mean velocity fields over the 10-year hindcast for May. Every 9th grid point velocity vector is shown. Arrows denote flow direction and colors denote flow speed in cm s^{-1}.

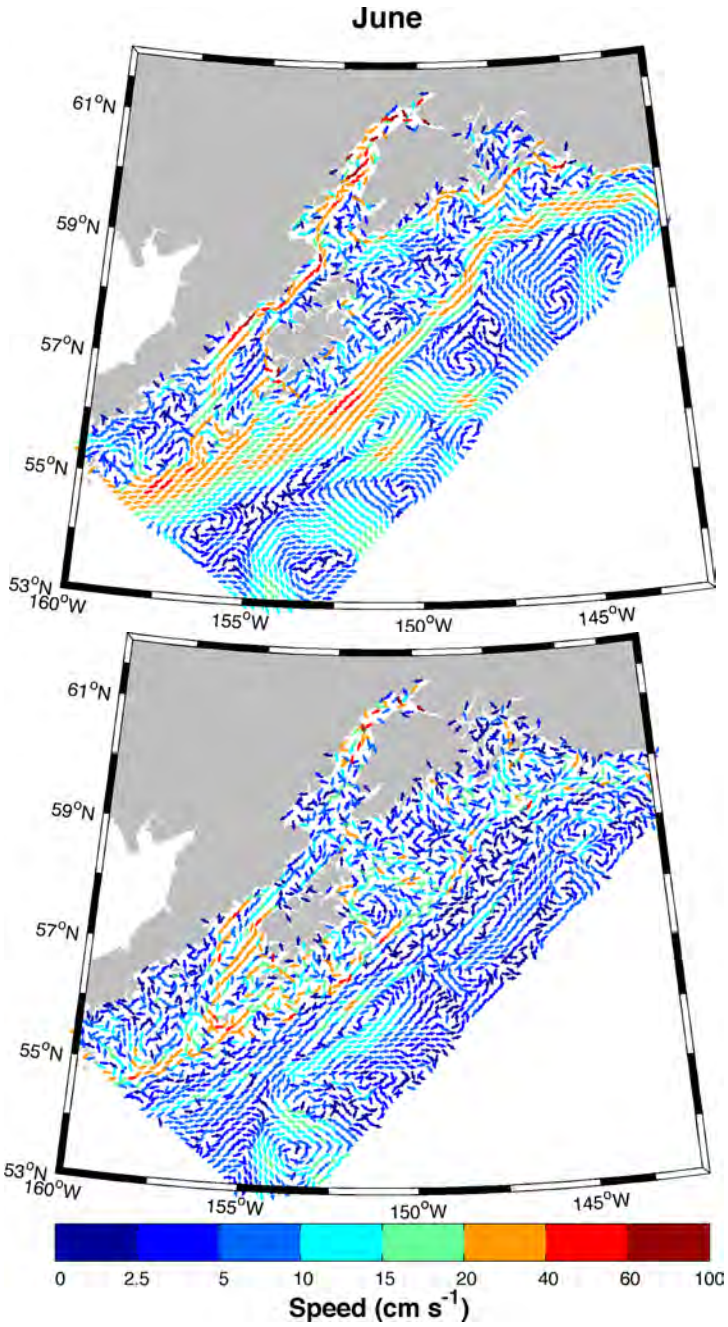

Figure A2.6: Surface (upper) and near-bottom (lower) mean velocity fields over the 10-year hindcast for June. Every 9th grid point velocity vector is shown. Arrows denote flow direction and colors denote flow speed in cm s^{-1}.

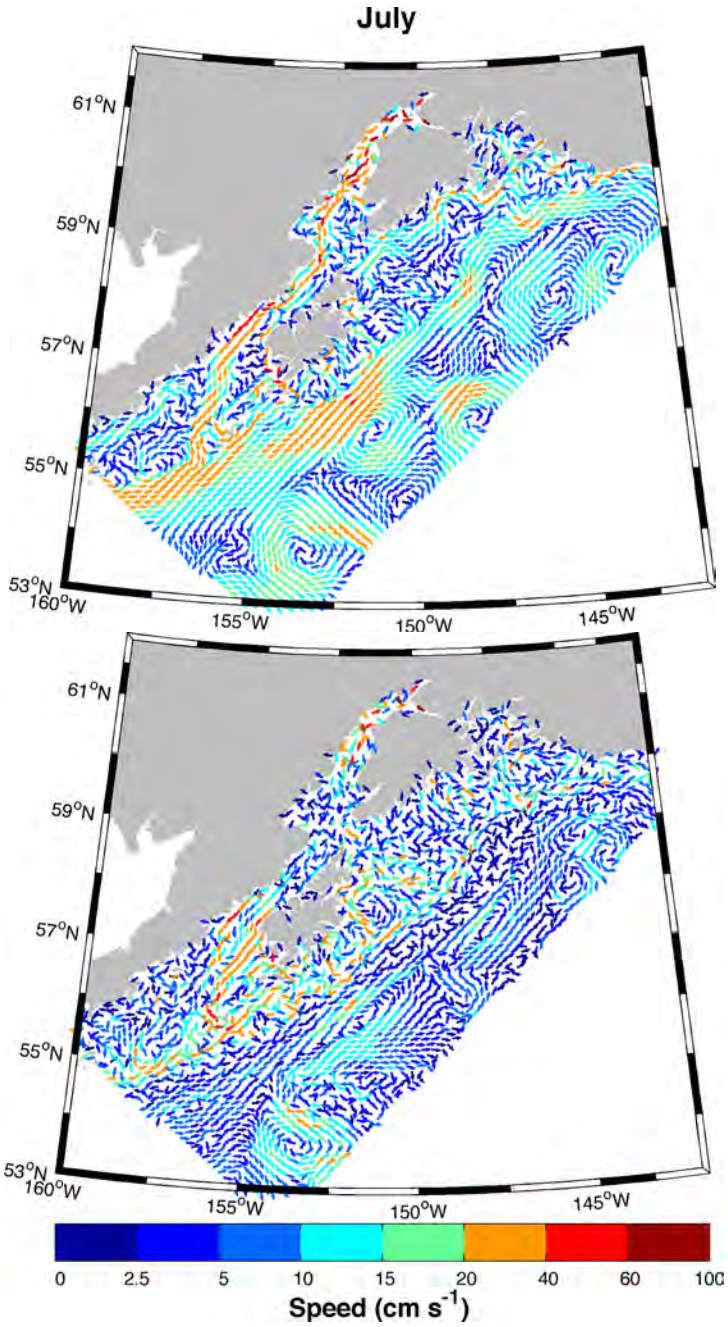

Figure A2.7: Surface (upper) and near-bottom (lower) mean velocity fields over the 10-year hindcast for July. Every 9th grid point velocity vector is shown. Arrows denote flow direction and colors denote flow speed in cm s^{-1}.

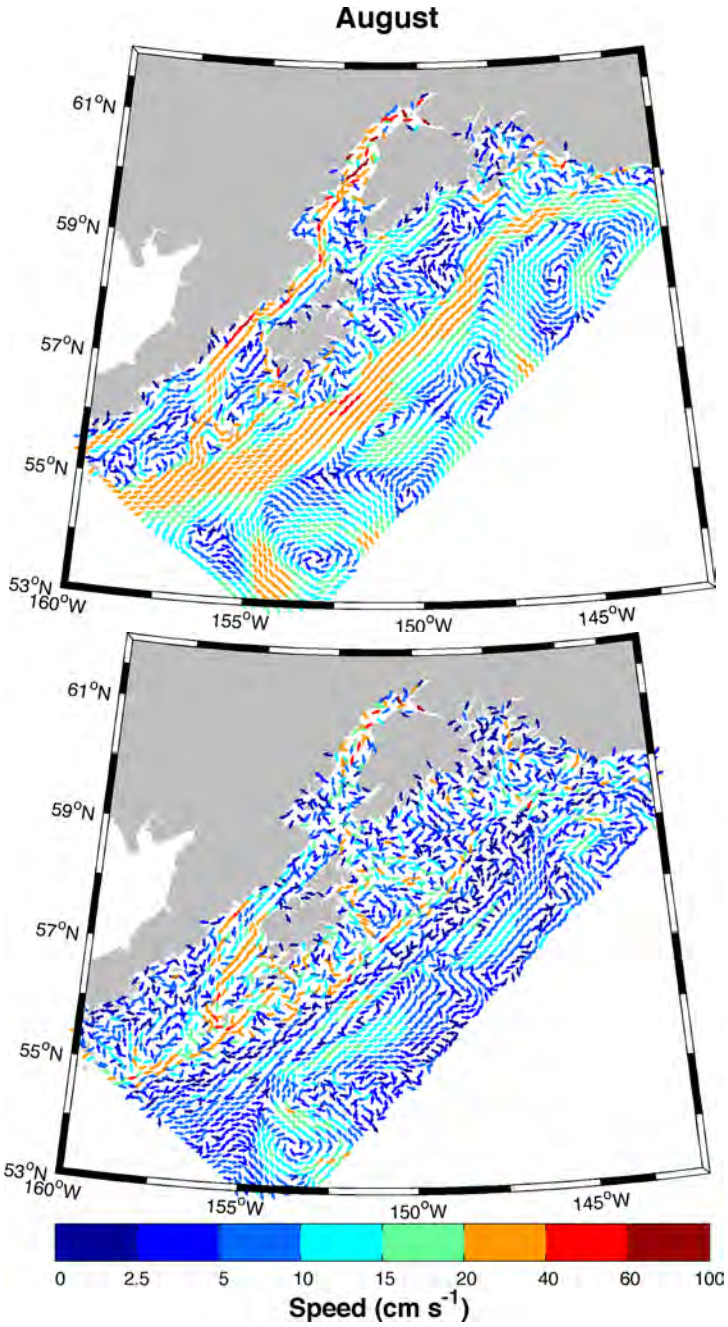

Figure A2.8: Surface (upper) and near-bottom (lower) mean velocity fields over the 10-year hindcast for August. Every 9th grid point velocity vector is shown. Arrows denote flow direction and colors denote flow speed in cm s^{-1}.

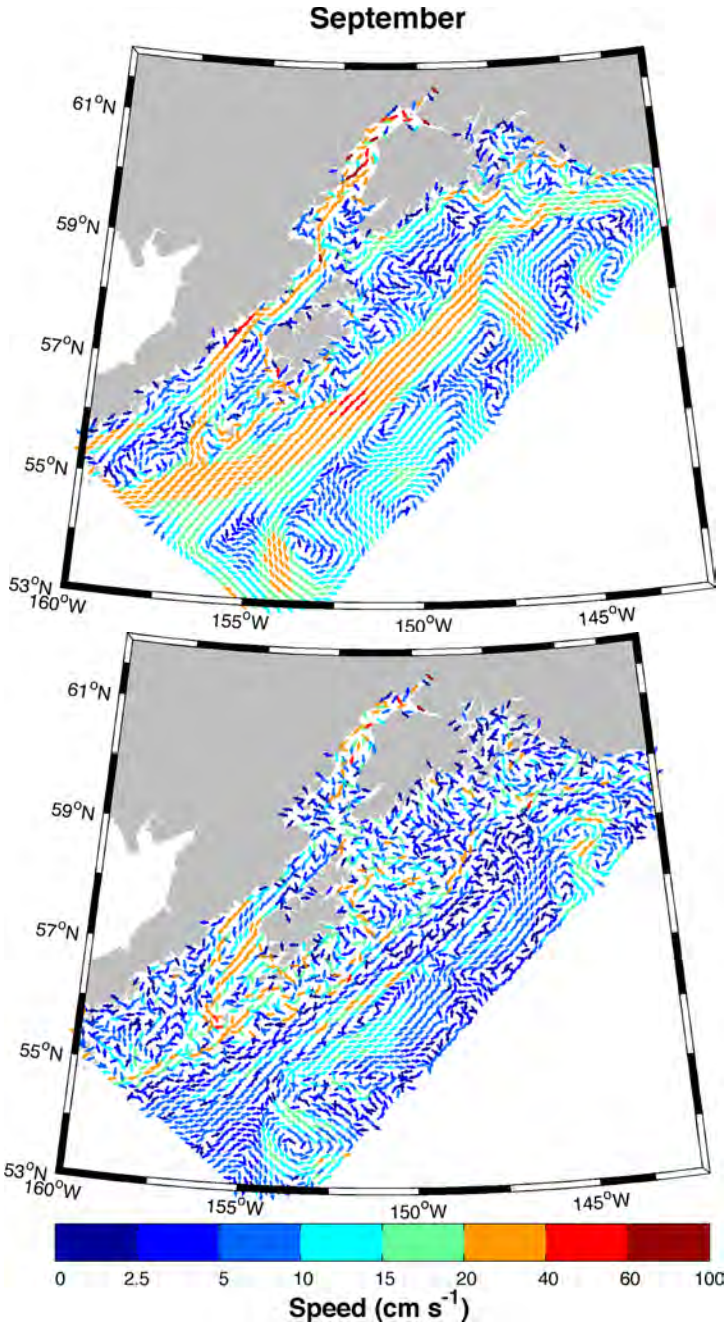

Figure A2.9: Surface (upper) and near-bottom (lower) mean velocity fields over the 10-year hindcast for September. Every 9th grid point velocity vector is shown. Arrows denote flow direction and colors denote flow speed in cm s^{-1}.

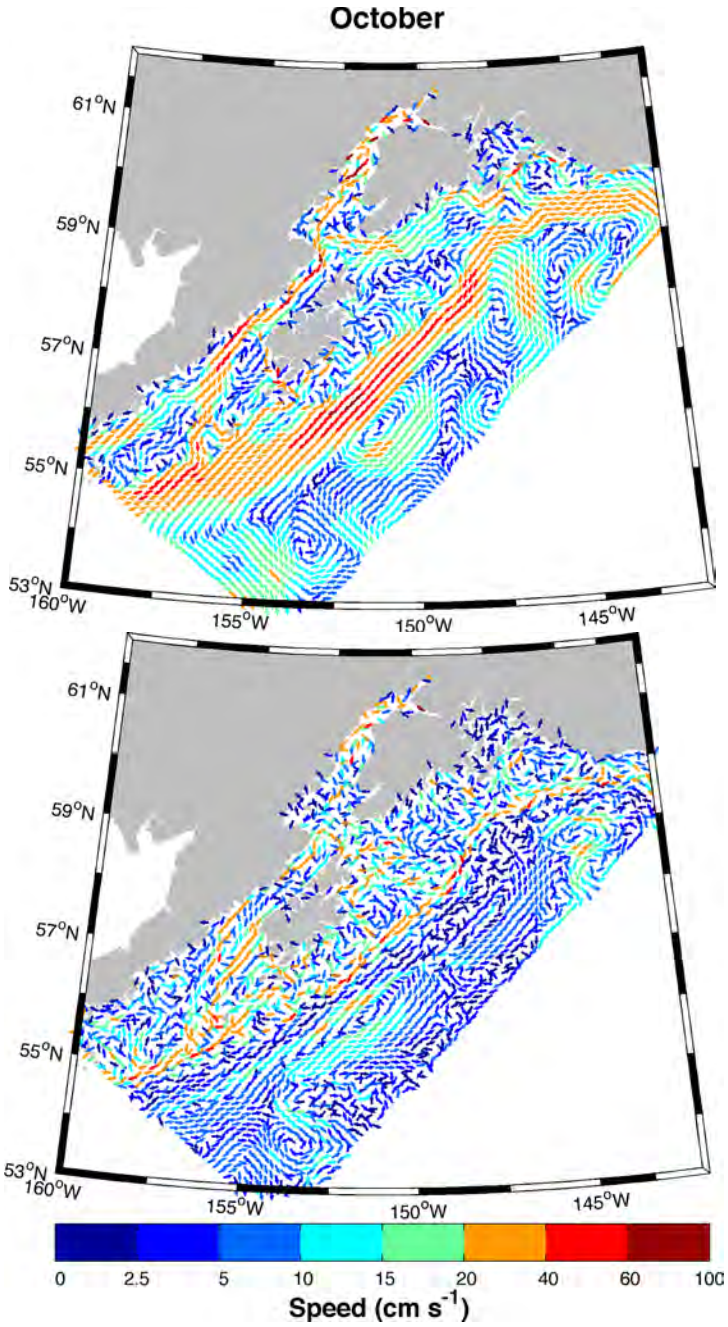

Figure A2.10: Surface (upper) and near-bottom (lower) mean velocity fields over the 10-year hindcast for October. Every 9th grid point velocity vector is shown. Arrows denote flow direction and colors denote flow speed in cm s^{-1}.

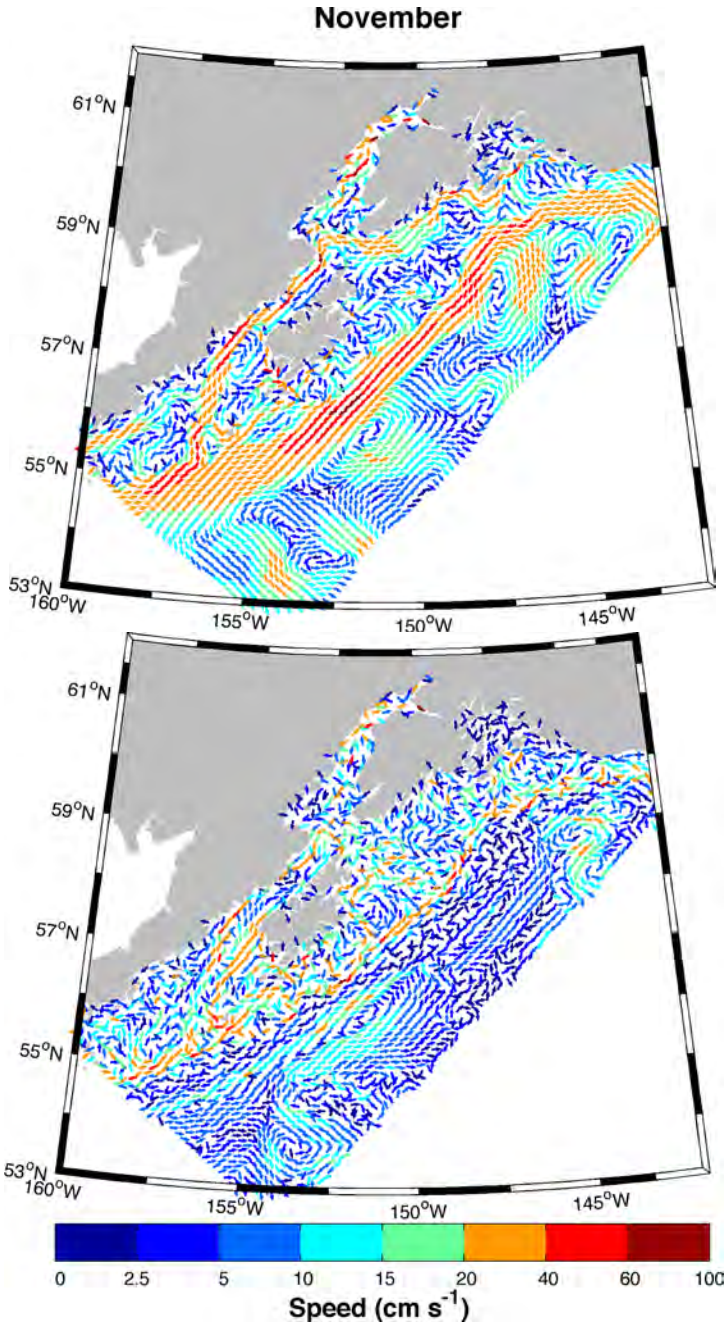

Figure A2.11: Surface (upper) and near-bottom (lower) mean velocity fields over the 10-year hindcast for November. Every 9th grid point velocity vector is shown. Arrows denote flow direction and colors denote flow speed in cm s^{-1}.

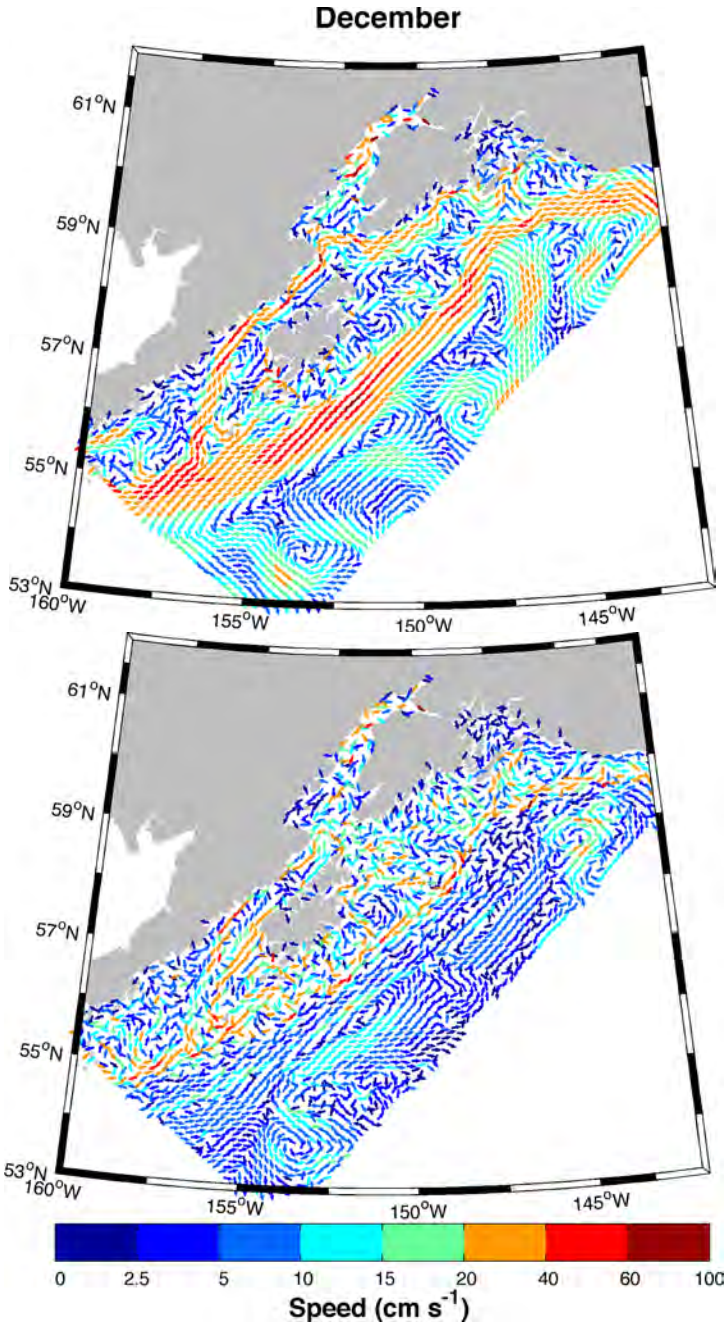

Figure A2.12: Surface (upper) and near-bottom (lower) mean velocity fields over the 10-year hindcast for Decmber. Every 9th grid point velocity vector is shown. Arrows denote flow direction and colors denote flow speed in cm s^{-1}.

Appendix 3: Monthly climatology, NWGOA modeled sea surface temperature.

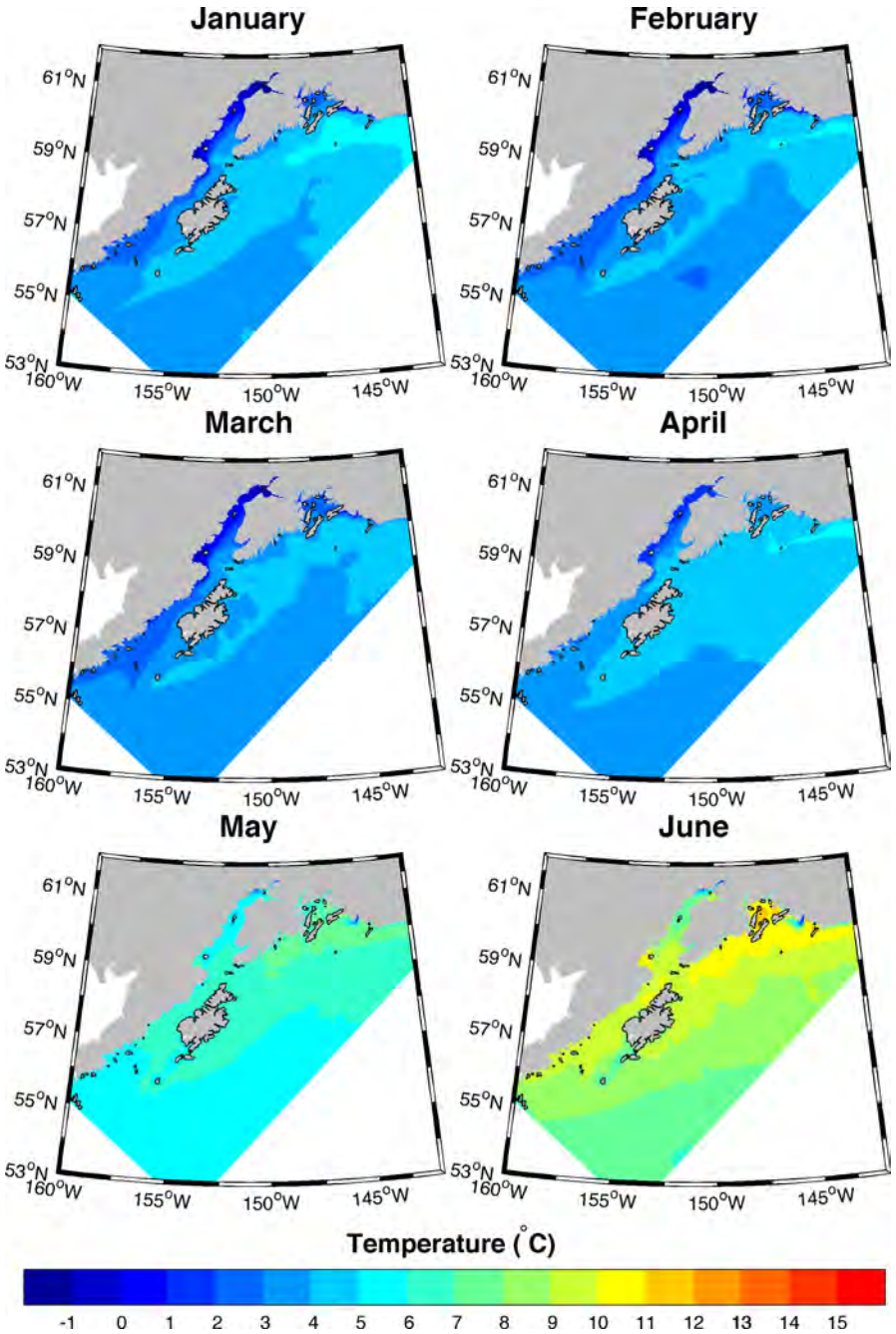

Figure A3.1: Monthly mean sea surface temperature (SST) over the 10-year hindcast for January-June over the NWGOA domain.

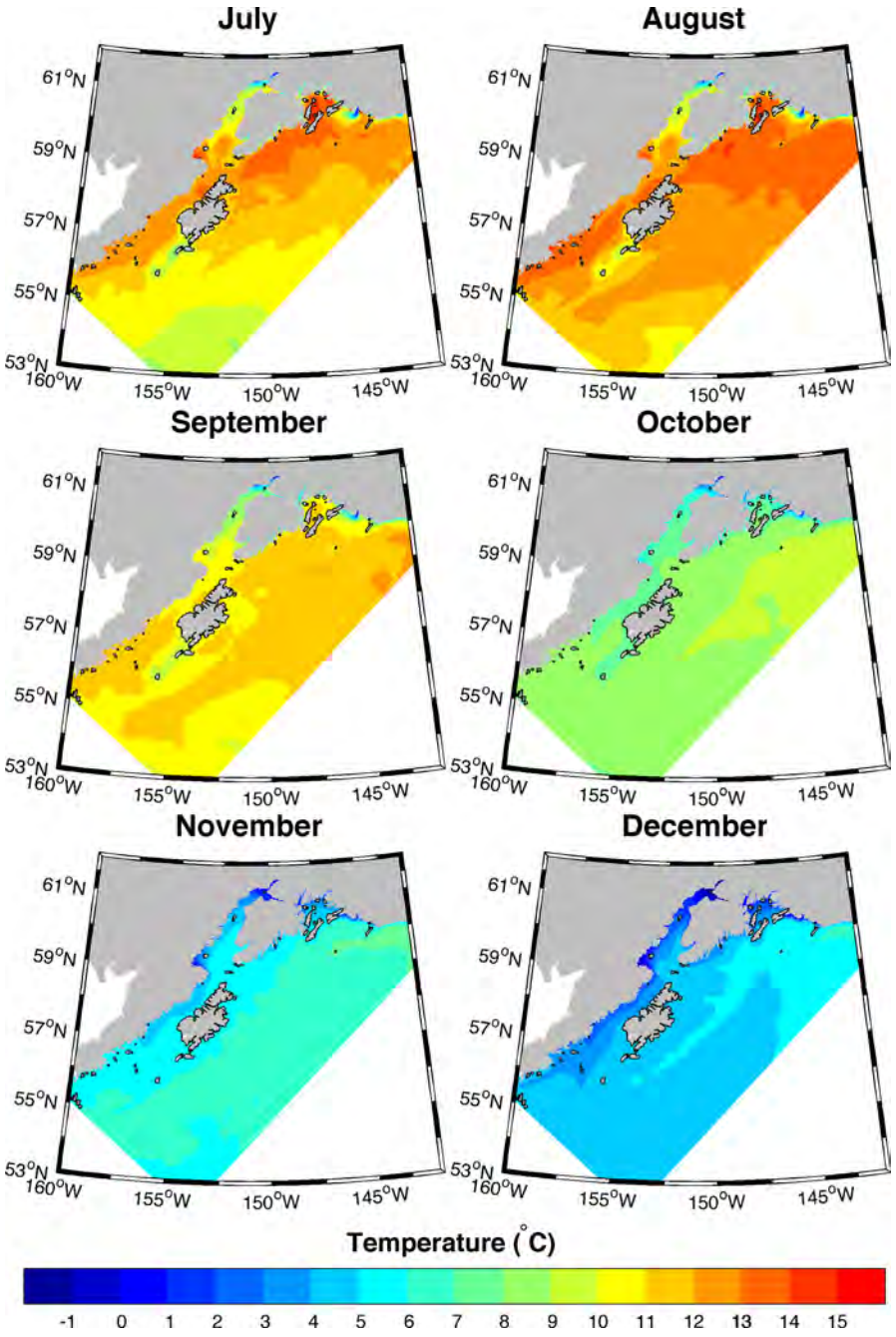

Figure A3.2: Monthly mean sea surface temperature (SST) over the 10-year hindcast for July-December over the NWGOA domain.

Appendix 4: Monthly climatology, NWGOA modeled sea surface salinity.

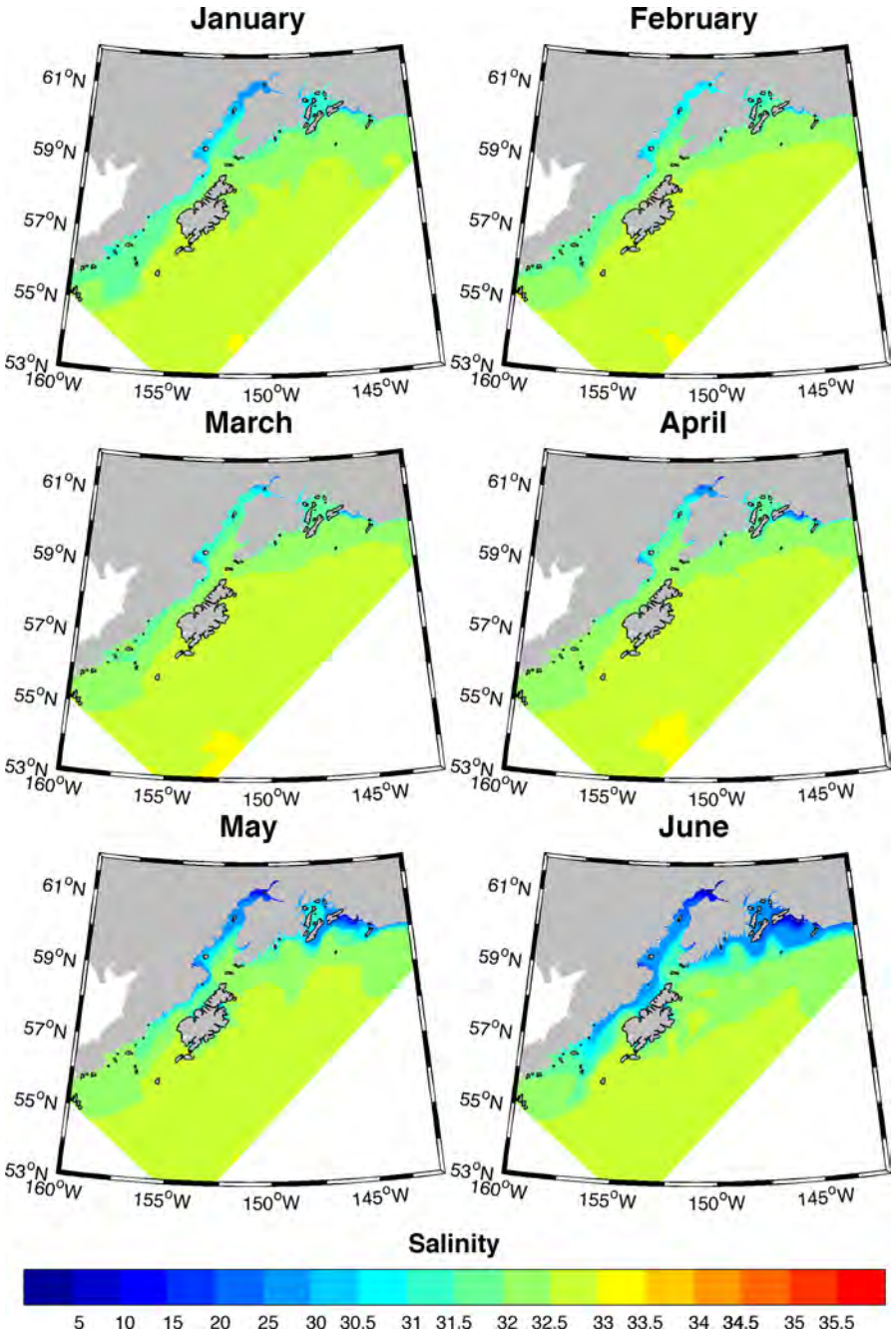

Figure A4.1: Monthly mean sea surface salinity (SSS) over the 10-year hindcast for January-June over the NWGOA domain.

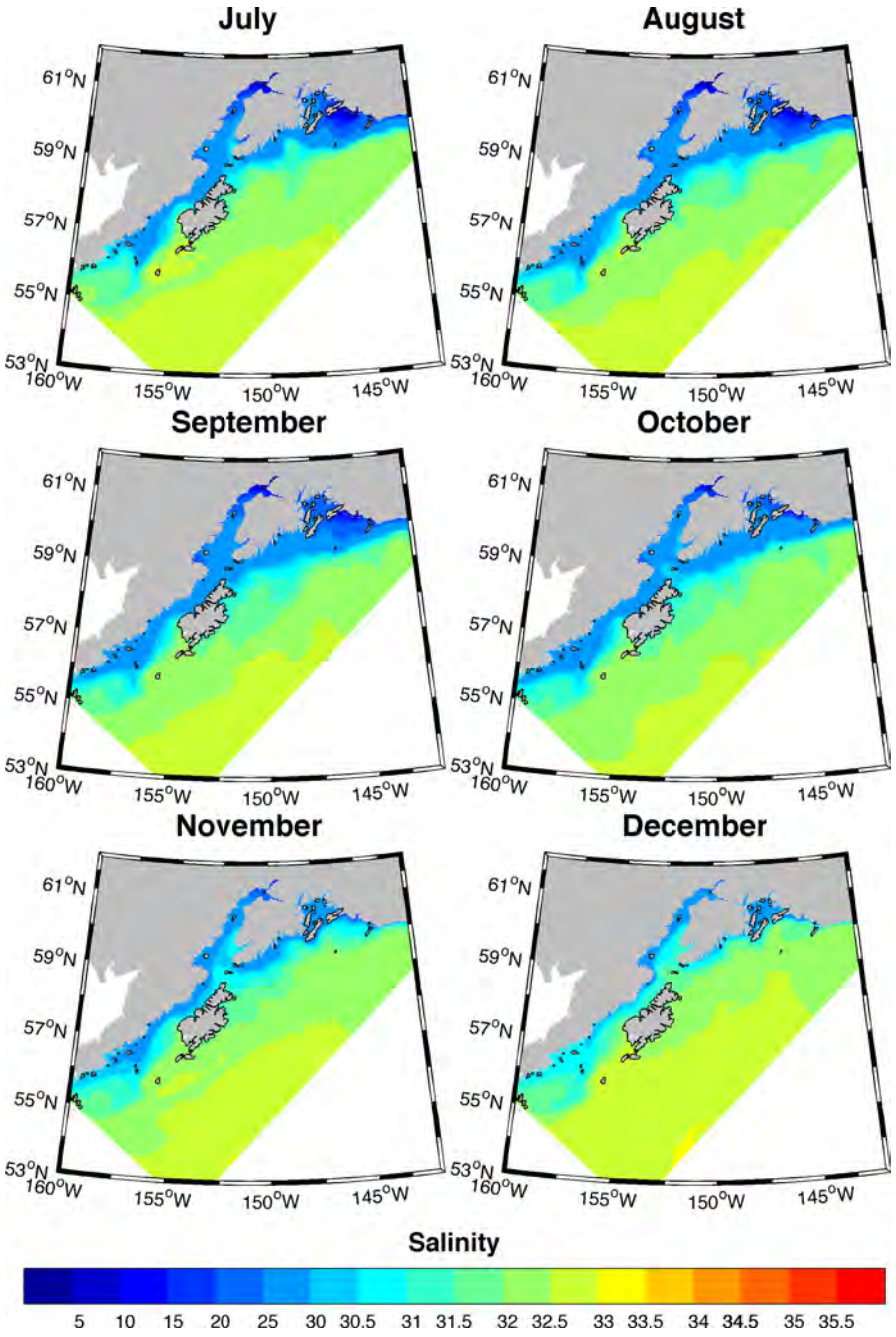

Figure A4.2: Monthly mean sea surface temperature (SST) over the 10-year hindcast for July-December.

Appendix 5: Monthly climatology, Cook Inlet modeled velocity near the surface and the bottom.

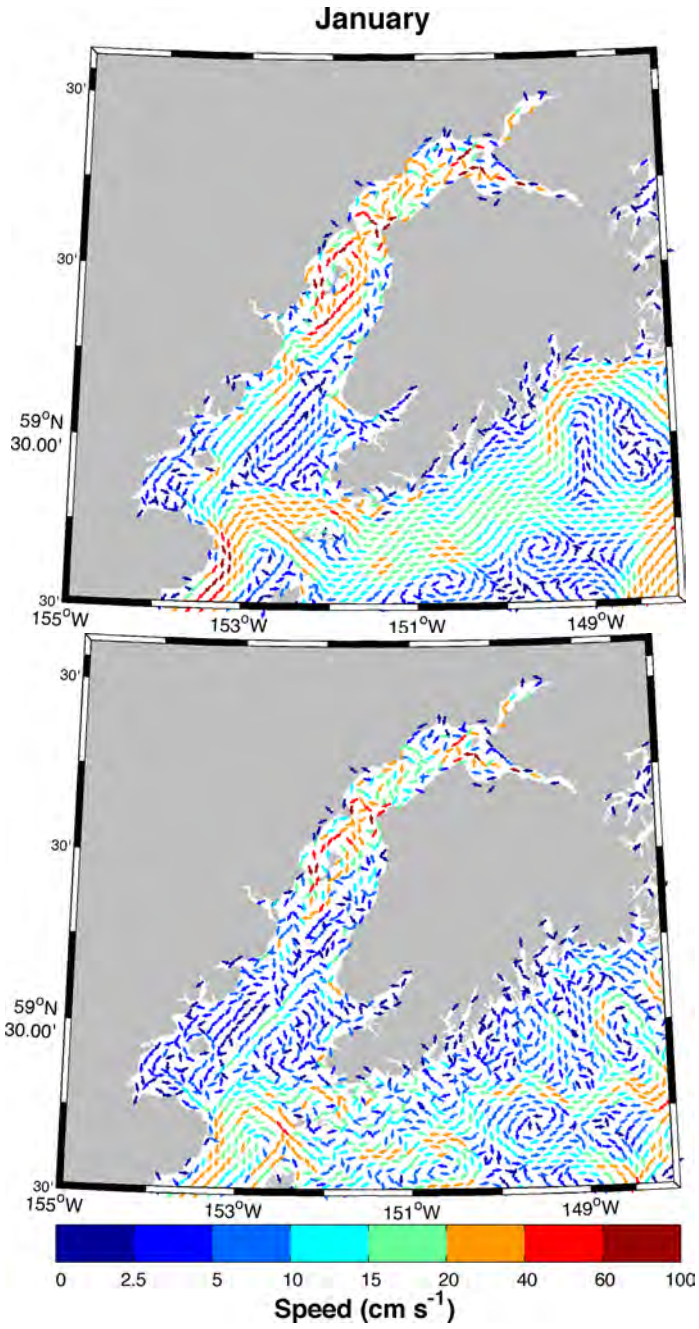

Figure A5.1: Surface (upper) and near-bottom (lower) mean velocity fields over the 10-year hindcast for January in Cook Inlet. Every 9th grid point velocity vector is shown. Arrows denote flow direction and colors denote flow speed in cm s^{-1}.

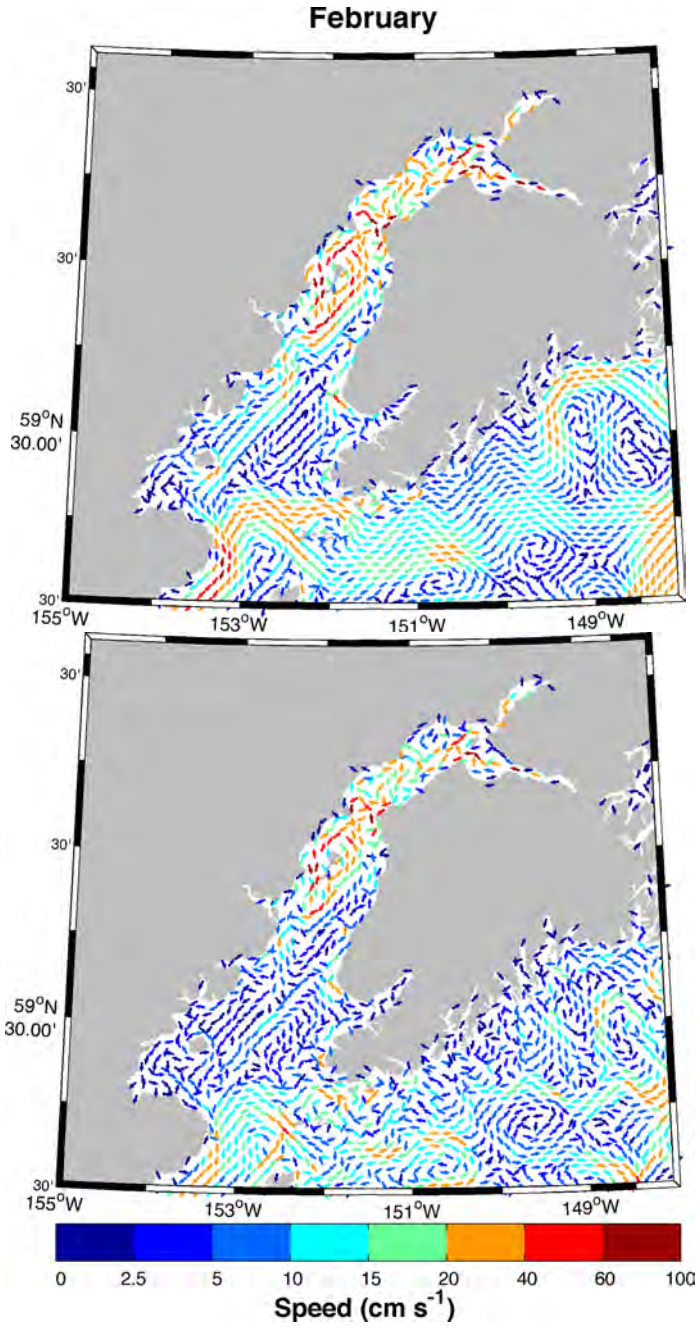

Figure A5.2: Surface (upper) and near-bottom (lower) mean velocity fields over the 10-year hindcast for February in Cook Inlet. Every 9th grid point velocity vector is shown. Arrows denote flow direction and colors denote flow speed in cm s^{-1}.

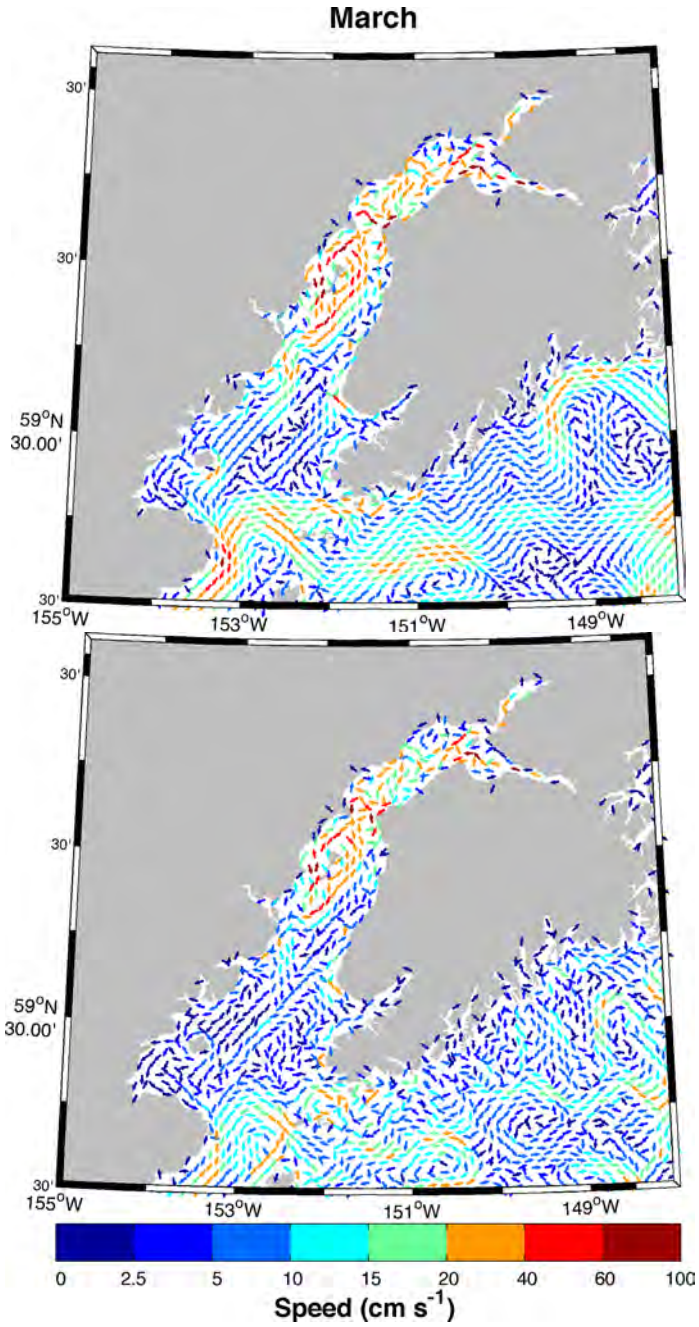

Figure A5.3: Surface (upper) and near-bottom (lower) mean velocity fields over the 10-year hindcast for March in Cook Inlet. Every 9th grid point velocity vector is shown. Arrows denote flow direction and colors denote flow speed in cm s^{-1}.

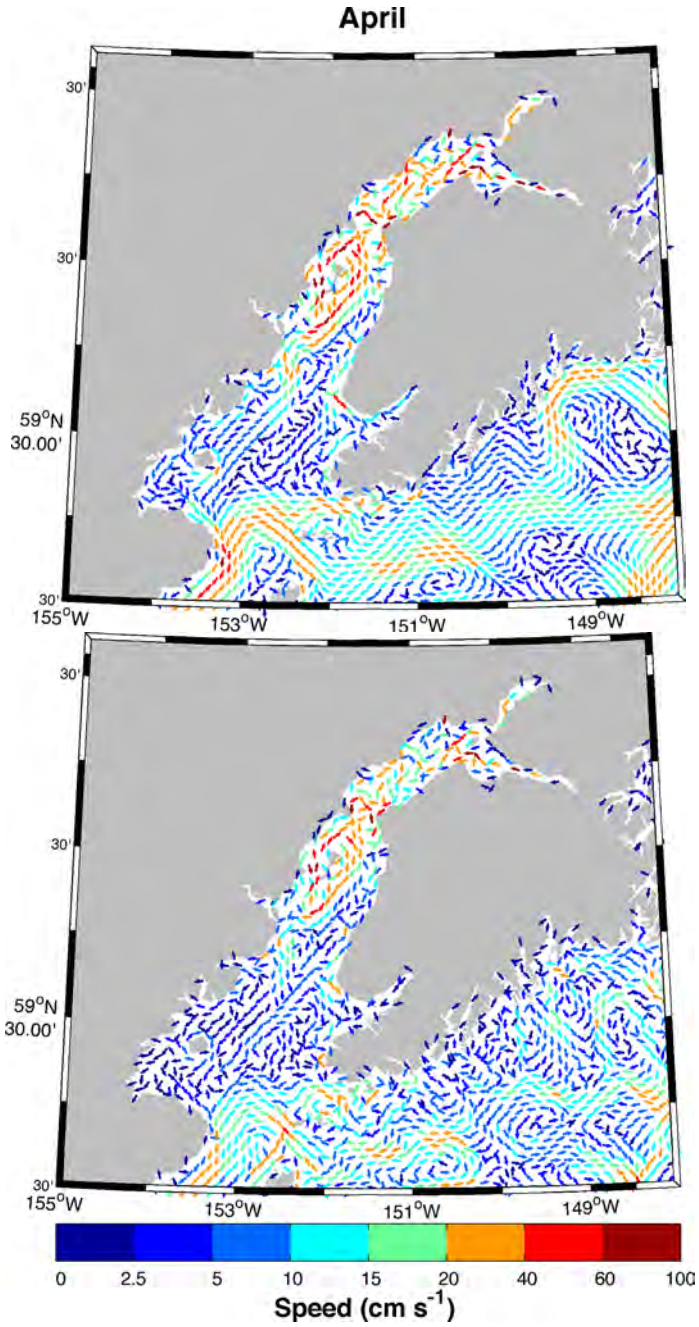

Figure A5.4: Surface (upper) and near-bottom (lower) mean velocity fields over the 10-year hindcast for April in Cook Inlet. Every 9th grid point velocity vector is shown. Arrows denote flow direction and colors denote flow speed in cm s^{-1}.

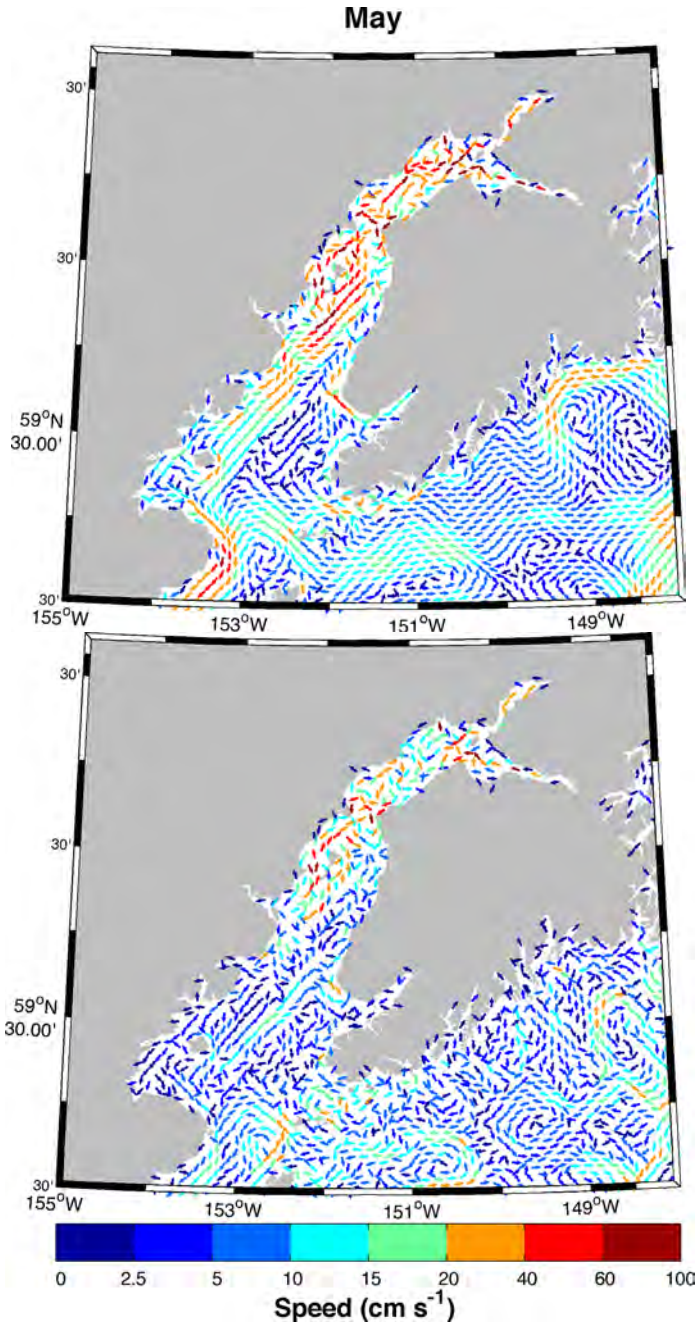

Figure A5.5: Surface (upper) and near-bottom (lower) mean velocity fields over the 10-year hindcast for May in Cook Inlet. Every 9th grid point velocity vector is shown. Arrows denote flow direction and colors denote flow speed in cm s^{-1}.

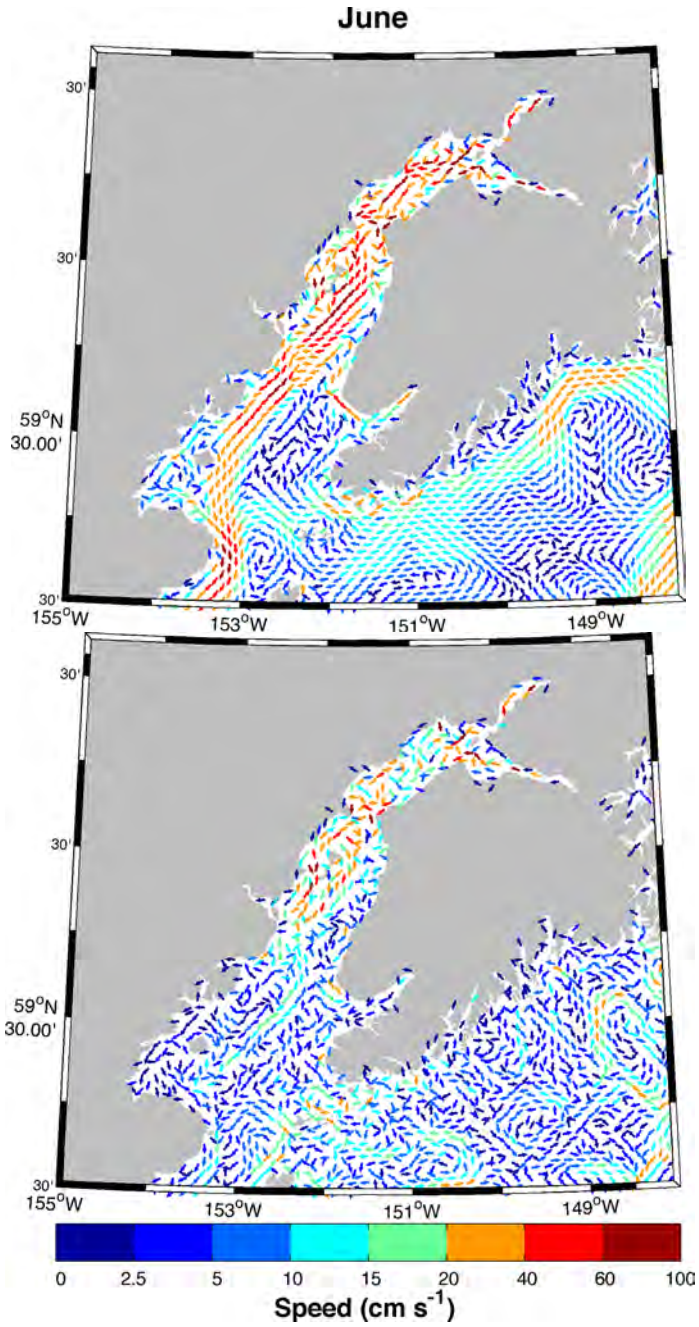

Figure A5.6: Surface (upper) and near-bottom (lower) mean velocity fields over the 10-year hindcast for June in Cook Inlet. Every 9th grid point velocity vector is shown. Arrows denote flow direction and colors denote flow speed in cm s^{-1}.

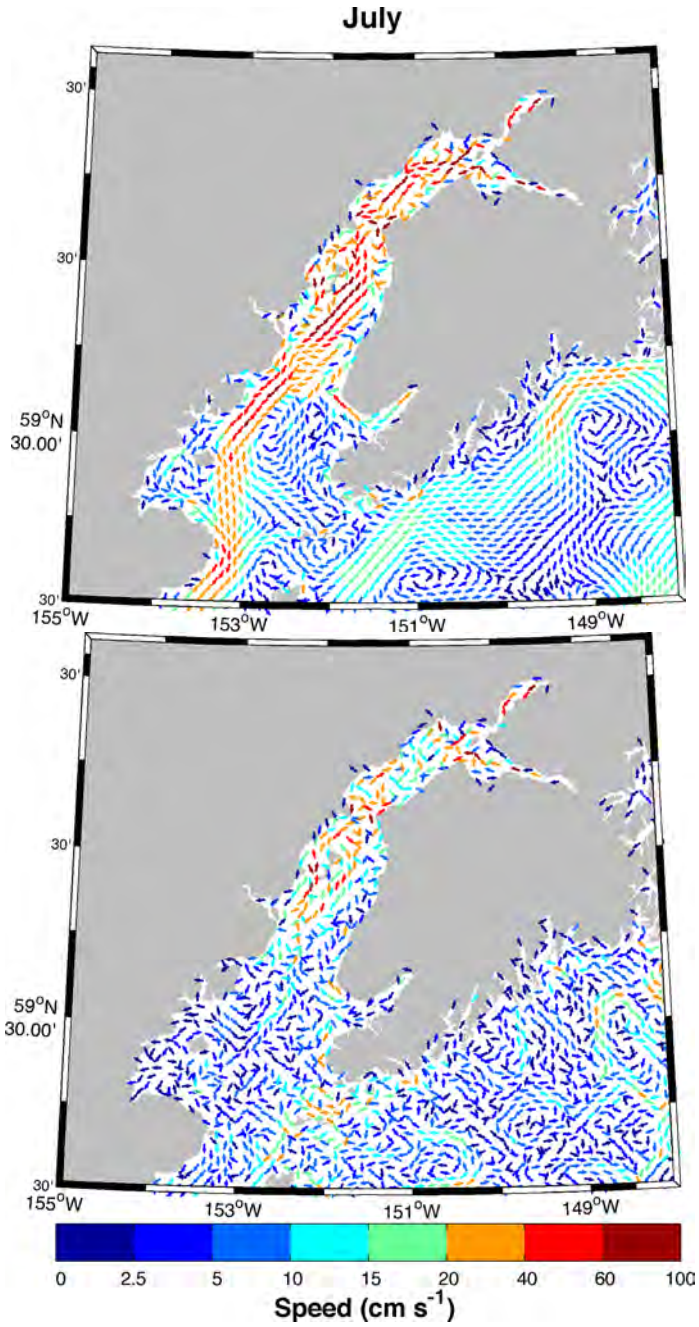

Figure A5.7: Surface (upper) and near-bottom (lower) mean velocity fields over the 10-year hindcast for July in Cook Inlet. Every 9th grid point velocity vector is shown. Arrows denote flow direction and colors denote flow speed in cm s^{-1}.

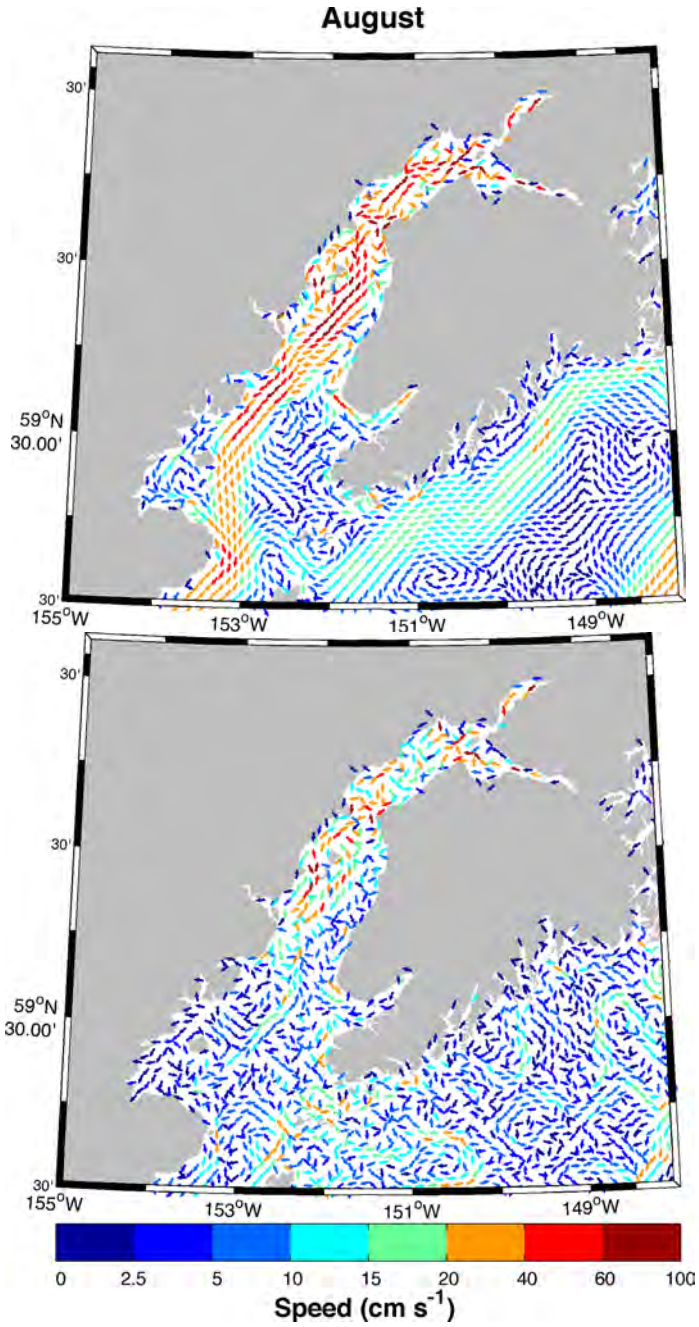

Figure A5.8: Surface (upper) and near-bottom (lower) mean velocity fields over the 10-year hindcast for August in Cook Inlet. Every 9th grid point velocity vector is shown. Arrows denote flow direction and colors denote flow speed in cm s^{-1}.

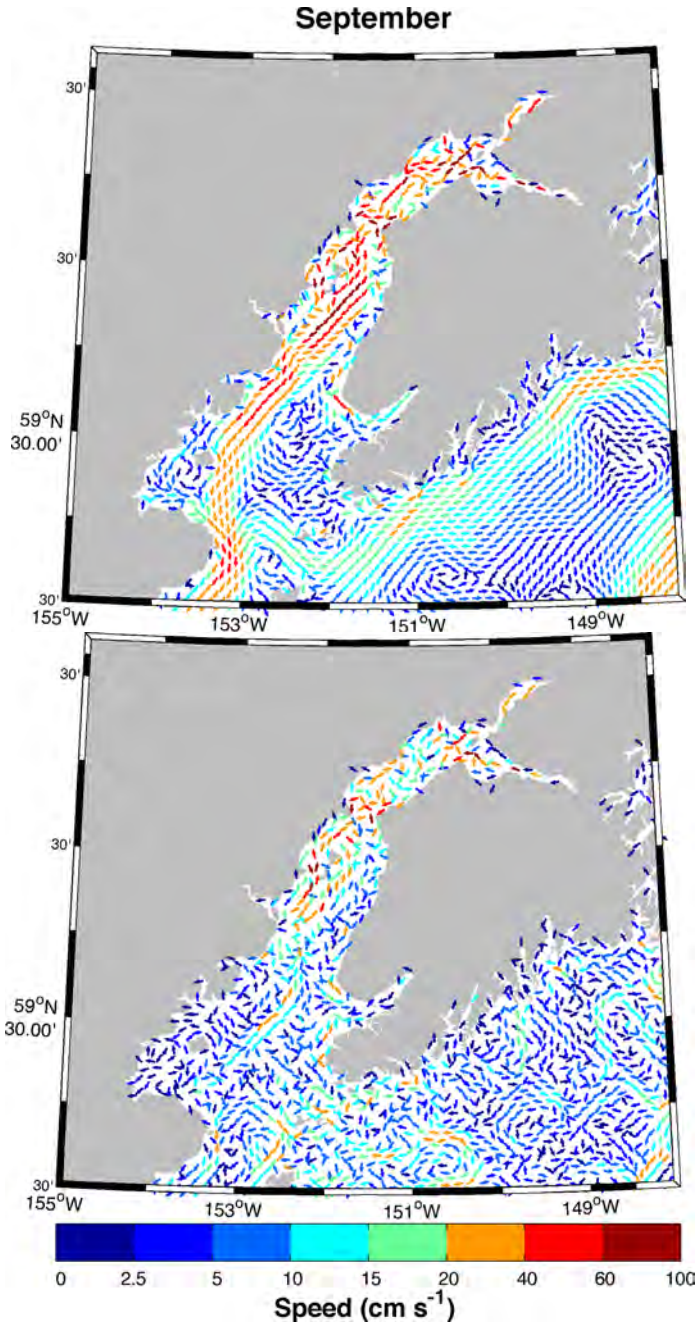

Figure A5.9: Surface (upper) and near-bottom (lower) mean velocity fields over the 10-year hindcast for September in Cook Inlet. Every 9th grid point velocity vector is shown. Arrows denote flow direction and colors denote flow speed in cm s^{-1}.

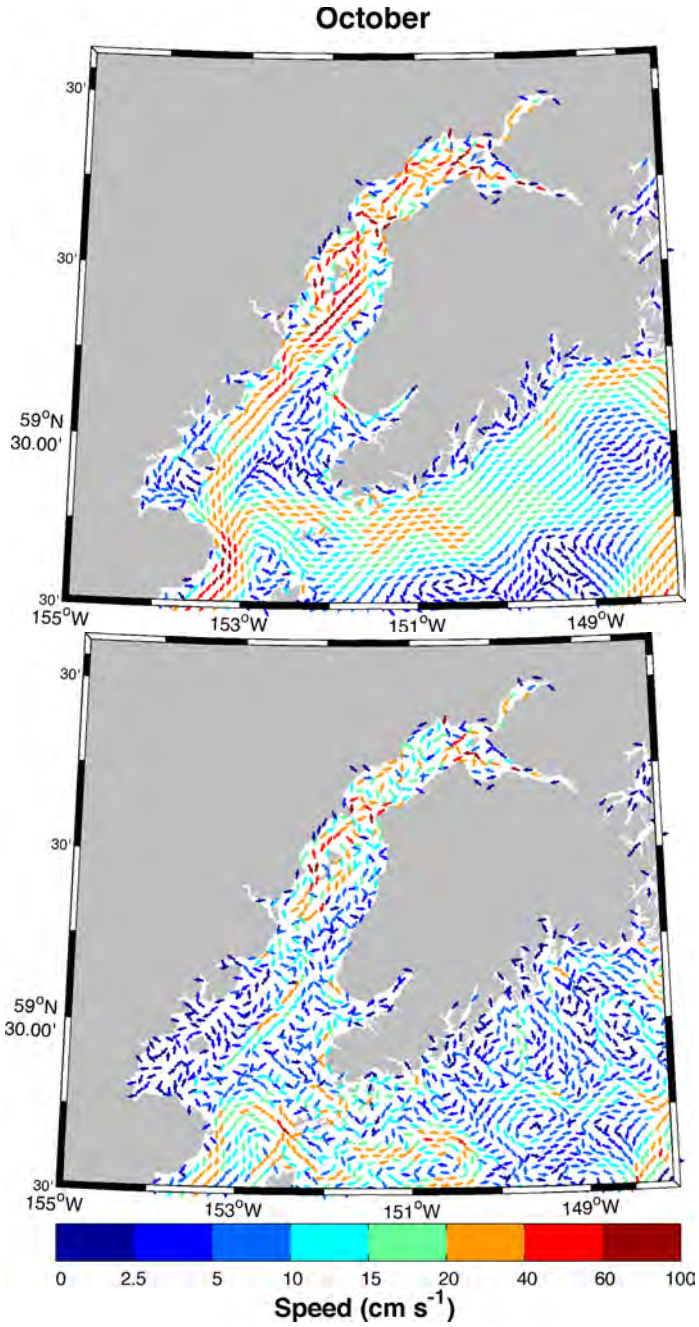

Figure A5.10: Surface (upper) and near-bottom (lower) mean velocity fields over the 10-year hindcast for October in Cook Inlet. Every 9th grid point velocity vector is shown. Arrows denote flow direction and colors denote flow speed in cm s^{-1}.

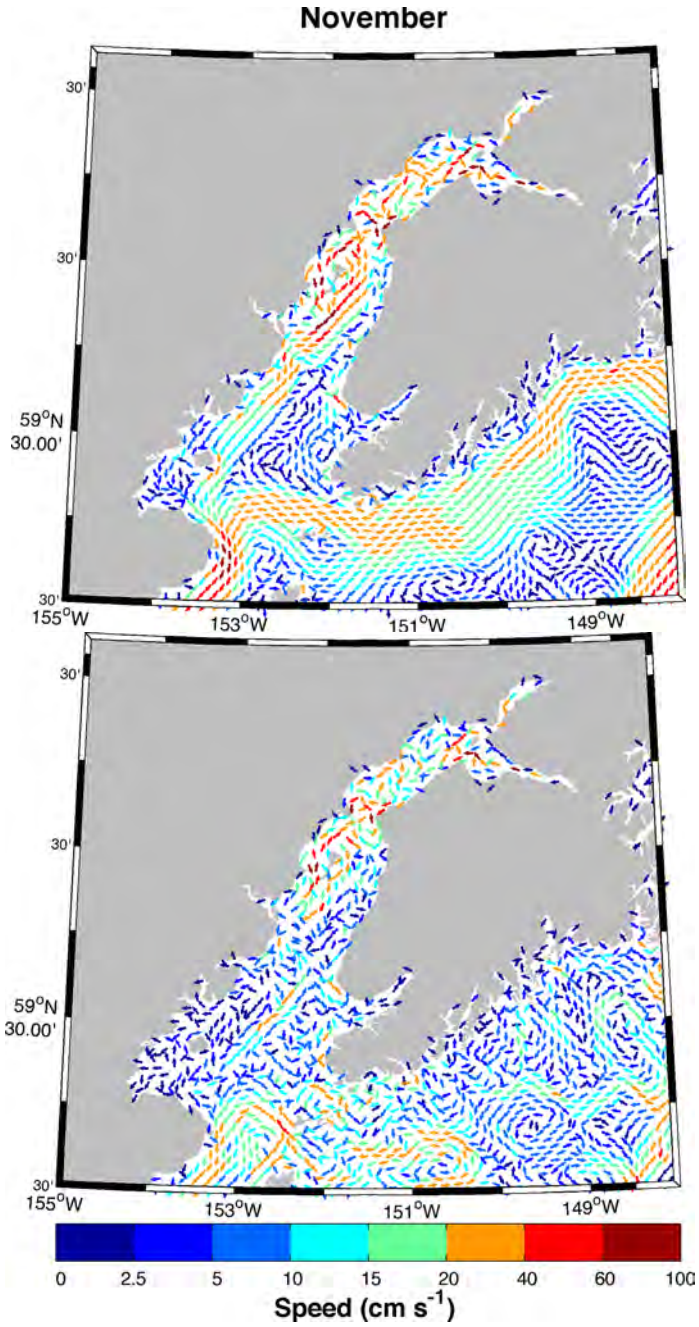

Figure A5.11: Surface (upper) and near-bottom (lower) mean velocity fields over the 10-year hindcast for November. Every 9th grid point velocity vector is shown. Arrows denote flow direction and colors denote flow speed in cm s^{-1}.

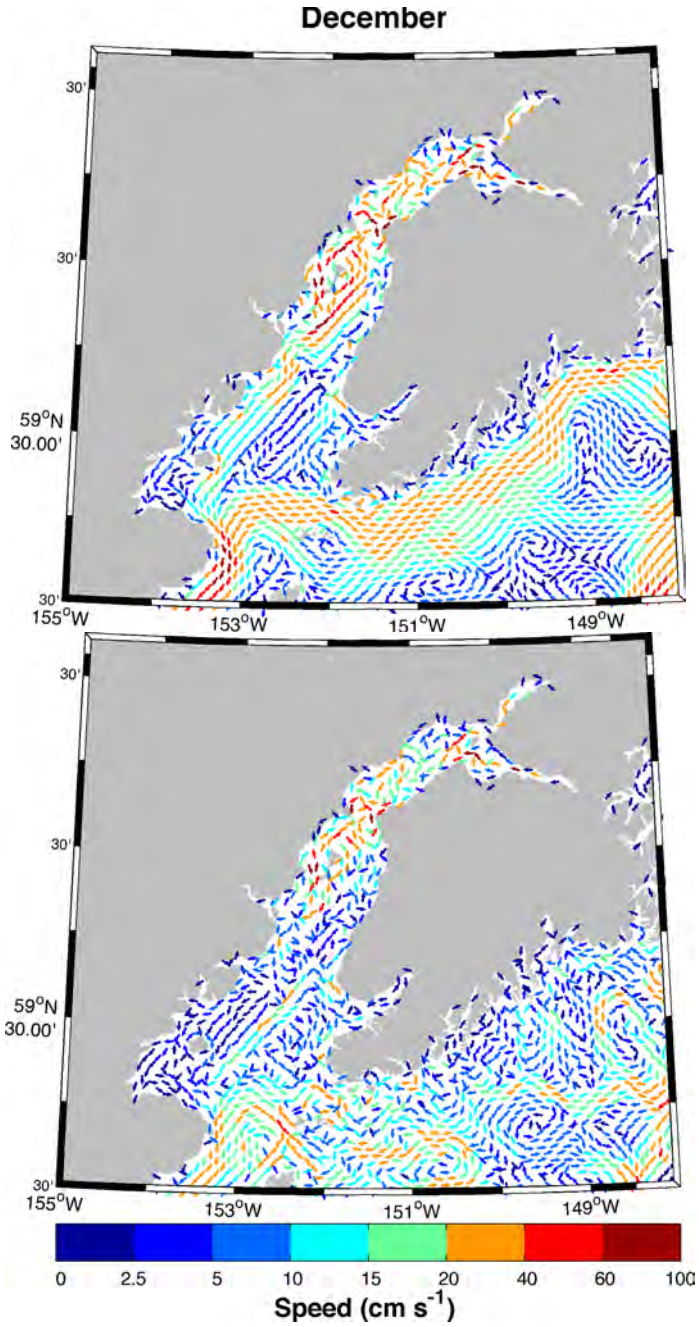

Figure A5.12: Surface (upper) and near-bottom (lower) mean velocity fields over the 10-year hindcast for December in Cook Inlet. Every 9th grid point velocity vector is shown. Arrows denote flow direction and colors denote flow speed in cm s^{-1}.

Appendix 6: Monthly climatology, Cook Inlet modeled sea surface temperature.

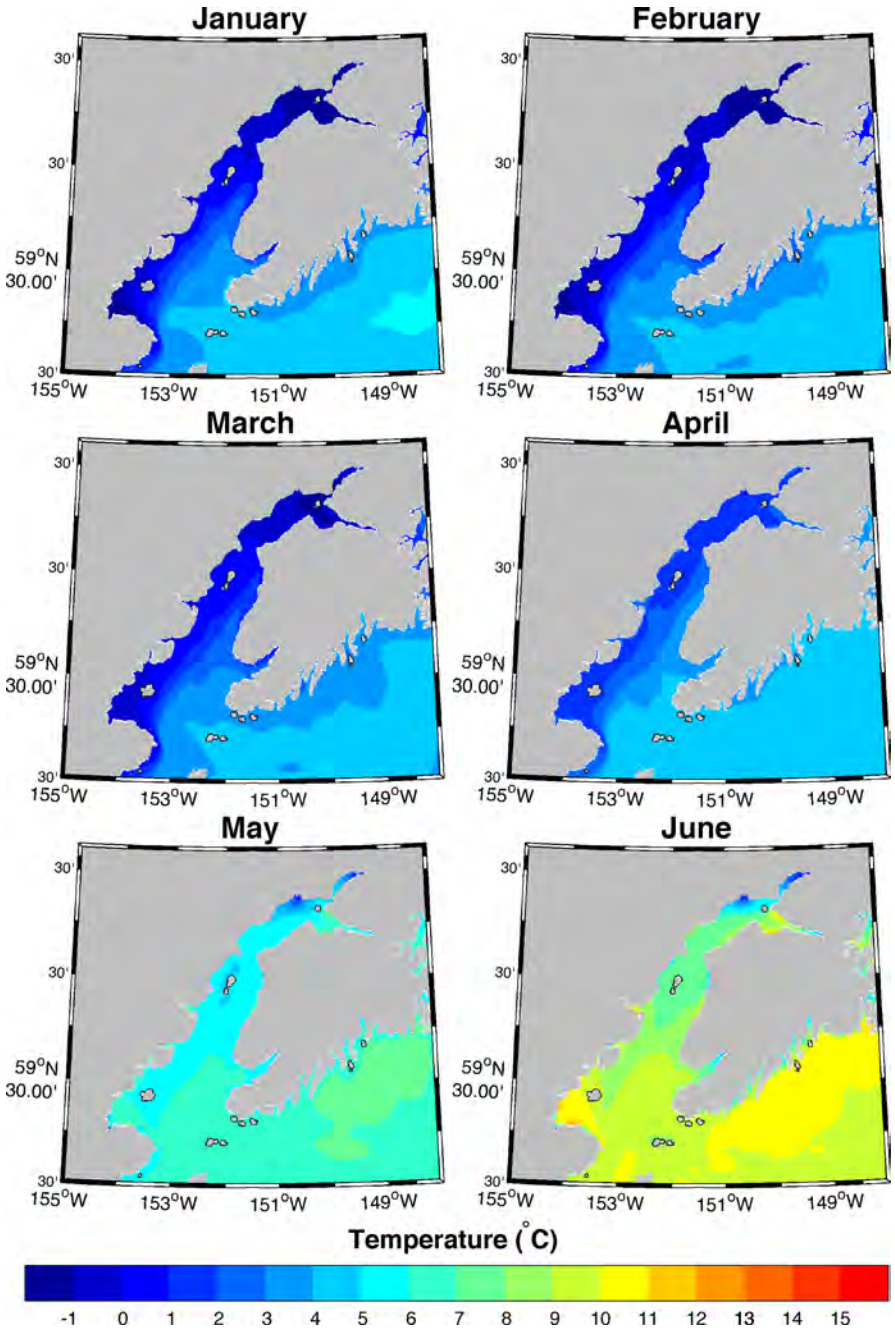

Figure A6.1: Monthly mean sea surface temperature (SST) over the 10-year hindcast for January-June in Cook Inlet.

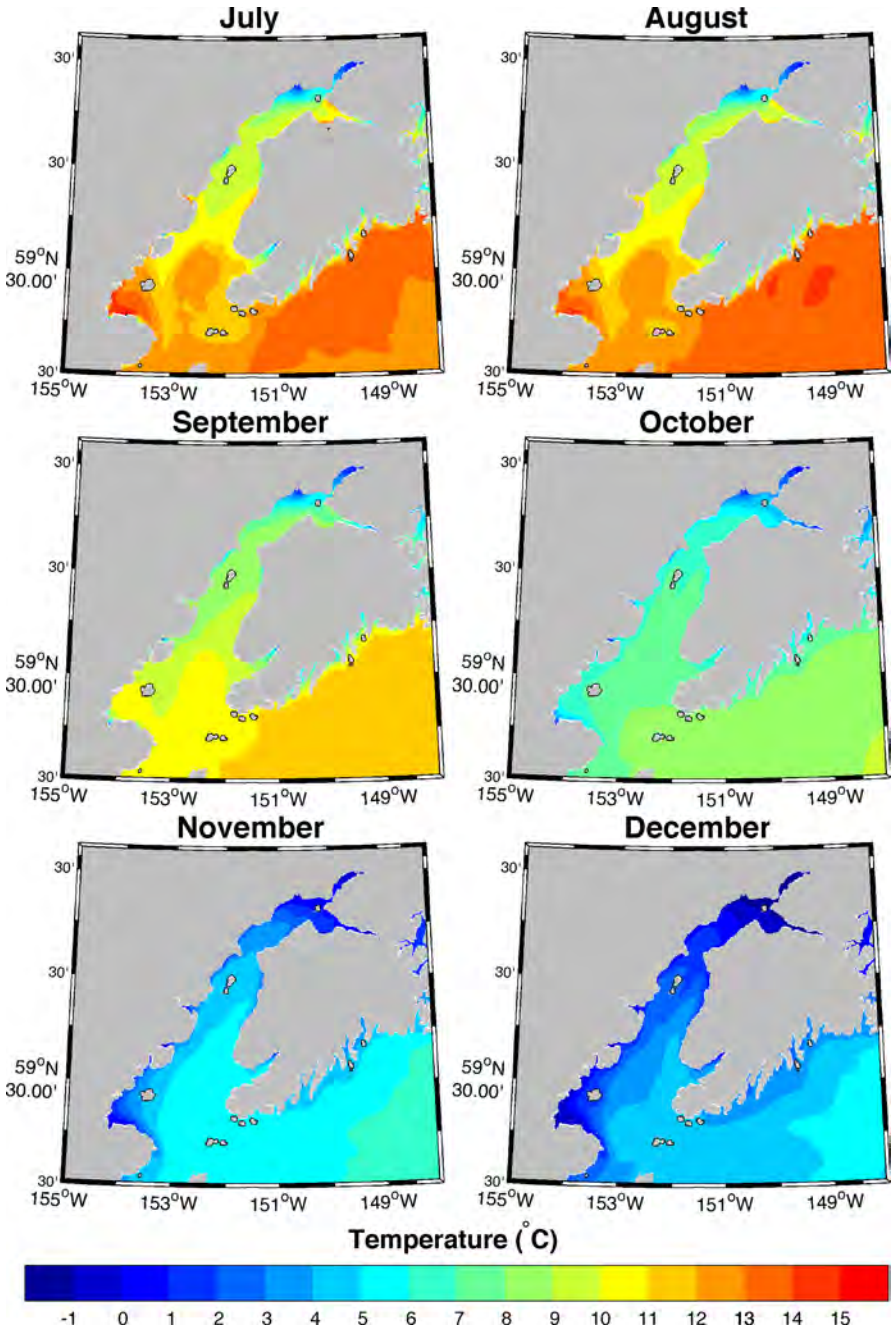

Figure A6.2: Monthly mean sea surface temperature (SST) over the 10-year hindcast for July-December in Cook Inlet.

Appendix 7: Monthly climatology, Cook Inlet modeled sea surface salinity.

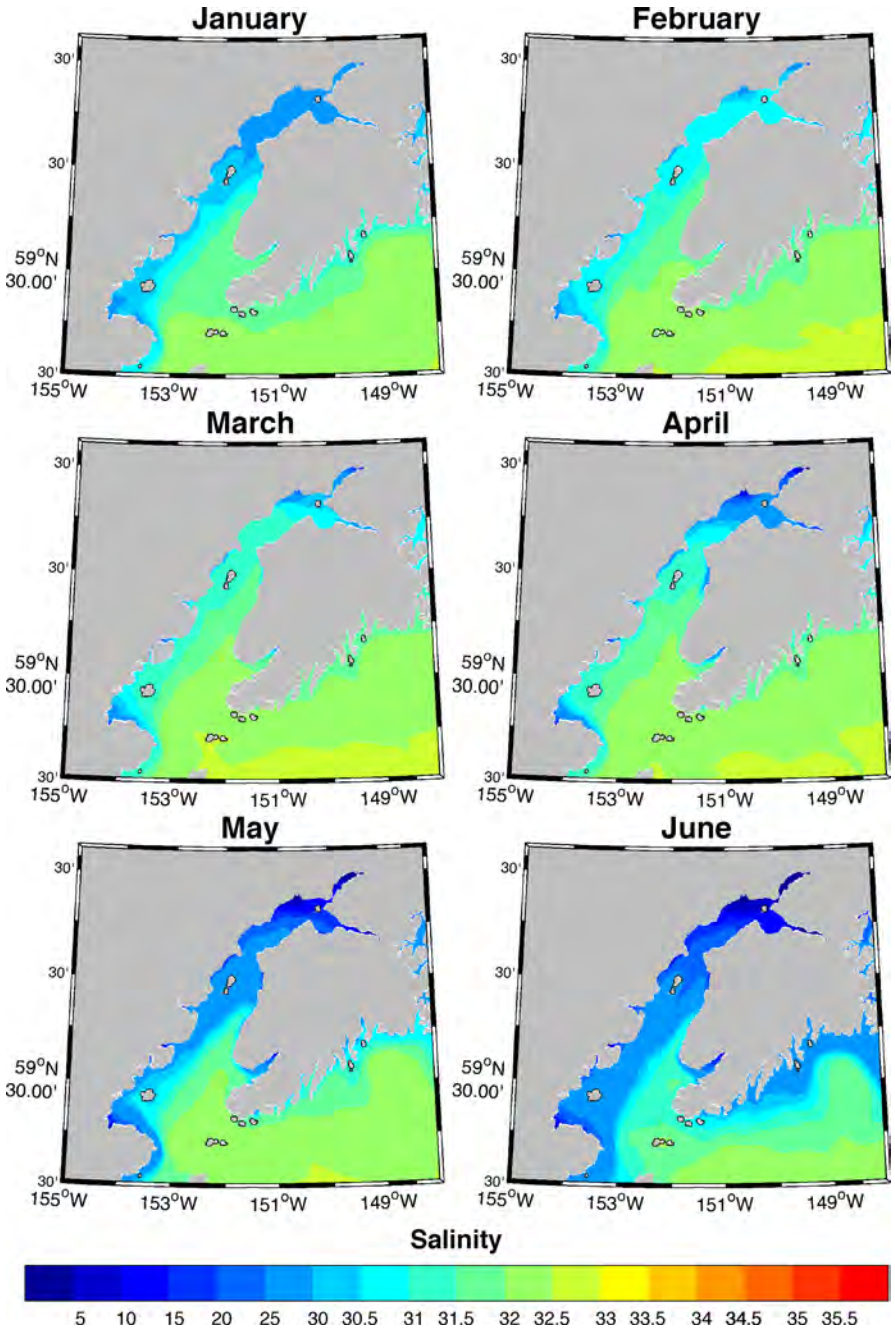

Figure A7.1: Monthly mean sea surface salinity (SSS) over the 10-year hindcast for January-June in Cook Inlet.

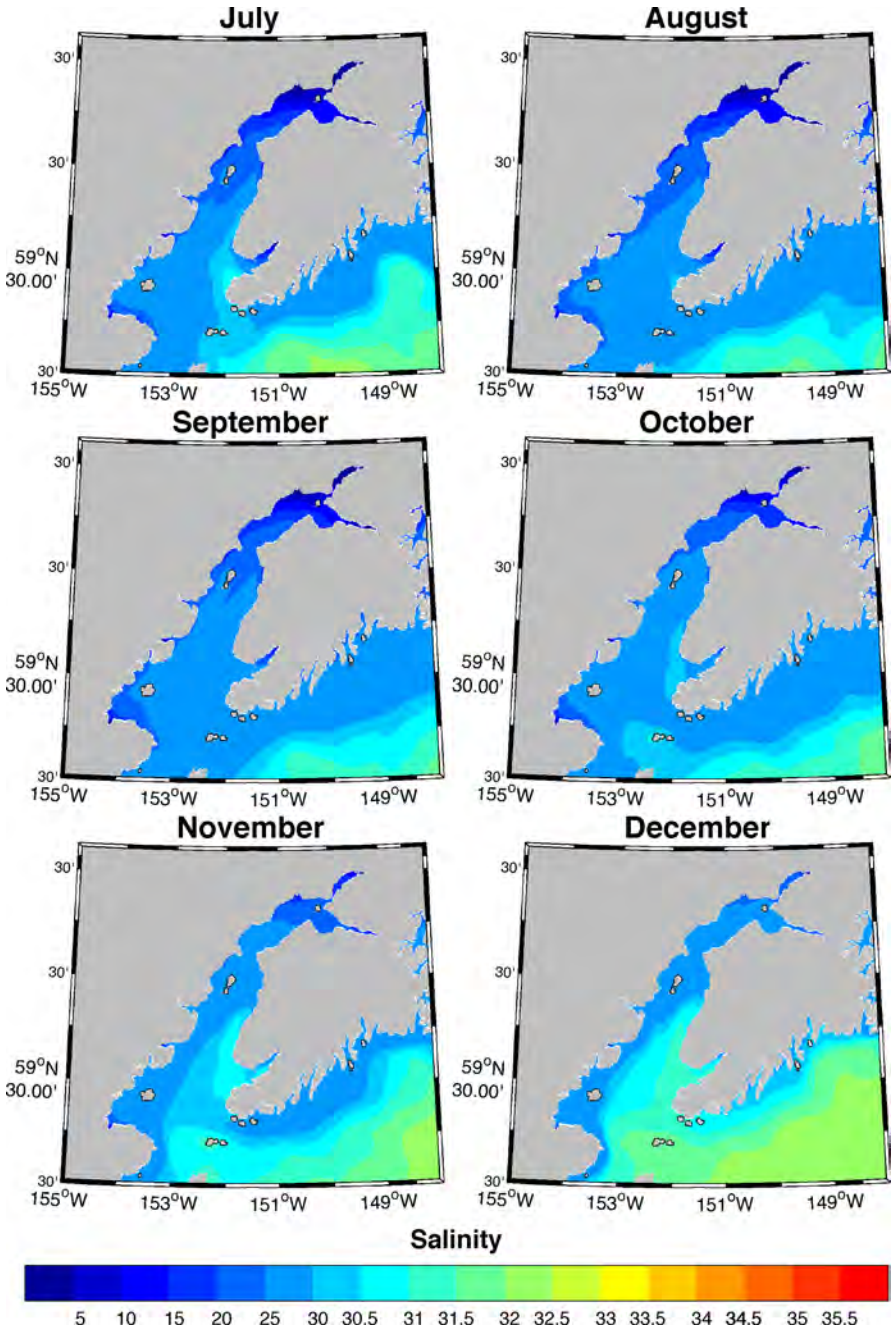

Figure A7.2: Monthly mean sea surface temperature (SST) over the 10-year hindcast for July-December in Cook Inlet.

Appendix 8: Modeled and Observed Hydrographic Transects

The figures in this Appendix show in-situ CTD data, model hindcasts at each station for the year, month, day and hour closest to which the CTD profiles were each collected, and the difference between the two.

Temperature contours occur every 1.0 °C from -2 °C to +16°C. Salinity contours occur every 5 salinity units from 0 to 30 and then every 0.5 units from 30 to 36. In the difference plots, white shading denotes differences smaller than 0.5 °C and 0.5 salinity units. The lightest shading indicated differences between 0.5 and 1 (for both temperature and salinity).

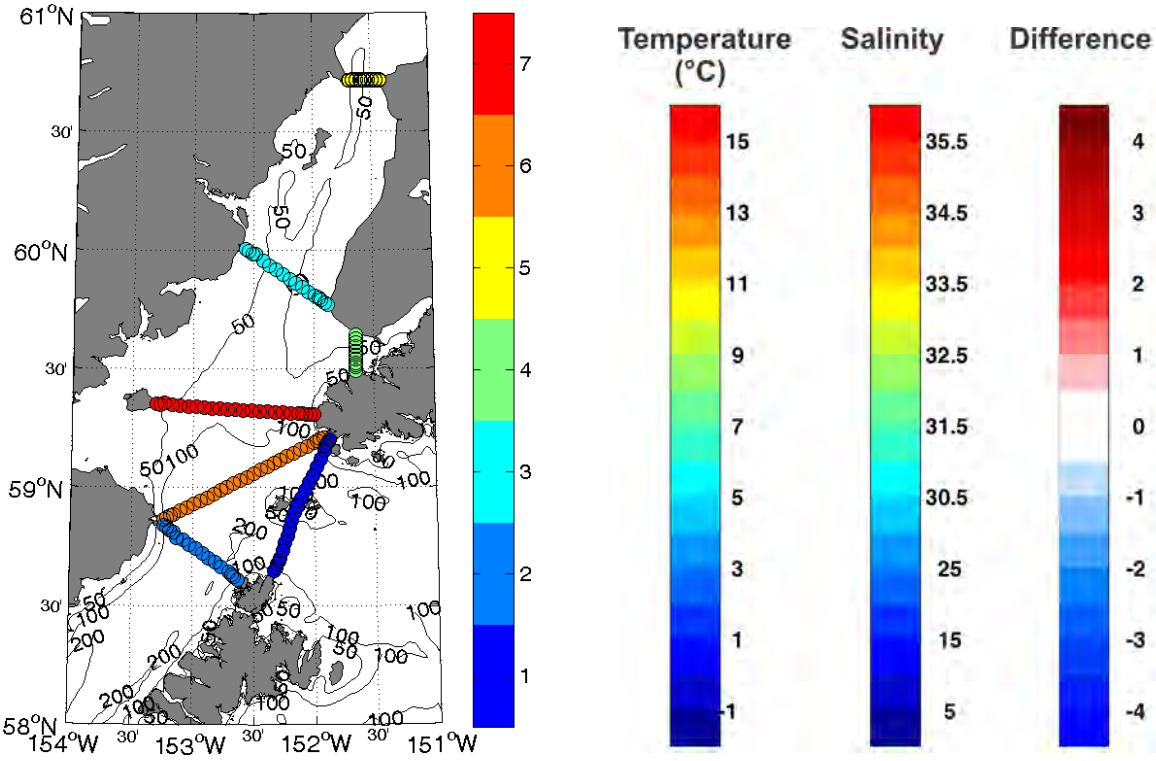

Figure A8.0 Map at left: Locations of seven repeat CTD transects [*Okkonen et al.*, 2009] in lower Cook Inlet, Kennedy-Stevenson Entrances and upper Shelikof Strait used for model-data comparisons. The CTDs of each transect are plotted with circles that are color-coded based on transect number shown with the associated colorbar. Three colorbars at right: Color contour legends for all temperature, salinity and difference fields shown below in Figures A8.1 through A8.79.

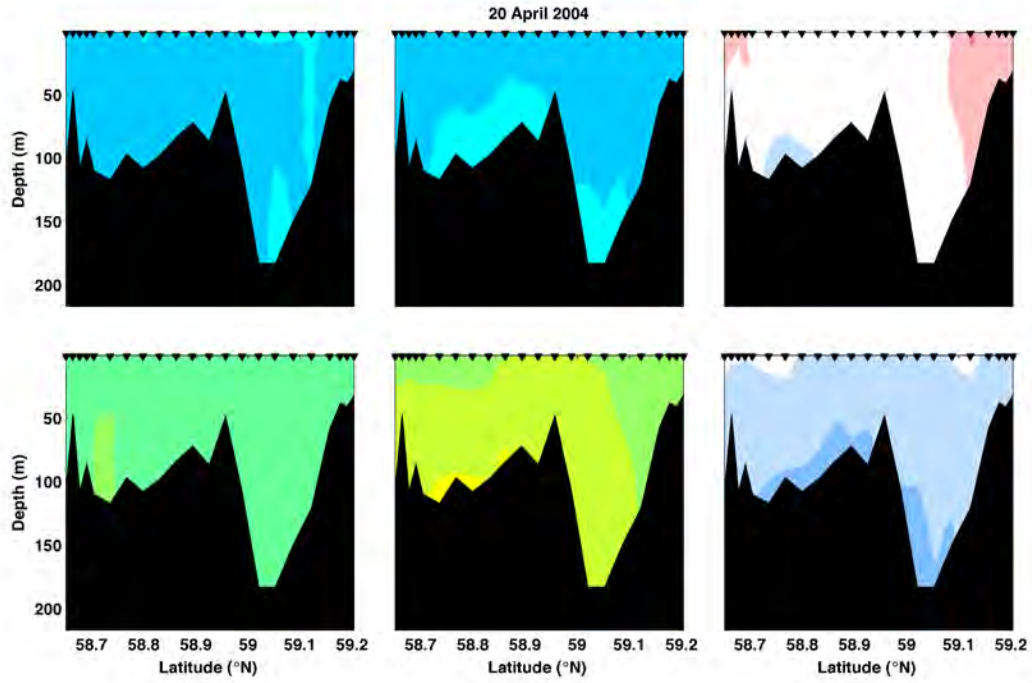

Figure A8.1: Transect 1.01 model-data comparison for temperature (top), salinity (bottom), with the observations shown on the left, the model in the center and the difference (observations-model) on the right.

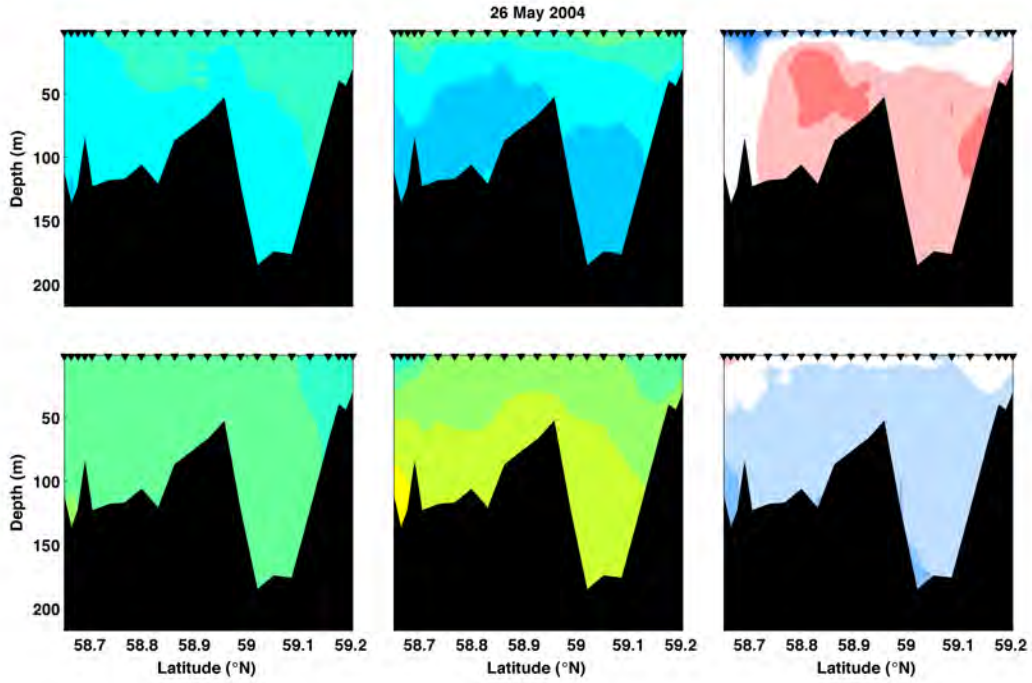

Figure A8.2: Transect 1.02 model-data comparison for temperature (top), salinity (bottom),with the observations shown on the left, the model in the center and the difference (observations-model) on the right.

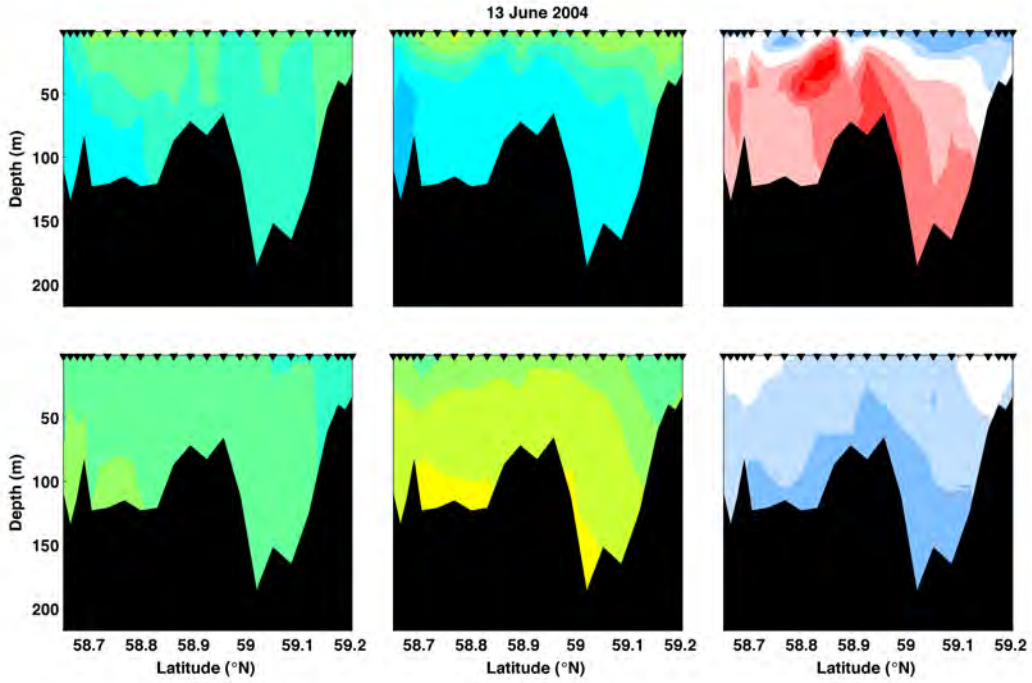

Figure A8.3: Transect 1.03 model-data comparison for temperature (top), salinity (bottom), with the observations shown on the left, the model in the center and the difference (observations-model) on the right.

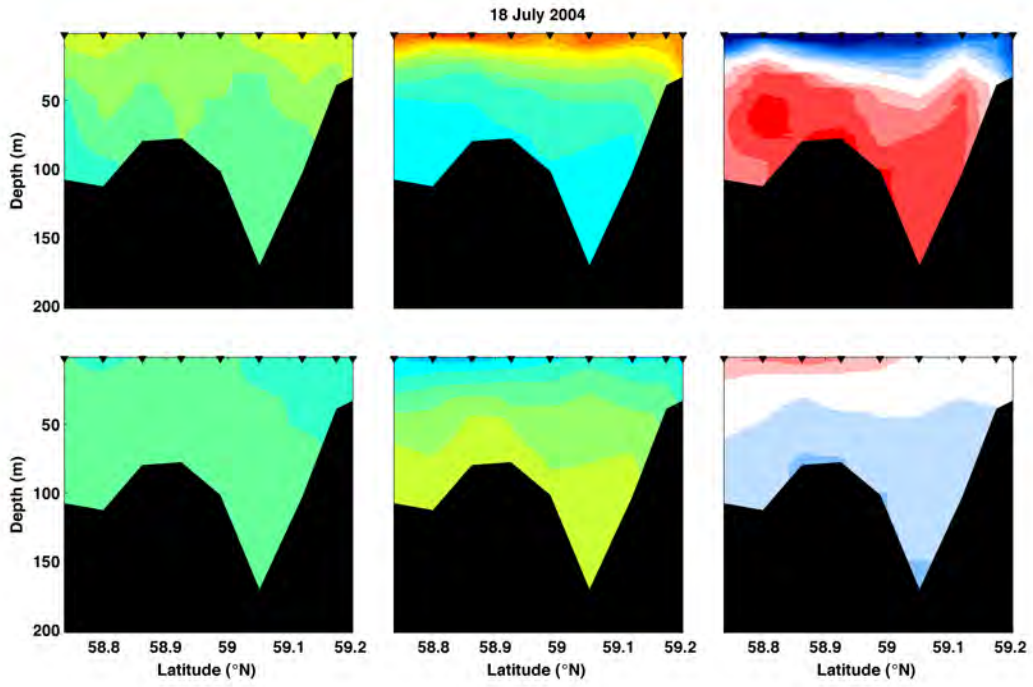

Figure A8.4: Transect 1.04 model-data comparison for temperature (top), salinity (bottom), with the

observations shown on the left, the model in the center and the difference (observations-model) on the right.

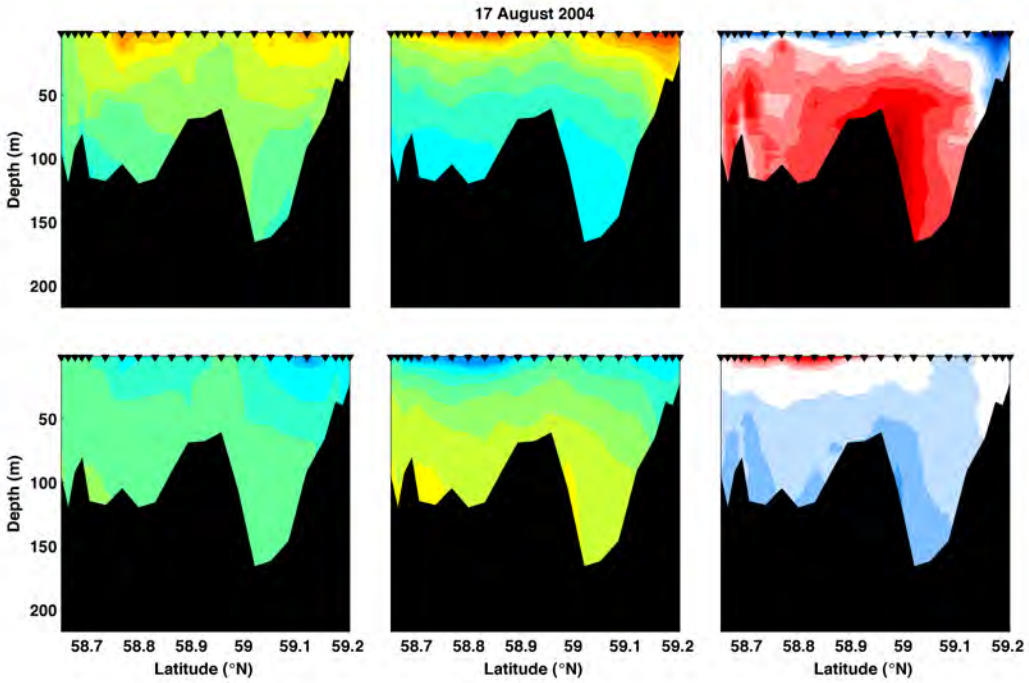

Figure A8.5: Transect 1.05 model-data comparison for temperature (top), salinity (bottom), with the observations shown on the left, the model in the center and the difference (observations-model) on the right.

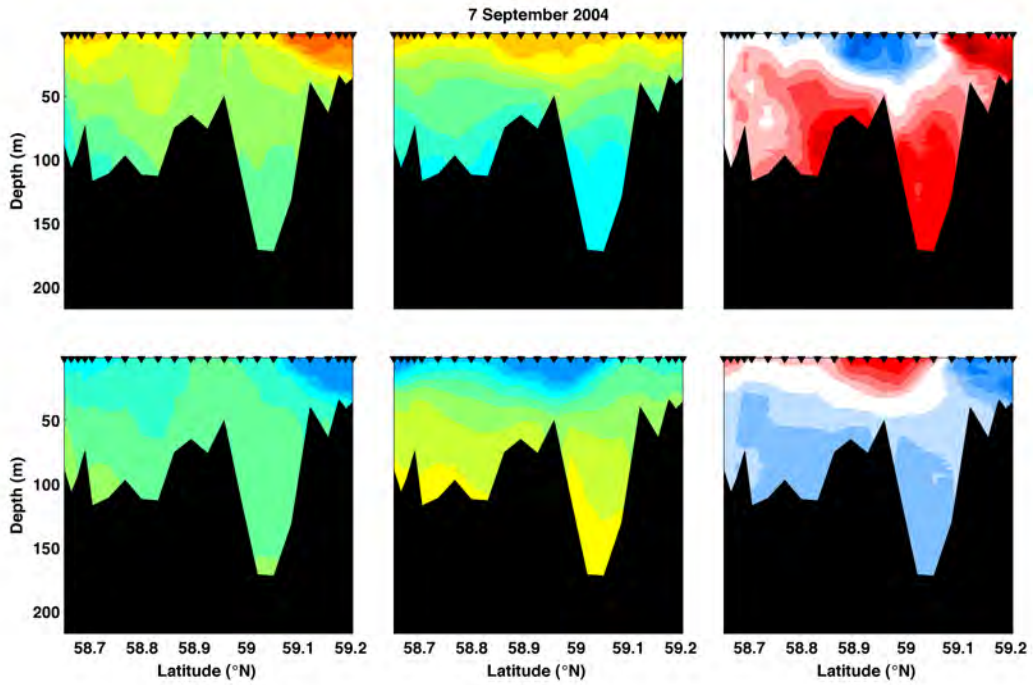

Figure A8.6: Transect 1.06 model-data comparison for temperature (top), salinity (bottom), with the observations shown on the left, the model in the center and the difference (observations-model) on the right.

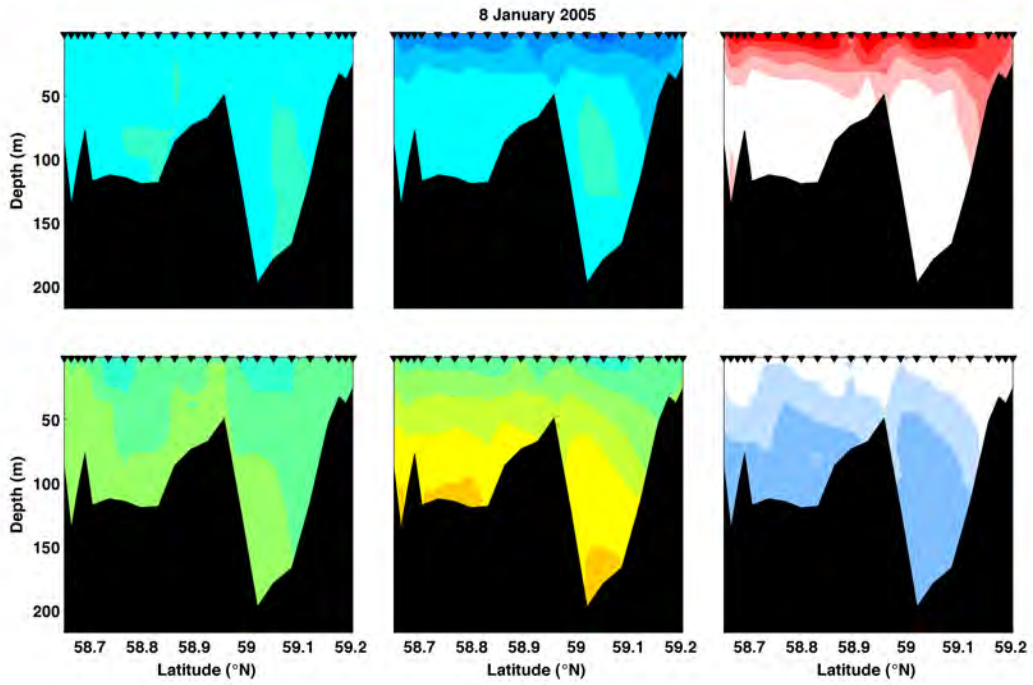

Figure A8.7: Transect 1.07 model-data comparison for temperature (top), salinity (bottom), with the

observations shown on the left, the model in the center and the difference (observations-model) on the right.

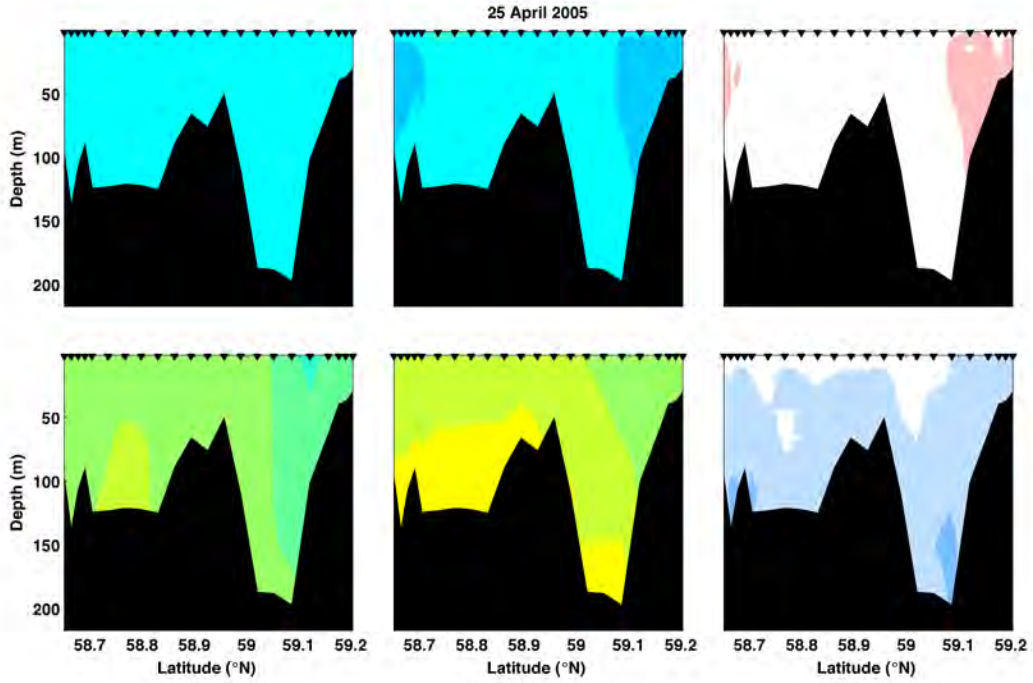

Figure A8.8: Transect 1.08 model-data comparison for temperature (top), salinity (bottom), with the observations shown on the left, the model in the center and the difference (observations-model) on the right.

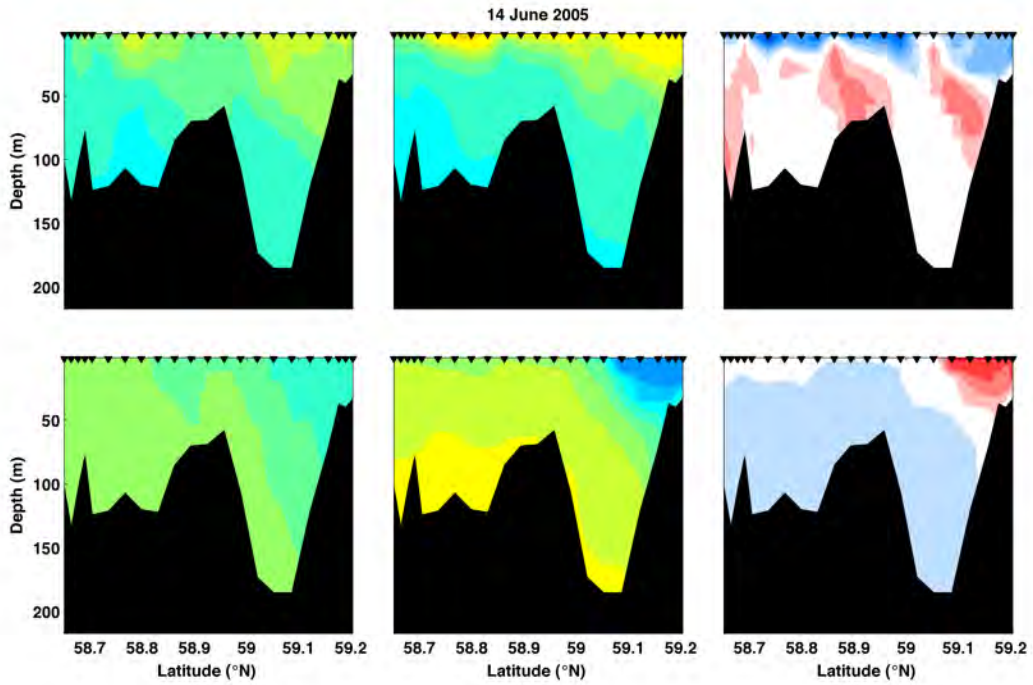

Figure A8.9: Transect 1.09 model-data comparison for temperature (top), salinity (bottom), with the observations shown on the left, the model in the center and the difference (observations-model) on the right.

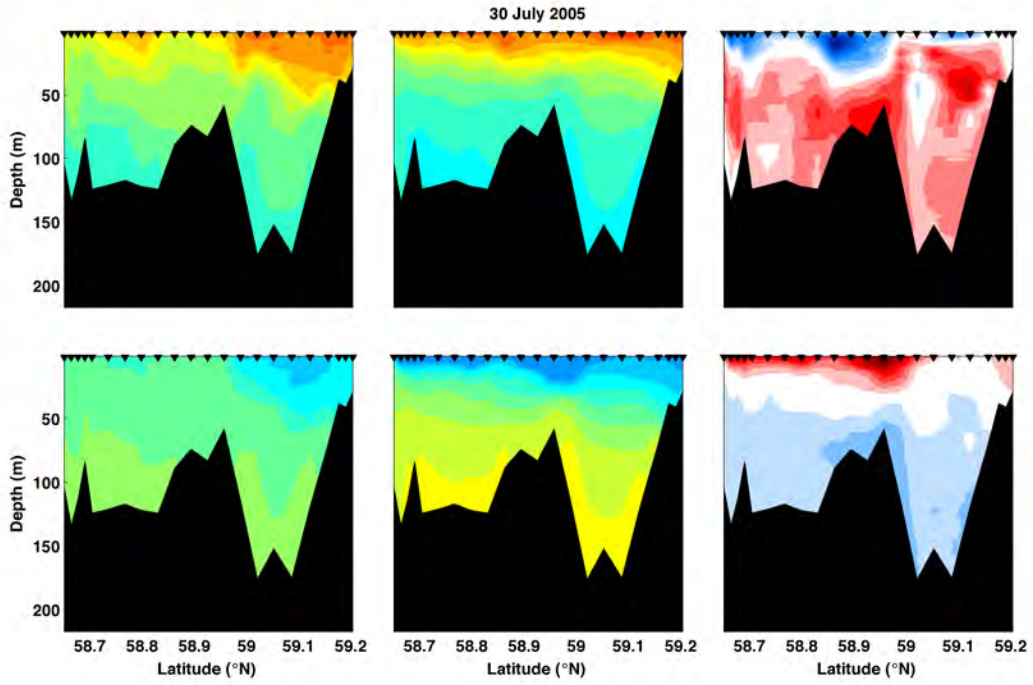

Figure A8.10: Transect 1.10 model-data comparison for temperature (top), salinity (bottom), with the observations shown on the left, the model in the center and the difference (observations-model) on the right.

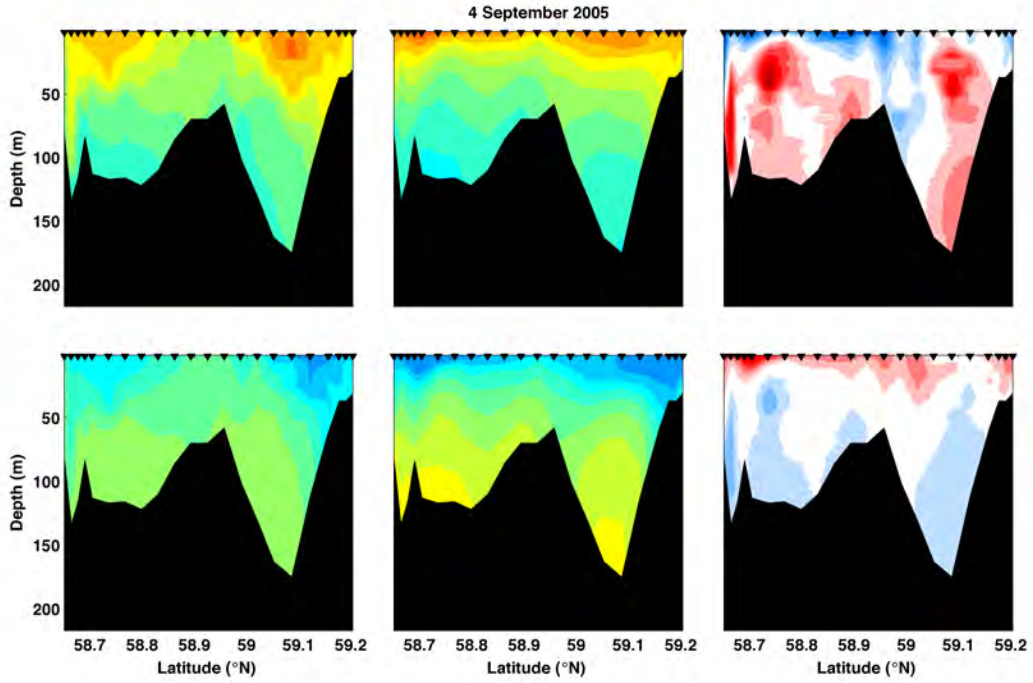

Figure A8.11: Transect 1.11 model-data comparison for temperature (top), salinity (bottom), with the observations shown on the left, the model in the center and the difference (observations-model) on the right.

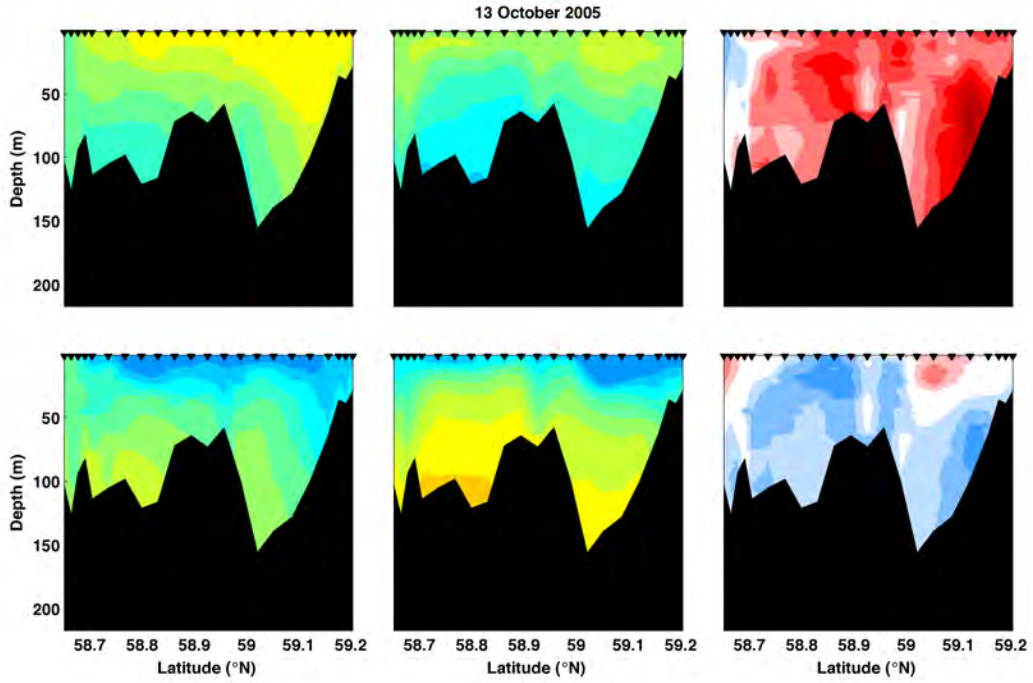

Figure A8.12: Transect 1.12 model-data comparison for temperature (top), salinity (bottom), with the

observations shown on the left, the model in the center and the difference (observations-model) on the right.

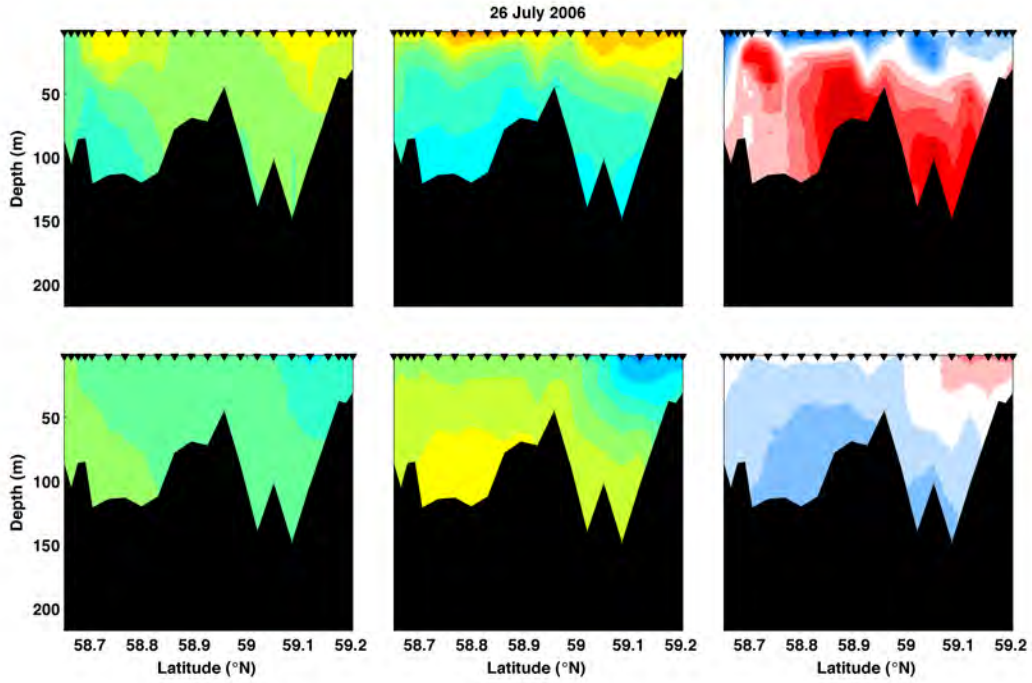

Figure A8.13: Transect 1.13 model-data comparison for temperature (top), salinity (bottom), with the observations shown on the left, the model in the center and the difference (observations-model) on the right.

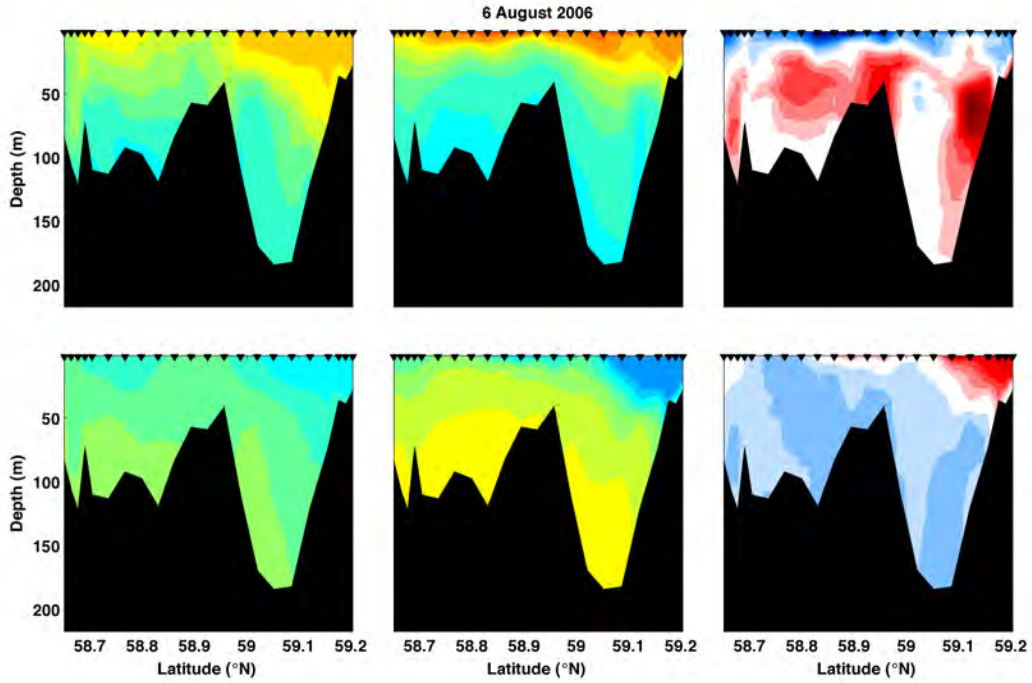

Figure A8.14: Transect 1.14 model-data comparison for temperature (top), salinity (bottom), with the observations shown on the left, the model in the center and the difference (observations-model) on the right.

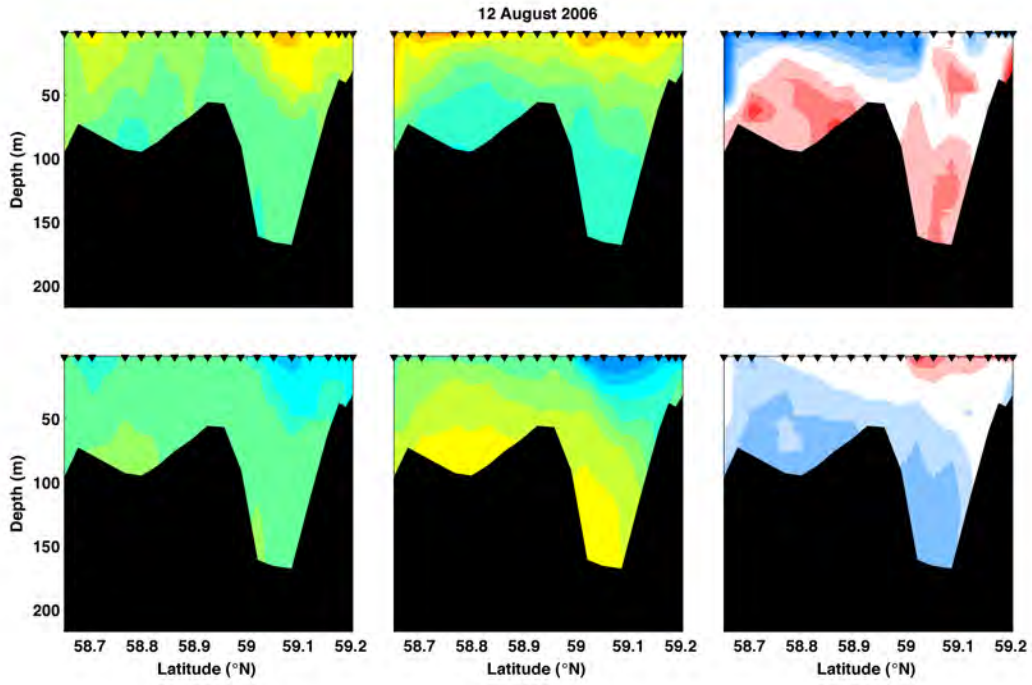

Figure A8.15: Transect 1.15 model-data comparison for temperature (top), salinity (bottom), with the observations shown on the left, the model in the center and the difference (observations-model) on the right.

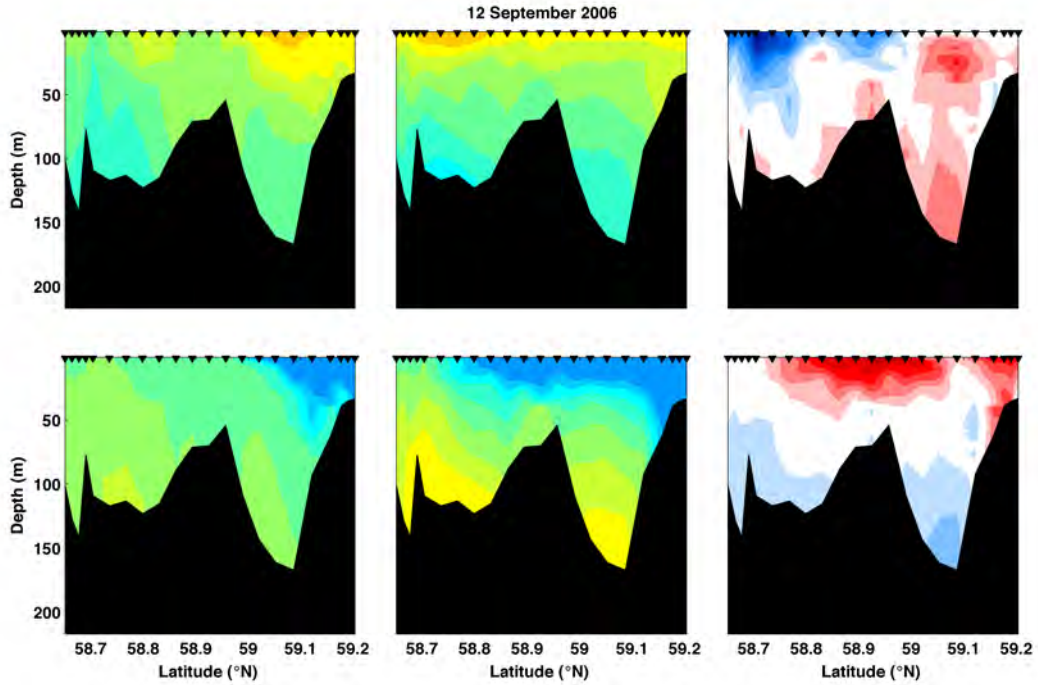

Figure A8.16: Transect 1.16 model-data comparison for temperature (top), salinity (bottom), with the observations shown on the left, the model in the center and the difference (observations-model) on the right.

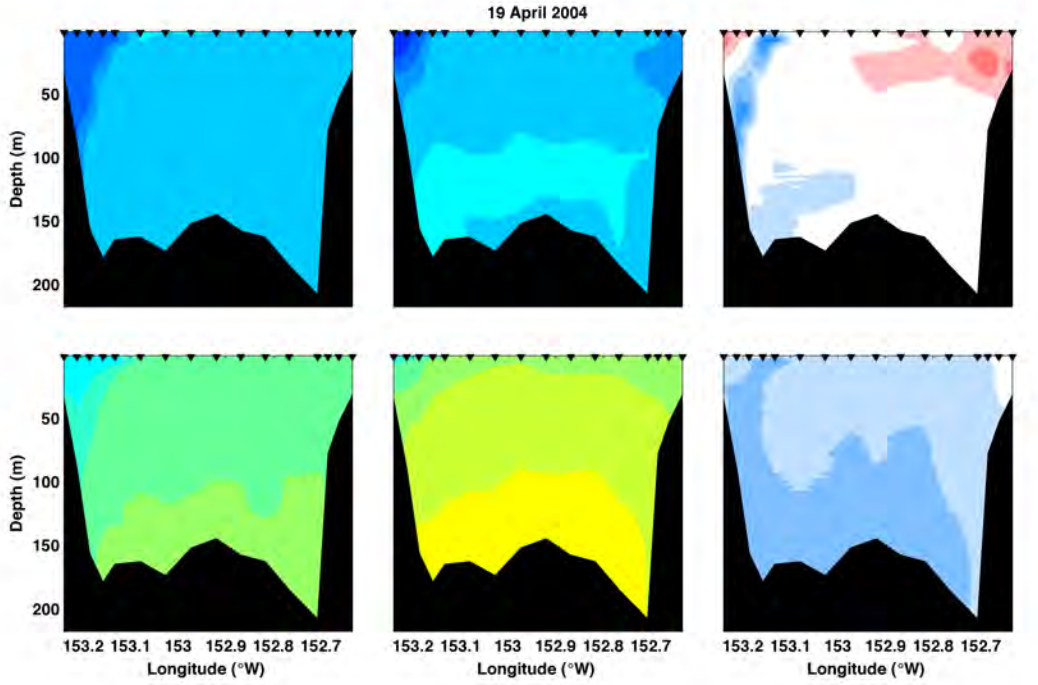

Figure A8.17: Transect 2.01 model-data comparison for temperature (top), salinity (bottom), with the observations shown on the left, the model in the center and the difference (observations-model) on the right.

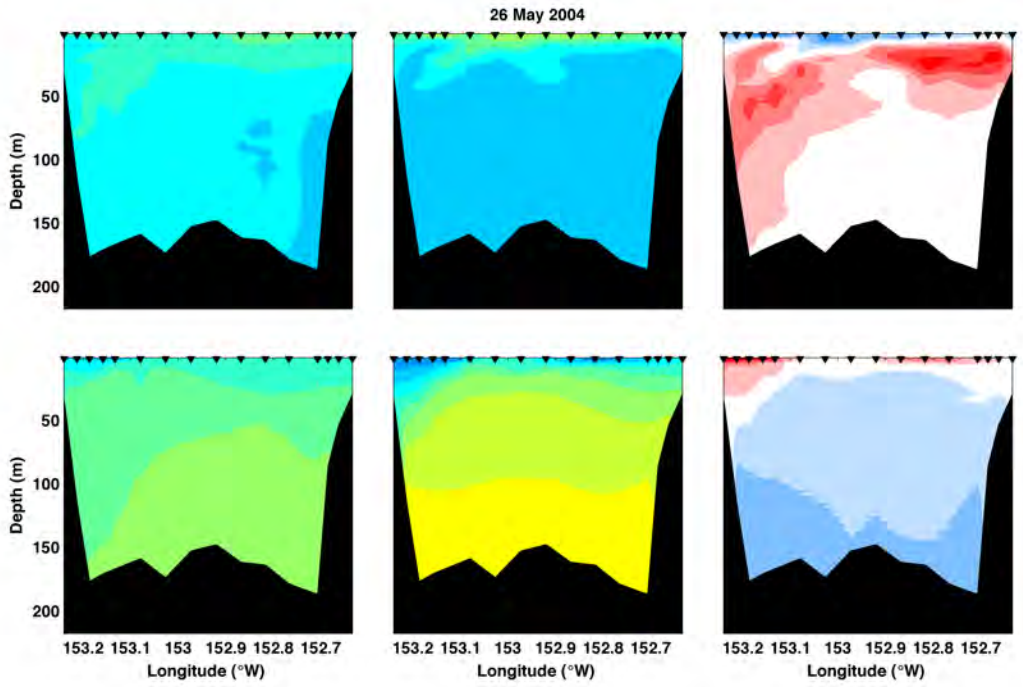

Figure A8.18: Transect 2.02 model-data comparison for temperature (top), salinity (bottom), with the observations shown on the left, the model in the center and the difference (observations-model) on the right.

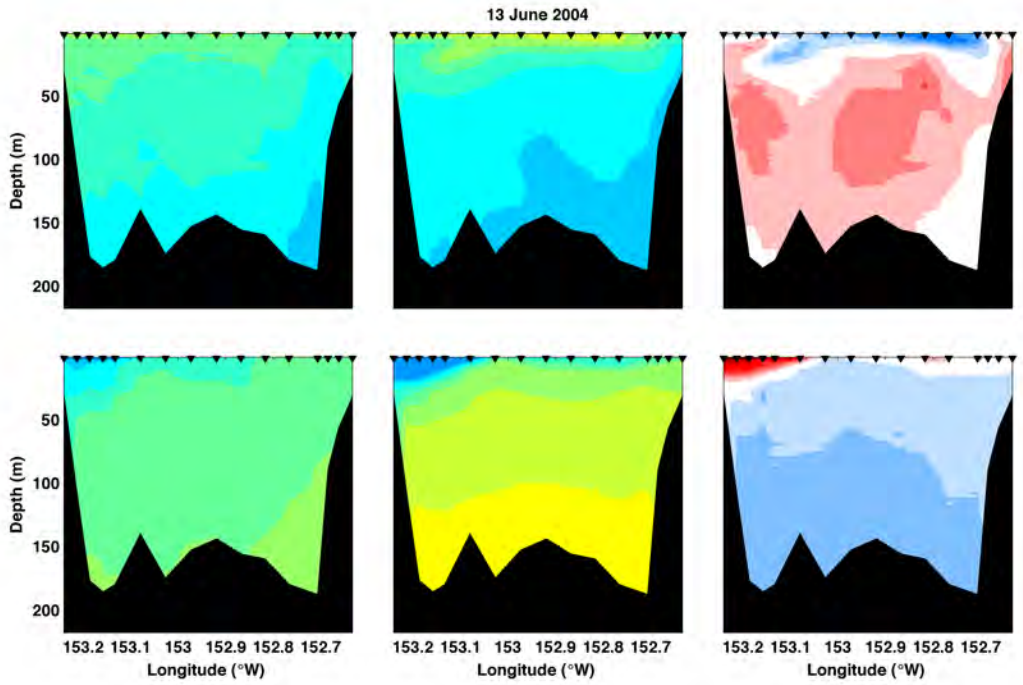

Figure A8.19: Transect 2.03 model-data comparison for temperature (top), salinity (bottom), with the

observations shown on the left, the model in the center and the difference (observations-model) on the right.

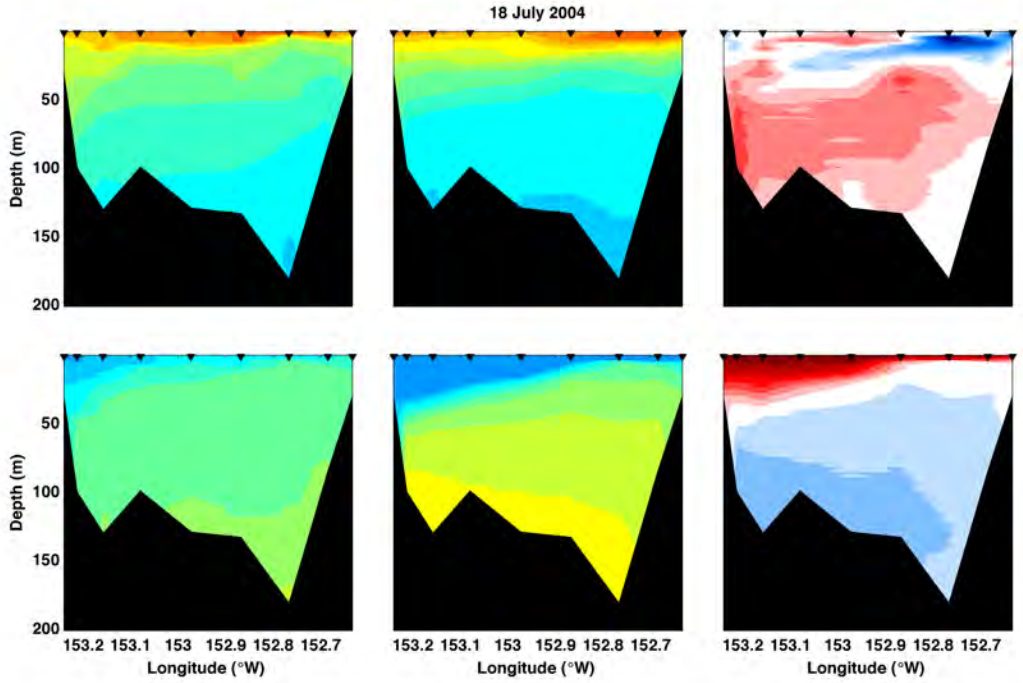

Figure A8.20: Transect 2.04 model-data comparison for temperature (top), salinity (bottom), with the observations shown on the left, the model in the center and the difference (observations-model) on the right.

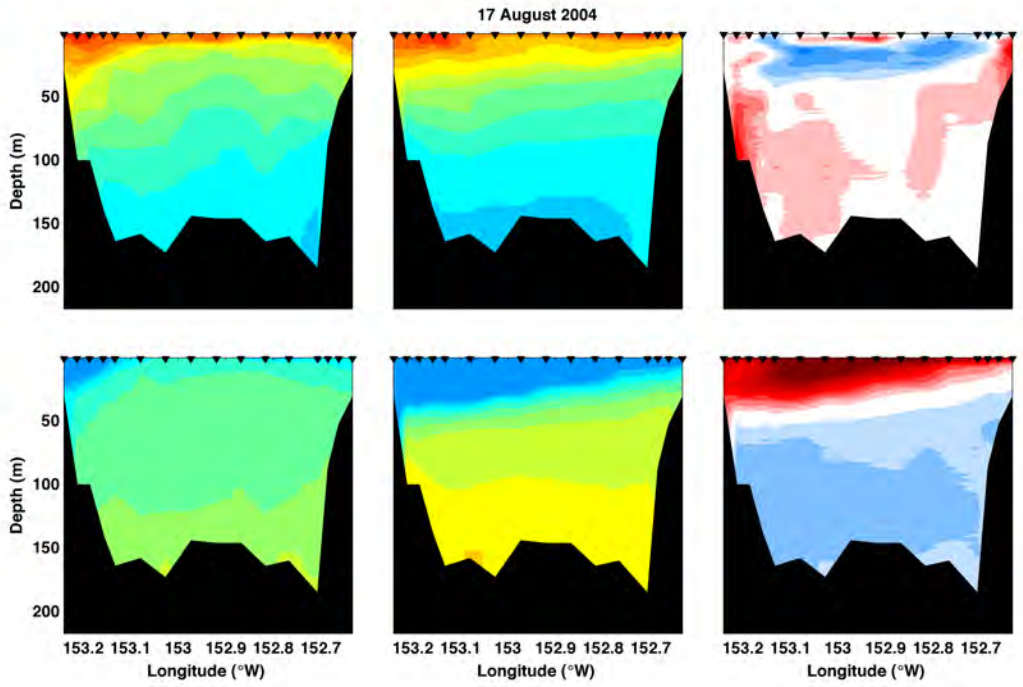

Figure A8.21: Transect 2.05 model-data comparison for temperature (top), salinity (bottom), with the observations shown on the left, the model in the center and the difference (observations-model) on the right.

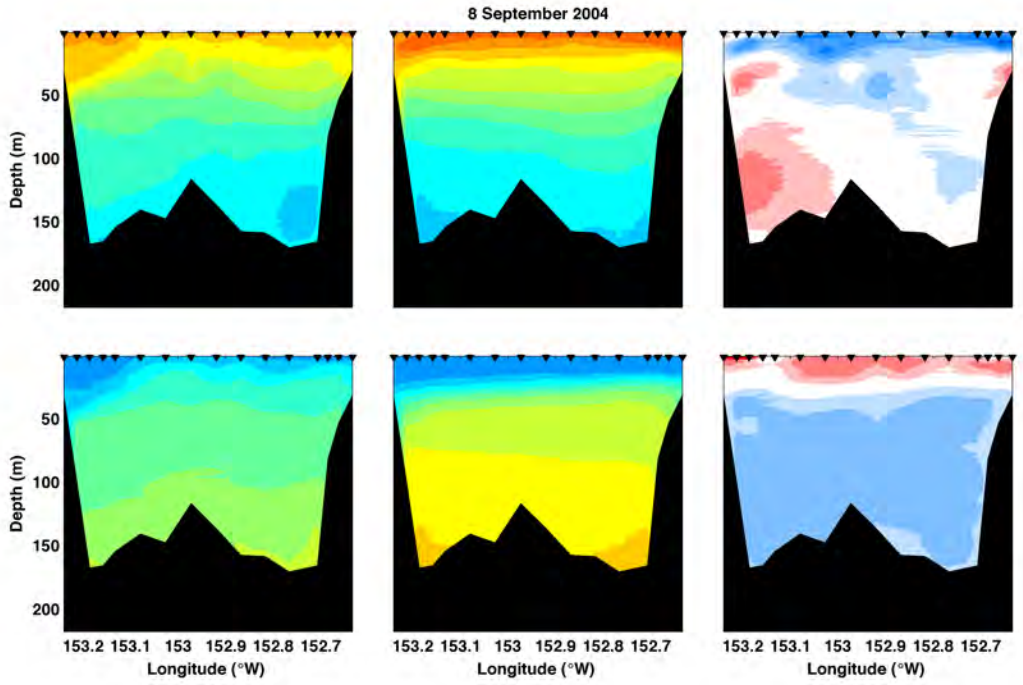

Figure A8.22: Transect 2.06 model-data comparison for temperature (top), salinity (bottom), with the observations shown on the left, the model in the center and the difference (observations-model) on the right.

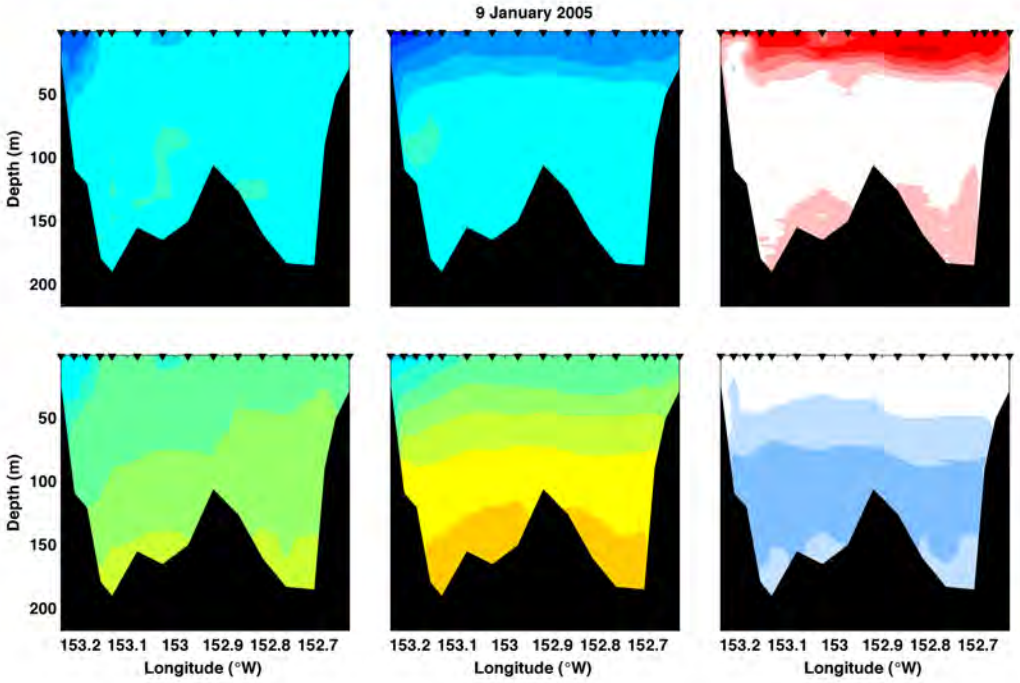

Figure A8.23: Transect 2.07 model-data comparison for temperature (top), salinity (bottom), with the observations shown on the left, the model in the center and the difference (observations-model) on the right.

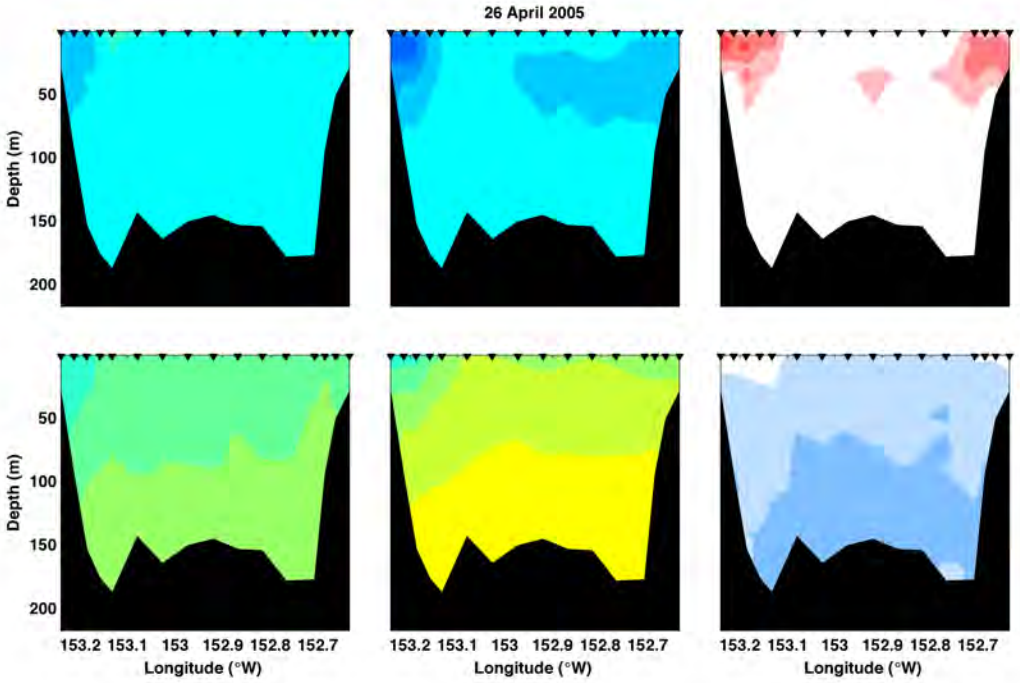

Figure A8.24: Transect 2.08 model-data comparison for temperature (top), salinity (bottom), with the

observations shown on the left, the model in the center and the difference (observations-model) on the right.

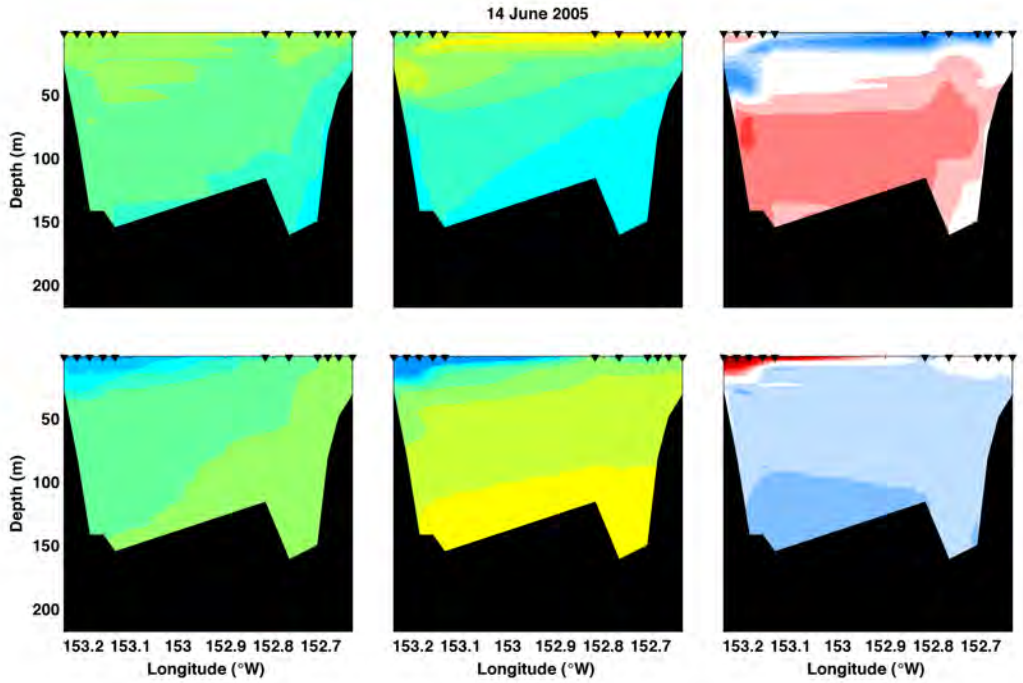

Figure A8.25: Transect 2.09 model-data comparison for temperature (top), salinity (bottom), with the observations shown on the left, the model in the center and the difference (observations-model) on the right.

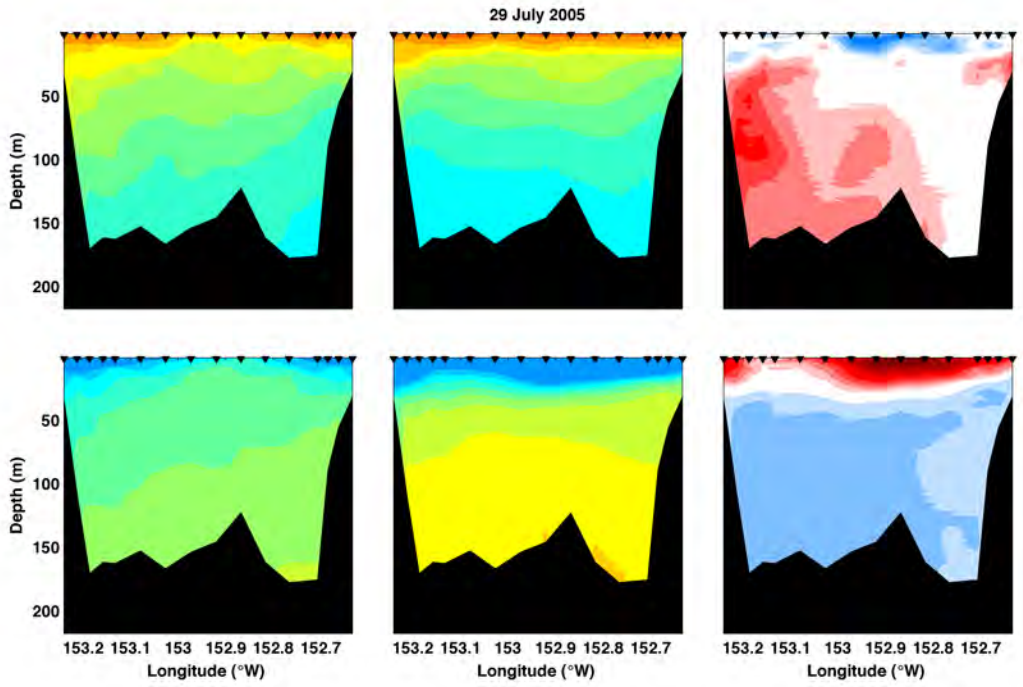

Figure A8.26: Transect 2.10 model-data comparison for temperature (top), salinity (bottom), with the observations shown on the left, the model in the center and the difference (observations-model) on the right.

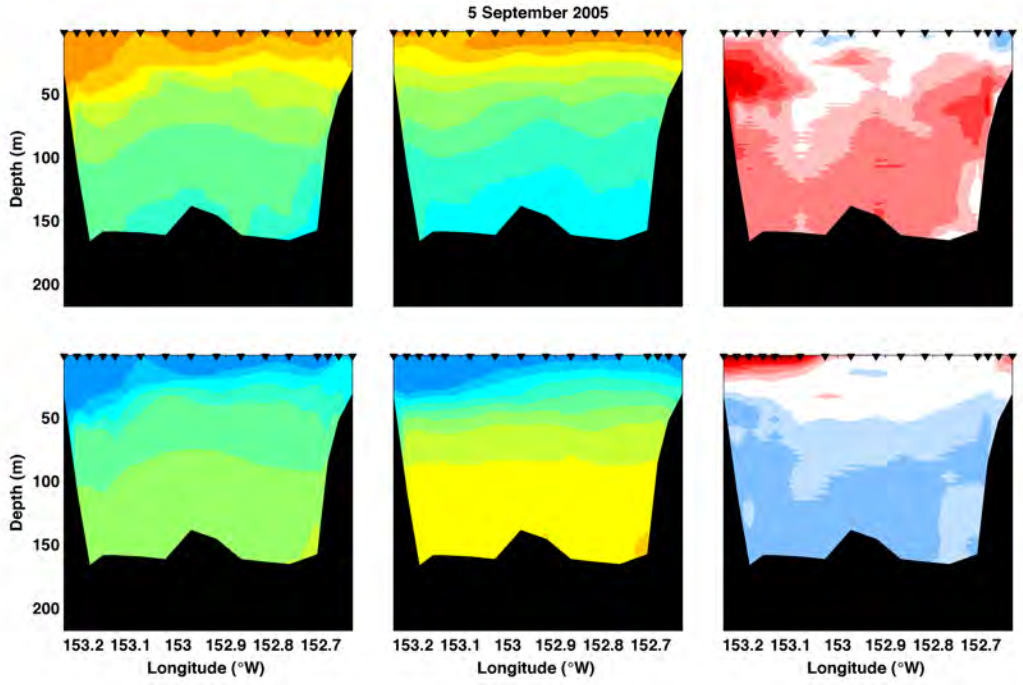

Figure A8.27: Transect 2.11 model-data comparison for temperature (top), salinity (bottom), with the

observations shown on the left, the model in the center and the difference (observations-model) on the right.

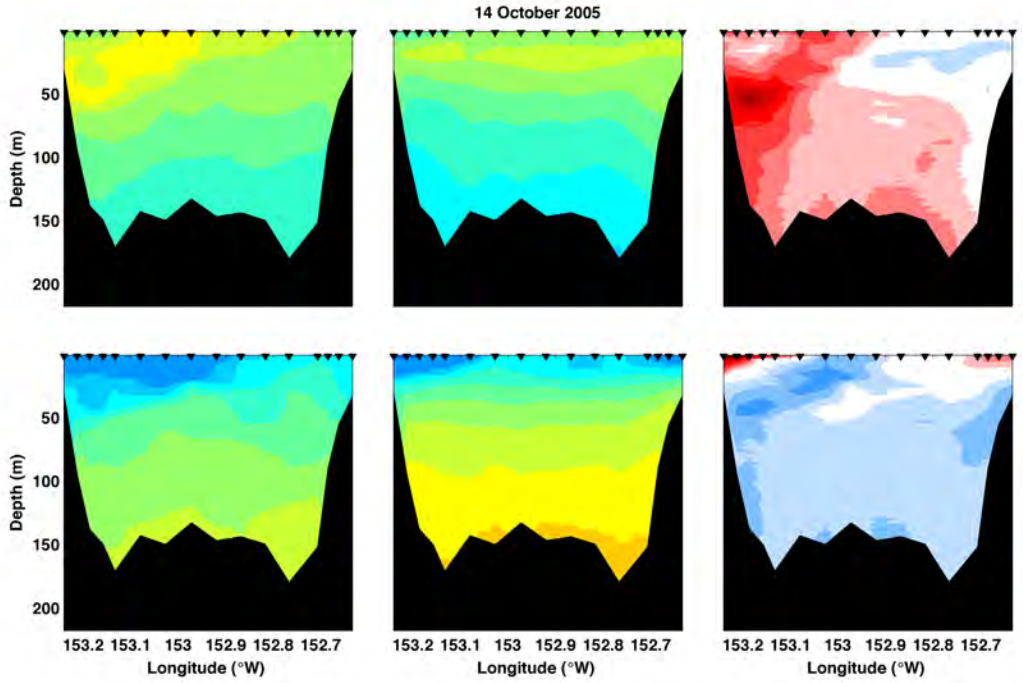

Figure A8.28: Transect 2.12 model-data comparison for temperature (top), salinity (bottom), with the observations shown on the left, the model in the center and the difference (observations-model) on the right.

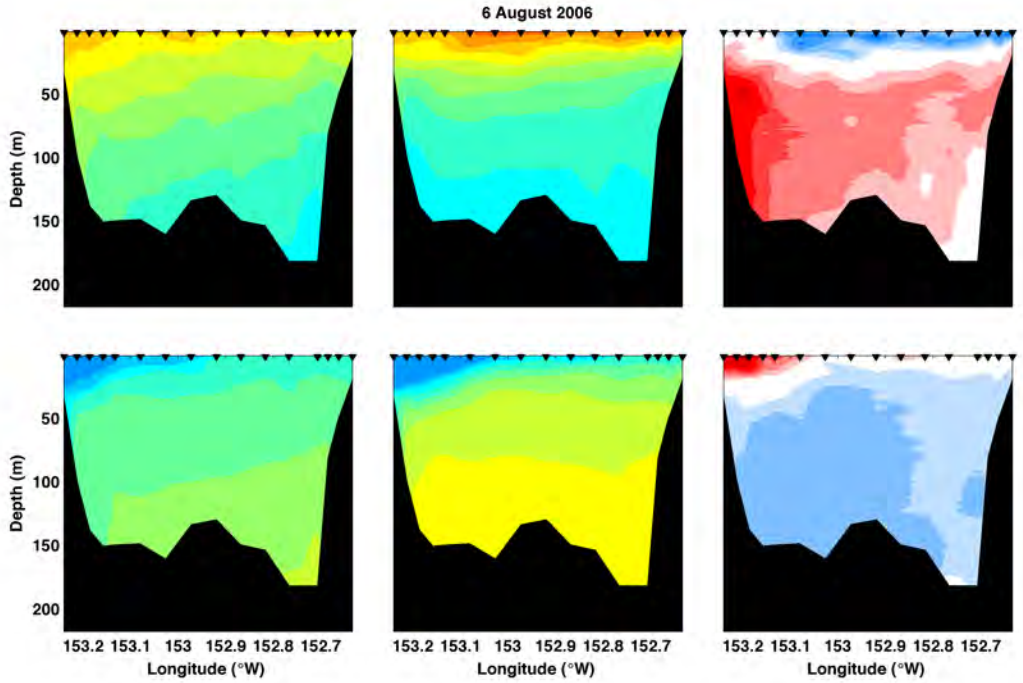

Figure A8.29: Transect 2.13 model-data comparison for temperature (top), salinity (bottom), with the observations shown on the left, the model in the center and the difference (observations-model) on the right.

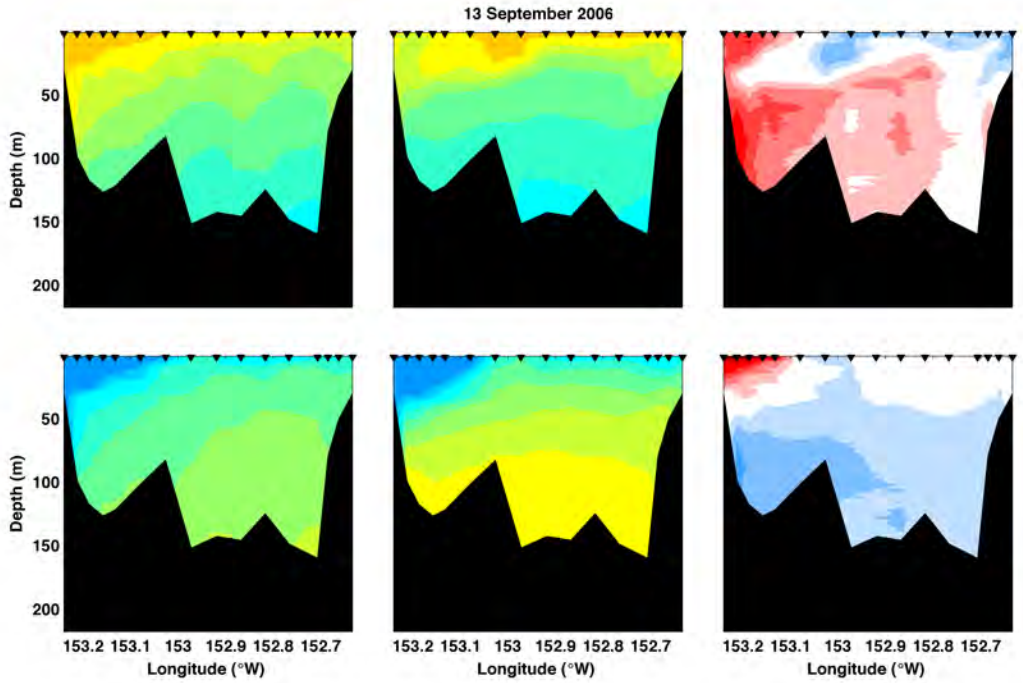

Figure A8.30: Transect 2.14 model-data comparison for temperature (top), salinity (bottom), with3 the observations shown on the left, the model in the center and the difference (observations-model) on the right.

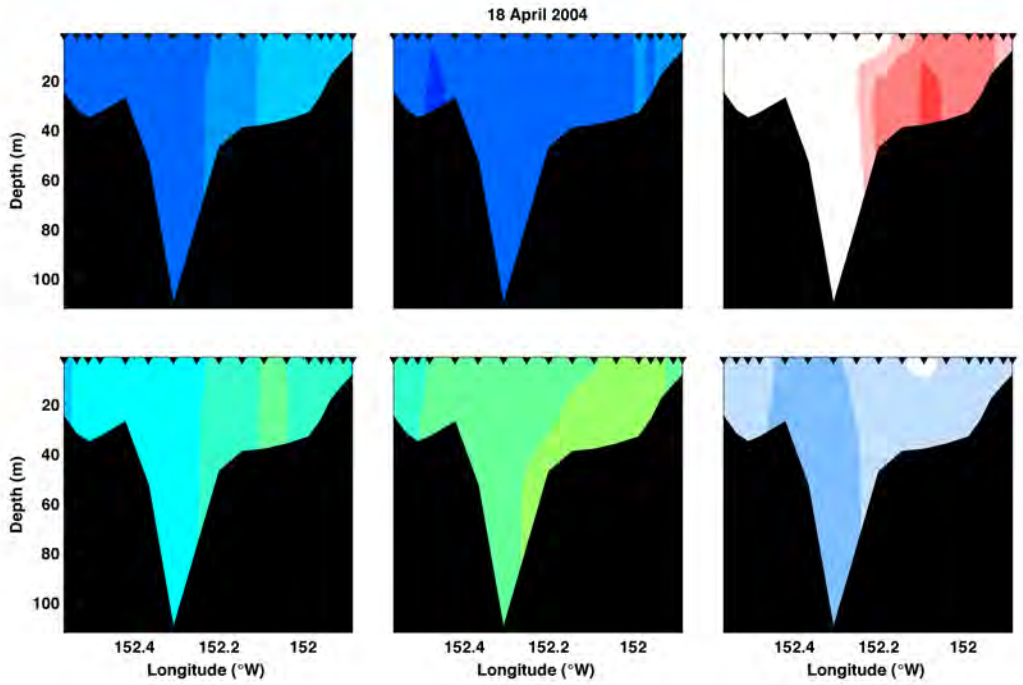

Figure A8.31: Transect 3.01 model-data comparison for temperature (top), salinity (bottom), with the observations shown on the left, the model in the center and the difference (observations-model) on the right.

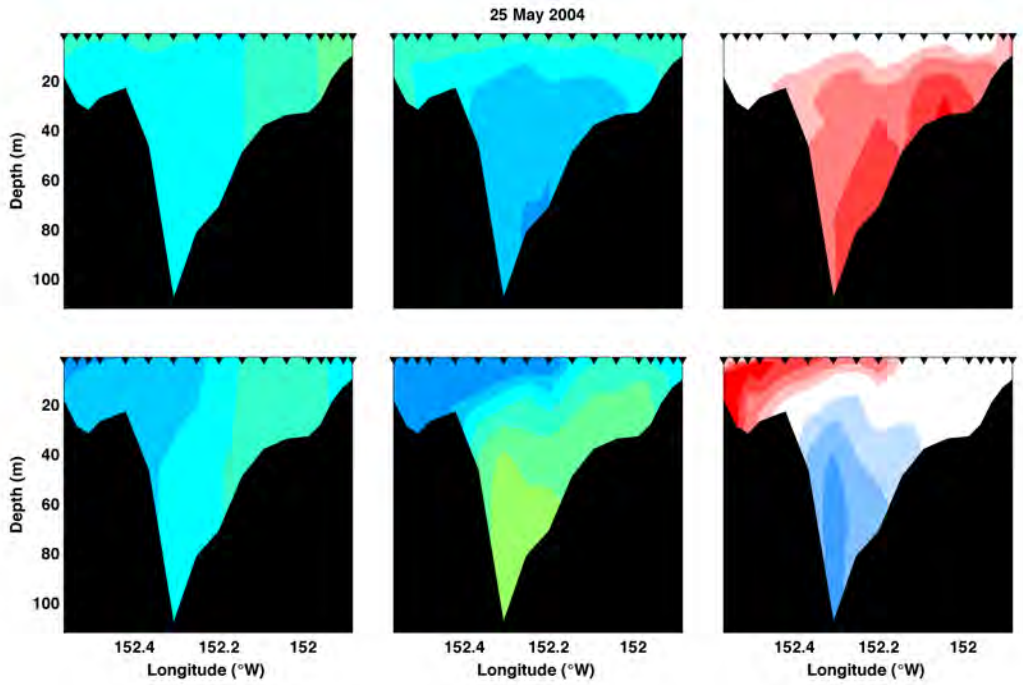

Figure A8.32: Transect 3.02 model-data comparison for temperature (top), salinity (bottom), with the

observations shown on the left, the model in the center and the difference (observations-model) on the right.

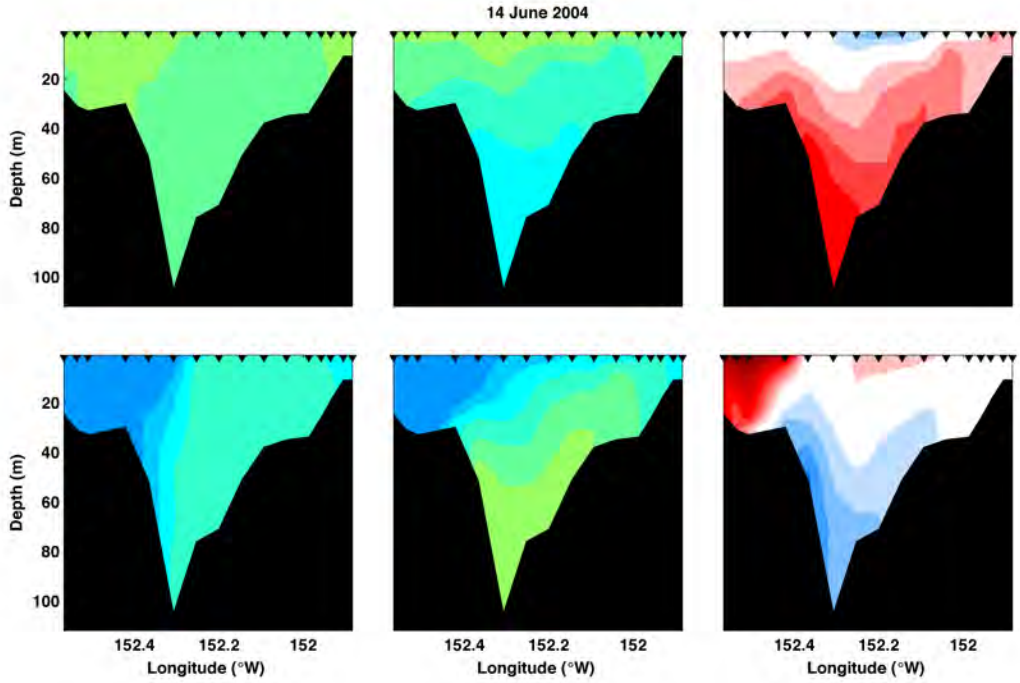

Figure A8.33: Transect 3.03 model-data comparison for temperature (top), salinity (bottom), with the observations shown on the left, the model in the center and the difference (observations-model) on the right.

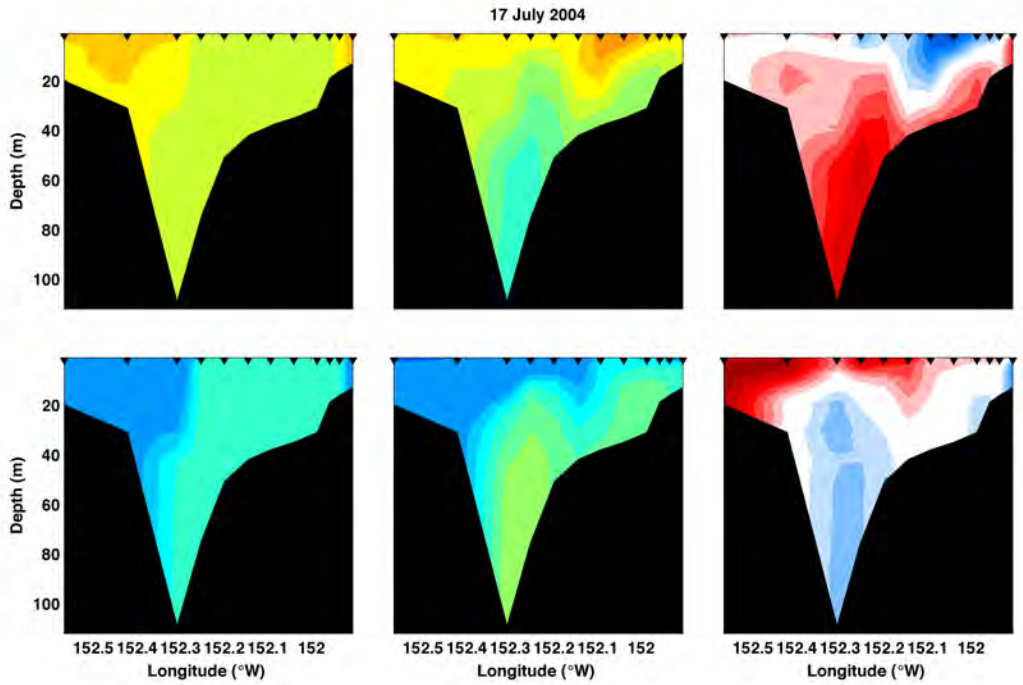

Figure A8.34: Transect 3.04 model-data comparison for temperature (top), salinity (bottom), with the observations shown on the left, the model in the center and the difference (observations-model) on the right.

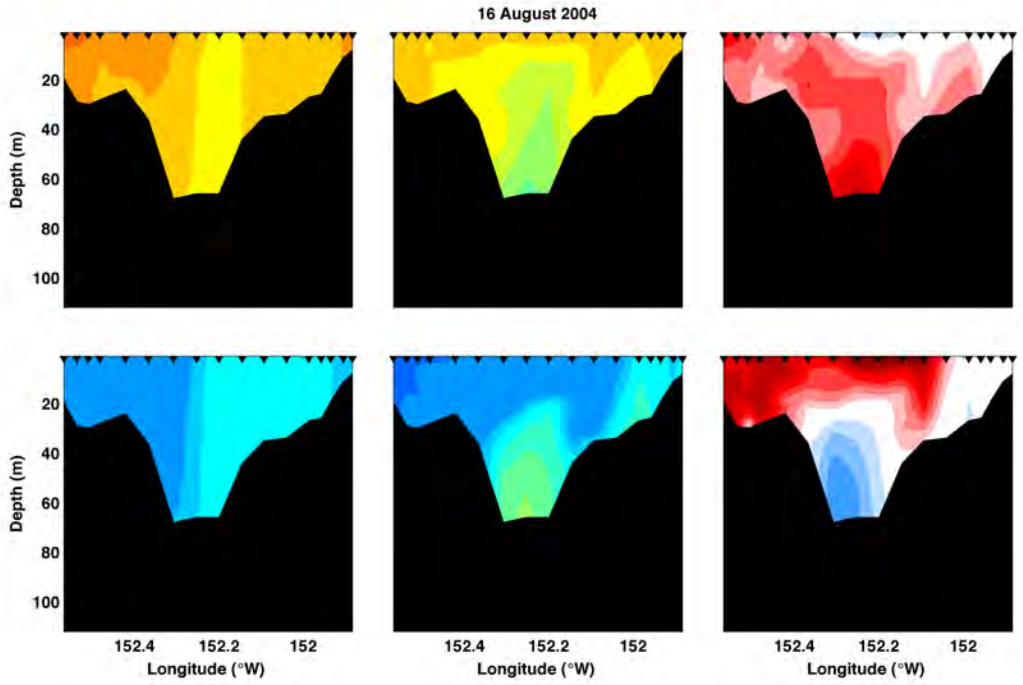

Figure A8.35: Transect 3.05 model-data comparison for temperature (top), salinity (bottom), with the observations shown on the left, the model in the center and the difference (observations-model) on the right.

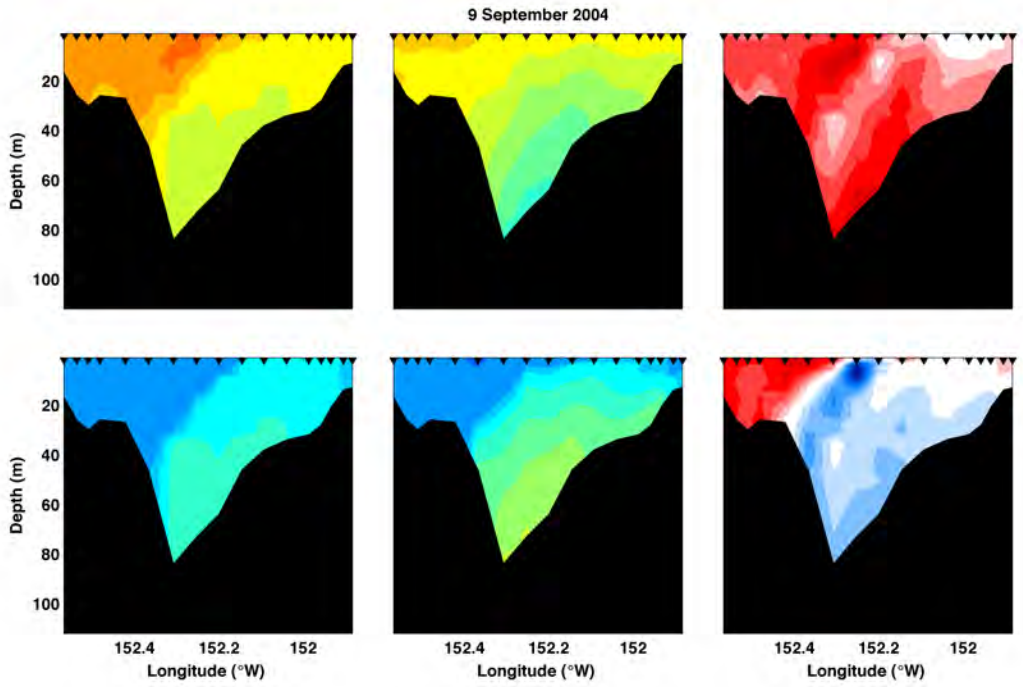

Figure A8.36: Transect 3.06 model-data comparison for temperature (top), salinity (bottom), with the observations shown on the left, the model in the center and the difference (observations-model) on the right.

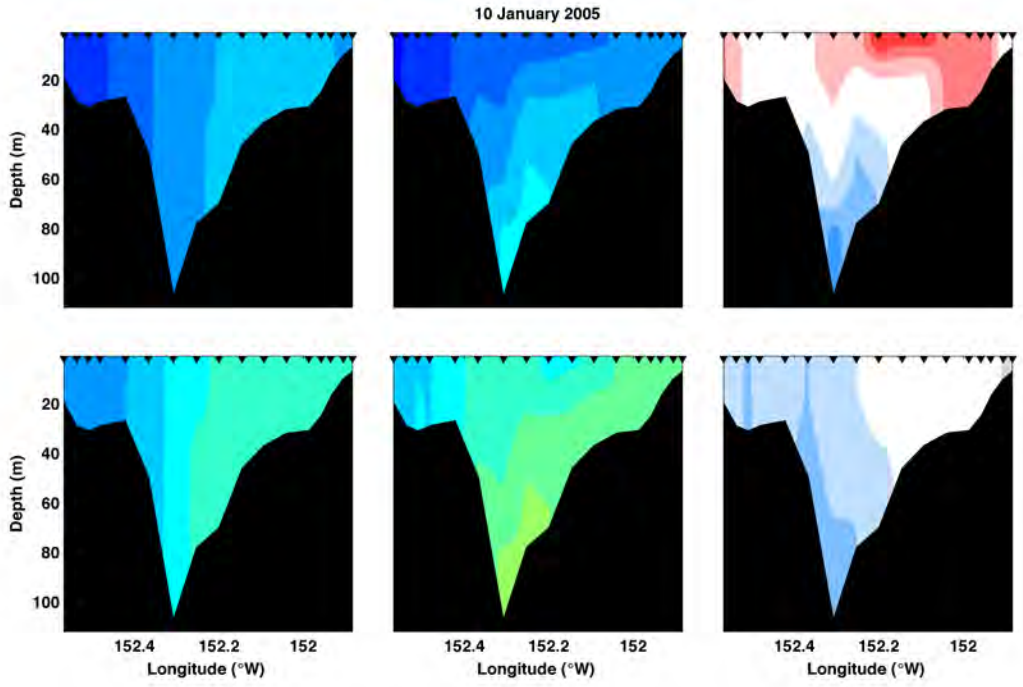

Figure A8.37: Transect 3.07 model-data comparison for temperature (top), salinity (bottom), with the observations shown on the left, the model in the center and the difference (observations-model) on the right.

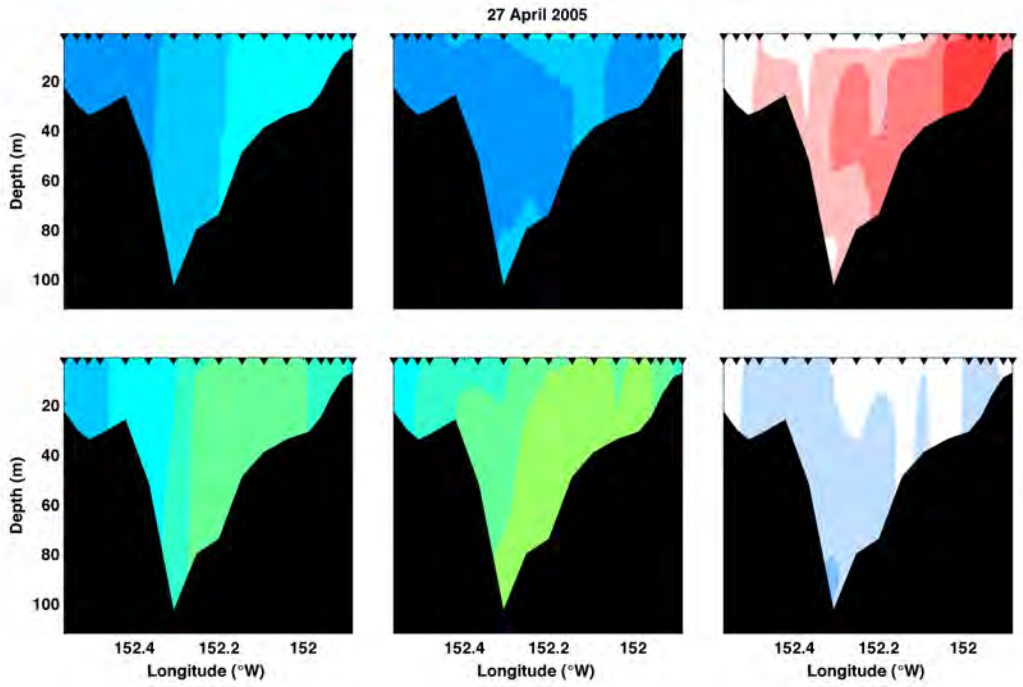

Figure A8.38: Transect 3.08 model-data comparison for temperature (top), salinity (bottom), with the observations shown on the left, the model in the center and the difference (observations-model) on the right.

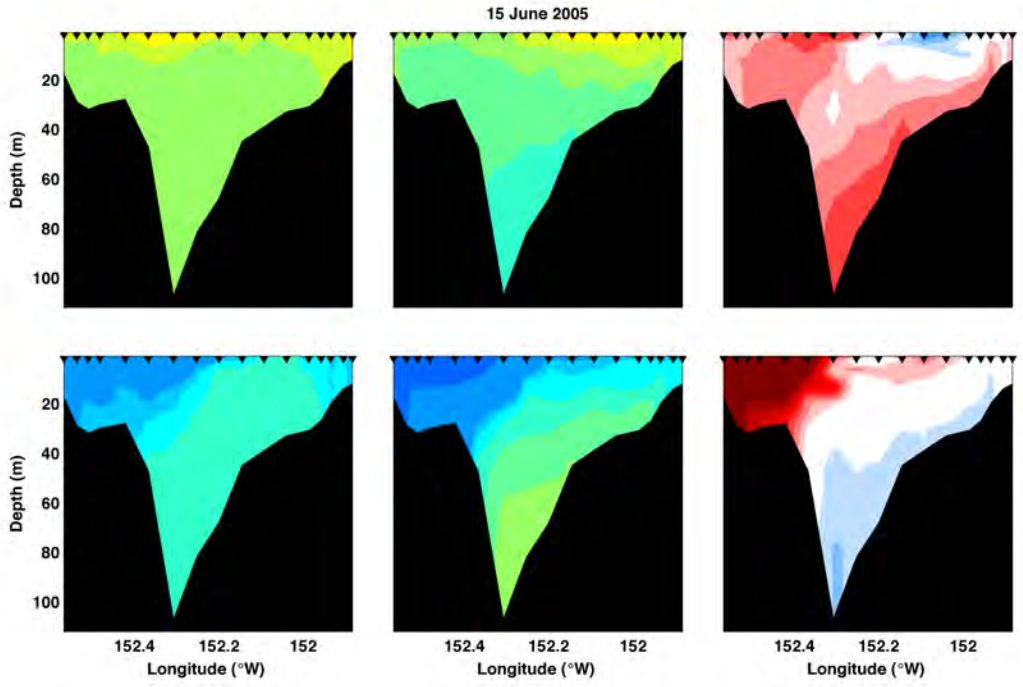

Figure A8.39: Transect 3.09 model-data comparison for temperature (top), salinity (bottom), with the observations shown on the left, the model in the center and the difference (observations-model) on the right.

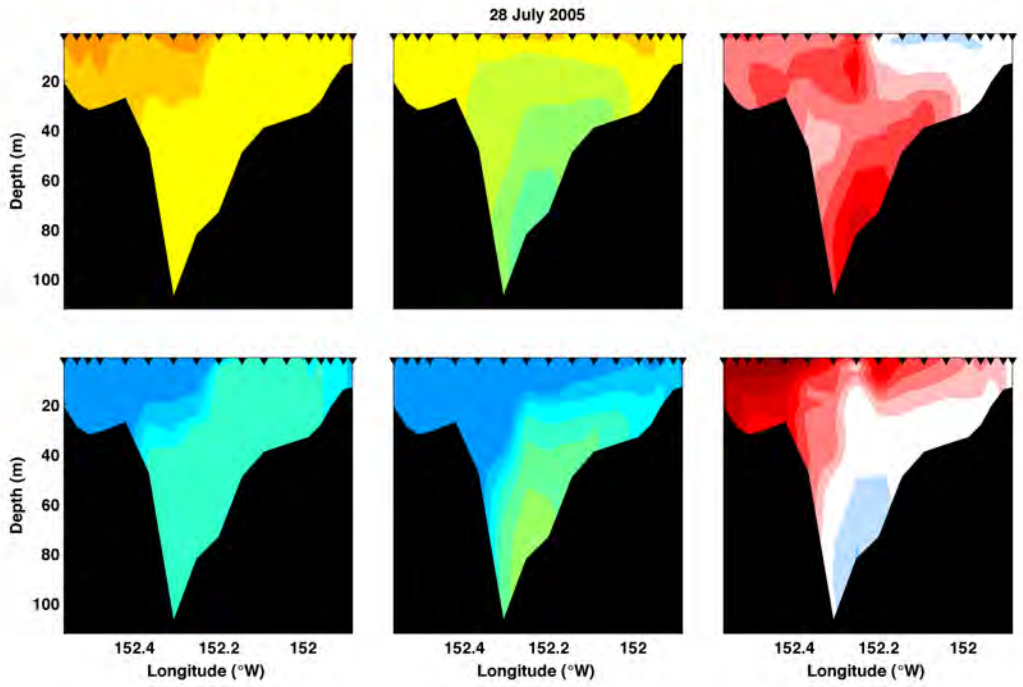

Figure A8.40: Transect 3.10 model-data comparison for temperature (top), salinity (bottom), with the observations shown on the left, the model in the center and the difference (observations-model) on the right.

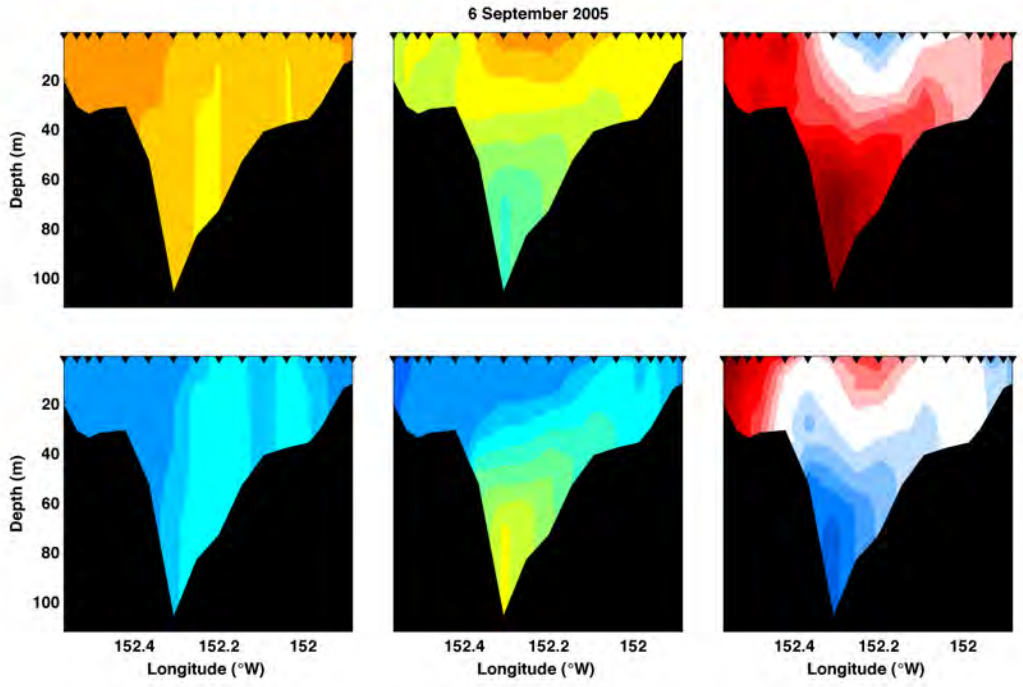

Figure A8.41: Transect 3.11 model-data comparison for temperature (top), salinity (bottom), with the observations shown on the left, the model in the center and the difference (observations-model) on the right.

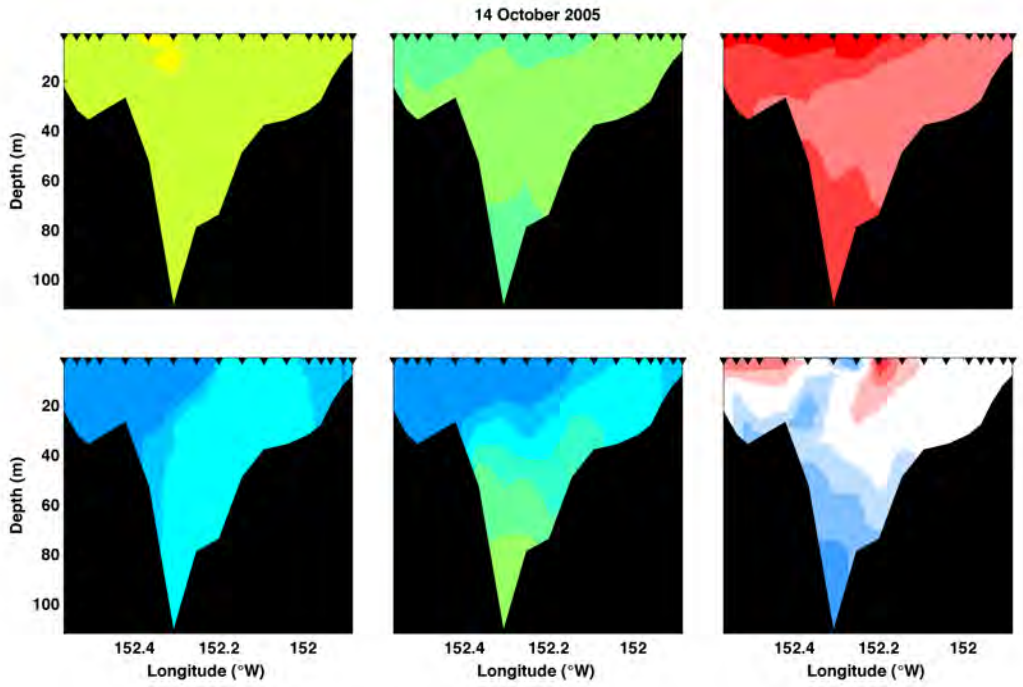

Figure A8.42: Transect 3.12 model-data comparison for temperature (top), salinity (bottom), with the observations shown on the left, the model in the center and the difference (observations-model) on the right.

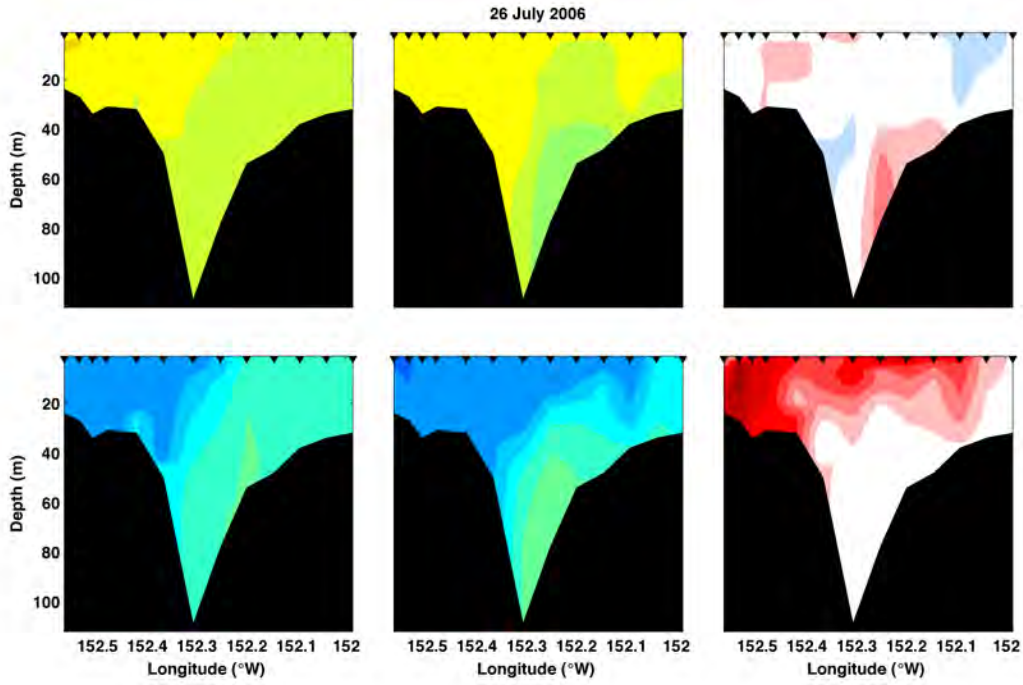

Figure A8:43 Transect 3.13 model-data comparison for temperature (top), salinity (bottom), with the observations shown on the left, the model in the center and the difference (observations-model) on the right.

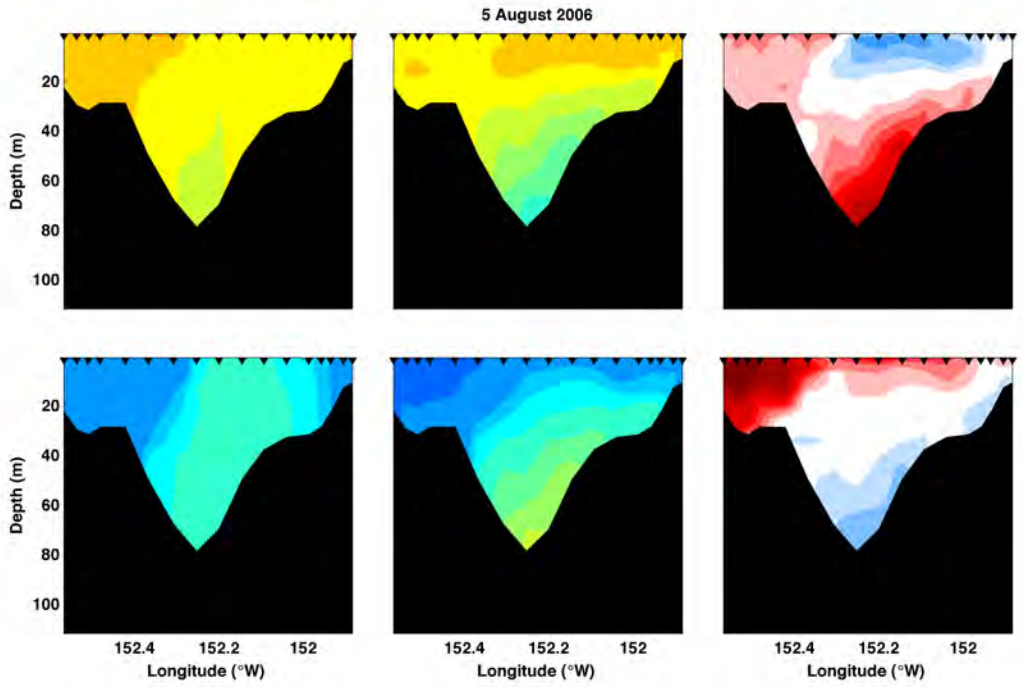

Figure A8.44: Transect 3.14 model-data comparison for temperature (top), salinity (bottom), with the observations shown on the left, the model in the center and the difference (observations-model) on the right.

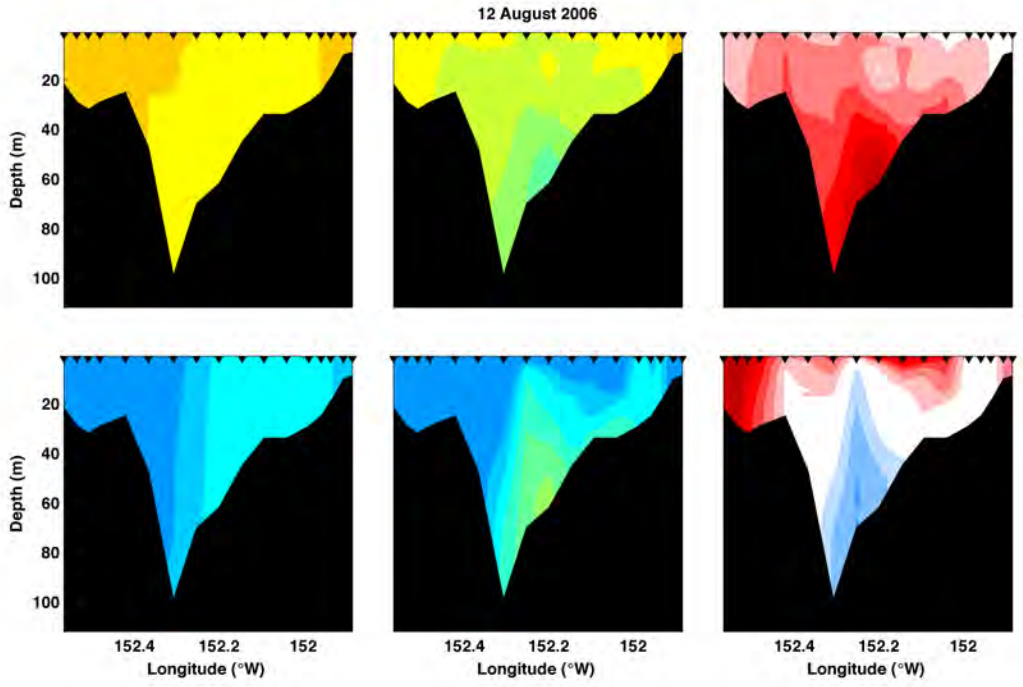

Figure A8.45: Transect 3.15 model-data comparison for temperature (top), salinity (bottom), with the observations shown on the left, the model in the center and the difference (observations-model) on the right.

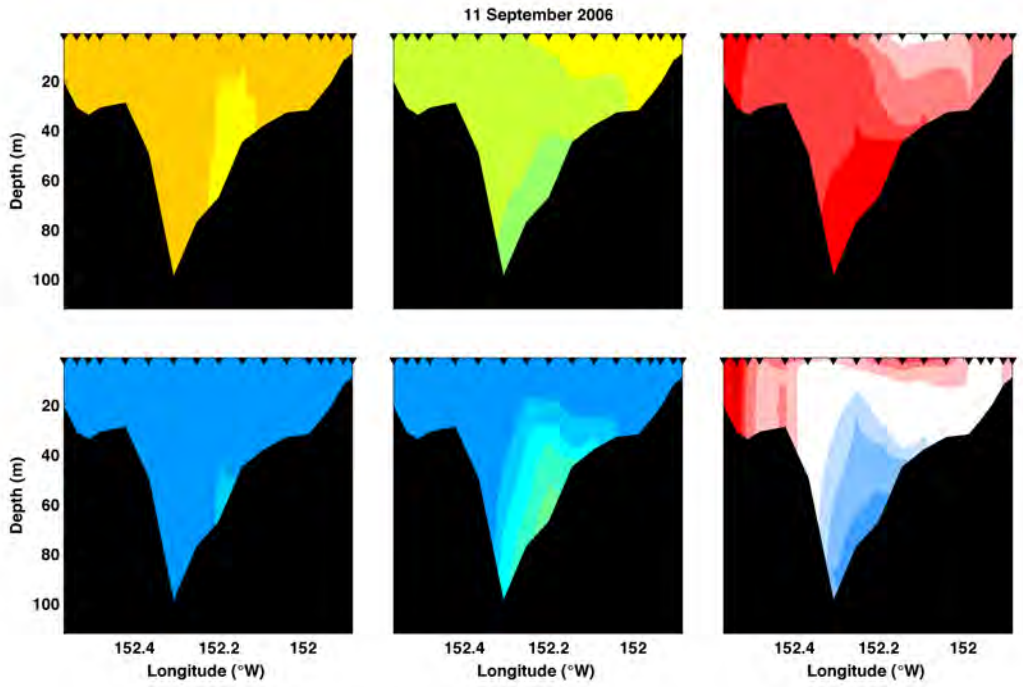

Figure A8.46: Transect 3.16 model-data comparison for temperature (top), salinity (bottom), with the observations shown on the left, the model in the center and the difference (observations-model) on the right.

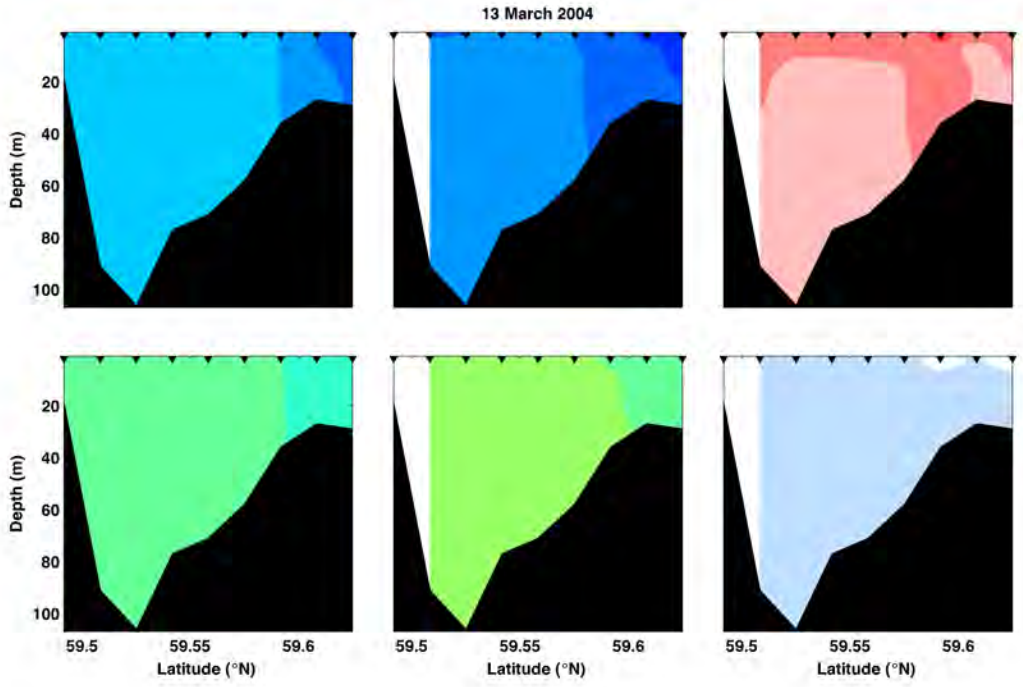

Figure A8.47: Transect 4.01 model-data comparison for temperature (top), salinity (bottom), with the observations shown on the left, the model in the center and the difference (observations-model) on the right.

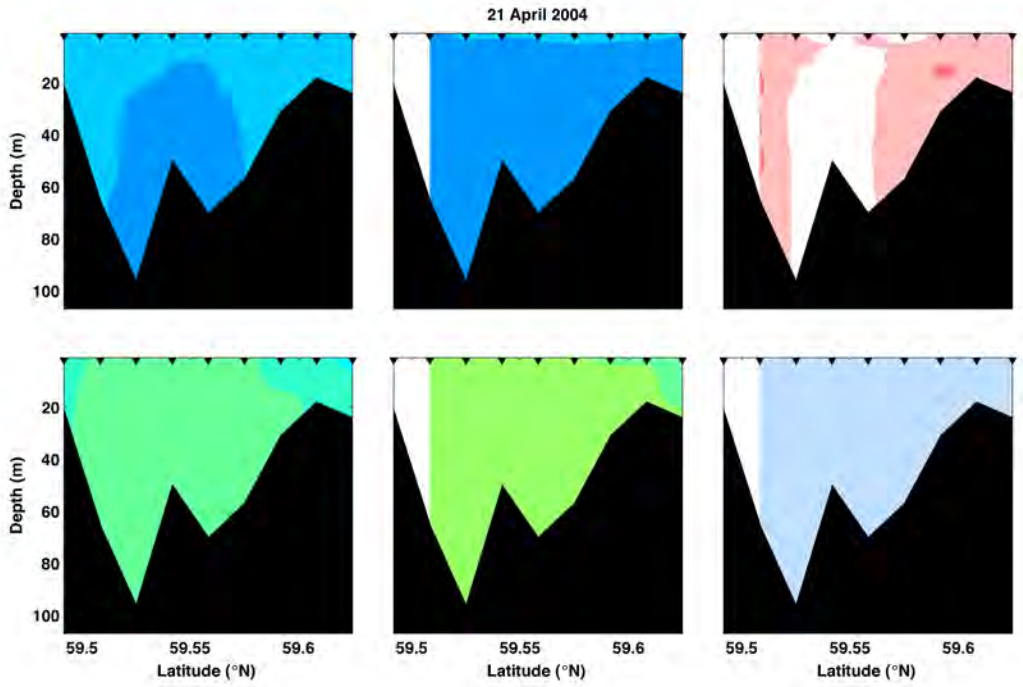

Figure A8.48: Transect 4.02 model-data comparison for temperature (top), salinity (bottom), with the observations shown on the left, the model in the center and the difference (observations-model) on the right.

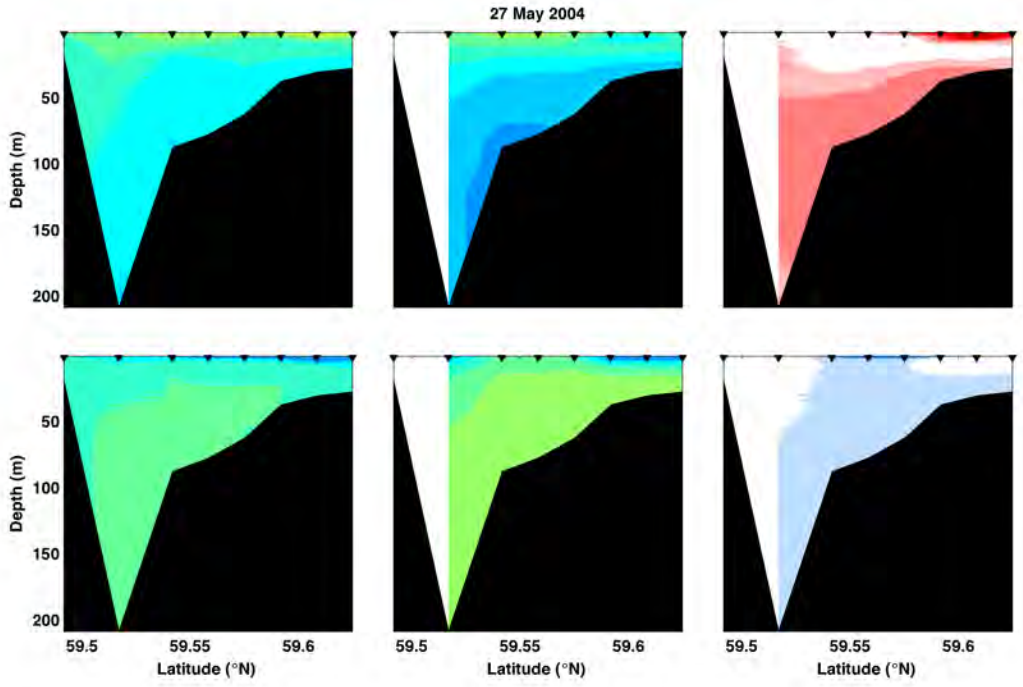

Figure A8.49: Transect 4.03 model-data comparison for temperature (top), salinity (bottom), with the observations shown on the left, the model in the center and the difference (observations-model) on the right.

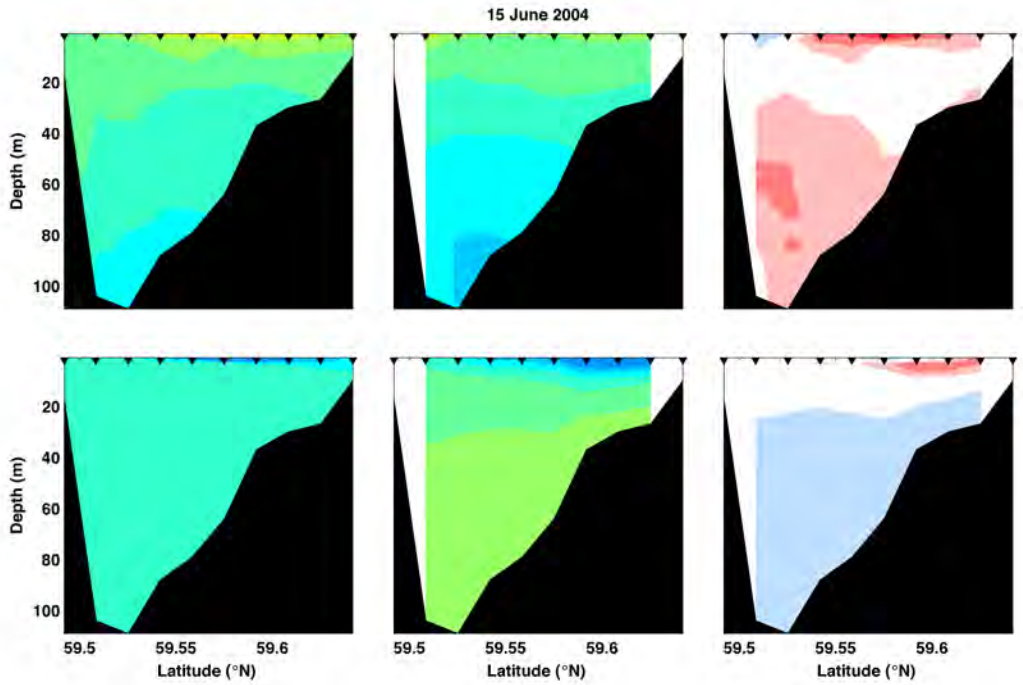

Figure A8.50: Transect 4.04 model-data comparison for temperature (top), salinity (bottom), with the observations shown on the left, the model in the center and the difference (observations-model) on the right.

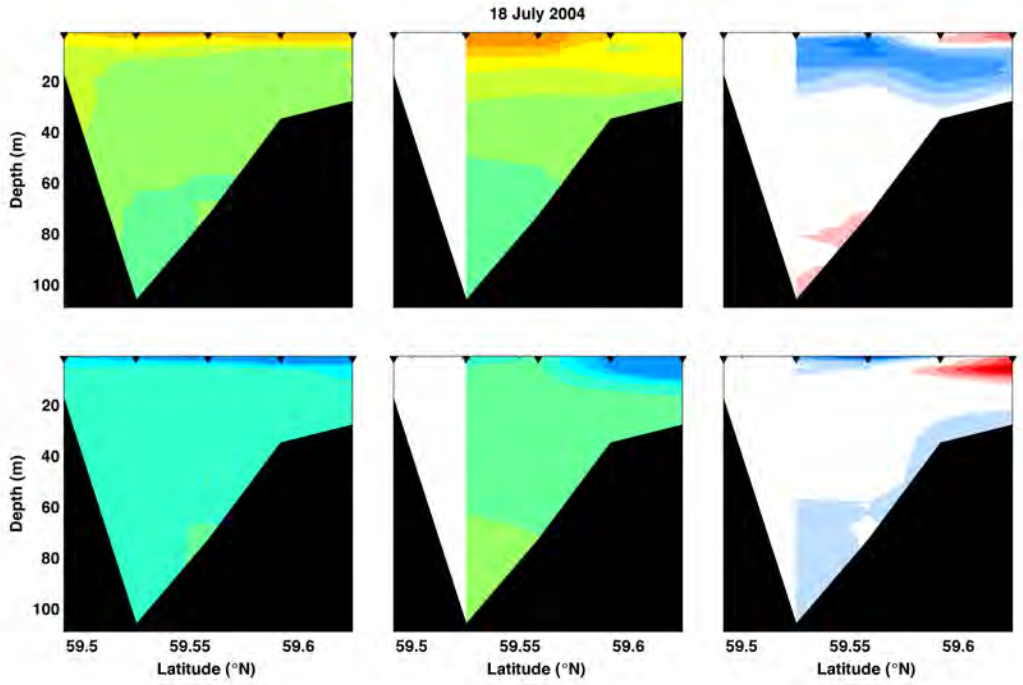

Figure A8.51: Transect 4.05 model-data comparison for temperature (top), salinity (bottom), with the observations shown on the left, the model in the center and the difference (observations-model) on the right.

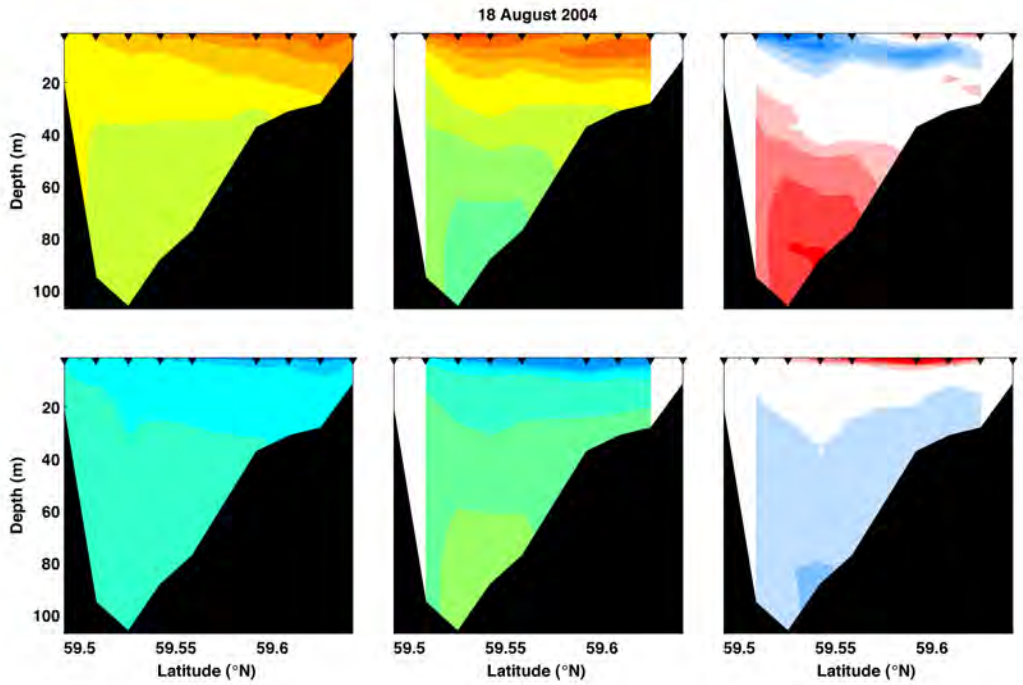

Figure A8.52: Transect 4.06 model-data comparison for temperature (top), salinity (bottom), with the observations shown on the left, the model in the center and the difference (observations-model) on the right.

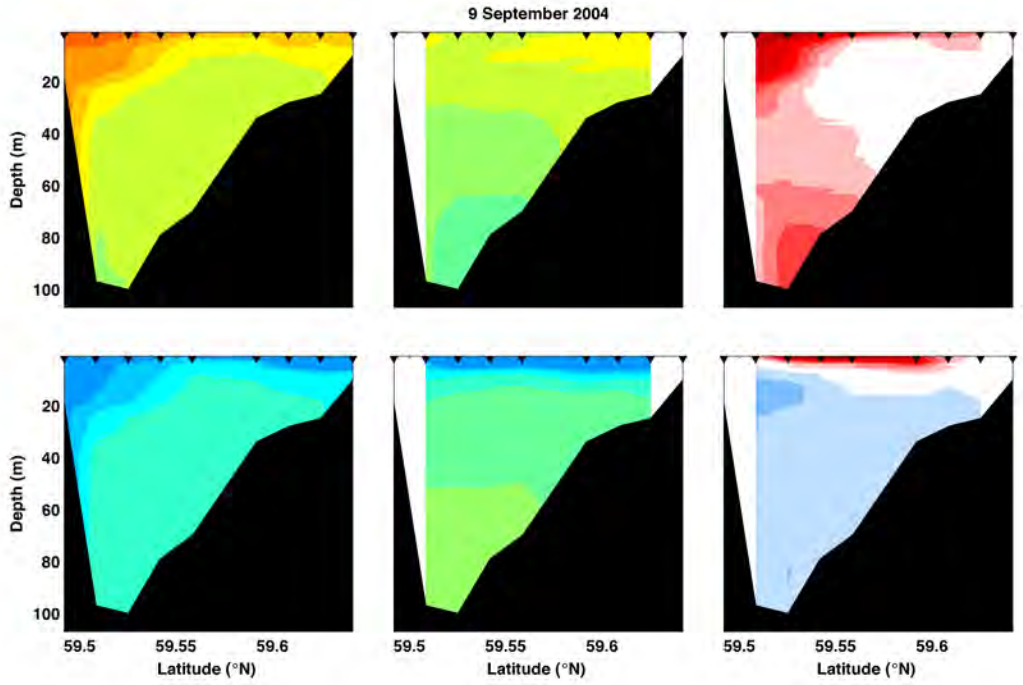

Figure A8.53: Transect 4.07 model-data comparison for temperature (top), salinity (bottom), with the observations shown on the left, the model in the center and the difference (observations-model) on the right.

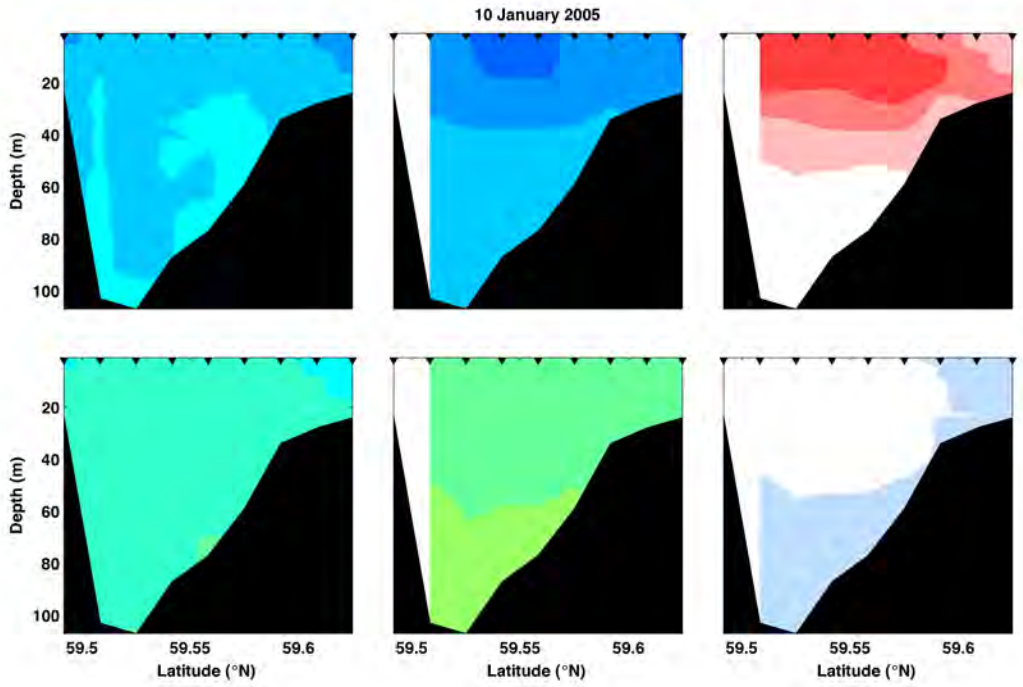

Figure A8.54: Transect 4.08 model-data comparison for temperature (top), salinity (bottom), with the observations shown on the left, the model in the center and the difference (observations-model) on the right.

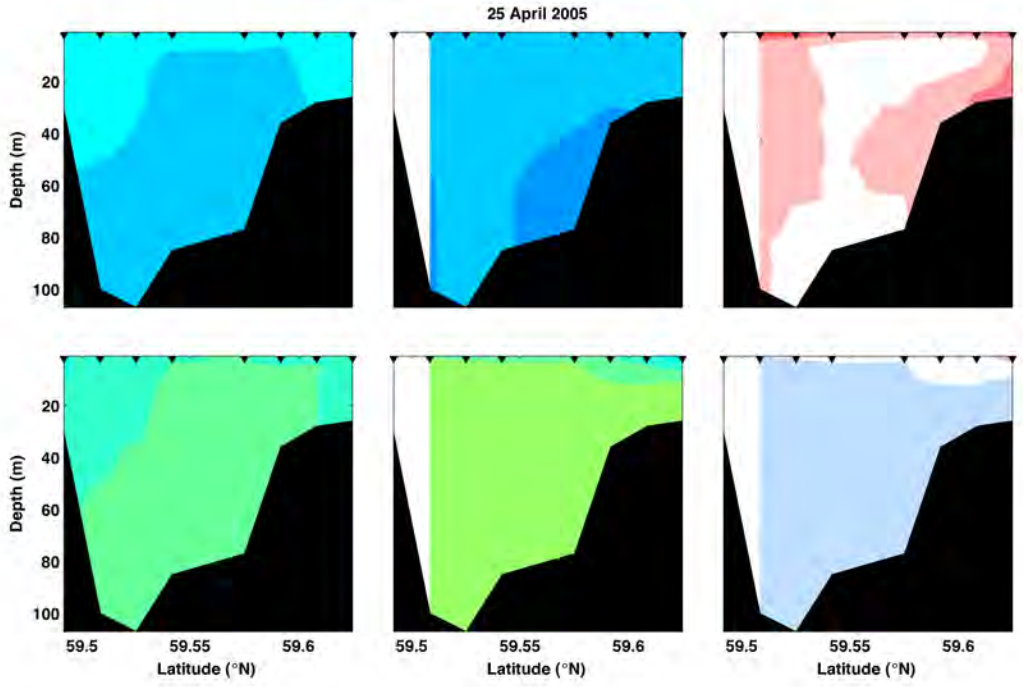

Figure A8.55: Transect 4.09 model-data comparison for temperature (top), salinity (bottom), with the observations shown on the left, the model in the center and the difference (observations-model) on the right.

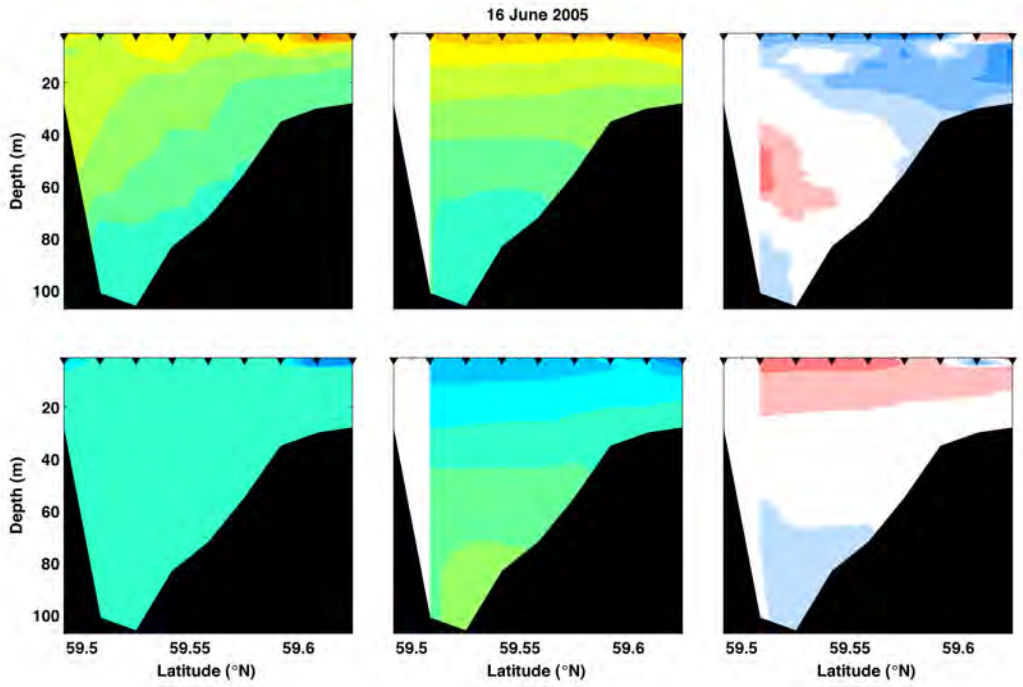

Figure A8.56: Transect 4.10 model-data comparison for temperature (top), salinity (bottom), with the observations shown on the left, the model in the center and the difference (observations-model) on the right.

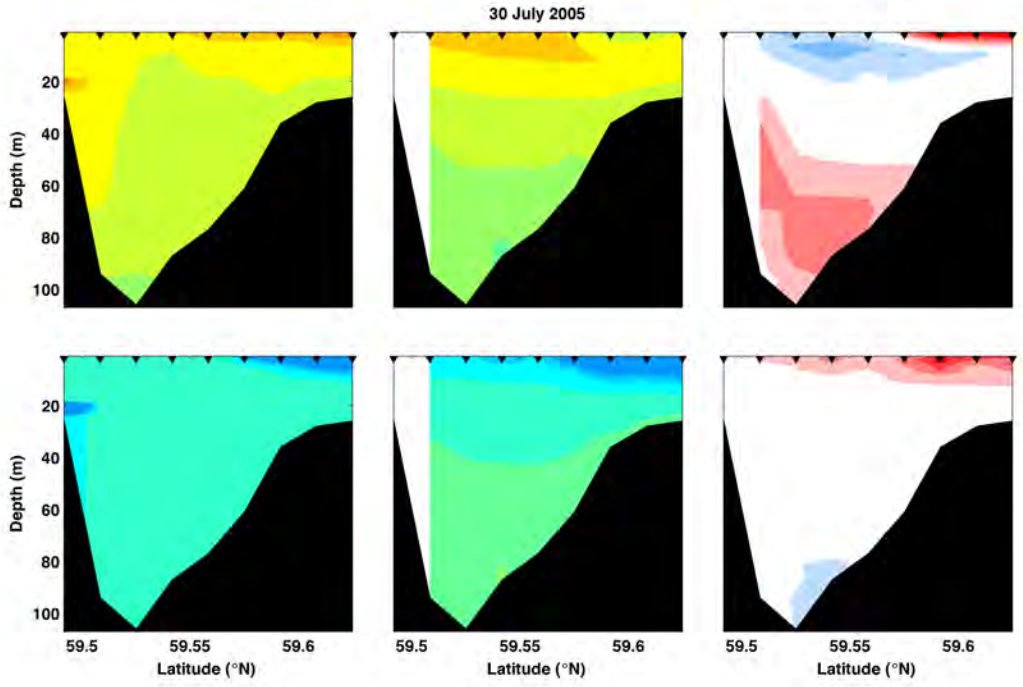

Figure A8.57: Transect 4.11 model-data comparison for temperature (top), salinity (bottom), with the observations shown on the left, the model in the center and the difference (observations-model) on the right.

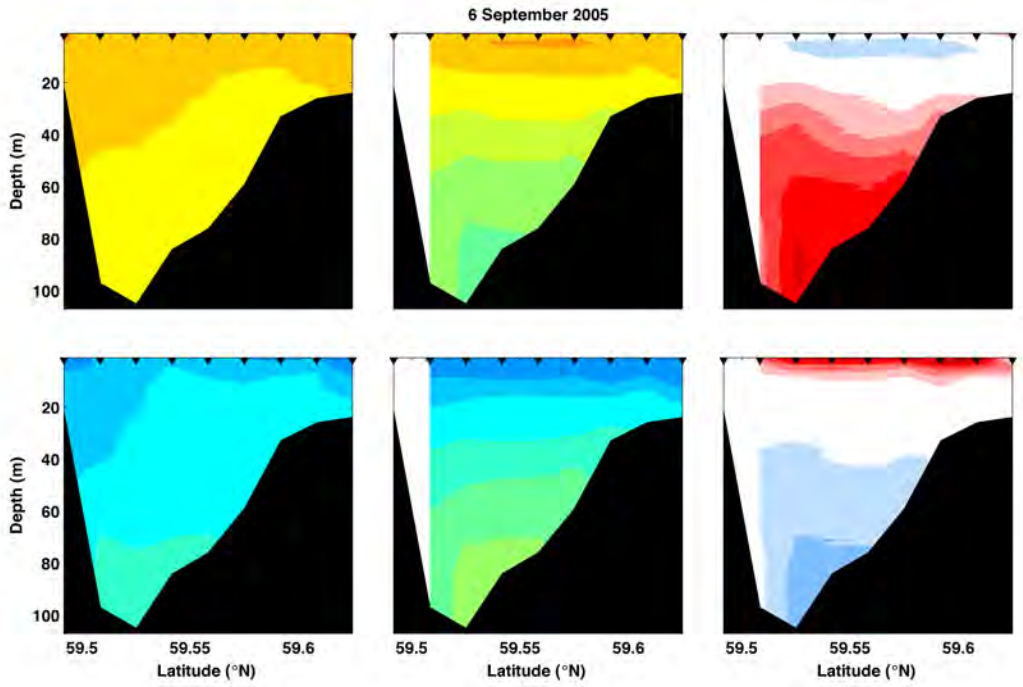

Figure A8.58: Transect 4.12 model-data comparison for temperature (top), salinity (bottom), with the observations shown on the left, the model in the center and the difference (observations-model) on the right.

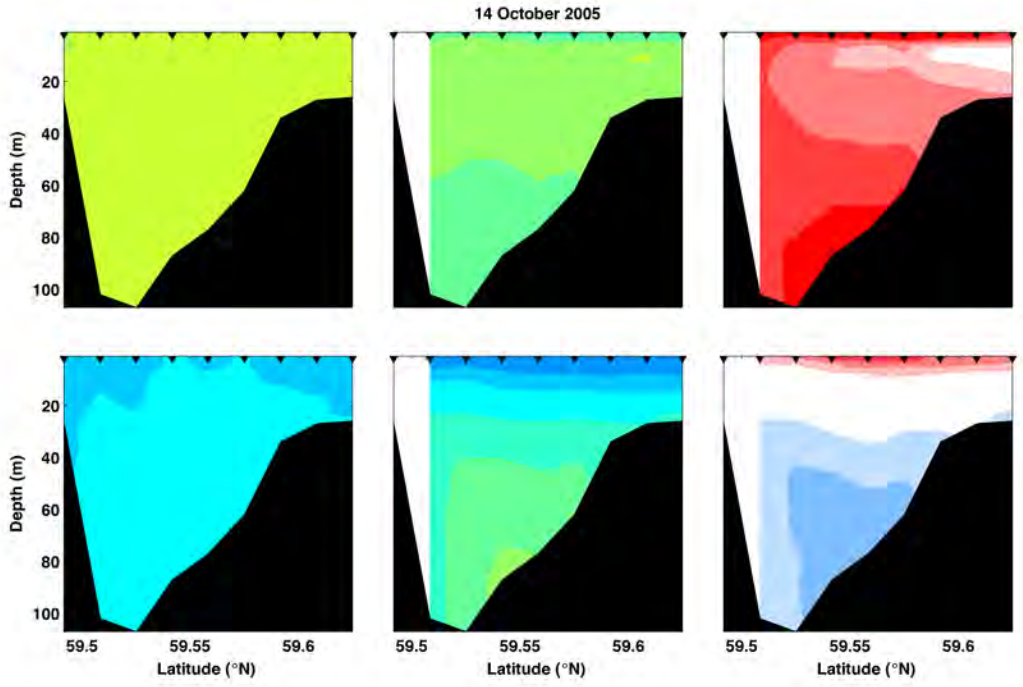

Figure A8.59: Transect 4.13 model-data comparison for temperature (top), salinity (bottom), with the observations shown on the left, the model in the center and the difference (observations-model) on the right.

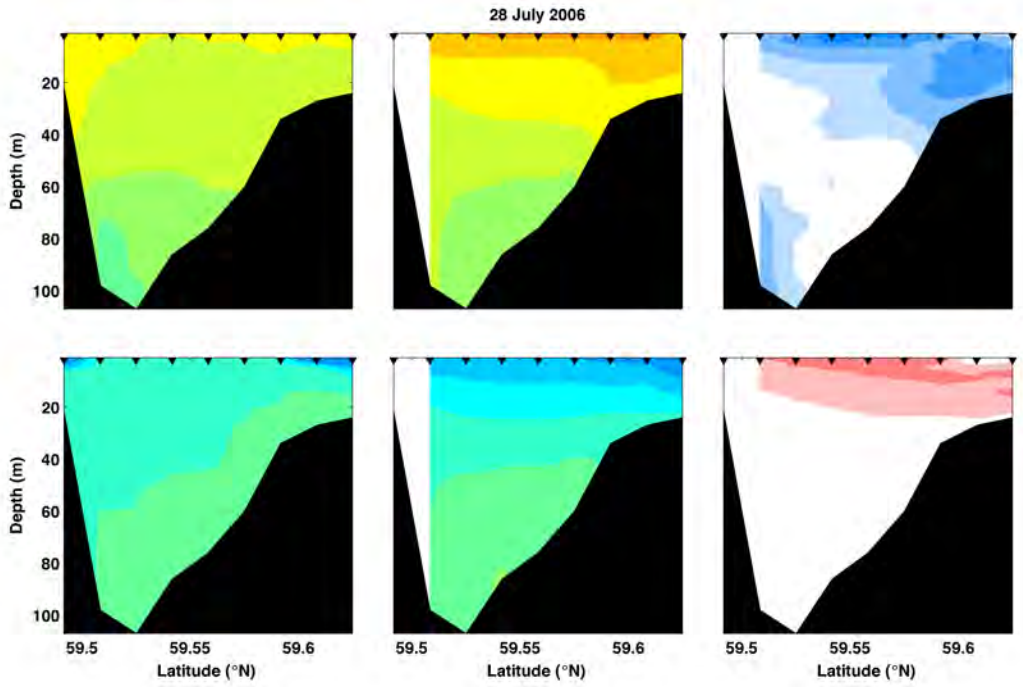

Figure A8.60: Transect 4.14 model-data comparison for temperature (top), salinity (bottom), with the observations shown on the left, the model in the center and the difference (observations-model) on the right.

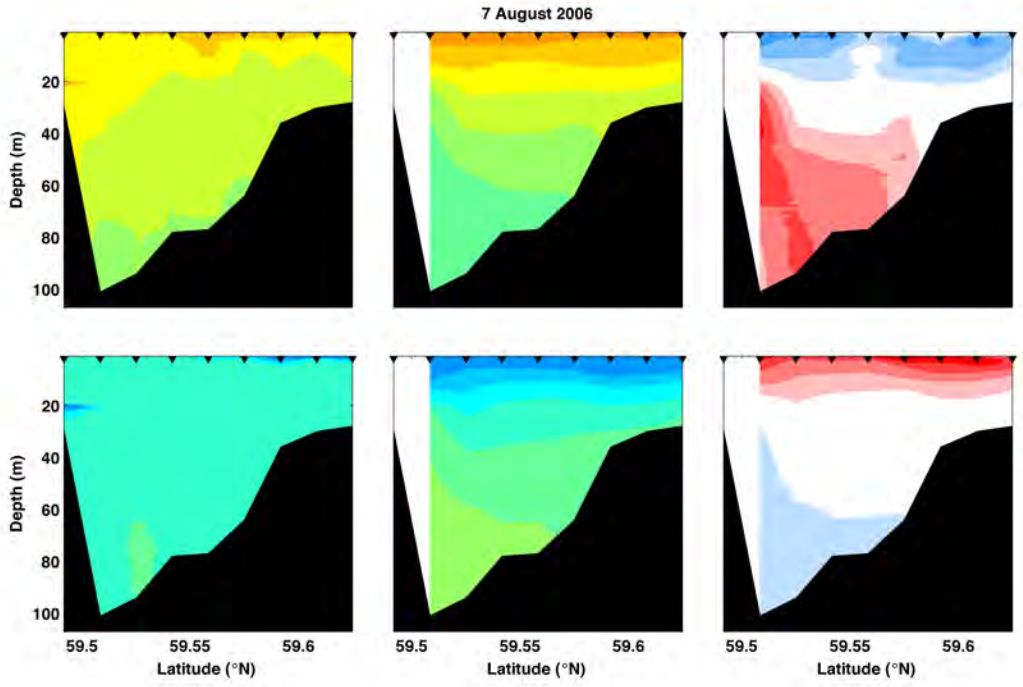

Figure A8.61: Transect 4.15 model-data comparison for temperature (top), salinity (bottom), with the observations shown on the left, the model in the center and the difference (observations-model) on the right.

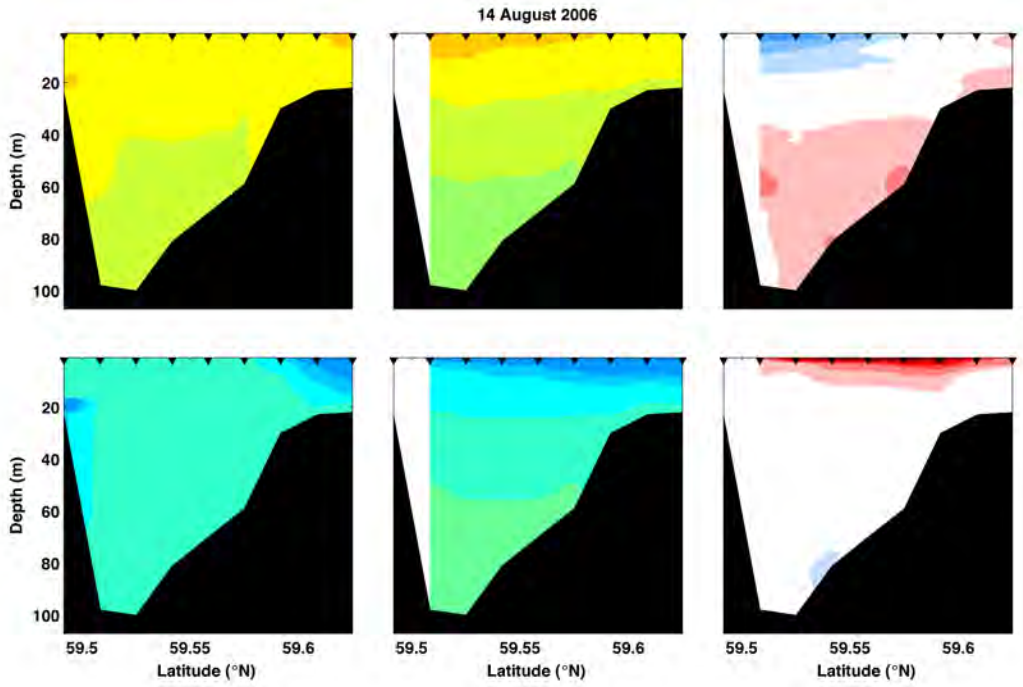

Figure A8.62: Transect 4.16 model-data comparison for temperature (top), salinity (bottom), with the observations shown on the left, the model in the center and the difference (observations-model) on the right.

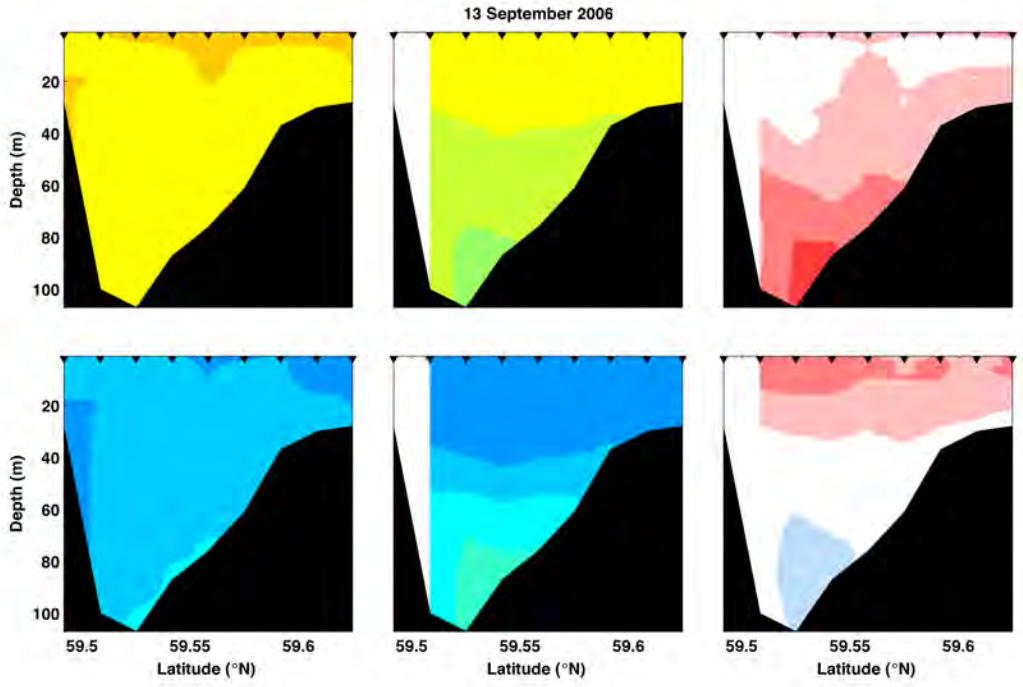

Figure A8.63: Transect 4.17 model-data comparison for temperature (top), salinity (bottom), with the observations shown on the left, the model in the center and the difference (observations-model) on the right.

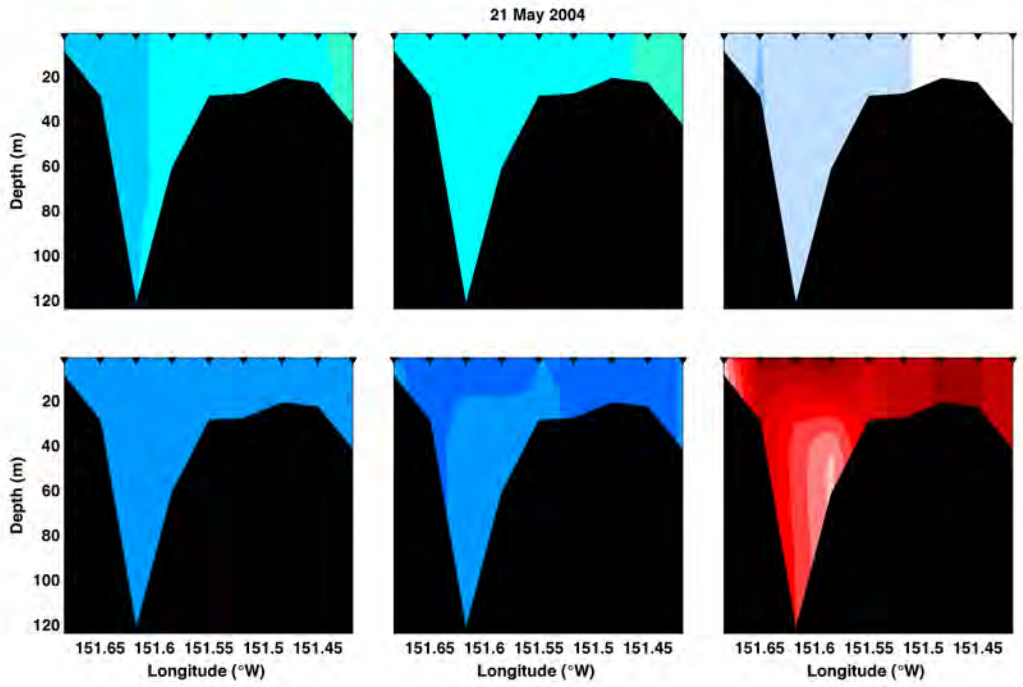

Figure A8.64: Transect 5.01 model-data comparison for temperature (top), salinity (bottom), with the observations shown on the left, the model in the center and the difference (observations-model) on the right.

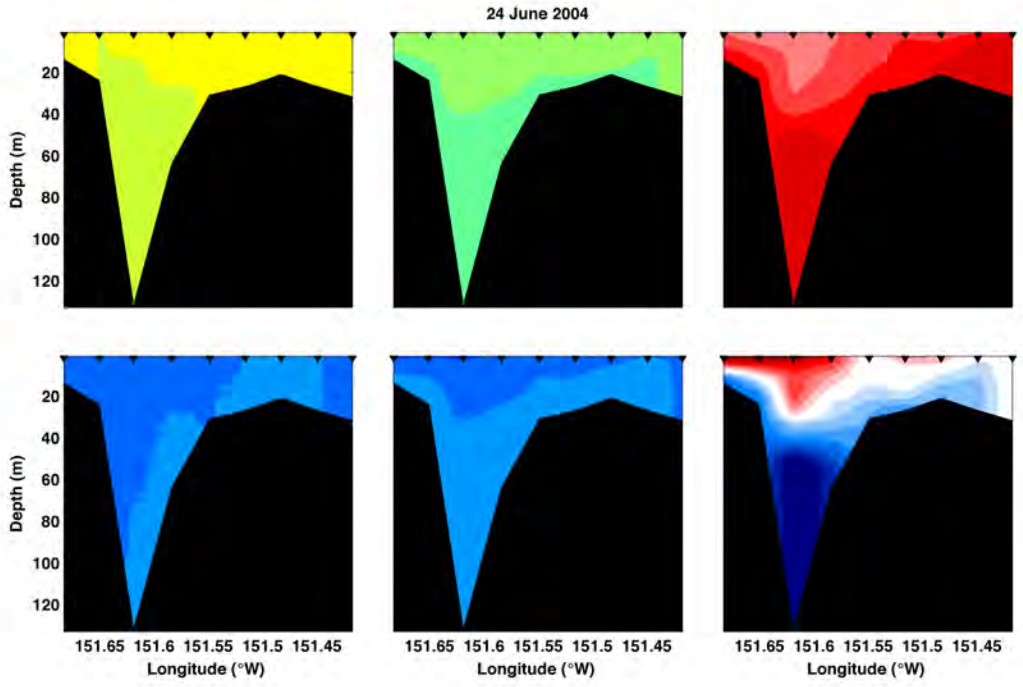

Figure A8.65: Transect 5.02 model-data comparison for temperature (top), salinity (bottom), with the observations shown on the left, the model in the center and the difference (observations-model) on the right.

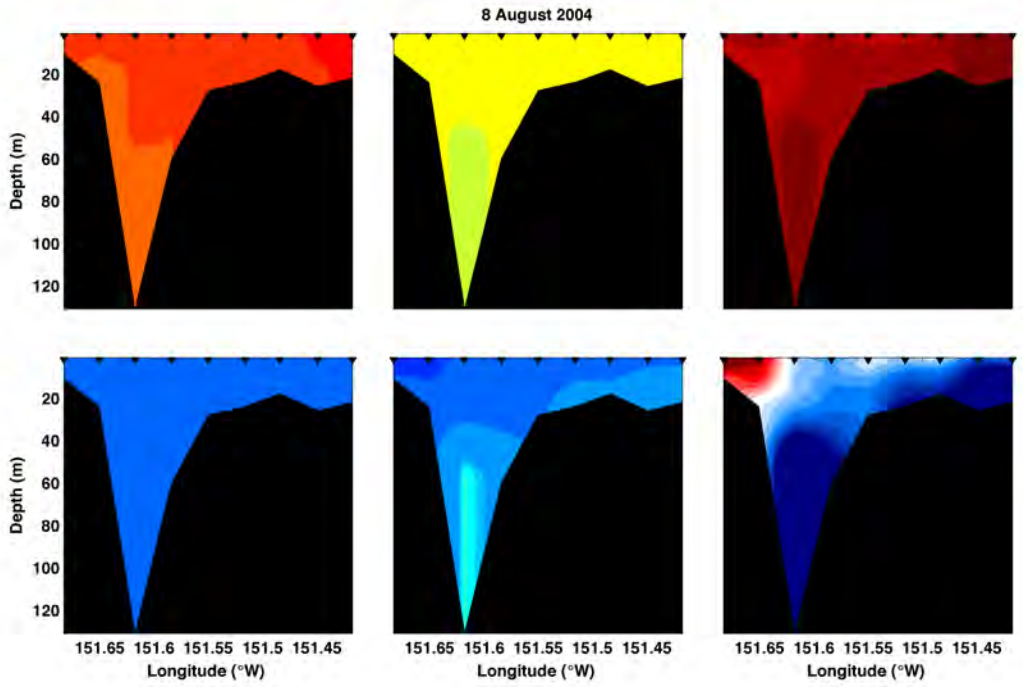

Figure A8.66: Transcect 5.03 model-data comparison for temperature (top), salinity (bottom), with the observations shown on the left, the model in the center and the difference (observations-model) on the right.

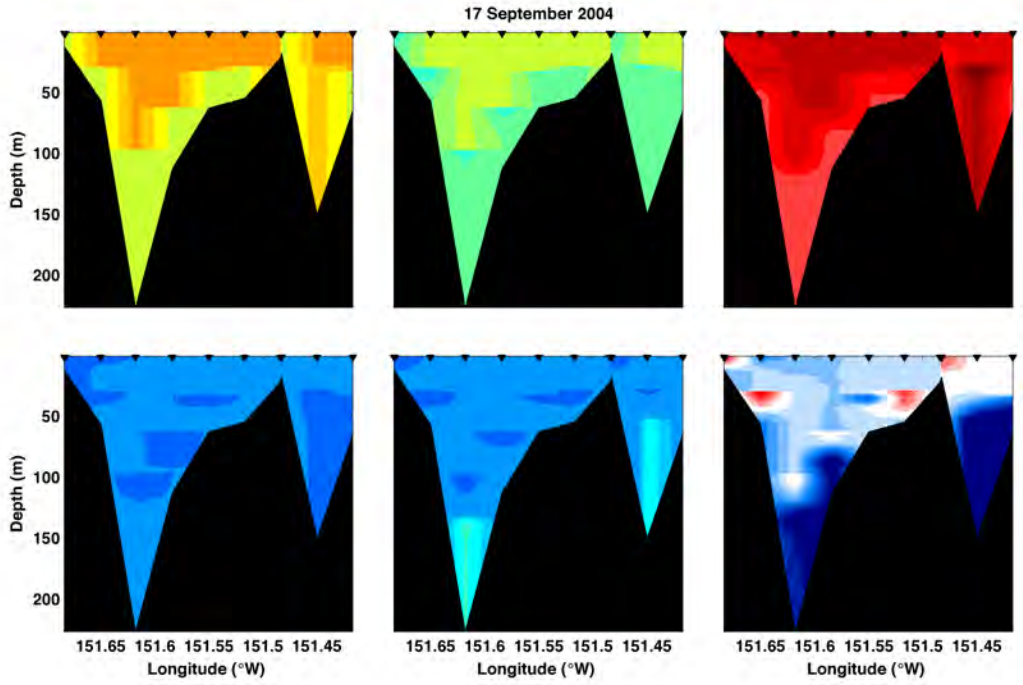

Figure A8.67: Transect 5.04 model-data comparison for temperature (top), salinity (bottom), with the observations shown on the left, the model in the center and the difference (observations-model) on the right.

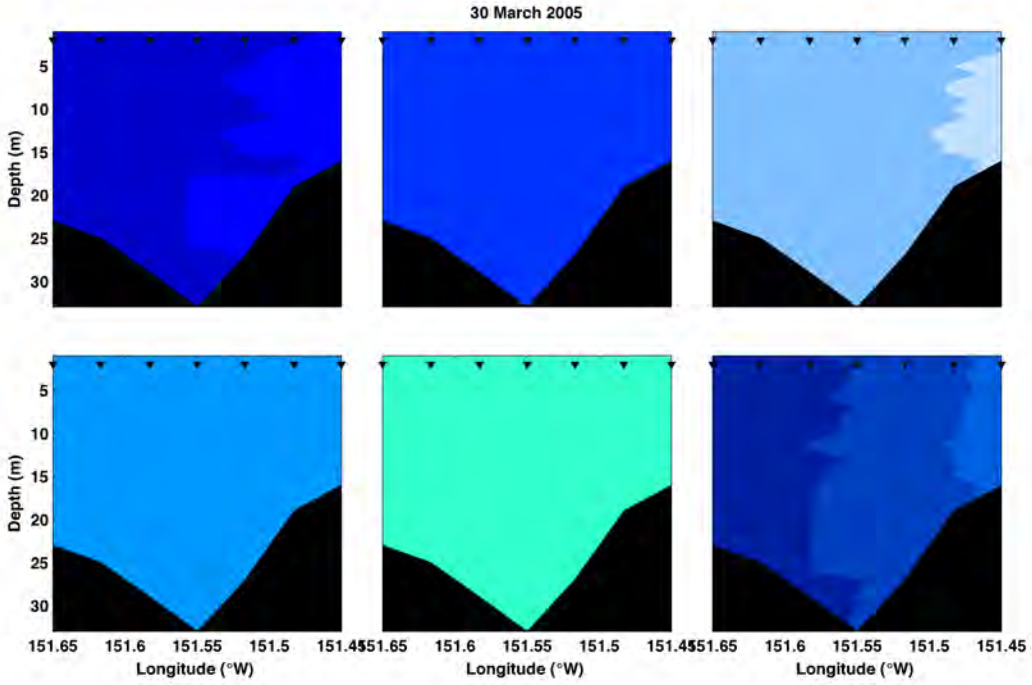

Figure A8.68: Transcect 5.05 model-data comparison for temperature (top), salinity (bottom), with the observations shown on the left, the model in the center and the difference (observations-model) on the right.

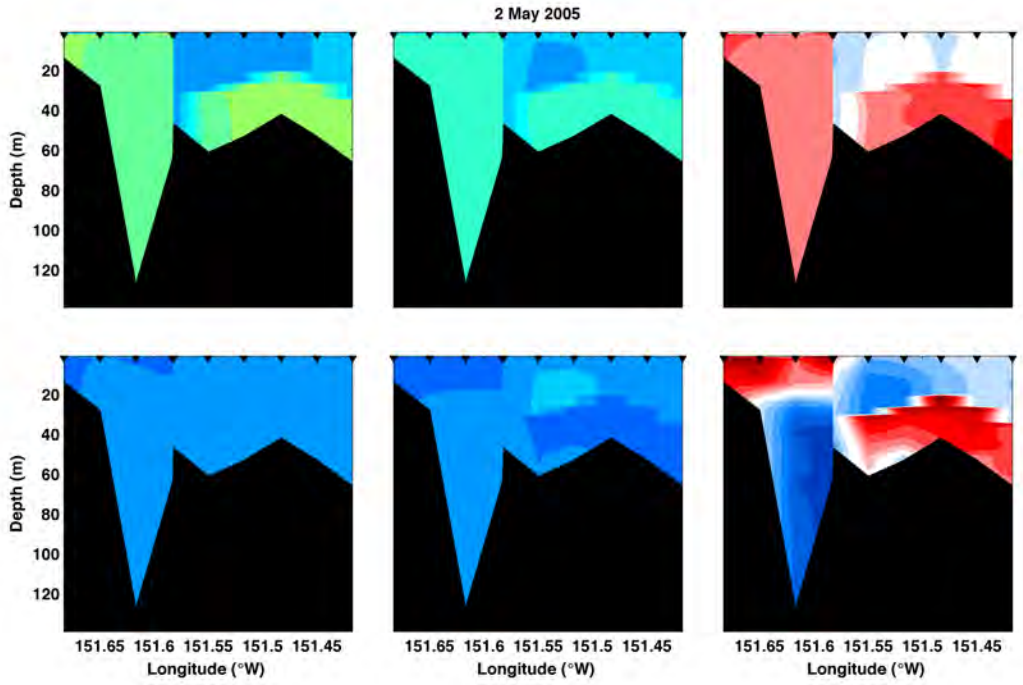

Figure A8.69: Transcect 5.06 model-data comparison for temperature (top), salinity (bottom), with the observations shown on the left, the model in the center and the difference (observations-model) on the right.

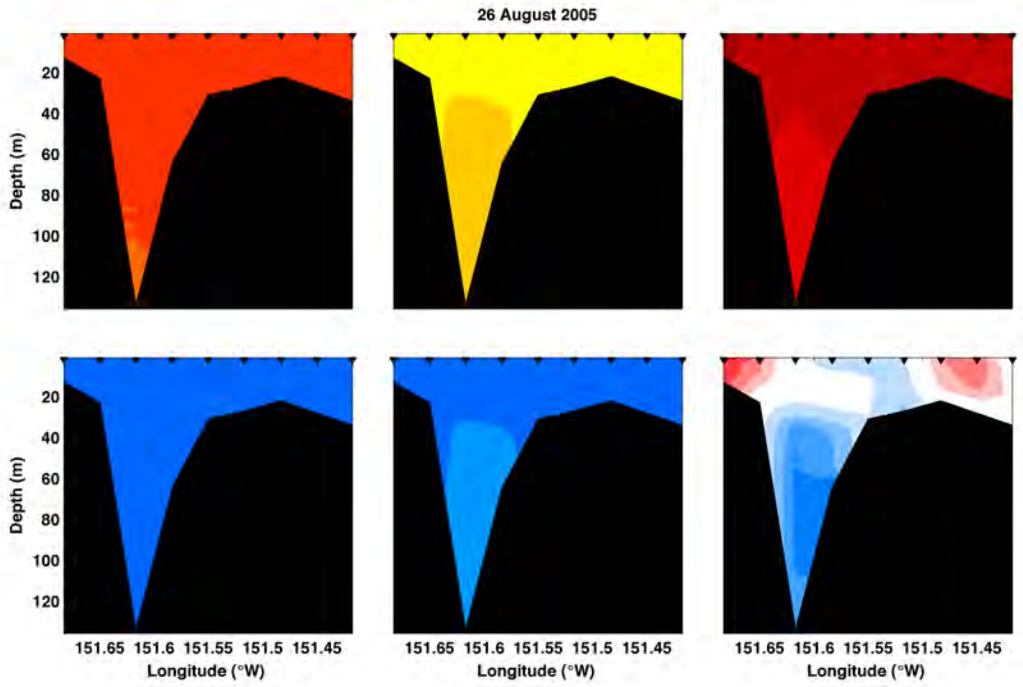

Figure A8.70: Transect 5.07 model-data comparison for temperature (top), salinity (bottom), with the observations shown on the left, the model in the center and the difference (observations-model) on the right.

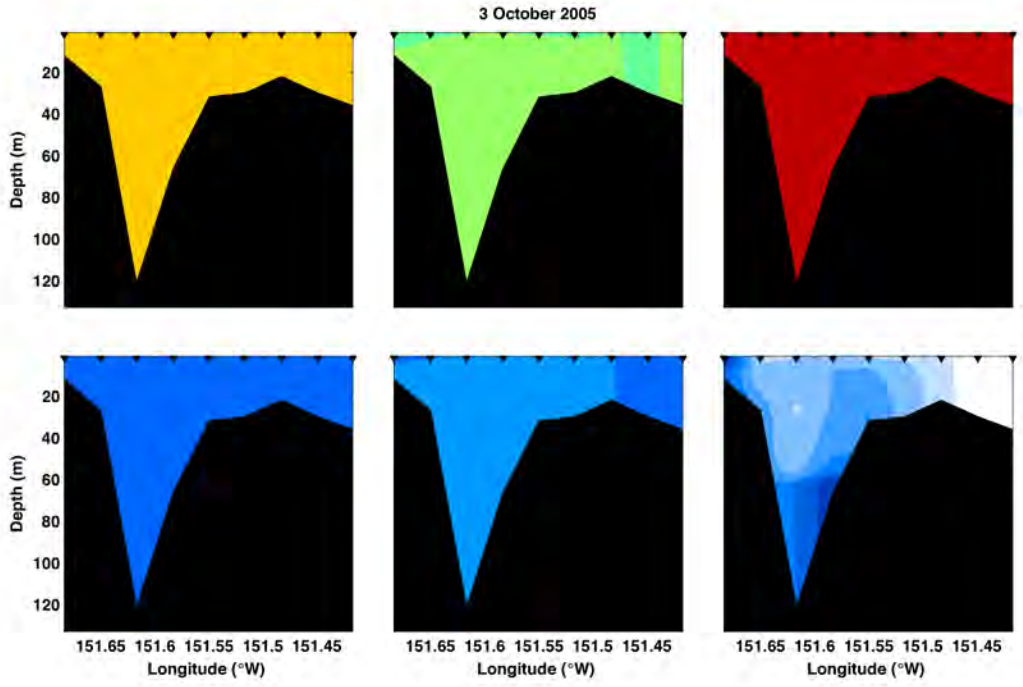

Figure A8.71: Transect 5.08 model-data comparison for temperature (top), salinity (bottom), with the observations shown on the left, the model in the center and the difference (observations-model) on the right.

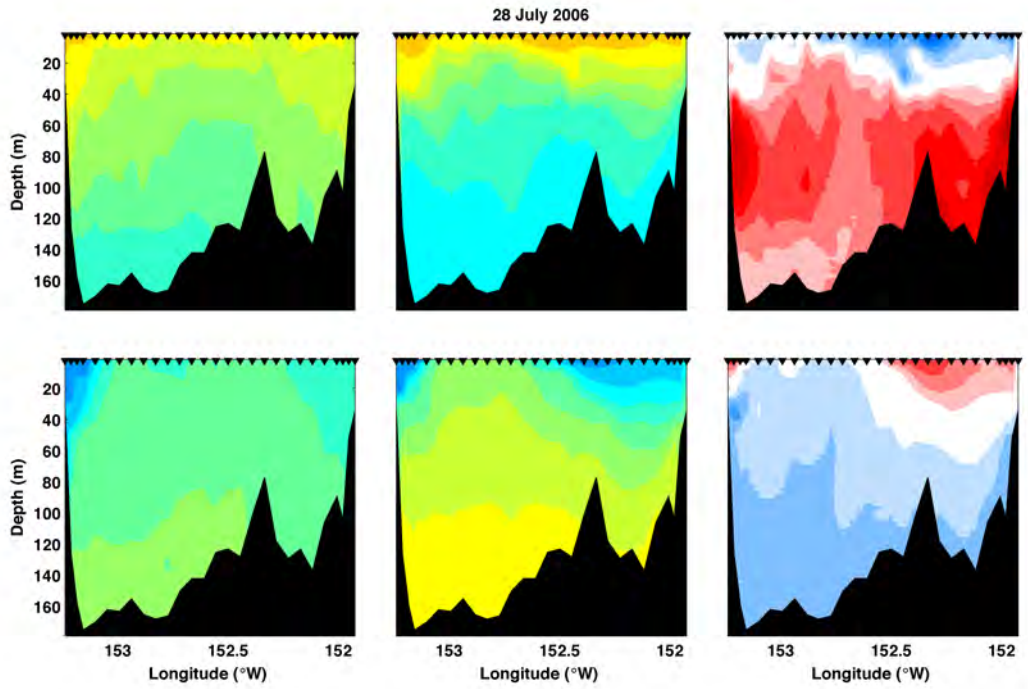

Figure A8.72: Transect 6.01 model-data comparison for temperature (top), salinity (bottom), with the observations shown on the left, the model in the center and the difference (observations-model) on the right.

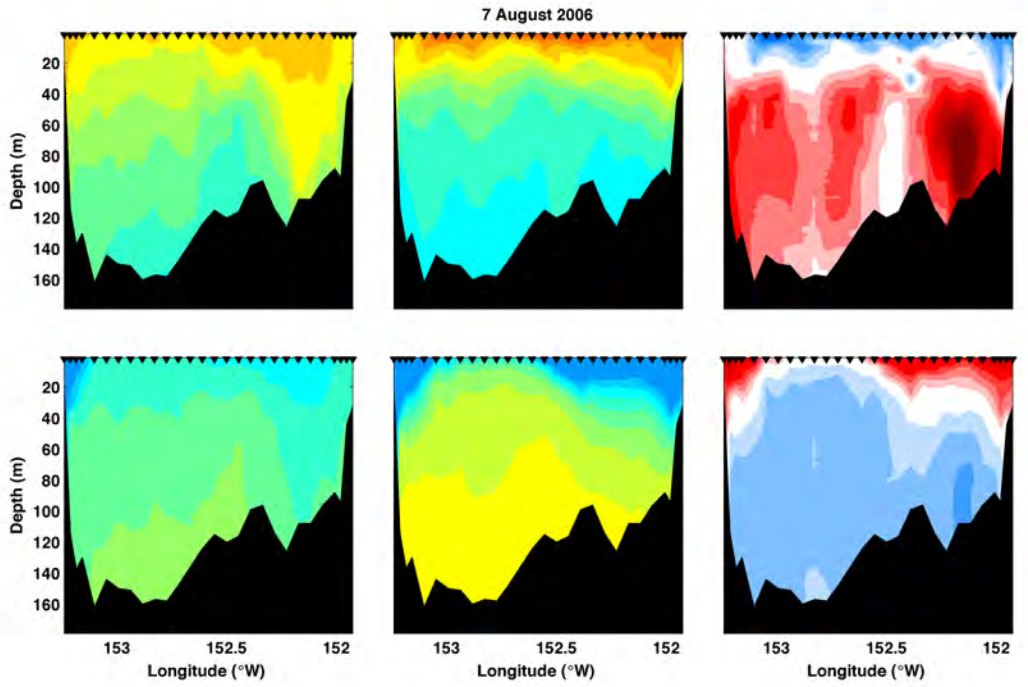

Figure A8.73: Transect 6.02 model-data comparison for temperature (top), salinity (bottom), with the observations shown on the left, the model in the center and the difference (observations-model) on the right.

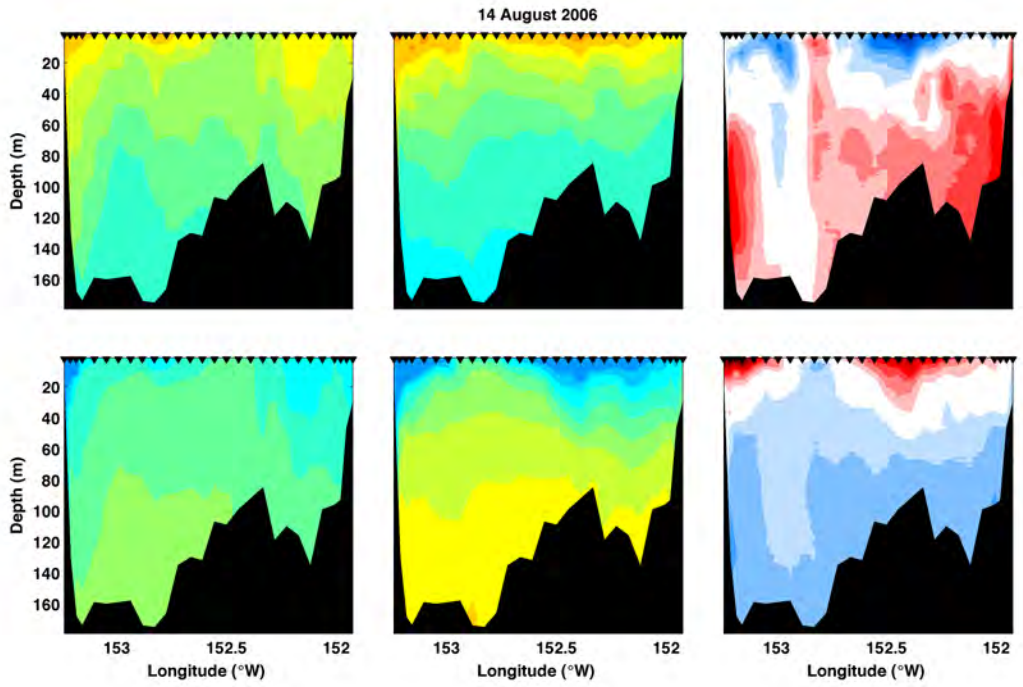

Figure A8.74: Transect 6.03 model-data comparison for temperature (top), salinity (bottom), with the observations shown on the left, the model in the center and the difference (observations-model) on the right.

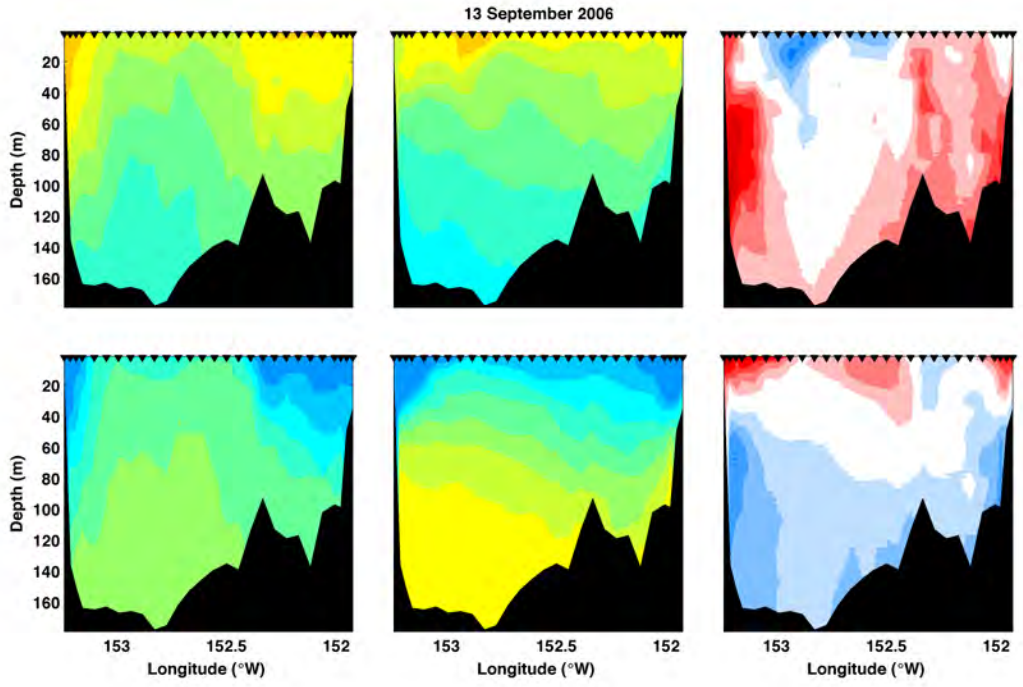

Figure A8.75: Transect 6.04 model-data comparison for temperature (top), salinity (bottom), with the observations shown on the left, the model in the center and the difference (observations-model) on the right.

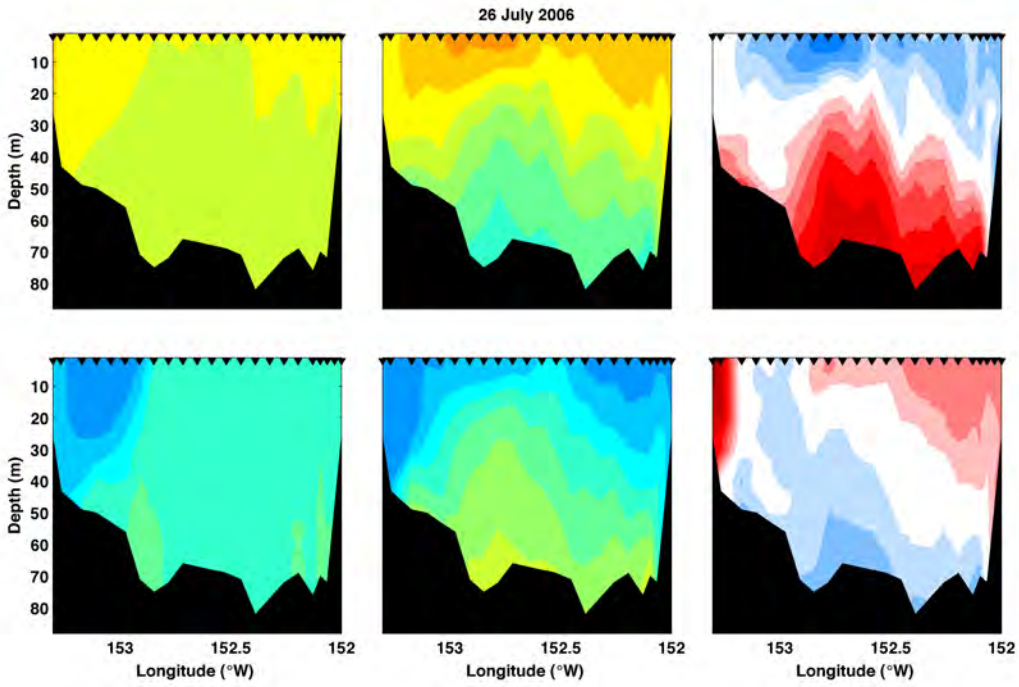

Figure A8.76: Transect 7.01 model-data comparison for temperature (top), salinity (bottom), with the observations shown on the left, the model in the center and the difference (observations-model) on the right.

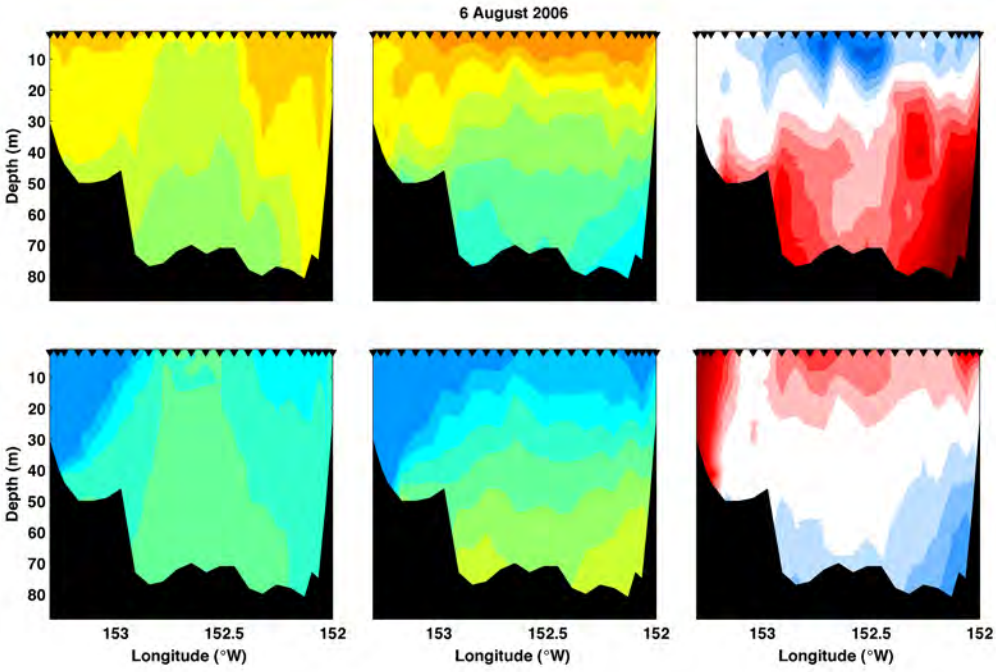

Figure A8.77: Transect 7.02 model-data comparison for temperature (top), salinity (bottom), with the observations shown on the left, the model in the center and the difference (observations-model) on the right.

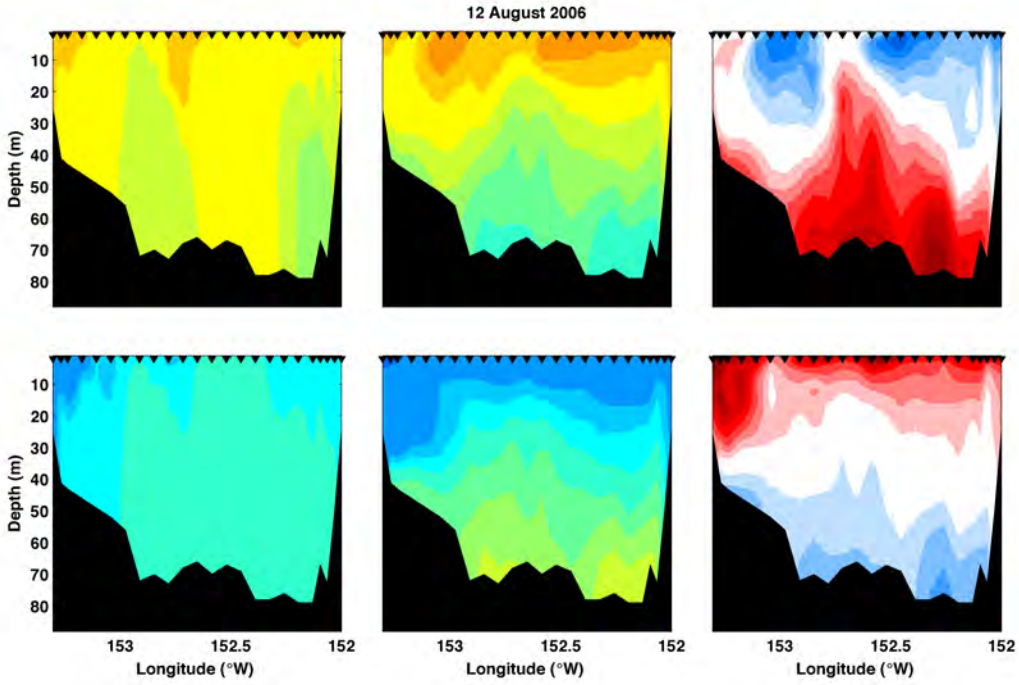

Figure A8.78: Transect 7.03 model-data comparison for temperature (top), salinity (bottom), with the observations shown on the left, the model in the center and the difference (observations-model) on the right.

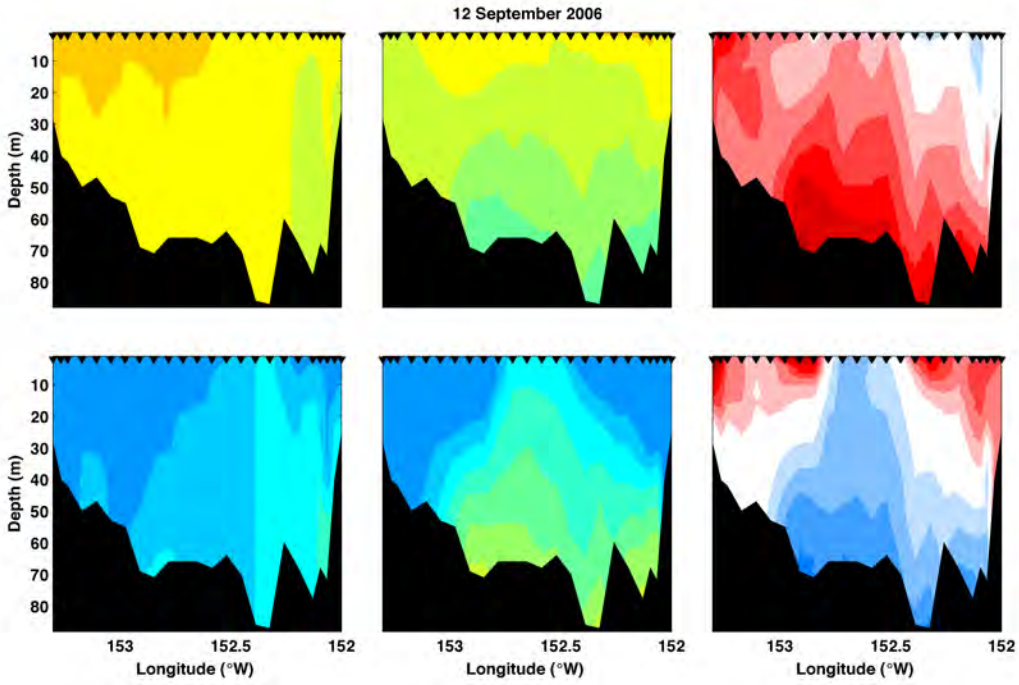

Figure A8.79: Transect 7.04 model-data comparison for temperature (top), salinity (bottom), with the observations shown on the left, the model in the center and the difference (observations-model) on the right.